Development and Application of Spectroscopic Techniques in the Mid-Infrared

A thesis submitted for the degree of Doctor of Philosophy

Kimberley Elaine Whittaker

Magdalen College, University of Oxford

Trinity Term 2014

Declaration of Authorship

I declare that this thesis titled 'Development and Application of Spectroscopic Techniques in the Mid-Infrared' and the work presented in it are my own. I confirm that the following statements are true.

- This work was done wholly while in candidature for a research degree at this University.
- Where any part of this thesis has previously been submitted for a degree or any other qualification at this University or any other institution, this has been clearly stated.
- Where I have consulted the published work of others, this is always clearly attributed.
- Where I have quoted from the work of others, the source is always given. With the exception of such quotations, this thesis is entirely my own work.
- I have acknowledged all main sources of help.
- Where the thesis is based on work done by myself jointly with others, I have made clear exactly what was done by others and what I have contributed myself.

Kimberley E Whittaker

_____

Signature

_____

Date

Development and Application of Spectroscopic Techniques in the Mid-Infrared

A thesis submitted for the degree of Doctor of Philosophy
Kimberley Elaine Whittaker, Magdalen College, University of Oxford
Trinity Term 2014

Abstract

Applications of laser absorption spectroscopy for trace gas detection are many and diverse, ranging from the environmental and atmospheric to the medical and industrial. The aim of creating a spectrometer which combines high sensitivities and selectivities (in order to measure small amounts of absorbers or species that are only weakly absorbing, in a complex background matrix) with a wide spectral coverage (to allow broadband absorbers or multi-component samples to be studied) can be realised by implementing three separate concepts: the exploitation of the strong, fundamental transitions of the mid-infrared; the use of sensitive spectroscopic techniques; and the selection of a widely tunable laser source. In this thesis, these ideas are investigated individually and in combination in order to achieve such a goal. Laser spectroscopic techniques based on optical cavities are used to build a high resolution spectrometer covering a large spectral range capable of selectively detecting low levels of gaseous compounds of interest, especially those of medical or environmental significance. Work in both the near- and mid-infrared is presented, including much of the initial, developmental work which was conducted in the former region.

The thesis begins with an overview of both narrowband and broadband near-infrared radiation sources, with a particular emphasis on commonly available diode lasers (DLs). A novel laser source, the digital supermode distributed Bragg reflector (DS-DBR) laser, is introduced as a useful laser source for spectroscopy, combining the usual benefits of telecom DLs with a wide tunability ($1563 - 1613$ nm). The laser can be operated in an internal or external ramping mode, allowing the output wavelength to be scanned or stepped across a desired region. The observation of mode-hopping during the application of the scanning methodology is examined and rationalised. The ability of the DS-DBR laser to perform high resolution spectroscopy over its entire spectral coverage is demonstrated by recording spectra of carbon dioxide (CO_2) over this range, covering transitions from two of the four Fermi resonance components of the $3\nu_1 + \nu_3$ combination band. The results of conducting wavelength modulation spectroscopy on CO_2 are also reported.

A system developed for performing cavity ring-down spectroscopy (CRDS), capable of the real-time retrieval of ring-down times (RDTs), is presented and discussed. The outcomes of initial tests performed with a conventional DL at 1557 nm, to study a calibrated mixture of CO_2 in air at various pressures, are given. In addition, the results of combining this system with the DS-DBR laser are discussed. The bandwidth of the DS-DBR laser was found to be larger than that of a standard DFB DL, resulting in the presence of noisy cavity modes. Despite this, the acquisition of reproducible RDTs is demonstrated, with single wavelength studies of an evacuated cavity at 1605.5 nm yielding a RDT of 24.54 ± 0.04 μs and Allan variance calculations signalling an attainable minimum detectable absorption coefficient,

$\alpha_{\min}$, of 2.8×10^{-10} cm^{-1} over 20 s. The ability to perform CRDS across the whole DS-DBR laser wavelength range without the need for cavity re-alignment is illustrated, and studies conducted on CO_2 in air, calibrated mixtures and breath are reported. Investigations are also described into the accurate determination of the $^{13}C/^{12}C$ ratio in exhaled CO_2 undertaken using CRDS and cavity enhanced absorption spectroscopy (CEAS) on CO_2 isotopologues, an approach which can be utilised as a diagnostic aid in determining *Helicobacter pylori* infection.

The focus of the thesis then moves to the mid-infrared, to describe quasi phase matching difference frequency generation (QPM-DFG) and its use to generate laser light at 3 µm by optically mixing near-infrared DLs. The theory behind this non-linear optical interaction is outlined, and the construction of a free-space QPM-DFG system using periodically poled lithium niobate is detailed and characterised.

This DL-based QPM-DFG arrangement has been coupled with the CRDS system developed to create a mid-infrared CRD spectrometer. The results of single wavelength studies indicate RDTs of ~ 6 µs and an achievable $\alpha_{\min}$ of 2.9×10^{-9} cm^{-1} over 44 s for an evacuated cavity. Spectroscopic investigations carried out on methane (CH_4), acetone and deuterium are documented; for the latter species, Dicke narrowing of the electric quadrupole $\nu(1 \leftarrow 0)$ $Q(2)$ transition at 2987.29 cm^{-1} is observed and the integrated absorption cross-section for the same transition measured as $2.29 \pm 0.03 \times 10^{-27}$ cm^{2}cm^{-1}molec^{-1}. The results of modifications made to the system, namely the use of a more powerful Nd:YAG laser as the pump radiation source, as well as a faster detector combined with a variable amplifier, are presented; these include the observation of an improved optimal $\alpha_{\min}$ of 6.4×10^{-10} cm^{-1} over 151 s for an empty cavity.

Finally, work utilising the DS-DBR laser as one of the near-infrared sources for the QPM-DFG set-up is presented. This configuration generates radiation covering a wide mid-infrared range ($3130 - 3330$ nm) and has been used to perform direct absorption and wavelength modulation spectroscopy on ro-vibrational transitions within the fundamental $\nu_3(F_2)$ band of CH_4. The spectrum of methanethiol (CH_3SH) over this region has also been investigated, with preliminary studies identifying a feature at 3040 cm^{-1} as a potential indicator for monitoring this biomarker in breath. The results of coupling this mid-infrared radiation with an optical cavity to perform CEAS combined with phase sensitive detection are subsequently reported. Studies were conducted on calibrated CH_4 mixtures and ambient air to examine two transitions of the fundamental $\nu_3(F_2)$ band of CH_4 in order to characterise the system: effective path lengths of ~ 700 m and $\alpha_{\min}$ of 6.2×10^{-8} cm^{-1} over 8 s were found. The $^RQ_4$ CH_3SH absorption feature at 3040 cm^{-1} was also further studied with this system using prepared samples of CH_3SH in N_2 at different concentrations, yielding a CH_3SH detection limit of 2.4 ppm at 19 Torr. The potential of such a cavity-based, DS-DBR sourced, QPM-DFG mid-infrared spectrometer for trace gas sensing having thus been demonstrated, possible improvements that could be implemented to increase the sensitivity of the system are then discussed.

Acknowledgements

Although I am bound to declare that 'this thesis and the work presented in it are my own', this statement is not really true, for there are so many people without whom this thesis would not have been possible and to whom I owe a huge debt of gratitude. First and foremost, my unending thanks must go to Grant, who accepted me into his group despite my association with 'the other place', and whose insights, ideas and ceaseless enthusiasm have been a source of inspiration and encouragement. Thanks are also due to Gus and Rob for all their advice and help over the years, a product of their enormous wealth of experience and knowledge.

I must also say a big thank you to the all the post-docs of the group, past and present, whose expertise and guidance have been invaluable. Above all, I am greatly indebted to Luca, who has taught me everything I know about difference frequency generation, spectral lineshapes and the Italian way of life - thank you so much for your kindness and patience in taking the time to explain everything to me! Particular thanks also go to Graham for knowing where everything is in the labs and to Michele for his computer modelling wizardry.

My peers within the group have also been a great source of help in times of trouble, as well as making the lab a jolly fun place to be. Thanks to Katy for my initial orientation and providing a continuous supply of doughnuts, to Ann for her assistance with the vac line and shared love of tea, to Lee for all his LaTeX help and Doctor Who chat, as well as to Beth, Martin, the two Riches, Julian, Gilly, James, Helen, Katherine and Sarah for entertaining tea-time conversation and tasty cakes. I have been really fortunate to have such a fantastic and friendly group of people to work with.

All the excellent people who toil away behind the scenes at the PTCL also deserve a massive round of applause. The electronics and mechanical workshops have worked wonders with broken equipment and malfunctioning appliances; I must especially thank Phil and Neville from electronics who have put up with my never-ending requests for modifications and improvements to pieces of kit - true masters of the soldering iron!

Aid from beyound these four walls also requires recognition. In particular, the help provided by Meez Islam from Teesside University on his summer visits to the group warrant a mention, and many thanks must also go to the Laser Chemistry, Spectroscopy and Dyanmics Group at the University of Bristol for past collaborations and continual loans of key pieces of equipment.

Finally, my acknowledgements would not be complete without thanking all my friends and family who have supported me during my time at Oxford and made the last four years so enjoyable. Old friends from school and Cambridge, as well as new ones from Magdalen

and Oxford, have meant I have never been stuck for people to talk to or things to do, and have given me another wonderful assortment of memories to treasure. Above all, it is the unwavering love and support from my Mum and Dad, as well as from my little brother, that have really sustained me during my time here, indeed throughout my whole life, and to them I am eternally grateful.

List of Publications

- **Demonstration of a widely tunable digital supermode distributed Bragg reflector laser as a versatile source for near-infrared spectroscopy**
  L. Ciaffoni, G. Hancock, P. L. Hurst, M. Kingston, C. E. Langley, R. Peverall, G. A. D. Ritchie, K. E. Whittaker
  Applied Physics B: Lasers and Optics, **110**, 139-145 (2013)

- **Combining a DS-DBR laser with QPM-DFG for mid-infrared spectroscopy**
  K. E. Whittaker, L. Ciaffoni, G. Hancock, M. Islam, R. Peverall, G. A. D. Ritchie
  Applied Physics B: Lasers and Optics, **109**, 423-432 (2012)

- **A DFG-based cavity ring-down spectrometer for trace gas sensing in the mid-infrared**
  K. E. Whittaker, L. Ciaffoni, G. Hancock, R. Peverall, G. A. D. Ritchie
  Applied Physics B: Lasers and Optics, **109**, 333-343 (2012)

- **Using a DS-DBR laser for widely tunable near-infrared cavity ring-down spectroscopy**
  K. E. Whittaker, L. Ciaffoni, G. Hancock, P. L. Hurst, R. Peverall, G. A. D. Ritchie
  Applied Physics B: Lasers and Optics, **116**, 157-168 (2014)

Contents

Nomenclature

Roman Symbols

a_m	Modulation amplitude/ cm^{-1}
A	Complex electric field amplitude
$A(\nu)$	Absorbance
A_m	Lock-in amplifier modulation amplitude/ mV
b	Modulation index
b	Confocal parameter
b_{opt}	Optimal confocal parameter
B^{ν}_{mn}	Einstein absorption coefficient for a transition $n \leftarrow m$, in terms of frequency
c	Speed of light $= 2.998 \times 10^8$ ms^{-1}
C	Concentration of absorbing species
d	Absorber path length inside cavity
d_{eff}	Effective non-linear susceptibility constant
D	Optical diffusion coefficient
D_0	Pressure-independent optical diffusion coefficient
D_m	Conventional mass diffusion coefficient
$D^*(\nu)$	Detectivity
e	Euler's number = 2.718

e	Elementary charge $= 1.602 \times 10^{-19}$ C
E	Energy
$E(t)$	Applied electric field
f	Focal length of lens
Δf	Detector bandwidth (frequency)
F	Total angular momentum quantum number, including nuclear spin
F	Cavity finesse
F_c	Coefficient of finesse
g	g-parameter
$G(\nu)$	Gaussian profile
h	Planck's constant $= 6.626 \times 10^{-34}$ Js
$\hbar$	$h/2\pi$
$h(\xi, \sigma, \mu, \alpha, L_{\text{crys}})$	Focusing function
i	Imaginary unit $= \sqrt{-1}$
i	Current
I	Intensity of radiation
J	Total angular momentum quantum number, excluding nuclear spin
$J(z)$	Photolysis rate constant at an altitude z
k	Propagation wavevector
k_B	Boltzmann constant $= 1.381 \times 10^{-23}$ JK^{-1}
Δk	Wavevector mismatch
Δk_{QPM}	Wavevector mismatch for QPM
K	Angular momentum quantum number for rotation about the symmetry axis
l	Absorption path length

L	Length of optical cavity
$L(\nu)$	Lorentzian profile
L_c	Coherence length
L_{crys}	Length of crystal
L_{eff}	Effective cavity path length
m	Mass of molecule
M_r	Relative molecular mass
n	Refractive index
n_{avg}	Number of ring-downs to record per point
$N(\nu)$	Galatry profile
p	Pressure
P	Power
$P(t)$	Induced electric polarisation
$q(z)$	Complex beam parameter
Q_r	Rotational partition function
r	Radius of curvature
$r_{13/12}$	Ratio of areas or heights of $^{13}\text{C}/^{12}\text{C}$ absorption features
R	Geometric mean of mirror reflectivities $= \sqrt{R_1 R_2}$
R_n	Mirror reflectivity of individual mirror, n
$\boldsymbol{R}_{nm}$	Transition dipole moment for a transition $n \leftarrow m$
$R_{13/12}$	Ratio of $^{13}\text{C}/^{12}\text{C}$ concentrations
$R_{13/12,0}$	Reference ratio of $^{13}\text{C}/^{12}\text{C}$ concentrations
R^2	Goodness of fit parameter, coefficient of determination
t	Time

t_{acq}	Acquisition time for one scan
t_{disc}	Initial time of ring-down decay discarded before fitting
t_{fit}	Length of time of ring-down decay used to fit exponential
t_{int}	Acquisition time for one spectral point in CRD spectrum
t_{off}	Time offset used to fit double exponential decay
t_{rec}	Length of time recorded by DAQ card
t_{sett}	Settling time between laser steps for laser stabilisation
T	Temperature
T_{crys}	Temperature of crystal
T_{opt}	Optimal crystal temperature
$V(\nu)$	Voigt profile
V_{amp}	Amplitude of voltage ramp applied to PZT
V_{freq}	Frequency of voltage ramp applied to PZT
V_{mod}	Output voltages of the DAQ card to step a laser diode current controller
V_{off}	Offset frequency of piezo driver
$w(z)$	Spot size of Gaussian beam
w_0	Beam waist of Gaussian beam
$W(z)$	Complex error function, Faddeeva function
z	Narrowing parameter

Greek Symbols

$\alpha(\nu)$	Absorption coefficient/ cm^{-1}
α_p	Peak absorption coefficient/ cm^{-1}
α_{min}	Minimum detectable absorption coefficient/ cm^{-1}
$\alpha_{\mathrm{min}}(BW)$	Bandwidth reduced minimum detectable absorption coefficient/ $\mathrm{cm}^{-1}\mathrm{Hz}^{-1/2}$

$\alpha_{\min}(TR)$	Time reduced minimum detectable absorption coefficient/ $\mathrm{cm^{-1}s^{1/2}}$
δ	Line shift parameter
$\delta^{13}\mathrm{C}$	Isotopic ratio of $^{13}\mathrm{C}/^{12}\mathrm{C}$ compared to reference/ ‰
$\Delta\nu$	Linewidth (FWHM)
$\Delta\nu_D$	Doppler width (FWHM)
$\Delta\nu'_D$	1/e Doppler half-width (HWHM)
$\Delta\nu_{\mathrm{FSR}}$	Free spectral range (FSR)
$\Delta\nu_G$	Gaussian width (FWHM)
$\Delta\nu_L$	Lorentzian width (FWHM)
$\Delta\nu_{\mathrm{mode}}$	Cavity mode linewidth (FWHM)
$\Delta\nu_V$	Voigt width (FWHM)
ϵ_0	Vacuum permittivity
ϵ_r	Relative permittivity
γ	Pressure broadening coefficient (HWHM)
Γ	Lineshape parameter
η	Quantum efficiency
η	DFG conversion efficiency
λ	Wavelength
Λ	Poling period
$\hat{\boldsymbol{\mu}}$	Electric dipole moment operator
μ_r	Relative permeability $\cong 1$
ν	Frequency
ν_0	Central frequency of absorption feature, line centre
$\tilde{\nu}$	Wavenumber

ω	Angular frequency
ω_1, ω_p	Pump radiation
ω_2, ω_s	Signal radiation
ω_3, ω_i	Idler radiation
ϕ	Molecular diameter
ϕ_i	Quantum yield of species i
ψ	Energy level wavefunction
$\rho(\nu)$	Spectral radiation density
σ	Phase mismatch parameter
$\sigma(\nu)$	Absorption cross-section coefficient/ cm^2molec^{-1}
σ_p	Peak absorption cross-section/ cm^2molec^{-1}
σ_{int}	Integrated absorption cross-section/ $cm^2cm^{-1}molec^{-1}$
τ	Time constant
$\tau(\nu)$	Ring-down time (RDT)
τ_{act}	True ring-down time
τ_0	Ring-down time of empty cavity
τ_{det}	Contribution to recorded ring-down time from the electronics
τ_{meas}	Ring-down time recorded
χ	Electric susceptibility

Acronyms

AO	Analogue output
AOM	Acousto-optic modulator
AR	Anti-reflection
AS	Absorption spectroscopy

ASE	Amplified spontaneous emission
BBCEAS	Broadband cavity enhanced absorption spectroscopy
BPM	Birefringent phase matching
BW	Bandwidth
CEAS	Cavity enhanced absorption spectroscopy
CE-DFCS	Cavity enhanced direct frequency comb spectroscopy
cgs	cgs system of units: cm for distance, g for mass and s for time
CRDS	Cavity ring-down spectroscopy
cw	Continuous wave
DAQ	Data acquisition
DAS	Direct absorption spectroscopy
DBR	Distributed Bragg reflector
DFB	Distributed feedback
DFG	Difference frequency generation
DL	Diode laser
DM	Dichroic mirror
DS-DBR	Digital supermode distributed Bragg reflector
EC	External cavity
ECDL	External cavity diode laser
ECL	External cavity laser
EDFA	Erbium doped fibre amplifier
EM	Electromagnetic
EOM	Electro-optic modulator
esu	Electrostatic unit

FM	Frequency modulation
FMS	Frequency modulation spectroscopy
FP	Front pair
FSR	Free spectral range
FTIR	Fourier transform infrared
FWHM	Full-width half-maximum
GC-IRMS	Gas chromatography isotope ratio mass spectrometry
H. pylori	*Helicobacter pylori*
HWHM	Half-width half-maximum
ICL	Interband cascade laser
ICOS	Integrated cavity output spectroscopy
IL	In-line
IR	Infrared
L	Lens
LDLS	Laser driven light source
LED	Light emitting diode
LIA	Lock-in amplifier
LRS	Linear regression of the sum
M	Mirror
MC	Mechanical chopper
MCT	Mercury-cadmium-telluride, HgCdTe
MCZT	Mercury-cadmium-zinc-telluride, HgCdZnTe
MEMS	Microelectromechanical systems
MG	Modulated grating

MKS	MKS (SI) system of units: m for distance, kg for mass and s for time
NDIR	Non-dispersive infrared
NEP	Noise equivalent power
NICE-OHMS	Noise immune cavity enhanced optical heterodyne molecular spectroscopy
NLO	Non-linear optics
OA	Off-axis
OF	Optical feedback
OF-CEAS	Optical feedback cavity enhanced absorption spectroscopy
OFCS	Optical frequency comb synthesiser
OI	Optical isolator
OPO	Optical parametric oscillator
OR	Optical rectification
p	Pulsed
PAS	Photoacoustic spectroscopy
PD	Photodiode
PDB	Pee Dee Belemnite
PM	Phase matching
PM	Polarisation maintaining
ppm	Parts per million, 10^6
ppb	Parts per billion, 10^9
ppt	Parts per trillion, 10^{12}
ppq	Parts per quadrillion, 10^{15}
PPLN	Periodically poled lithium niobate
PS	Phase shift

PS-CRDS	Phase shift cavity ring-down spectroscopy
PZT	Piezoceramic transducer
QCL	Quantum cascade laser
QE	Quartz enhanced
QPM	Quasi phase matching
QW	Quantum well
RAM	Residual amplitude modulation
RDT	Ring-down time
RF	Radio frequency
rms	Root mean square
RMSE	Root mean square error
RT	Room temperature
rtp	Room temperature and pressure: $T = 298.15$ K, $p = 100$ kPa
RUT	Rapid urease test
SA	Spectrum analyser
SBS	Stimulated Brillouin scattering
SC	Supercontinuum
SCAR	Saturated-absorption cavity ring-down spectroscopy
SFG	Sum frequency generation
SG	Sampled grating
SHG	Second harmonic generation
SLED	Superluminescent light emitting diode
SNL	Shot noise limit
SNR	Signal-to-noise ratio

SOA	Semiconductor optical amplifier
stp	Standard temperature and pressure: $T = 273.15$ K, $p = 100$ kPa
TEC	Thermoelectric cooler
TEM_{mn}	Transverse electromagnetic modes
UBT	^{13}C-urea breath test
UV	Ultraviolet
VOC	Volatile organic component
WM	Wavelength modulation
WMS	Wavelength modulation spectroscopy
YDFA	Ytterbium doped fibre amplifier

"Equipped with his five senses, man explores the universe around him and calls the adventure Science"

Edwin Powell Hubble, *The Exploration of Space*, 1929

Chapter 1

Introduction

Applications for trace gas detection are numerous and diverse, ranging from the environmental and atmospheric to the industrial and medical. In many cases, absolute number densities are required and absorption spectroscopy is one technique that can provide such quantitative analysis. Often high sensitivity and selectivity are also needed in order to monitor weakly absorbing species or those at low concentrations within a multi-component matrix. In this chapter, the principles of absorption spectroscopy are explained and the methods by which the achievable sensitivities can be increased are outlined. In particular, techniques based on optical cavities are discussed, as well as the advantages of exploiting the strong absorptions in the mid-infrared. Some examples of the applications of absorption spectroscopy to gas sensing are presented before concluding the chapter with an overview of the content and scope of this thesis.

1.1 Absorption Spectroscopy

1.1.1 The interaction of light and matter

Electromagnetic (EM) radiation is comprised of electric and magnetic field components oscillating in phase perpendicular to each other and to the direction of wave propagation and energy transfer [1–3]. This radiation, which includes the traditional 'visible' light as well as radiation of longer and shorter wavelengths, exhibits wave-like behaviour as it travels through space, but under certain conditions it can also be observed to act as particles called photons [4]. This wave-particle duality means the energy of the radiation, E, can be expressed in terms of either its wave or particle properties:

$$E = h\nu = pc \tag{1.1}$$

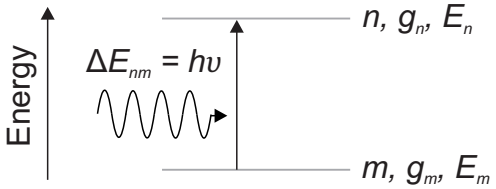

Figure 1.1: Energy level diagram of an absorption transition from a lower state, m, with energy E_m and degeneracy g_m, to an upper state n, with energy E_n and degeneracy g_n. The energy of the photon required to cause this transition must be equal to the energy difference between the two levels, ΔE_{nm}.

where h is Planck's constant, ν is the frequency of the wave, p is the momentum of the photon and c is the speed of light. The frequency of the radiation is related to its wavelength, λ, by $c = \nu\lambda$.

Spectroscopy is the study of the interaction between light and matter and it can reveal a wealth of information about the identities, amounts, structures and energy levels of species [4]. The energy level structure of matter at an electronic level and in its rotational, vibrational and translational movements means that a substance consists of states at discrete, fixed energies, and so transitions between these states have fixed energies too. Optical transitions to a lower energy level result in the emission of radiation from a material, whereas transitions to a higher energy level occur if radiation is absorbed on its passage through the substance. Absorption spectroscopy is the study of this absorption of radiation when it interacts with a sample, and relates to both the energies (frequencies) at which this occurs and the magnitude (intensity) of the absorption.

The absorption of a photon, causing a transition from an initial, lower level m to a final, higher level n, will only occur if certain selection rules are fulfilled. Firstly, the energy of the absorbed photon must be equal to the energy difference between the states, *i.e.* $\Delta E_{nm} = E_n - E_m = h\nu$ (Figure 1.1). The interaction between the electric field of the radiation and the electric dipole moment of the molecular transition of interest must also be considered [5]. This interplay is known as the transition amplitude or transition dipole moment, $\boldsymbol{R}_{nm}$, and for the transition $n \leftarrow m$ it is defined as [3–5]:

$$\boldsymbol{R}_{nm} = \int \psi_n^* \hat{\boldsymbol{\mu}} \psi_m \mathrm{d}\tau \tag{1.2}$$

where $\hat{\boldsymbol{\mu}}$ is the electric dipole moment operator, ψ_m and ψ_n are the wavefunctions of the levels m and n, respectively, and the integral is evaluated over all spatial, temporal and spin coordinates. $\boldsymbol{R}_{nm}$ represents the degree of coupling between the initial and final states and quantum mechanically describes how the electric dipole moment operator acts on the initial state to transform it to the final state. The size of this transition dipole can be thought of as a measure of the charge redistribution that occurs during the transition.

The rate of change of the population of the lower state m, N_m, due to stimulated absorption is given by [3]:

$$\frac{\mathrm{d}N_m}{\mathrm{d}t} = -B^{\nu}_{mn} N_m \rho(\nu) \tag{1.3}$$

where $\rho(\nu)$ is the spectral radiation density per unit frequency interval and B^{ν}_{mn} is the Einstein absorption coefficient for the transition $n \leftarrow m$ in terms of these frequency units. B^{ν}_{mn} is related to the transition dipole by [4–6]:

$$B^{\nu}_{mn} = \frac{|\boldsymbol{R}_{nm}|^2}{6\epsilon_0 \hbar^2} \tag{1.4}$$

where ϵ_0 is the vacuum permittivity and $\hbar = h/2\pi$. Thus the probability that the transition will take place is proportional to the square of the transition dipole moment, thereby supplying a second, gross selection rule which must be satisfied in order for the dipole transition to occur: the transition dipole moment must be non-zero, *i.e.* $\boldsymbol{R}_{nm} \neq 0$. It is worth noting that forbidden transitions between energy levels may still occur based on non-electric dipole interactions, either by other mechanisms such as quadrupole transitions or by the mixing of states if the structure of the material allows the internal electric and magnetic fields to break certain symmetries so that originally dipole-forbidden transitions become possible (*e.g.* ions embedded in a crystal lattice or glass). These processes, however, are much less likely, and are therefore only of weak intensity.

The greater the transition rate, the greater the measured absorption. Equation 1.3 indicates that this depends upon the magnitude of the Einstein absorption coefficient, which is also given by [7, 8]:

$$B^{\nu}_{mn} \frac{h\nu}{c} = \int_0^{\infty} \sigma_{mn}(\nu) \mathrm{d}\nu = \sigma_{\mathrm{int}} \tag{1.5}$$

where $\sigma_{mn}(\nu)$ is the frequency-dependent absorption cross-section for the transition $n \leftarrow m$, and σ_{int} is the integrated absorption cross-section. This can be used to derive the well-known Beer-Lambert law [7, 9]:

$$I(\nu) = I_0(\nu) \mathrm{e}^{-\sigma(\nu) C l} \tag{1.6}$$

where $I(\nu)$ and $I_0(\nu)$ are the intensities of the transmitted and incident radiation, respectively, $\sigma(\nu)$ is the frequency-dependent absorption cross-section, l is the absorption path length and C is the concentration of the absorbing species. This law describes the intensity attenuation of light as it passes through a sample, which varies with frequency. The product $\sigma(\nu)Cl$ is commonly referred to as absorbance, $A(\nu)$, and $\sigma(\nu)C$ as the absorption coefficient, $\alpha(\nu)$.

1.1.2 Absorption profiles

The energy levels in systems are usually regarded as sharp, distinct states with clearly defined energies, which would result in transitions between pairs of states with fixed energies leading to the presence of single lines or δ functions in the spectrum. However, this is not the case. Instead, the observed lineshape of a transition is a result of many contributing factors and broadening processes. These broadening mechanisms can either be homogeneous or inhomogeneous. Homogeneous broadening occurs in situations when the particles are treated equivalently; this includes natural and pressure broadening and results in Lorentzian profiles. Inhomogeneous broadening, in contrast, takes places when the properties or environment of the particles are non-identical so the shifts and perturbations of absorption frequencies vary between the molecules or atoms; this includes Doppler broadening and gives rise to Gaussian profiles.

Natural broadening [10] is an intrinsic and inescapable process that arises for all transitions. It is due to the fact that all the states are not at distinct, defined energies but rather spread out over a small, finite energy range because of the uncertainty in measuring the energy. By analogy with Heisenberg's uncertainty principle, the energy-time uncertainty relation can be derived which states that the product of the uncertainty in the energy measurement, ΔE, and the time interval required to perform this evaluation, Δt, is $\Delta E \Delta t \approx \hbar/2$ [5]. As the excited particle can only be observed for a period equivalent to its lifetime, τ, this then becomes:

$$\tau \Delta E \approx \frac{\hbar}{2} \tag{1.7}$$

Using the relationship $E = h\nu$, this can be further reorganised to:

$$\Delta\nu \approx \frac{1}{2\pi\tau} \tag{1.8}$$

indicating that the longer the lifetime of a state, the smaller the natural broadening. If the lower state is not the ground state, then the amount of natural broadening depends on the lifetimes of both the upper and lower states. Additional substitutions for expressions of the lifetime and Einstein coefficients yield the result that $\Delta\nu$ varies with ν^3, and also that the consequential lineshape of this type of broadening is a Lorentzian profile [10]:

$$L(\nu) = \frac{2}{\pi} \frac{\Delta\nu_L}{\Delta\nu_L^2 + 4(\nu - \nu_0)^2} \tag{1.9}$$

where ν_0 is the central frequency of the absorption feature and $\Delta\nu_L$ is the full-width half-maximum (FWHM) Lorentzian width.

For rotational-vibrational (ro-vibrational) spectra of molecular gases, this natural broadening is overwhelmed by the presence of other broadening mechanisms so it forms only a small

component of the overall lineshape (from 10^{-4} Hz for rotational transitions to several MHz for excited electronic levels). The other major homogeneous broadening process is pressure, or collisional, broadening. This is due to the interactions of an absorbing particle with its neighbours. As the collision frequency increases, the lifetime of both states involved in the transition is reduced, which through Equation 1.7 raises the uncertainty of the transition energy and so causing further variations in the absorbed frequency and a broadening of the lineshape. These collisions may be hard or soft collisions with neutral particles, collisions with charged particles or via long range intermolecular interactions such as Van der Waals forces. Pressure broadening also produces a Lorentzian profile (Equation 1.9), with $\Delta\nu_L$ given by:

$$\Delta\nu_L = 2\gamma p \tag{1.10}$$

where γ is the pressure broadening coefficient and p the pressure of the broadening gas. In actuality, the contribution to the pressure broadening depends on the nature of the species with which the molecule or atom of interest collides, so Equation 1.10 can be regarded as [11, 12]:

$$\Delta\nu_L = 2\gamma_{\text{self}}p_{\text{self}} + 2\gamma_{\text{buff}}p_{\text{buff}} = 2\gamma_{\text{self}}p_{\text{self}} + 2\sum_x \gamma_x p_x \tag{1.11}$$

where the subscripts 'self' and 'buff' refer to the species of interest and other species present in the mixture, respectively, and where x denotes all the different types of foreign gases present in the sample and their respective broadening coefficients and partial pressures. In the HITRAN database [13–15], the γ values are reported as half-width half-maximum (HWHM) figures (hence the factor of two in Equations 1.10 and 1.11) and for a constant temperature (γ also displays a temperature dependence which has been omitted here).

The other main source of line broadening observed is the inhomogeneous process of Doppler broadening. At a given temperature, the particles in a sample possess a range of velocities according to the Maxwell-Boltzmann distribution [7] so the molecules may be moving away from or towards the observer and at a variety of speeds. The motion of the particles relative to the source of the radiation passing through the sample results in a shift in the absorption frequency observed for each molecule: the frequency has been Doppler shifted, and because different particles have different velocities they are all Doppler shifted by different amounts. Thus the velocity distribution of the particles leads to a distribution of the absorption frequencies, resulting in a broadened lineshape with a Gaussian profile [10]:

$$G(\nu) = \frac{2}{\Delta\nu_G}\sqrt{\frac{\ln 2}{\pi}}\exp\left[-\frac{4\ln 2(\nu-\nu_0)^2}{\Delta\nu_G^2}\right] \tag{1.12}$$

where $\Delta\nu_G$ is the FWHM Gaussian width, which in the case of Doppler broadening is equal to the Doppler width given by:

$$\Delta\nu_D = 2\nu_0\sqrt{\frac{2k_BT\ln 2}{mc^2}} \tag{1.13}$$

where k_B is the Boltzmann constant, T is the temperature and m the mass of the molecule.

In low pressure regimes (a few Torr or less) at room temperature, Doppler broadening is the dominant line broadening process so the absorption feature exhibits a Gaussian profile with a linewidth given by the Doppler width. However, in pressure regimes where the contributions from Doppler broadening and pressure broadening are similar, so that the Doppler Gaussian width is comparable to the pressure-induced Lorentzian width ($\sim 10 - 100$s Torr), the absorption profile can be described by a convolution of the Gaussian and Lorentzian lineshapes known as the Voigt profile [10]:

$$V(\nu) = \frac{2}{\Delta\nu_G}\sqrt{\frac{\ln 2}{\pi}}\frac{y}{\pi}\int_{-\infty}^{+\infty}\frac{\mathrm{e}^{-t^2}}{y^2+(x-t)^2}\mathrm{d}t \tag{1.14}$$

where x and y are given by:

$$x = \sqrt{\ln 2}\frac{2(\nu-\nu_0)}{\Delta\nu_G} \qquad y = \sqrt{\ln 2}\frac{\Delta\nu_L}{\Delta\nu_G} \tag{1.15}$$

Equation 1.14 cannot be evaluated analytically so instead must be calculated numerically. This is often accomplished using the approximation [10]:

$$V(\nu) = \frac{2}{\Delta\nu_G}\sqrt{\frac{\ln 2}{\pi}}\mathrm{Re}\left[W(z)\right] \tag{1.16}$$

where $z = x + y\mathrm{i}$ and $W(z)$ is the complex error function or Faddeeva function [16]:

$$W(z) = \mathrm{e}^{-z^2}\mathrm{erfc}(-\mathrm{i}z) = \mathrm{e}^{-z^2}\left(1 + \frac{2\mathrm{i}}{\sqrt{\pi}}\int_0^z \mathrm{e}^{t^2}\mathrm{d}t\right) \tag{1.17}$$

where erfc is the complementary error function. Alternative approaches to evaluating the Voigt profile are also available in the literature [17], and the Voigt FWHM, $\Delta\nu_V$, for cases when $\Delta\nu_L \approx \Delta\nu_G$ can be estimated as [18, 19]:

$$\Delta\nu_V \approx 0.5346\Delta\nu_L + \sqrt{0.2166\Delta\nu_L^2 + \Delta\nu_G^2} \tag{1.18}$$

These three major lineshape profiles - Gaussian, Lorentzian and Voigt - are illustrated in Figure 1.2. Other, more complex lineshape profiles also exist, including Galatry [20] and Rautian [21] profiles which are required when collisional narrowing effects occur. These processes take place when the upper state lifetime is large compared to the time between

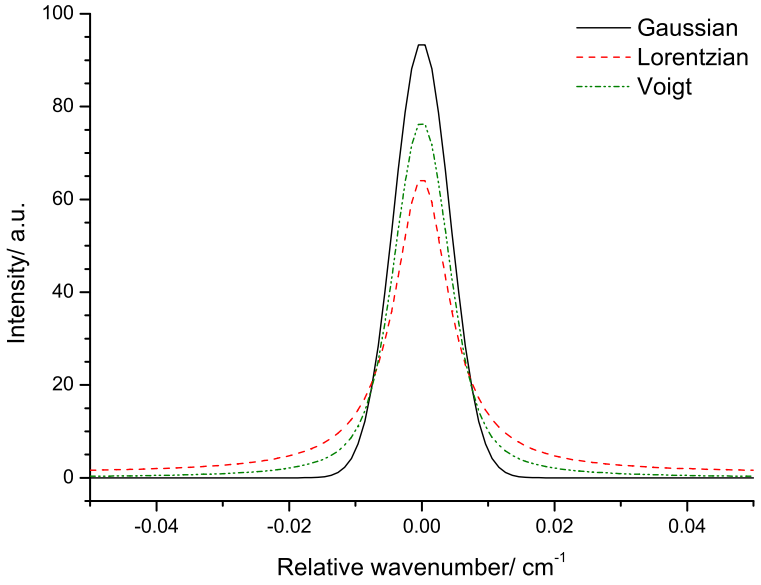

Figure 1.2: A comparison of the Gaussian, Lorentzian and Voigt profiles, simulated with unitary area and FWHM of 0.01 cm^{-1}.

collisions so the mean free path of the absorber is much smaller than the wavelength of transition of interest, resulting in the occurrence of many velocity changing, elastic collisions during the absorption of the photon. This leads to an averaging over several Doppler states and a reduction in the linewidth known as Dicke narrowing [22, 23].

For practical applications, we often want to relate σ_{int}, which is independent of environmental conditions (except temperature) and hence is a constant for a given transition of a given species, to the absorption cross-section at the peak of the absorption feature, σ_p. This is achieved through the relation:

$$\sigma_p = \frac{\sigma_{\text{int}}}{\Gamma \Delta\nu} \tag{1.19}$$

where $\Delta\nu$ is the FWHM linewidth of the absorption signal and Γ is the lineshape parameter, which is a numerical constant associated with the form of the manifested lineshape under particular experimental conditions and can be approximated as [19]:

$$\Gamma = 1.065 + 0.447\frac{\Delta\nu_L}{\Delta\nu_V} + 0.058\left(\frac{\Delta\nu_L}{\Delta\nu_V}\right)^2 \tag{1.20}$$

1.1.3 Sensitivity

Absorption spectroscopy can be a highly selective and highly sensitive technique. Selectivity is the ability to differentiate between the absorption feature of interest and those due to other absorbers which may be present in a sample, and is particularly important

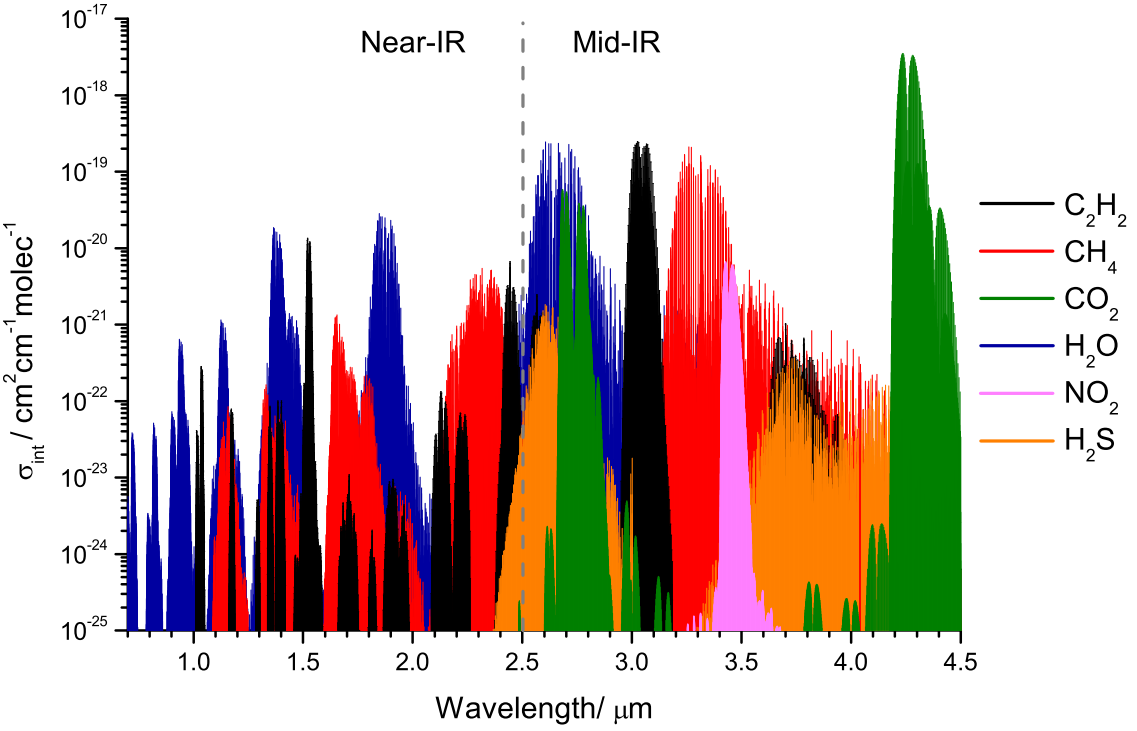

Figure 1.3: Integrated absorption cross-sections of a selection of molecules for their near- and mid-IR transitions [15]. Transitions in the near-IR can be several orders of magnitude smaller than those in the mid-IR.

when dealing with complex mixtures such as breath. Sensitivity, on the other hand, relates to the capacity to observe low levels of absorption. Conventional direct absorption spectroscopy, by measuring the attenuation of light on its passage through a sample, is not very sensitive as it consists of measuring progressively smaller changes upon a large, often varying background. However, it can be improved by either reducing the noise of the system or increasing the absorbance observed. Inspection of the Beer-Lambert law (Equation 1.6) implies that an increase in absorption (leading to an increase in sensitivity) can be obtained by either increasing the absorber concentration, extending the path length, measuring a transition with a greater absorption cross-section or using a mixture of these three ideas. Often the first of these options is not feasible as the unknown concentration is the parameter which is desired to be determined. This leaves two approaches: firstly, using the spectral regions where absorption cross-sections are highest and, secondly, using sensitive detection techniques based on either noise reduction and/or path length enhancement.

The infrared (IR) region of the EM spectrum includes radiation with wavelengths between 700 nm and 1 mm and corresponds to energies of ro-vibrational transitions. The region can be further sub-divided into the near- ($0.7 - 2.5$ μm), mid- ($2.5 - 12$ μm) and far- ($12 - 1000$ μm) IR ranges. Whereas only weaker overtone and combination bands at lower intensities of the ro-vibrational transitions take place in the near-IR, strong fundamental

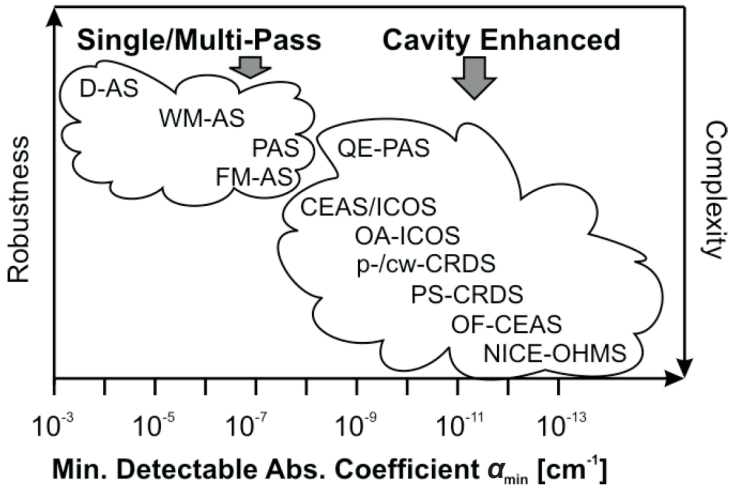

Figure 1.4: A comparison of various absorption spectroscopy techniques according to their complexity, robustness and sensitivity (represented by their typically achieved minimum detectable absorption coefficients, $\alpha_{\min}$). Abbreviations are given in the Nomenclature. Reproduced from Welzel *et al.* [27].

transitions with large absorption cross-sections occur in the mid-IR [24]. Strong absorptions by C−H, N−H and O−H stretches around 3 μm are of particular significance. This variation in intrinsic linestrengths with wavelength is illustrated in Figure 1.3, with absorption intensities typically $10 - 10,000$ times stronger in the mid-IR than those in the near-IR [25]. Selective detection of many species is also more feasible in this region as the transition line centres are more widely dispersed and the lower frequencies result in reduced lineshape broadening (Section 1.1.2) so less interference and overlap between absorption features occur. Thus mid-IR spectroscopy has many benefits. However, it is limited by the experimental equipment available at these wavelengths, such as inadequate low noise detectors, a lack of very highly reflective optical components and laser sources of insufficient power and beam quality [26], though technological advances to improve this situation are constantly being made. Hence the near-IR region is worse in terms of fundamental linestrengths but better in terms of available spectroscopic equipment, whilst the opposite is true in the mid-IR.

Many different sensitive detection techniques have been developed in order to monitor weakly absorbing species or those at low concentrations, and these are summarised in Figure 1.4. These include phase sensitive detection methods to reduce the noise (using techniques such as wavelength modulation (WM) or frequency modulation (FM) spectroscopy [28, 29]) and those based on path length enhancement [30], the latter comprising the use of either multi-pass cells (such as Herriott [31] or White cells) or optical cavities [32, 33]. A range of cavity enhanced methods exist, including cavity enhanced absorption spectroscopy (CEAS) [34, 35], optical feedback cavity enhanced absorption spectroscopy (OF-CEAS) [36], cavity

ring-down spectroscopy (CRDS) [37, 38], phase shift cavity ring-down spectroscopy (PS-CRDS) [39], saturated-absorption cavity ring-down spectroscopy (SCAR) [40] and noise immune cavity enhanced optical heterodyne molecular spectroscopy (NICE-OHMS) [41]. In all instances, path lengths of the order of $1 - 10$ km are readily achievable. CEAS and CRDS are discussed in more detail in Section 1.2.2.

Noise is the series of unwanted signals observed at the output of a detection system, masking the true signal. There are three main types of noise associated with absorption spectroscopy: detector noise, laser excess noise and interference fringes [42]. Detector noise is comprised of three different constituents [10], one of which is thermal or Johnson noise. This originates from the random thermal motion of electric charges present in all conducting components of a detector, but especially of the electrons generated at the semiconductor $p-n$ junction [43]. The root mean square (rms) value of the thermal noise current, i_T, is given by:

$$i_T = \sqrt{\frac{4k_B T \Delta f}{R}} \tag{1.21}$$

where Δf is the frequency bandwidth of the detector and R is the detector resistance. It can thus be seen that the level of thermal noise is independent of the frequency and intensity of the radiation, and can be reduced by either increasing the resistance of the detector, lowering its temperature or reducing its bandwidth.

Another component of detector noise is shot noise, also known as quantum noise, which is caused by fluctuations in the photocurrent due to the random generation of mobile charge carriers in photodiodes. The rms shot noise current, i_s, is:

$$i_s = \sqrt{\frac{2e^2 \eta \Delta f P}{h\nu}} \tag{1.22}$$

where e is the elementary charge, P is the incident power and η is the quantum efficiency, which is the ratio of the number of carriers produced to the number of absorbed photons. This, like Johnson noise, does not depend on frequency; such sources of noise where the power spectral density is invariant with frequency are termed white noise.

The last component of detector noise is $1/f$ noise, caused by, among other factors, the presence of lattice defects and impurities in the semiconductor, the diffusion of charge carriers and the interactions of the charge carriers with the surface of the material. It is called $1/f$ noise because it is exhibits an inverse dependence on frequency, and dominates in situations where measurements are recorded at low frequencies (< 1 kHz).

All three of these contributions to detector noise depend on the bandwidth, so any process which lowers the bandwidth, such as signal integration or low pass filtering, will improve the sensitivity of the detection system. The performance of a photodetector is characterised

Detector	*Thorlabs* DET410	*Thorlabs* DET10C/M	*Vigo Systems* PVI-2TE-4 /VPDC-0.1l	*Vigo Systems* PVI-4TE-3.4 /MIPDC-F-20
Material	InGaAs	InGaAs	HgCdZnTe	HgCdZnTe
Spectral response/ μm	$0.7 - 1.8$	$0.8 - 1.7$	$2.5 - 4.0$	$2.5 - 3.4$
Peak wavelength, λ_p/ μm	1.5	1.55	4.0	3.4
Rise-fall time/ ns	5	10	3500	18
Peak response/ AW^{-1}	0.95	0.95	2.9	0.96
$D^*(\lambda_p)$/ $cmHz^{1/2}W^{-1}$	8.9×10^{12}	3.6×10^{12}	5.5×10^{11}	9.1×10^{11}
NEP(λ_p)/ $WHz^{1/2}$	1.0×10^{-14}	2.5×10^{-14}	1.8×10^{-13}	1.1×10^{-13}
Active area/ mm^2	0.8	0.8	1	1
Operating temperature/ °C	$0 - 85$	$10 - 50$	-51	-78
Cooling required	None	None	2-stage TEC	4-stage TEC

Table 1.1: A comparison of near- and mid-IR detectors used in this thesis [45, 46]. The $D^*(\lambda_p)$ and NEP(λ_p) values listed for the *Vigo Systems* detectors refer to just the photovoltaic detector chips, rather than the complete detection module. The $D^*(\lambda_p)$ and NEP(λ_p) values for the detection modules are 3.3×10^{11} $cmHz^{1/2}W^{-1}$ and 3.0×10^{-13} $WHz^{1/2}$ for the PVI-2TE-4/VPDC-0.1l *Vigo Systems* detector, and 3.8×10^{10} $cmHz^{1/2}W^{-1}$ and 2.6×10^{-12} $WHz^{1/2}$ for the PVI-4TE-3.4/MIPDC-F-20 *Vigo Systems* detector, respectively.

by its detectivity, $D^*(\nu)$ [10]:

$$D^*(\nu) = \frac{V_S}{V_N}\frac{\sqrt{A\Delta f}}{P} \tag{1.23}$$

where A is the detector area and V_S and V_N represent the signal and noise voltages, respectively, so that the fraction V_S/V_N is the signal-to-noise ratio (SNR). Another way the sensitivity levels of a detector can be reported is via the noise equivalent power (NEP) [10]:

$$\text{NEP} = \frac{\sqrt{A}}{D^*(\nu)} \tag{1.24}$$

Detectors are fundamentally worse in the mid-IR due to the lower quantum efficiencies in this spectral region, which result in fewer electrons per photon being generated in the detector material and hence significant cooling is necessary in order to monitor the small resultant changes in current. This means that despite the inherently large absorptions present in the mid-IR, and thus the potentially better detection levels, the overall sensitivity of a mid-IR spectrometer is frequently constrained by the noisier detectors available at these wavelengths compared to those in the near-IR, which often results in similar overall performances of near- and mid-IR spectrometers. However, some recent progress has been made to improve the performance of mid-IR detectors [44]. Table 1.1 summarises both the near- and mid-IR detectors used in this thesis, highlighting the difference in performance between these wavelength ranges.

Another noise associated with absorption spectroscopy, laser excess noise, is caused by fluctuations in laser power and frequency. It can either be intrinsic to the system (inherent behaviour of the laser source) or caused by external effects (such as noise in the injection currents, temperature instabilities or mechanical vibrations). Noise also arises from the presence of undesired interference fringes from Fabry-Perot etalons between reflective surfaces in an experimental set-up. These fringes cannot simply be subtracted (as temperature and mechanical variations mean the etalons change over time) but can be minimised by using reflective rather than refractive optics, jittering reflective surfaces and avoiding sharp focuses.

The sensitivity of the detection system is thus dependent on the varying contributions from all of these different sources of noise. Even if all other sources are eliminated, the unavoidable shot noise gives a 'shot noise limited' (SNL) value to the SNR [10]:

$$\mathrm{SNR_{SNL}} = \frac{\eta P}{2h\nu\Delta f} \tag{1.25}$$

though in practice this limit is rarely achieved due to the other noise sources outlined above.

One way the sensitivity of the absorption measurement can be reported is in terms of the minimum detectable absorption coefficient, α_{min}, given by:

$$\alpha_{\mathrm{min}} = \frac{\alpha_p}{\mathrm{SNR}} \tag{1.26}$$

where α_p is the peak absorption coefficient given by $\alpha_p = \sigma_p C$. The time for data acquisition, and the bandwidth, can also be accounted for by using either a time reduced or bandwidth reduced form of Equation 1.26. The time reduced and bandwidth reduced minimum detectable absorption coefficients, $\alpha_{\mathrm{min}}(TR)$ and $\alpha_{\mathrm{min}}(BW)$, respectively, are:

$$\alpha_{\mathrm{min}}(TR) = \alpha_{\mathrm{min}}\sqrt{nt_{\mathrm{acq}}} \tag{1.27}$$

$$\alpha_{\mathrm{min}}(BW) = \alpha_{\mathrm{min}}\sqrt{n/\Delta f} \tag{1.28}$$

where n is the number of averages, t_{acq} is the period for one acquisition scan and the bandwidth of the detector is generally related to the time constant of the detection system, τ, by $\Delta f = 1/\pi\tau$. These quantities have units of $\mathrm{cm^{-1}s^{1/2}}$ and $\mathrm{cm^{-1}Hz^{-1/2}}$, respectively, and the form adopted depends on the nature of experiment used. In this thesis, sensitivities are quoted either as α_{min} along with the measurement time or as $\alpha_{\mathrm{min}}(BW)$.

1.2 Sensitive Spectroscopic Strategies

1.2.1 Modulation techniques

Modulation techniques, namely wavelength modulation spectroscopy (WMS) [28, 47] and frequency modulation spectroscopy (FMS) [29], improve the sensitivity by reducing the noise in the absorption signal. In both cases, a high frequency modulation is applied on top of the relatively low frequency modulation used to tune the laser frequency over the target absorption feature. For a diode laser, this additional modulation can be achieved by superimposing a high frequency sinusoidal modulation on to the laser injection current [48]. The detected signal varies at the high modulation frequency applied and so must be demodulated at a harmonic of that modulation frequency to obtain the desired absorption feature. This recovery is accomplished by use of a lock-in amplifier, which filters out the signal components which are at a different frequency and phase to the superimposed high frequency modulation applied to the laser.

As described in Section 1.1.3, the main sources of noise are white noise (thermal and shot noise) and $1/f$ noise (from external sources such as thermal, mechanical and acoustic fluctuations, as well as intrinsic amplitude and phase noise of the laser). The contributions from the latter are signal-dependent and as they vary according to $1/f$, can be reduced by moving to a higher frequency regime. However, the resultant improvement in sensitivity on execution of this methodology depends on the relative contributions from the other noise sources.

Modulation spectroscopy is classified either as WMS or FMS depending on whether the frequency of the applied modulation is smaller ($\sim$kHz) or larger ($\sim$MHz-GHz) than the FWHM linewidth of the feature of interest ($\Delta\nu$), respectively [28, 49]. While the higher frequencies of FMS result in lower $1/f$ noise, this does not always translate to a higher sensitivity as the faster detectors required often have higher bandwidths and so increased levels of white noise (though the majority of this additional noise is filtered out with the lock-in amplifier). Therefore, WMS, using less complex electronics, is generally the preferred technique.

1.2.1.1 Wavelength modulation spectroscopy (WMS)

When a modulation with a frequency ω_m and an amplitude a_m is applied to a laser centred at frequency ω_0, the instantaneous output laser frequency at a time t is given by:

$$\omega(t) = \omega_0 + a_m \cos(\omega_m t) \tag{1.29}$$

Using this definition of ω, the time-varying intensity of the modulated light, $I(\omega)$, is a periodic, even function described by a cosine Fourier series:

$$I(\omega) = \sum_{n=0}^{\infty} H_n(\omega_0)\cos(n\omega_m t) \tag{1.30}$$

where $H_n(\omega_0)$ is the n^{th} harmonic. This indicates that the modulated signal is comprised of the harmonics of the fundamental modulation frequency ω_m; these different harmonics can be selected and detected by the lock-in amplifier. In the presence of an absorber the intensity, $I(\omega)$, is described by the Beer-Lambert law (Equation 1.6). The $H_n(\omega_0)$ coefficients are thus:

$$H_n(\omega_0) = \frac{2}{\pi}\int_0^{\pi} I(\omega)\cos(n\omega_m t)\mathrm{d}(\omega_m t) \tag{1.31}$$

$$= \frac{2}{\pi}\int_0^{\pi} I_0(\omega)\mathrm{e}^{-\sigma(\omega)Cl}\cos(n\omega_m t)\mathrm{d}(\omega_m t) \tag{1.32}$$

In the limit of weak absorptions ($\sigma(\omega)Cl \leq 0.003$) and assuming that the incident laser intensity is independent of wavelength tuning, then the Maclaurin expansion can be used to approximate the exponential term in the Beer-Lambert Law, reducing Equation 1.32 to:

$$H_n(\omega_0) = \frac{2I_0Cl}{\pi}\int_0^{\pi} -\sigma(\omega)\cos(n\omega_m t)\mathrm{d}(\omega_m t) \tag{1.33}$$

illustrating that the demodulated n^{th} harmonic of the signal is directly proportional to the species concentration, C, *i.e.* there is a linear correspondence between the peak-to-peak amplitude of the WMS signal and the number density of the absorber.

In the derivative limit, when $a_m << \Delta\nu$, Equation 1.33 can be expressed as a Taylor series. In this case, the WMS signal, recovered by demodulation at $n\omega_m$, is proportional to the n^{th} derivative of the spectral lineshape, $\sigma(\omega)$, as:

$$H_n(\omega_0) \approx \frac{2^{1-n}I_0Cla_m^n}{n!}\left|\frac{\mathrm{d}^n\sigma(\omega)}{\mathrm{d}\omega^n}\right|_{\omega=\omega_0} \tag{1.34}$$

In practice, the derivative limit is rarely used as it does not give the largest WMS signals. Rather, other parameters are manipulated in order to optimise the signal. One of these is the dimensionless modulation index (or depth), b, given by:

$$b = \frac{2a_m}{\Delta\nu} \tag{1.35}$$

which represents the maximum deviation (in terms of frequency half-widths) from the carrier frequency and is altered by varying a_m. On increasing b, the magnitude of the WMS signal initially increases, but so too does the modulation broadening [50]. This broadening

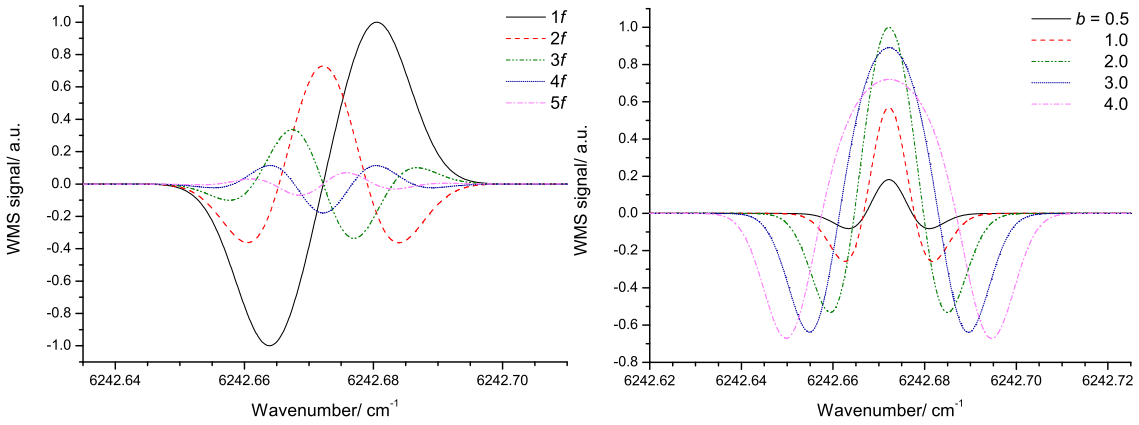

Figure 1.5: WMS simulations of the CO_2 $R(20)$ transition within the $3\nu_1+\nu_3$ combination band at 6242.67 cm^{-1} in the Doppler limited (Gaussian lineshape, $\Delta\nu_G = 348$ MHz) regime at (a) different demodulation harmonics and (b) different modulation depths for the $2f$ component.

distorts the lineshape and causes the height of the WMS signal to actually decrease at high b values (Figure 1.5(b)). Hence the optimum b value is chosen as a compromise between maximising the WMS signal height whilst suppressing broadening [51]. This broadening, however, must still be correctly accounted for to reconstruct the true absorption profile.

Another element to consider is the harmonic at which to demodulate. As seen in Figure 1.5(a), as the harmonic increases, the signal decreases, implying $1f$-WMS would be the best choice. However, lower harmonics are more susceptible to residual amplitude modulation (RAM) noise which arises from power variations resulting from the modulation applied to the laser. Thus WMS measurements are frequently conducted using the second harmonic, $2f$, scheme as a compromise between obtaining a high signal and lowering the noise in order to maximise the SNR.

An additional important factor is the bandwidth (BW) of the detection system, which determines the range of frequencies around the central frequency of the target WMS feature at the harmonic chosen for demodulation which are accepted and so contribute to the final signal. The bandwidth needs to be large enough in order to cover the whole of this peak, but small enough so that it removes any noise present in the wings. The bandwidth is inversely proportional to the time constant, τ, which is defined by the lock-in amplifier. So τ is set as large as possible whilst maintaining an appropriate lineshape and, if it is chosen correctly, will lead to a noticeable reduction in baseline noise.

Other parameters which can be adjusted to optimise the signal include the sensitivity level, phase offset and modulation frequency (generally three, or more, orders of magnitude greater than the laser scan rate) on the lock-in amplifier, and the laser tuning frequency

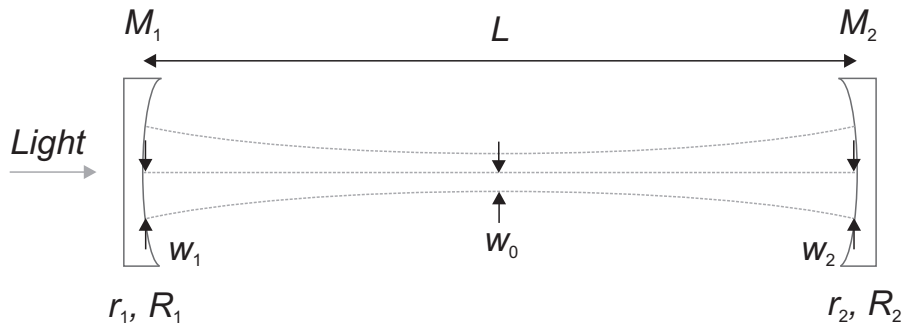

Figure 1.6: A schematic depicting an optical cavity of length L formed of two mirrors, $M_{1,2}$, with radii of curvature $r_{1,2}$ and reflectivities $R_{1,2}$. Inside is a Gaussian beam with a beam waist of w_0 and spot sizes at the mirrors of $w_{1,2}$.

and amplitude. Overall, all of these factors must be carefully chosen to attain the right balance between the signal amplitude, complexity of fitting and background noise in order to produce the best results.

Modulation spectroscopy typically affords sensitivities $10 - 100$ times greater than traditional homodyne techniques, but one of its main drawbacks is that it is not self-calibrating: direct absorption measurements must be recorded as well on a different, stronger absorption feature in order to provide an absolute calibration. Self-calibrating methods have been proposed and demonstrated [50, 52, 53], but these impose limitations on the flexibility of the technique. Cavity-enhanced methods, in contrast, are self-calibrating and so yield absolute concentrations directly from their output spectra.

1.2.2 Cavity enhanced techniques

1.2.2.1 Optical cavities

While multi-pass cells, such as White and Herriott cells, can achieve path lengths of $50 - 250$ m [31], these often require relatively large and impractical cell volumes. An alternative method for path length enhancement is to utilise optical cavities, where path lengths of $1 - 10$ km are readily achievable in combination with small cell volumes [33]. An optical cavity consists of a pair of highly reflective mirrors, $M_{1,2}$, with radii of curvature $r_{1,2}$ and reflectivities $R_{1,2}$, separated by a distance L, as illustrated in Figure 1.6. Light is injected into the cavity and, whilst a small amount of radiation leaks out at each reflection, the high mirror reflectivities mean that the majority is reflected back and forth between the mirrors. This results in the light travelling many km through any sample that may be present in the cavity, yielding a large effective absorption path length.

The principal properties of an optical cavity can be derived from the theory of a Fabry-Perot resonator [38, 54]. The light transmitted through this cavity, I_T, on illumination

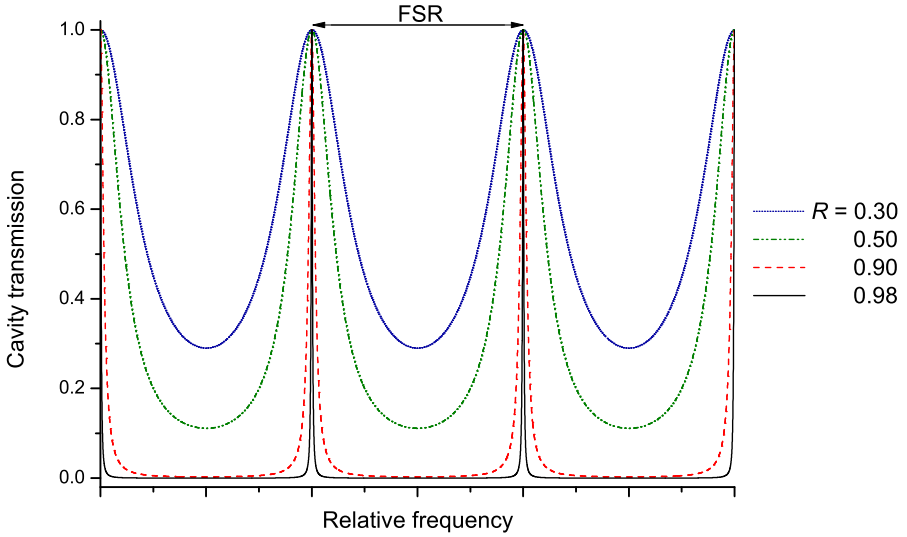

Figure 1.7: Cavity transmission profiles for various mirror reflectivity values modelled using the Airy function [1]. The FSR is the frequency difference between the maxima.

with coherent, white light is given by the Airy function [1]:

$$\frac{I_T}{I_0} = \frac{1}{1 + F_c \sin^2(\delta/2)} \tag{1.36}$$

where I_0 is the incident radiation, δ is the phase difference between successive transmitted waves and F_c is the coefficient of finesse given by:

$$F_c = \frac{4R}{(1-R)^2} \tag{1.37}$$

where R is the geometric mean of the cavity mirror reflectivities, $R = \sqrt{R_1 R_2}$. This generates a comb-like transmission profile, as shown in Figure 1.7. The equally spaced transmission maxima correspond to longitudinal cavity modes and arise from constructive interference which occurs when the cavity mirror separation equals an integer number of half wavelengths, *i.e.* $L = q\lambda/2$, where q is an integer indicating the longitudinal mode order. These longitudinal modes are separated by a frequency range called the free spectral range (FSR):

$$\Delta\nu_{\mathrm{FSR}} = \frac{c}{2nL} \tag{1.38}$$

where n is the refractive index of the medium inside the cavity. In the limit $F_c \to \infty$, each of these maxima has a Lorentzian profile with a linewidth (FWHM) of:

$$\Delta\nu_{\mathrm{mode}} = \frac{\Delta\nu_{\mathrm{FSR}}}{F} \tag{1.39}$$

where F is the cavity finesse, related to the coefficient of finesse by $F = \pi/(2\arcsin(1/\sqrt{F_c}))$ and so can be approximated for $R > 0.5$ to:

$$F = \frac{\pi\sqrt{F_c}}{2} \tag{1.40}$$

$$= \frac{\pi\sqrt{R}}{1-R} \tag{1.41}$$

The relationship given in Equation 1.39 implies that as the mirror reflectivity and finesse increase, the bandwidth of the cavity modes decreases. This can be rationalised as follows: on scanning the laser wavelength or cavity length, a perturbation is introduced into the system, which is greater the higher the reflectivity of the mirrors owing to the resultant longer effective path lengths; this causes a reduction in the frequency range over which the requisite resonance condition is fulfilled, thus narrowing the cavity modes. This tightening of cavity mode widths also allows the amount of circulating power inside the cavity to increase, with the maximum amount obtainable equal to the product of F and the incident power [33]. So F, in addition to quantifying the ability of the cavity to support constructive interference over a long path length, also controls the lineshape of the cavity modes and the power circulating inside the optical system.

The cavity geometry must satisfy several criteria in order for it to be optically stable so that the resonator can support the cavity modes, effectively confine the radiation within the cell and maintain low diffraction losses. A cavity is optically stable if [55]:

$$0 \leq g_1 g_2 \leq 1 \tag{1.42}$$

where $g_{1,2}$ are the g-parameters for the mirrors $M_{1,2}$:

$$g_i = 1 - \frac{L}{r_i} \tag{1.43}$$

If the two mirrors have an identical radius of curvature, r, this condition reduces to $0 < L < 2r$ [33]. Certain geometries occur on the edge of the stability curve; these include symmetric confocal ($r_1 = r_2 = L$), plane parallel ($r_1 = r_2 = \infty$) and concentric ($r_1 = r_2 = L/2$) geometries.

The frequencies of the resonant Gaussian modes inside the cavity are given by [55, 56]:

$$\nu_{qmn} = \frac{c}{2L}\left(q + \frac{n+m+1}{\pi}\arccos(\sqrt{g_1 g_2})\right) \tag{1.44}$$

where q, m, n are the mode indices that define the longitudinal (q) and transverse (m, n) properties of the EM field of the modes; the first index indicates the gross frequency of the mode, whereas the latter two describe the spatial geometry of the mode in its electric

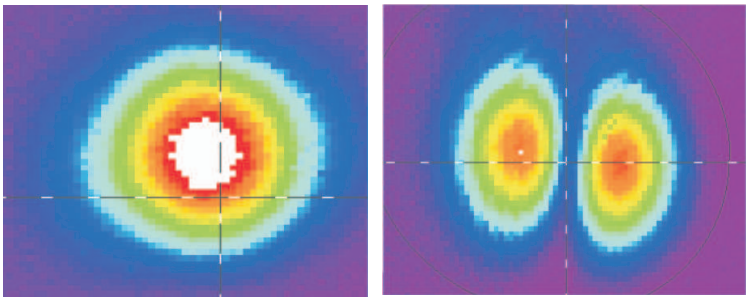

(a) TEM_{00} **(b)** TEM_{10}

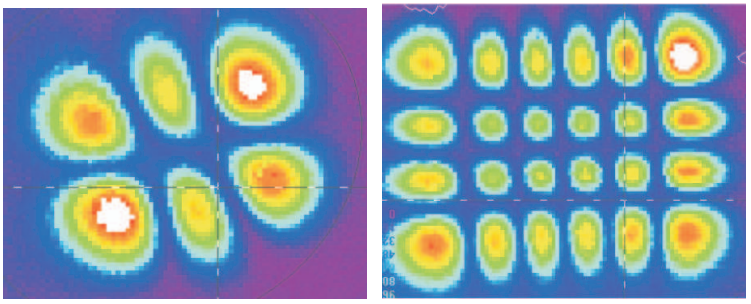

(c) TEM_{21} **(d)** TEM_{53}

Figure 1.8: Experimental cavity transmissions for different TEM_{mn} modes.

field variations perpendicular to the cavity axis. The frequency difference between two longitudinal modes, *i.e.* those with same m, n but different q, is the FSR. Modes with the same q but different m and/or n are called transverse modes and are labelled as TEM_{mn} [33, 57]. Some examples of the cavity mode outputs for different TEM_{mn} modes, demonstrating the different transverse spatial distributions of the electric field, are given in Figure 1.8.

In the ideal case for a system with Cartesian symmetry, the radiation trapped inside the resonator has a Gaussian beam profile with solutions to the three dimensional paraxial wave equation given by the Hermite-Gaussian mode-set, denoted by the TEM_{mn} notation; other solutions to the wave equation also exist for systems with different symmetries, such as Laguerre-Gaussian modes for cases with cylindrical symmetry or Ince-Gaussian modes for ones with an elliptical nature. The width of this Gaussian beam varies with the axial distance travelled from the narrowest point of the beam, z, and can be quantified by the spot size, $w(z)$, which is defined as the radius at which the field amplitude and intensity drop to $1/e$ and $1/e^2$ of their axial values, respectively. It represents the transverse extent of the optical electric field inside the cavity. The minimum spot size occurs at the 'waist' and is often referred to as the beam waist, w_0; this occurs at the centre of the cavity if the two mirrors are identical. The beam waist and spot sizes at the mirrors, $w_{1,2}$, for the lowest

order Gaussian mode, TEM_{00}, are given by [57]:

$$w_0 = \sqrt{\frac{L\lambda}{\pi}} \left[\frac{g_1 g_2 (1 - g_1 g_2)}{(g_1 + g_2 - 2g_1 g_2)^2} \right]^{0.25} \tag{1.45}$$

$$w_{1,2} = \sqrt{\frac{L\lambda}{\pi}} \left[\frac{g_{2,1}}{g_{1,2}(1 - g_1 g_2)} \right]^{0.25} \tag{1.46}$$

Information on the propagation of the Gaussian beam through the cavity and its spot sizes at the mirrors and waist is required to enable mode-matching, a technique where the laser beam is focused into the resonator in such a way that the wavefront radii of curvature and beam waist of the input radiation present within the cavity match and overlap with those of the lowest order mode of the cavity, thus preferentially exciting the TEM_{00} mode and coupling maximum light into the system. This is achieved by the use of appropriate mode-matching optics (usually one or two lenses) placed before the cavity, and is necessary for certain cavity-based spectroscopic techniques, including cavity ring-down spectroscopy. More details are given in Appendix A.

There are a variety of experimental techniques which make use of optical cavities for performing spectroscopic measurements. The two most commonly used, and employed in this thesis, are cavity ring-down spectroscopy (CRDS) [30, 33, 37, 38, 58–63] and cavity enhanced absorption spectroscopy (CEAS) [30, 33–35, 64], which operate in the time and amplitude domains, respectively. These techniques are described in the following sections.

1.2.2.2 Cavity ring-down spectroscopy (CRDS)

CRDS involves the measurement of the temporal evolution of the transmitted light intensity of an optical cavity when the injected radiation is rapidly switched off after allowing for the power levels inside the cavity to build up. Early CRDS work was conducted using pulsed lasers as this provided an unambiguous point at which to begin measuring this decay in transmitted light [37]. Assuming that the duration of the input pulse of laser radiation of intensity I_{in} is shorter than the round trip time within the cavity of $2L/c$, the transmitted intensity after one pass of light through the cavity is [33, 65]:

$$I_0(\nu) = I_{in}(1 - R)^2 \mathrm{e}^{-\alpha(\nu)d} \tag{1.47}$$

where d is the length of the region occupied by the absorber inside the cavity and R is the frequency-dependent, geometric mean of mirror reflectivities (though notation explicitly emphasising the frequency dependence of R is dropped in this and subsequent equations). This corresponds to the transmitted intensity measured at time t_1 in Figure 1.9(a). The $(1 - R)^2$ term in Equation 1.47 refers to the transmission of the mirrors, while the $\mathrm{e}^{-\alpha(\nu)d}$

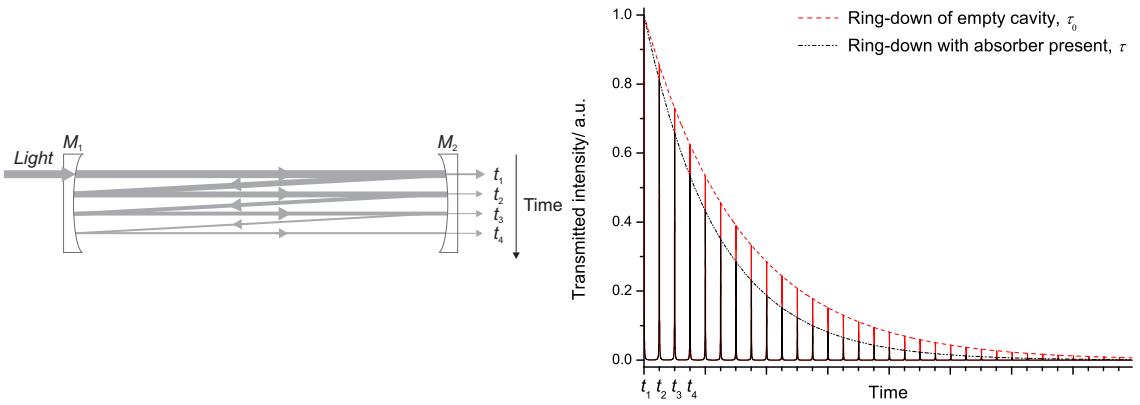

(a) Schematic of the temporal variation in light intensity in the cavity.

(b) Observed transmitted intensities.

Figure 1.9: Explanation of CRDS. (a) demonstrates the variation in light intensity inside the cavity over time. Injected light is reflected back and forth between the mirrors, with a small amount leaking through at each reflection. The detector, placed after the second mirror, measures the transmitted radiation intensity over time. The same proportion of radiation leaks through on each pass, so that the absolute amount lost decreases at each reflection and a decreasing (exponentially decaying) signal is observed, as shown in (b). In (b), the average transmitted intensity exponential decays detected in the absence (τ_0) and presence (τ) of an absorber are displayed, together with the individual transmitted intensities at each reflection at M_2 for both cases.

factor represents the absorption and scattering losses caused by the sample present inside the resonator. Each subsequent round trip results in the attenuation of the intensity by a further factor of $R^2 \mathrm{e}^{-\alpha(\nu)d}$, so after m round trips the transmitted intensity is:

$$I_m(\nu) = I_0(\nu) R^{2m} \mathrm{e}^{-2m\alpha(\nu)d} \tag{1.48}$$

Equation 1.48 implies that, given a sufficiently fast detector, a series of discrete pulses with exponentially decreasing magnitudes would be observed. Generally, however, the response time of the detector and the duration of the input pulse mean that instead these distinct peaks are smoothed into a pure exponential decay, as illustrated in Figure 1.9(b). The discrete variable m can be re-written in terms of the continuous time variable t using $t = 2Lm/c$, so Equation 1.48 becomes:

$$I(\nu, t) = I_0(\nu) \mathrm{e}^{-t/\tau(\nu)} \tag{1.49}$$

indicating that the observed transmitted light intensity signal is an exponential decay with a decay time constant, or ring-down time (RDT), of $\tau(\nu)$ given by:

$$\tau(\nu) = \frac{L}{c(-\ln R + \alpha(\nu)d)} \tag{1.50}$$

which in the limit of highly reflective mirrors ($R \to 1$) becomes:

$$\tau(\nu) = \frac{L}{c\left[(1-R) + \alpha(\nu)d\right]} \tag{1.51}$$

This RDT corresponds to the time taken for the light intensity to reach 1/e of its original value. It clearly depends on the length of the resonator, the reflectivity of the cavity mirrors and the absorption and scattering properties of the sample within the cavity, but is independent of the laser intensity, making CRDS invariant to fluctuations in laser power. In the absence of an absorbing or scattering medium, the RDT is given by $\tau_0(\nu)$:

$$\tau_0(\nu) = \frac{L}{c(1-R)} \tag{1.52}$$

So the presence of an absorbing medium reduces the RDT and this change can be used to calculate the absorption coefficient, $\alpha(\nu)$, according to:

$$\alpha(\nu) = \frac{L}{cd}\left(\frac{1}{\tau(\nu)} - \frac{1}{\tau_0(\nu)}\right) \tag{1.53}$$

which can be used to ascertain information about either the concentration or absorption cross-section of the absorbing species as $\alpha(\nu) = \sigma(\nu)C$.

A true, single exponential decay is recorded only when a single cavity mode is excited. Multi-exponential decays are seen when the excitation of several cavity modes take place, each mode exhibiting a slightly different RDT. This can lead to interference or beating between the modes, resulting in a modulation being superimposed on the single exponential decay. Such situations occur when using multi-mode or broadband laser sources, or when the injected laser light excites several different cavity modes concurrently. In can be reduced by careful cavity alignment and the use of mode-matching [66] to ensure only the TEM_{00} mode is excited (Appendix A). In addition to this, the RDTs may suffer from another type of interference effect arising from the etalon-type behaviour that occurs within the substrates of some mirrors, which can cause a frequency-dependent sinusoidal oscillation to be present in the observed RDTs. This is minimised by misaligning the mirrors slightly or using wedged substrates [33].

Although the use of pulsed lasers for CRDS has the advantage that the injection light is automatically switched off [57], these lasers cannot perform high resolution work owing to their large bandwidths and they also often excite many modes simultaneously due to their poor spatial properties. Instead, continuous wave (cw) radiation, such as that emitted from diode lasers (Section 2.1.1) can be utilised [67]. When using a cw laser source, additional electronics or components are required to rapidly disrupt the resonance condition of the cavity mode once it is achieved. This can be accomplished either by halting the injection

of light once it is in resonance with the cavity by using a fast optical switch, such as an acousto-optic modulator [68], or by swift tuning of the laser frequency away from the resonance frequency by changing the diode injection current [69]. In both cases, the action needs to be quick to avoid influencing the expected pure exponential decay.

The sensitivity of a CRD spectrometer is described by the minimum detectable absorption coefficient, $\alpha_{\min}$ [33]:

$$\alpha_{\min} = \frac{L}{cd\tau_0}\frac{\Delta\tau^0_{\min}}{\tau_0} \tag{1.54}$$

where $\Delta\tau^0_{\min}$ is the minimum change in τ_0 that can be measured, often taken as the standard deviation in τ_0.

CRDS was the chosen technique for many experiments in this thesis due to the high sensitivities which it affords from its amplitude-noise insensitive time-domain acquisition, meaning that fluctuations in the input power are unimportant. However, the experimental set-up is critical as good cavity alignment is necessary to excite only the lowest order fundamental cavity modes, and CRDS using cw lasers requires reasonably fast electronics and optical switches. Furthermore, quick detectors are essential, as the detector must have a response time shorter than the RDT in order to record the exponential decay. Detection is especially difficult with low input powers, due to the compromise required between the gain-bandwidth and the noise performance of the detection system.

1.2.2.3 Cavity enhanced absorption spectroscopy (CEAS)

In CEAS, also called integrated cavity output spectroscopy (ICOS), radiation is constantly injected into an optical cavity and the time-integrated light intensity transmitted by the resonator is simultaneously measured [34, 35, 64]. The continuous input of light into the cavity replaces any radiation lost meaning that the light intensity exiting the cavity eventually reaches a steady value. This technique is closely related to CRDS, with the integrated transmitted intensity at any given frequency being proportional to the cavity RDT [35, 70]. But whereas in CRDS good cavity alignment is crucial in order to excite solely the TEM_{00} cavity mode, in CEAS the concurrent excitation of many, higher order modes, including re-entrant modes, is required so that the mode structure is highly congested yielding a quasi-continuous transmission. This is accomplished by scanning the laser rapidly over frequency ranges greater than one FSR [70], misaligning the cavity to excite higher order modes [71–74], introducing mechanical vibrations to randomly change the cavity length (*e.g.* using a piezoelectric transducer to jitter one of the cavity mirrors at a high frequency or to modulate the angle of injection into the cavity) [64] or a combination of these techniques. Thus a large number of modes are randomly and continuously excited

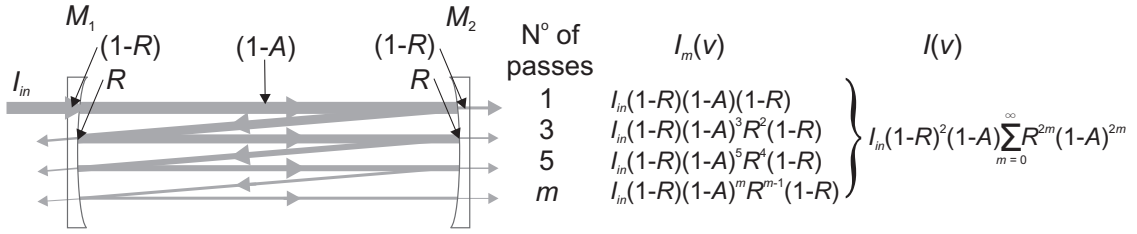

Figure 1.10: Explanation of CEAS. The transmitted intensity varies after each odd number of passes through the cavity. The overall output intensity recorded at the detector placed after M_2, however, measures the superposition of all these various intensities at any given time. Each component of the propagating beam has been vertically offset for clarity.

as the laser is scanned repeatedly across the spectral region of interest. On averaging these sweeps, a smooth transmission profile is attained with an improved SNR.

The theory underlying CEAS can be derived by considering an optical cavity with a mode-free transmission and composed of identical, non-absorbing, non-scattering cavity mirrors, such that the transmission through each mirror is equal to $T = 1 - R$, where R is the mirror reflectivity [33]. The incident cw radiation, I_{in}, is attenuated at many stages on its journey through the cavity to the detector by different factors: $(1 - R)$ on transmission through the first mirror; $(1 - A)$ on each pass through the cavity due to absorption by the sample; R at each mirror reflection due to radiation leaking from the cavity; and another $(1 - R)$ on the transmission through the final, second mirror. This is illustrated in Figure 1.10.

This attenuation scheme can be extended to an infinite number of passes. Because the light is being continuously injected into the cavity, all of these individual transmitted intensities after each and every number of odd passes, $I_m(\nu)$, occur simultaneously so the actual transmitted intensity measured by the detector at a given time, $I(\nu)$, is the sum of all these $I_m(\nu)$:

$$I(\nu) = I_{in}(\nu)(1 - R)^2(1 - A) \sum_{m=0}^{\infty} R^{2m}(1 - A)^{2m} \tag{1.55}$$

If $R < 1$ and $A < 1$, this simplifies to:

$$I(\nu) = I_{in}(\nu)\frac{(1 - R)^2(1 - A)}{1 - R^2(1 - A)^2} \tag{1.56}$$

When no absorber is present in the cavity, this becomes $I_0(\nu) = I_{in}(\nu)(1 - R)/(1 + R)$. Substitution of $\mathrm{e}^{-\alpha(\nu)d}$ for A as according to the Beer-Lambert law (Equation 1.6) gives:

$$\frac{I_0(\nu)}{I(\nu)} = \frac{1 - (R\mathrm{e}^{-\alpha(\nu)d})^2}{(1 - R)^2\mathrm{e}^{-\alpha(\nu)d}} \tag{1.57}$$

where d is the length of the region occupied by the absorber inside the cavity and $I_0(\nu)$ and $I(\nu)$ denote the output intensities in the absence and presence of an absorber, respectively.

In the limit of low absorptions ($\alpha \to 0$) and high reflectivities ($R \to 1$), this reduces to:

$$\frac{I_0(\nu) - I(\nu)}{I(\nu)} = \frac{\alpha(\nu)d}{1-R} \tag{1.58}$$

which allows information about the sample to be extracted from the absorption spectrum if R is known. The determination of R, and so calibration of the CEA spectrum, can be achieved by either using CRDS to measure τ_0 or performing CEAS measurements with samples of known concentrations and absorption cross-sections. However, these two methods may provide an inaccurate value for R: in the first one, the two different alignments required to perform CRDS and CEAS use different sections of the cavity mirrors and suffer from different diffraction losses, so may have intrinsically different R; in the second, a precise knowledge of the pressure of the absorber and its cross-section is necessary.

Another potential problem of CEAS occurs if the laser emits amplified spontaneous emission (ASE). This additional radiation will contribute to the detected signal, resulting in a broad, frequency-independent background in the CEA spectrum. This issue can be overcome by filtering the output of the laser or by measuring this ASE signal. The latter approach involves misaligning the cavity and measuring the light incident on the detector, which is now purely due to the uncoupled light passing straight through the cavity. If $I_{\text{base}}(\nu)$ is the baseline intensity measured at the detector due to this ASE and other background sources, then Equation 1.58 can be written as:

$$\alpha(\nu) = \frac{I_0(\nu) - I(\nu)}{I(\nu) - I_{\text{base}}(\nu)} \frac{1-R}{d} \tag{1.59}$$

The sensitivity of a CEA spectrometer is described by the minimum detectable absorption coefficient, α_{min} [33]:

$$\alpha_{\text{min}} = \frac{1-R}{L} \frac{\Delta I_{\text{min}}}{I_0} \tag{1.60}$$

where ΔI_{min} is the minimum detectable change in output intensity on introduction of an absorbing species.

CEAS is easier to set-up and implement than CRDS as it is less demanding in terms of mechanical stability, optical alignment and the speeds of detectors and electronics, as many cavity modes must be excited rather than just the fundamental ones. Continuous data acquisition is also possible and its straightforward and robust experimental arrangement make it suitable for many practical applications. However, CEAS is intensity-dependent, so it is susceptible to errors due to fluctuations in input power and is thus unable to reach the high sensitivities obtained from CRDS (10^{-8}–10^{-9} cm^{-1}Hz$^{-1/2}$ compared to 10^{-9} cm^{-1}Hz$^{-1/2}$ for CEAS and CRDS, respectively [38]). CEAS also requires calibration and an accurate determination of R, which may be difficult, and produces only small signals which must be detected.

1.3 Applications of Laser Spectroscopy to Gas Sensing

Applications of absorption spectroscopy for trace gas detection are varied and plentiful, encompassing uses in environmental, industrial and medical situations. A multitude of examples of these uses have been documented and the topic is the subject of many books and reviews [24, 26, 32, 75–92]. A selection of examples from the different fields of application are outlined below.

1.3.1 Environmental applications

Laser absorption spectroscopy can be deployed in many situations relating to environmental monitoring or research. There are many reports in the literature of laser-based ambient air gas sensors for compounds such as methane (CH_4) [93], ethane (C_2H_6) [94] and nitrous oxide (N_2O) [95], as well as examples where a combination of these and/or other species are measured simultaneously [25, 96, 97]. Detectors for indoor air monitoring of chemicals that are harmful to health, such as formaldehyde (H_2CO), have also been developed [98, 99].

Absorption spectroscopy has also found uses in geochemistry and biochemistry, including the study of volcanic emissions [100], the measurement of the rare ^{14}C isotope for age assessment of biogenic samples [101] and even the search for life on other planets [102]. But the biggest area of environmental research which exploits absorption spectroscopy is atmospheric chemistry.

Laser absorption spectroscopy can be used to address a range of problems within atmospheric chemistry. Firstly, it can be employed to determine the concentrations of different species present at different levels in the atmosphere. Documented examples of this include measuring CH_4 [103], N_2O [104] and hydrocarbons [105, 106] in the lower troposphere; various iodine and nitrogen compounds at the marine boundary layer [107]; carbon dioxide (CO_2) at the topsoil of forest floors [108]; and CH_4 [109], N_2O [110] and hydrochloric acid (HCl) [111] in the upper troposphere and lower stratosphere.

In addition, absorption spectroscopy can be utilised in the assessment of important kinetic parameters which are required to model the evolution in the concentrations of atmospheric species. This can be done by either directly measuring the rate constants of important reactions or, in the case of a species' photoreactivity, by finding the absorption cross-section of a species of interest, i, which allows its photolysis rate constant, $J_i(z)$, at different heights in the atmosphere, z, to be calculated using [112]:

$$J_i(z) = \int_\nu \phi_i(\nu) I(\nu, z) \sigma_i(\nu) \mathrm{d}\nu \tag{1.61}$$

where ϕ_i is the quantum yield of species i, the integral is performed over all frequencies at which i absorbs and $I(\nu, z)$ is the photon intensity at the frequency ν and altitude z given by:

$$I(\nu, z) = I_\infty(\nu) \mathrm{e}^{-\sum_j C_j(z)\sigma_j(\nu)\Delta z} \tag{1.62}$$

where $I_\infty(\nu)$ is the photon intensity at top of atmosphere, the sum is taken over all molecular species j that absorb at frequency ν, $C_j(z)$ is the concentration of the species j at the height z and Δz is the geometric path through the atmosphere, accounting for the solar zenith angle. For example, the ClO dimer (ClOOCl) plays a crucial role in stratospheric Antarctic ozone (O_3) loss [113–115] and its photolysis constant must be accurately evaluated in order to successfully model this O_3 depletion and fully understand all the processes involved; hence much work has been invested in ascertaining the ClOOCl absorption cross-section [116].

Finally, isotopic ratio studies of atmospheric species are also extremely useful, as this reveals information about the source and history of a sample under investigation, as well as knowledge about the processes which occurred at the source. Of particular significance is the isotopic composition of atmospheric CH_4, which can vary widely as the sources and sinks for CH_4 differentiate not only between $^{13}C/^{12}C$ isotopes, but also between D/H. For instance, the burning of fossil fuels generates emissions with a lower $^{13}CH_4/^{12}CH_4$ ratio than those from biological sources, *e.g.* rice fields or the rumen of livestock. Therefore quantitative measurements of the atmospheric CH_4 isotopologues can supply important information about the global CH_4 budget and such sensors to quantify the $^{13}CH_4/^{12}CH_4$ ratio have accordingly been developed [117–120].

1.3.2 Industrial applications

There are many examples of using laser spectroscopy for gas sensing in an industrial setting, such as searching for explosives [121] and in safety monitoring. The latter has included the development of a sensor for the rapid and quantitative detection of distillate fuel vapours for the identification of fire hazards in military vehicles [122]; this sensor could be applied to any trace gas with an unresolved absorption spectrum, though pyridine (C_5H_5N) was targeted in this case. Laser spectroscopy has also been used to assess the efficiency of new products and catalysts; in one example, the reaction kinetics of carbon monoxide (CO) oxidation over a platinum catalyst were followed by monitoring the amount of CO_2 produced [123].

Another area in which laser spectroscopy is useful for industrial applications is the monitoring of combustion processes in order to measure combustion efficiency and the levels of emitted pollutants. This can be achieved by studying the change in concentration of

hydroxy (OH) radicals [124], H_2O [125] or CO [126, 127]. Ammonia (NH_3) is an important species for the removal of nitrogen oxides (NO_x), which are potent greenhouse gases, from post-combustion mixtures and consequently sensors to monitor the emission of excess unconverted NH_3, itself a harmful pollutant, have been developed [128, 129].

1.3.3 Medical applications

The major field of development where laser absorption spectroscopy is being used to resolve medical problems is that of breath diagnostics. Absorption spectroscopy has many advantages over traditional breath analysis techniques such as mass spectrometry, including the bench-top size of apparatus and fast retrieval times, allowing for point-of-care instrumentation and time resolved measurements. Normal human breath comprises of several atmospheric compounds, *e.g.* N_2, CO_2, O_2 and H_2O, at relatively high concentrations; various volatile organic components (VOCs), *e.g.* acetone, isoprene and propanols, at parts per million (10^6, ppm) levels or lower; and approximately 400 other VOCs at parts per billion (10^9, ppb) or parts per trillion (10^{12}, ppt) concentrations [130, 131]. These species may be present in breath either because they were initially inhaled or because they have been produced endogenously as a result of a particular physiological status or process. Indeed, the presence of certain compounds at particular concentrations can be indicative of a specific disease or metabolic disorder of a patient [88, 89, 132–134]; such compounds are classed as biomarkers and some examples are listed in Table 1.2. Two different types of breath analysis can be identified: the measurement of breath metabolites after administration of a drug or substrate and the measurement of breath compounds produced naturally inside the patient.

Laser-based sensors to measure the $^{13}CO_2/^{12}CO_2$ in breath have been developed [135–137]. The ability to measure the deviation in the exhaled $^{13}CO_2/^{12}CO_2$ isotopic ratio, $\delta^{13}C$, from its natural baseline is extremely important. This $\delta^{13}C$ value of exhaled breath can be a real-time biomarker of cachexia associated with an acute phase response due to endotoxemia [138]. Furthermore, monitoring the $\delta^{13}C$ levels after administering a substance to a patient can also be extremely informative. One such breath test is the ^{13}C-urea breath test [139, 140], where an increase in $^{13}CO_2$ in exhaled breath following ingestion of ^{13}C-labelled urea can indicate metabolic activity associated with *Helicobacter pylori* infections such as gastritis, peptic ulcers, and stomach cancer [141, 142]. A temporal change in the concentration of $^{13}CO_2$ after administration of ^{13}C-methacin may also be used in a human liver capacity test [143]. In medical diagnostics, a short-term precision of $0.5 - 1‰$ in the $\delta^{13}C$ measurement is usually required [138, 142, 143].

Biomarker	IR absorption / μm	Conc. range	Physiological basis	Metabolic disorder
Acetaldehyde (CH_3CHO)	$9.2 - 9.8$	ppb	Ethanol metabolism	Alcoholism, liver-related diseases, lung cancer
Acetone ($(CH_3)_2CO$)	7.3	ppm	Decarboxylation of acetoacetate	Diabetes, lung cancer, congestive heart failure, brain seizure
Ammonia (NH_3)	10.3	ppb	Protein/bacterial metabolism	Renal diseases, asthma
Carbon dioxide (CO_2)	4.2	%	Respiration	Isotopic labelling used to diagnose presence of *Helicobacter pylori*, oxidative stress
Carbon monoxide (CO)	4.7	ppm	Haem catabolism by haem oxygenases	Catalysed oxidative stress, respiratory infection, anaemias
Carbonyl sulphide (OCS)	4.9	ppb	Gut bacterial oxidation of reduced sulphur species	Liver related diseases
Ethane (C_2H_6)	$3.3, 6.8$	ppb	Lipid peroxidation	Oxidative stress, vitamin E deficiency in children, peroxidation of lipids
Ethanol (C_2H_5OH)	$9.2 - 9.8$	ppb	Gut bacterial metabolism of sugars	Production of gut bacteria
Ethene (C_2H_4)	10.6	ppb	Lipid peroxidation	UV radiation damage of skin, peroxidation of lipids
Hydrogen (H_2)	–	ppm	Carbohydrate metabolism	Colonic fermentation, intestinal upset
Hydrogen sulphide (H_2S)	$1.6, 2.7, 3.7, 7.8$	ppb	Anaerobic bacterial metabolism of thiol proteins	Liver related diseases
Isoprene (CH_2CCHCH_2)	11.1	ppb	Cholesterol biosynthesis	Blood cholesterol
Methane (CH_4)	$3.3, 7.9$	ppm	Gut bacterial metabolism of carbohydrates	Intestinal problems, colonic fermentation
Methanethiol (CH_3SH)	$3.3 - 3.5$	ppb	Methionine metabolism	Halitosis, liver related diseases
Methylamine (CH_3NH_2)	12.2	ppb	Protein metabolism	Protein metabolism in body
Nitric oxide (NO)	5.3	ppb	Involved in vasodilation, or neurotransmission	Asthma, bronchiectasis, hypertension, rhinitis, lung diseases
Pentane (C_5H_{12})	6.8	ppb	Lipid peroxidation	Liver disease, schizophrenia, breast cancer, rheumatoid arthritis
Water (H_2O)	$1.3 - 1.5, 1.8 - 2$ $2.5 - 3, 5 - 8$	%	Respiration	Respiratory problems

Table 1.2: A summary of the typical compounds found in breath together with their absorption regions, normal concentration levels (Conc. range) and physiological cause. Deviations from the expected concentration for a given molecule may imply the presence of a particular metabolic disorder or disease, which are also listed in the table. Adapted from Wang and Sahay [88] and Risby and Tittel [89].

Sensors have also been created to measure CH_4 [74, 144, 145] and C_2H_6 [146–148]. Typical concentrations of CH_4 in breath vary from ambient air levels to 30 ppm [149], but it has been found that CH_4 levels in breath can be used as a biomarker for colonic fermentation and intestinal problems such as irritable bowel syndrome [150–153]. C_2H_6, on the other hand, is considered a significant biomarker of free-radical induced lipid peroxidation, with increased levels of C_2H_6 in breath implying that extensive cell damage caused by reactive oxygen species has taken place.

Elevated levels of acetone in breath is a key indicator of conditions such as type 1 diabetes [154, 155] as well as congestive heart failure [156]. Acetone concentrations can also be related to a patient's lifestyle, such as diet, exercise, smoking and obesity [157]. Given these notable correlations, several laser-based devices and techniques to measure breath acetone have been documented [158–160]. Devices to monitor NH_3 [145, 161] and nitric oxide (NO) [162] in exhaled breath have been developed too, the former compound being a strong indicator for renal failure [163] and the latter associated with lower airway inflammation disorders such as asthma, chronic obstructive pulmonary disorder and cystic fibrosis [164, 165].

1.4 Overview of Thesis

Section 1.3 is testament to the many different applications of laser absorption spectroscopy for trace gas analysis in a wide range of situations. The best spectrometers will combine high sensitivities and selectivities with a wide spectral coverage. The first of these aspects can be achieved by performing spectroscopy in the mid-IR region of the spectrum (which allows high sensitivities and selectivity to be attained by use of the strong, fundamental transitions therein) and/or using sensitive spectroscopic techniques (*e.g.* those based on optical cavities); the latter factor can be realised by careful selection of the laser source itself.

The aim of this thesis is to amalgamate the advantages of these separate concepts by combining cavity-based spectroscopic techniques with a widely tunable, mid-IR laser source. Such a highly sensitive and selective spectrometer in the 3 μm region would be greatly beneficial in the detection of multiple species or broadband absorbers for both medical and environmental applications.

In order to accomplish this goal, preliminary work was first conducted in the near-IR. In Chapter 2, the range of available near-IR laser light sources are reviewed, including cw telecommunication based diode lasers, which possess many desirable characteristics such as compactness, room temperature operation, narrow laser linewidths and continuous, rapid

tunability. They do, however, suffer from the drawback of limited spectral coverage, and so a novel, broadband laser source called a digital supermode distributed Bragg reflector (DS-DBR) laser is introduced. This laser retains the favourable attributes of normal diode lasers, but is widely tunable. The first ever demonstrations of this laser for spectroscopy are presented, highlighting its ability to perform high resolution studies across a wide wavelength range. This DS-DBR laser is then combined with CRDS and CEAS in Chapter 3. The resultant near-IR, cavity-based spectrometers are characterised and used to study CO_2 in air, calibrated mixtures and breath samples. In this last case, investigations are also undertaken concerning the accurate determination of the $^{13}C/^{12}C$ ratio in exhaled CO_2, this being an approach for medical diagnosis of *Helicobacter pylori* infection.

The focus of the thesis then shifts to the mid-IR. After a review of possible mid-IR radiation sources, the technique of difference frequency generation (DFG) is discussed in detail as the chosen method for the generation of mid-IR laser light in this work. DFG mixes two input laser beams to produce a third at a different frequency, and transfers the attributes of the two input light rays to the output beam; hence it can be used to translate the desirable characteristics of lasers operating in the near-IR to the mid-IR. In Chapter 4, the experimental set-up of such a system using near-IR diode lasers is described and the results of its combination with the CRD spectrometer developed in Chapter 3 are given in Chapter 5. This includes the characterisation of the mid-IR CRDS system created and demonstrations of its spectroscopic potential through investigations carried out on CH_4, acetone and deuterium.

Finally, Chapter 6 reports on the use of the DS-DBR laser as one of the near-IR sources in the DFG system in order to create a broadband mid-IR radiation source. Studies performed using this set-up for both direct and WM spectroscopy are presented, as well as the results of incorporating this DS-DBR DFG mid-IR source with cavity-based spectroscopic techniques. This represents the ultimate objective of the project: the combination of the DS-DBR laser, DFG and optical cavities to create a widely tunable, highly sensitive spectrometer in the mid-IR.

Throughout the thesis, the potential applications of any studies, especially those of a medical nature, are identified. These, along with the overall conclusions of this thesis and the possibilities for future work, are summarised in Chapter 7.

Chapter 2

Laser Light Sources in the Near-Infrared

Infrared light is the region of the electromagnetic spectrum between microwaves and visible light, encompassing wavelengths between 700 nm and 1 mm. On a macroscopic scale it is often associated with thermal activity as it correlates with energies of objects near room temperature, and on a molecular level it corresponds to energy changes associated with ro-vibrational transitions. IR radiation can be further sub-divided according to wavelength, with the near-IR comprising of light with wavelengths between $0.7 - 2.5$ μm, the mid-IR ranging over $2.5 - 12$ μm and the far-IR covering $12 - 1000$ μm. Lasers are more commonly available in the first of these ranges, and this chapter begins with an overview of both narrowband and broadband laser light sources available in the near-IR. A novel, widely-tunable, near-IR laser source, known as a digital supermode distributed Bragg reflector (DS-DBR) laser, is then introduced and described in detail. This laser is subsequently characterised and its use in near-IR spectroscopy demonstrated for the first time.

2.1 Near-Infrared Laser Light Sources

Many considerations must be taken into account in the selection of an appropriate coherent light source for absorption spectroscopy for gas sensing [24]. Perhaps of paramount importance is the wavelength of the chosen source, as, in order to perform absorption spectroscopy, a light source that is in resonance with the gaps between internal energy levels is required to selectively probe the species of interest. Overlap between the laser operating wavelength and the strongest absorption signature of the target molecule should be sought to improve sensitivity, though care must be taken to avoid intense spectral interferences: a

compromise between selectivity and sensitivity must thus be found. Light sources with narrow spectral linewidths and continuous, rapid tunability are, likewise, essential. Optimal beam profile, single-mode behaviour and moderate output powers (μW-mW) are also highly desirable or even crucial depending on the detection scheme adopted and the sensitivity levels required. In addition, the source should ideally have low intensity noise, be invariant to changes in environmental conditions and suffer no long term wavelength drifts. Compactness, robustness, reliability, low cost, room temperature operation and fibre-coupling are also extremely beneficial attributes, especially when designing commercial sensors or devices for field measurements.

Near-IR lasers can thus be used for gas detection as they can access wavelengths corresponding to the energies of overtones and combination bands of the ro-vibrational transitions of many species. The near-IR laser sources available can be divided into two categories: narrowband and broadband sources. Narrowband sources allow data to be recorded in small frequency steps over an absorption feature of interest, permitting high resolution measurements and lineshape determination of single ro-vibrational transitions in small, gas phase molecules. Due to the demand from the telecommunications industry, much effort has been invested in the development of these narrowband, near-IR lasers and so they possess many favourable characteristics; however, these sources tend to have limited wavelength tuning. Conversely, broadband sources cover an extended wavelength tuning range but often at the expense of spectral resolution. These sources are thus useful for studies involving the detection of multiple species that absorb at many different, widely separated wavelengths, or of larger, more complex molecules which exhibit complex, broadened spectral features rather than single, well-defined transitions ('broadband absorbers').

2.1.1 Narrowband sources

The most prevalent class of narrowband, near-IR laser sources are semiconductor diode lasers (DLs) [48, 91]. These are photon-emitting semiconductor $p-n$ junction diodes and their operation is explained in Figure 2.1. The laser material contains a band gap which separates the conduction and valence bands, and at the $p-n$ junction one side contains an excess of electrons in the conduction band (the n-doped side) and the other an excess of electron vacancies or 'holes' in the valence band (the p-doped side). When no potential difference is applied across the junction, the system is at thermodynamic equilibrium and the electrons fill up to one, uniform Fermi level, as shown in Figure 2.1(a). But on application of a forward-bias voltage, as in Figure 2.1(b), the energy band structure is distorted so that there are two, distinct Fermi energy levels either side of the junction. Consequently electrons flow from the n-type side of the junction into the conduction band whilst the holes are injected into the valence band from the p-type side; this creates a population inversion

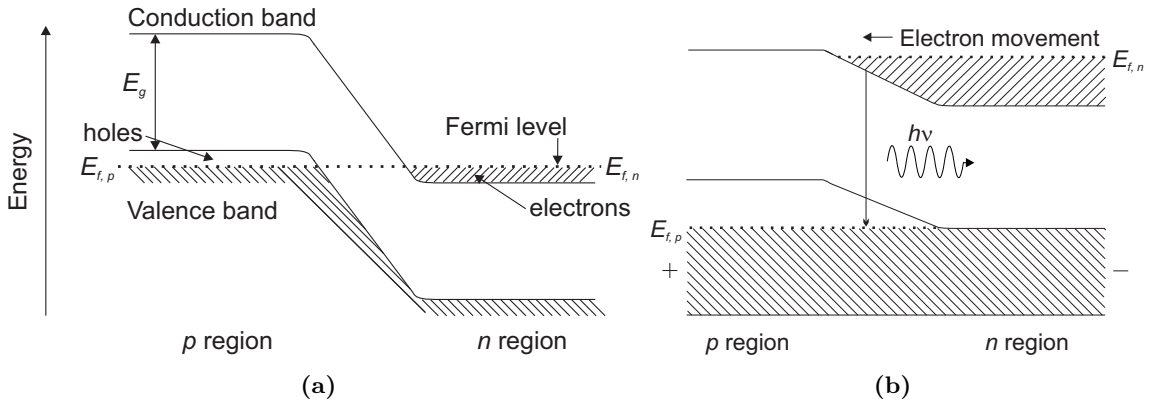

Figure 2.1: A diagram illustrating the band structure of a $p-n$ junction of a diode laser when (a) no voltage and (b) a forward voltage is applied across the junction. In (a), the two Fermi level energies either side of the $p-n$ junction, $E_{f,p}$ and $E_{f,n}$, are the same, *i.e.* $E_{f,p} = E_{f,n}$. In (b), these Fermi energies are different, with $E_{f,p} < E_{f,n}$, thereby inducing a population inversion. E_g is the band gap energy. Adapted from Demtröder [7].

to satisfy the lasing condition $N_u/g_u > N_l/g_l$, where N_i is the population of state i, g_i is its degeneracy and the subscripts u and l refer to the upper and lower states, respectively. Radiative recombination of the electron-hole pairs across the band gap at the junction leads to photon emission. Optical feedback can then result in the stimulated emission of further photons, so generating a laser output [7, 10, 166].

The $p-n$ junction can either be homojunction (consisting of layers of the same semiconducting material with different impurity dopants added either side) [7] or heterojunction (made of layers of different semiconducting materials) [43]. Recent designs involve double heterojunction structures, consisting of thin layers ($\sim 5-20$ μm) of an active semiconductor medium (*e.g.* GaAs) sandwiched between films of a higher energy band gap material (*e.g.* AlGaAs); such a structure induces quantum well confinement that raises the density of charge carriers thereby ensuring elevated recombination probabilities and output powers ($1-100$ mW) [43].

The output laser wavelength is determined by the size of the band gap between the conduction and valence bands, which is itself dependent on the chemical nature of the active material used; the wavelength can be adjusted a modest amount (±1 nm) by altering the refractive index of the active material via either temperature or injection current tuning. As the gain bandwidth of the device is typically tens of nm wide, it is necessary to use optical feedback not only to stimulate photon emission and so provide the lasing action of the device, but also to enhance the output at the desired frequency and suppress the output at others. In one configuration, optical feedback is provided by a wavelength selective diffraction grating. The wavelength selecting element can be placed either externally, *e.g.* external cavity diode lasers (ECDLs), or internally, *e.g.* distributed feedback (DFB)

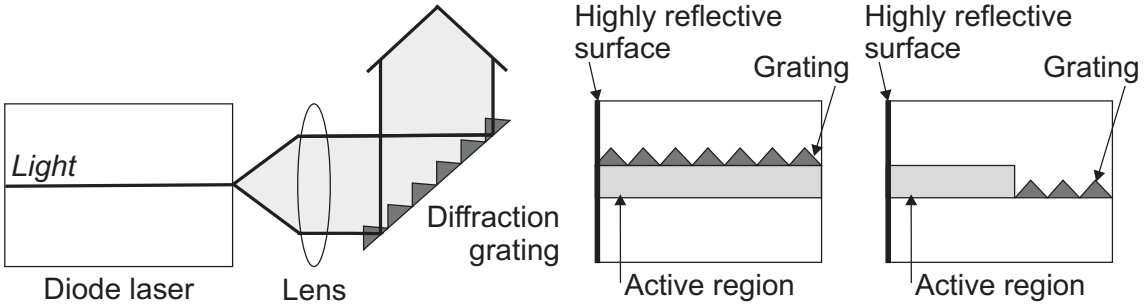

(a) ECDL **(b)** DFB **(c)** DBR

Figure 2.2: Standard designs of single frequency diode lasers: (a) ECDL, (b) DFB laser, (c) DBR laser.

and distributed Bragg reflector (DBR) lasers. In ECDLs (Figure 2.2(a)), the wavelength is modified by tuning the angle of the external grating structure [7]. In DFB lasers (Figure 2.2(b)), a Bragg diffraction grating, also known as a Bragg reflector, is etched into one of the layers surrounding the active medium of the laser [7]. This grating is made of a sequence of layers of materials with disparate refractive indices so that only the wavelength which satisfies the condition $\lambda = 2\Lambda n_{\text{eff}}$, where n_{eff} is the effective refractive index and Λ the period of the grating, is strongly reflected. A DBR laser (Figure 2.2(c)) is similar to a DFB laser but with the grating situated at one or both ends outside of the active region [10].

Diode lasers have many advantageous properties: they are robust, compact, economical, efficient, readily available, capable of single-mode room temperature operation and emit coherent, monochromatic, tunable radiation with a narrow linewidth (< 10 MHz) at relatively high powers. However, these lasers suffer from two major drawbacks: their limited spectral coverage to the visible and near-IR, which restricts their spectroscopic investigations to the weaker overtone and combination bands of molecules found in this region, and also their narrow wavelength tuning range.

2.1.2 Broadband sources

While diode lasers (Section 2.1.1) have many advantageous attributes, they only possess a modest tuning range (typically $\sim 1 - 2$ nm). It would be highly beneficial to have a laser source with tunability across a large wavelength range as it would enable multi-species detection or the study of broadband absorbers. Many different options for a broadband source exist, including Xe arc lamps, which are large, highly divergent and power hungry devices that mainly operate in the ultraviolet (UV) and visible regions of the EM spectrum, as well as light emitting diodes (LEDs) and their derivative, superluminescent light emitting

diode (SLEDs) [167]. Invented in 1986 [168], SLEDs couple the high power of diode lasers with the broad spectral range of LEDs and, as usual for semiconductor devices, consist of a $p-n$ junction across which a voltage is applied. Their applicability to near-IR spectroscopy has already been demonstrated [169].

Supercontinuum (SC) sources, based on third-order non-linear processes [170, 171] also provide near-IR broadband radiation. The generation of SC radiation was first observed in 1970 by focusing an intense narrowband laser pulse onto various crystals and glasses [172]. This resulted in a broadened spectral output due to non-linear optical effects [173, 174]. Recently, laser devices based on Raman-soliton SC generation in photonic fibres have been developed and utilised for spectroscopy [175]. This source offers broad wavelength coverage (several μm) and high output power (several W), but at a large financial cost ($>$ £30,000 compared with light emitting diodes at $<$ £5 [176]). Extending the spectral range to longer wavelengths beyond 4 μm is also proving technologically difficult [177].

Recently, a new type of broadband light source, known as a laser driven light source (LDLS), has become commercially available [178]. These sources use a cw laser to directly heat a Xe plasma to high temperatures (20,000 K), inducing the emission of broadband radiation. With a long lifetime ($>$ 10,000 hrs), broad spectral range ($0.2 - 2.1$ μm), small size, relatively high intensities, excellent power stability and a good spatial beam quality, these sources offer great potential for sensitive absorption spectroscopy. Indeed, demonstrations of such a combination have already been conducted: gaseous acetone and ambient O_2 have been measured at 280 nm and 760 nm, respectively, using a LDLS and broadband CEAS (BBCEAS), achieving $\alpha_{\min}(BW)$ values of $10^{-6} - 10^{-7}$ cm^{-1}Hz$^{-1/2}$ [176]. LDLSs have also been proposed as an alternative light source in fluorescence microscopy [179], though their comparatively high costs ($\sim$ £10,000) currently prevent widespread use.

Femtosecond pulses have broad spectral bandwidths which pave the way for another class of near-IR laser sources: optical frequency combs. These provide many sharp spectral components (frequency comb teeth) evenly spread across a broad bandwidth. Tunability over 200 nm in the telecom region has been reported allowing for the simultaneous, real-time monitoring of CO_2 isotopic ratios and CO in breath, as well as the detection of trace amounts of NH_3 in H_2O, with a spectral resolution of 800 MHz across $1.5 - 1.7$ μm and an $\alpha_{\min}$ of 8×10^{-10} cm^{-1} [161]. However, expense and experimental difficulties, due to its use of femtosecond laser technology, constitute disadvantages to this broadband source.

Driven by interest from the telecommunications industry, broadband sources based on extending the continuous tunability of the traditional diode lasers of Section 2.1.1 have also been developed [180, 181], with the aim of covering more than 50 nm across the entire C- ($1530 - 1565$ nm) or L- ($1565 - 1625$ nm) telecommunications band. These sources include using arrays of individual lasers, adopting either piezo-driven or microelectromechanical

systems (MEMS)-based external cavity configurations [182, 183] and monolithic tunable lasers [184, 185]. This latter class of devices achieve wavelength tuning by use of a comb reflector with multiple reflection peaks, coupled with a second dispersive element for peak selection. Both gratings are integrated into the monolithic platform, conferring mechanical stability and the possibility of fast modulation: for monolithic devices, modulation rates of the order of MHz via electronic tuning are possible, compared with the kHz modulation rates achievable via mechanical tuning for external cavity lasers (ECLs) [186]. Examples of these monolithic devices include modulated grating Y-branch (MG-Y) [187, 188] and sampled grating distributed Bragg reflector (SG-DBR) [186, 189] lasers, which utilise Vernier tuning between the two grating combs to alter the wavelength. Another monolithic design has also been developed: the digital supermode distributed Bragg reflector (DS-DBR) [190–194] laser. This device, devised as telecommunication equipment for optical switching and wavelength division multiplexing, can cover a 50 nm spectral region by means of a highly uniform comb reflector coupled with a multi-grating structure for quasi-digital selection of a sub-band of the total tuning range.

It is this last type of laser, the DS-DBR, that provides the novel near-IR laser source utilised in this thesis. The rest of this chapter describes the design and operation of the DS-DBR and also presents the first ever examples of its use in spectroscopy; these simple, direct absorption and wavelength modulation experiments in the near-IR were performed in order to characterise the source and to demonstrate its suitability for spectroscopy. Further examples of the spectroscopic applications of this laser are given later in this thesis in Sections 3.4 and 3.3, where it is used in near-IR CEAS and CRDS, and in Chapter 6, where it is combined with difference frequency generation to produce mid-IR light.

2.2 Digital Supermode Distributed Bragg Reflector Laser

2.2.1 Digital supermode distributed Bragg reflector (DS-DBR) laser

The DS-DBR laser is an indium phosphide (InP) diode laser, constructed by conventional ridge laser processing techniques as a monolithic, multi-section platform by *Bookham Technologies* (now *Oclaro Inc.*) [190, 195–197]. Its design has been extensively reported in the literature [191, 198] and is illustrated in Figure 2.3(a). It consists of four sections: a rear phase-grating section, a phase control section, a multi-quantum well gain section and a multi-contact front chirped-grating section. The platform has also been monolithically integrated with a semiconductor optical amplifier (SOA) to enhance the output power. It is based on a conventional three-section DBR laser where the rear Bragg grating, which defines the emitted wavelength, is separated from the gain medium and phase section, which

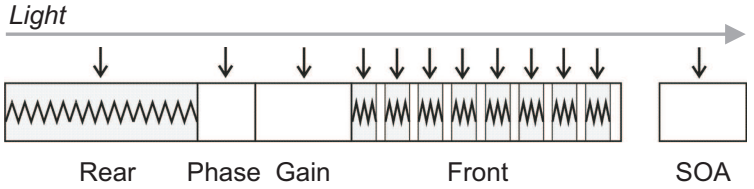

(a) Schematic diagram of the multiple sections of the DS-DBR. The rear reflector and front multi-grating structure surround the gain and phase sections, with the arrows representing the electrical contacts. The SOA is not part of the laser cavity, but is positioned next to the front grating. Light output occurs to the right of/after the SOA.

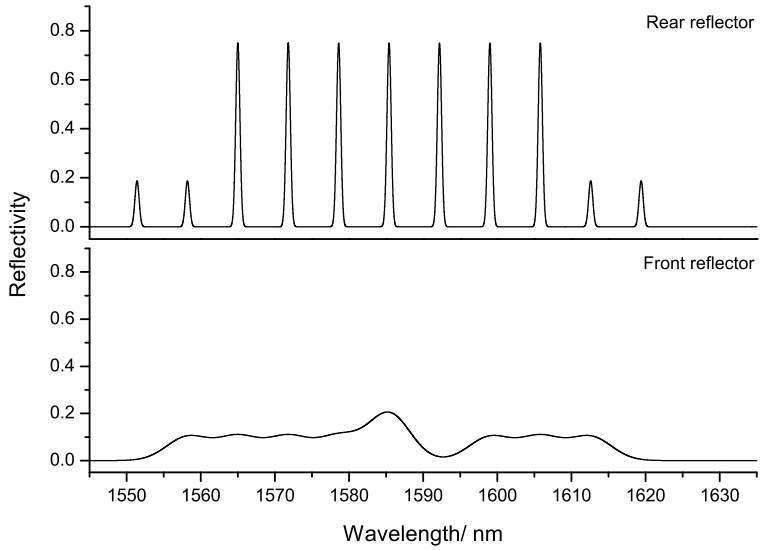

(b) The responses of the rear reflector and front grating on injection of current into one of the front contacts.

Figure 2.3: Schematics illustrating (a) the DS-DBR sections and (b) their responses to current injection. Both adapted from Ward *et al.* [191].

provide optical amplification and continuous, fine, wavelength tuning (by longitudinal mode tracking), respectively.

The DS-DBR is capable of covering an extended spectral region of $\sim$ 50 nm and this is achieved by essentially combining several DBR devices which operate within sequential wavelength ranges with a front grating section to select between them. The tuning mechanism consists of a rear comb reflector and a multi-contact front grating [191], each of which exhibits different designs and spectral responses. The rear reflector section comprises a phase-grating formed by e-beam processing which, by careful choice of the positions of the phase shifts by varying the component grating lengths, generates a top-hat comb of seven sharp reflection peaks [191], as shown in Figure 2.3(b); these 'supermodes' are of equivalent heights and spacings ($\sim$ 6.8 nm) and have a good side-mode suppression ratio [199, 200]. In contrast, the front section features a longitudinal sequence of compact ($20-50$ μm) holographic gratings with different pitches, each of which possesses its own electrical contact.

The short length of the gratings means that in the absence of an applied current to this section, the front reflector gives a broad, featureless, non-selective reflectance profile.

Coarse wavelength tuning across the wavelength range is achieved in quasi-digital style by injecting current into one front contact pair, so inducing a change in refractive index across the selected pair. This results in the first grating of the pair returning a blue-shifted response which increases the reflectivity of the adjacent, second grating at that wavelength. The strengthened reflectance overlaps with just one supermode of the rear comb (Figure 2.3(b)). Fine wavelength tuning is then performed by synchronously varying the injection currents of the rear and phase sections. The exact position of the supermode, which governs the lasing wavelength, can be adjusted by altering the current applied to the rear section. Each supermode includes several longitudinal modes (whose spectral separation is dictated by the laser cavity geometry) and changes to the phase injection current allows one of these to be selectively tracked. In consequence, each supermode can thus be considered as a separate three-section DBR device, tunable over $\sim$ 8 nm in small frequency steps through selection and tuning of the longitudinal modes by varying the rear and phase currents. Access to the next, adjacent wavelength sub-band or supermode in the series is accomplished by simply switching the injection current of the front section to the next front grating contact pair in the sequence; this injects the current at a different position, thus changing the length, and coarse wavelength output, of the laser. Hence by selection of the front pair contacts and the injection currents of the different sections, the whole wavelength range of the laser can be accessed, and each front pair effectively corresponds to a different supermode.

DS-DBR lasers covering $\sim$ 50 nm across either the C- or L-telecoms band are available [193], and research into extending the range even further, ultimately with the goal of producing a device which covers both the C- and L-band, is underway [201]. The DS-DBR employed in this thesis [202–206] operates over $1563 - 1613$ nm in the L-band. It has an internal thermoelectric cooler (TEC) and is packaged in a standard 26-pin butterfly pigtail module. This module was placed in a commercial diode laser mount (*ILX Lightwave*, LDM-4989), but controlled by a custom-built laser driver unit which permitted the current levels for the different sections to be specified independently; more details of the laser driver are given in Section 2.2.2. By changing the injection current settings applied to the various sections of the DS-DBR by this laser driver, the output wavelength could be tuned across the $1563 - 1613$ nm range. The fibre-coupled output power was measured as $\sim$ 20 mW (22.6 mW and 24.2 mW at wavelengths near the opposite ends of the DS-DBR spectral range of 1570.435 nm and 1605.489 nm, respectively) and the linewidth reported in the literature as 1 MHz [194].

The DS-DBR offers a wide wavelength coverage coupled with the high resolution characteristics of single-mode diode lasers. As such, it has the potential to be a powerful spectroscopic instrument, facilitating high resolution measurements of species across a large spectral region. The laser is able to rapidly switch between static frequencies [207, 208] as required by the telecommunications industry, but for spectroscopy it is necessary to sweep or step the device continuously over a desired spectral window in order to probe the absorption features of interest (though the capacity for fast switching between widely separated, discrete spectral segments of the DS-DBR may prove useful in the detection of multiple species that absorb at very different wavelengths). Accordingly, in order to determine the suitability of the DS-DBR for sensitive, high resolution spectroscopy, it was essential to investigate the laser response to such operating conditions. This was undertaken by monitoring the well-characterised ro-vibrational absorption features of CO_2 found within the spectral output of the laser, as discussed in Sections 2.2.2 and 2.3.

2.2.2 Modes of operation

The DS-DBR laser was controlled by a home-made driver unit that permitted independent settings of the currents for the different sections of the device. A particular 'front pair' (FP) of the multi-contact front section was selected for the location for the injection of current into the front grating, referred to by the number of the first front contact, *e.g.* 'front pair 3' meant the first front contact (Front 1) was 3 and the second front contact (Front 2) was 4. The first front contact was always held at a fixed current of 5.5 mA. Constant currents were also injected into the SOA (120 mA) and the gain (150 mA) sections of the device to deliver a stable output power. Modulated currents were then applied to the second front contact, rear and phase section, labelled as i_f, i_r and i_p, respectively.

The laser was controlled in two alternative ways: by internal ramping of the injection currents to the different sections [202, 205] or by the application of external voltage ramps [206]. These two methods are described below.

2.2.2.1 Internal ramping

In the internal ramping mode, a waveform generator built into the laser driver supplied input currents with a sawtooth modulation to the rear grating, phase section and second front contact concurrently, as shown in Figure 2.4. These three waveforms had the same frequency (variable between $0.5 - 1000$ Hz) but different offsets and amplitudes, dependent on the target wavelength and determined from the manufacturer's look-up table.

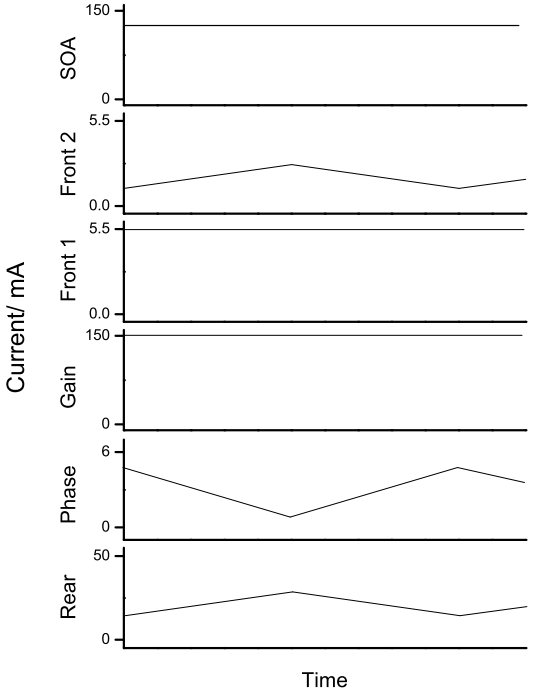

Figure 2.4: The current waveforms applied to the different sections of the DS-DBR laser when operated in the internal ramping mode. The sections are arranged from bottom to top in the order in which they appear in the laser module. The values on the abscissa are the upper and lower current limits imposed on the various sections.

To investigate the behaviour of the laser wavelength on scanning the sections in various ways, the transmission spectrum of CO_2 was measured under different operating conditions. The laser light was injected into a multi-pass cell with a path length of 416 cm filled with 85 Torr of CO_2. The attenuated radiation was then detected by a near-IR detector (*Thorlabs*, DET410) and recorded on an oscilloscope (*Agilent*, MSO8104A Infiniium, 1 GHz, 4 GSa/s). Simultaneous wavelength measurements were also made using a spectrum analyser with a FSR of 2.32 GHz (*Melles Griot*, 13SAE906) and a wavemeter (*Burleigh*, WA-1000) for relative and absolute frequency calibrations, respectively.

CO_2 was the chosen molecule for these studies as transitions in the $3\nu_1 + \nu_3$ vibrational band of CO_2 occur throughout the $1563 - 1613$ nm range of the DS-DBR. Specifically, the R and P branches of the $\nu(30012 \leftarrow 00001)$ and $\nu(30013 \leftarrow 00001)$ transitions occur at $1565 - 1585$ nm ($6310 - 6390$ cm^{-1}) and $1595 - 1615$ nm ($6190 - 6270$ cm^{-1}), respectively, with each transition labelled as (ν_1 ν_2 l ν_3 r), where ν_i is the quantum number for the i^{th} fundamental mode of vibration (ν_1 is the symmetric stretch, ν_2 is the bending mode and ν_3 is the antisymmetric stretch), l is the vibrational angular momentum quantum number associated with ν_2 and r is the index denoting the Fermi resonance [14, 209].

Figure 2.5(a) shows an example of the transmission spectrum and spectrum analyser trace recorded when i_r and i_p were ramped simultaneously with FP 7. Absolute wavelength

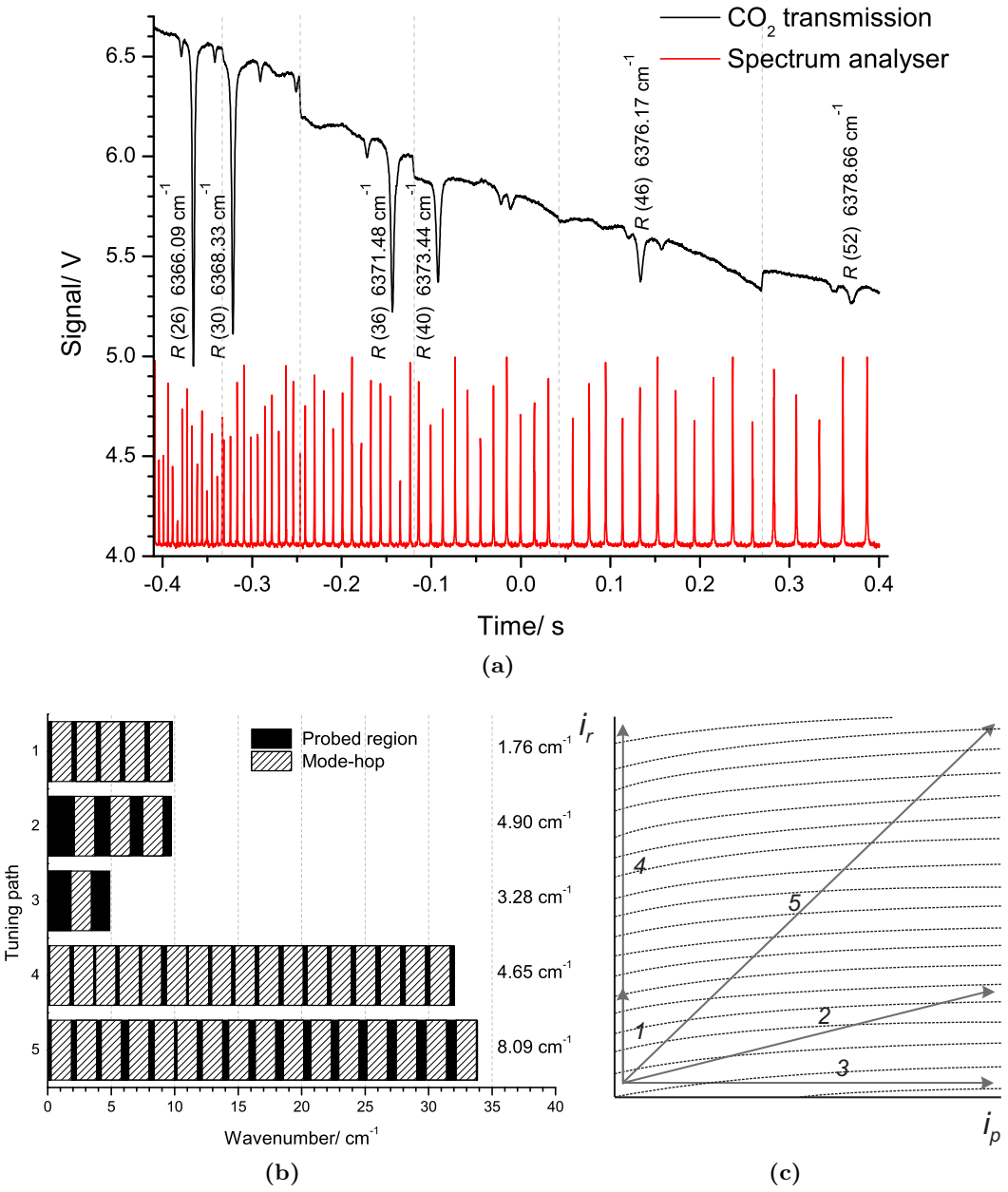

Figure 2.5: Understanding and quantifying the mode-hop behaviour of the DS-DBR when operated in the internal ramping mode. (a) The CO_2 transmission spectrum ($l = 416$ cm, 85 Torr) and 2.32 GHz spectrum analyser trace observed when the currents applied to the rear and phase sections are modulated simultaneously. Mode-hops are indicated by dashed vertical lines and the major CO_2 absorptions due to R branch transitions in the $3\nu_1 + \nu_3$ vibrational band have been assigned. (b) Bar chart reporting the tuning ranges achieved by scanning the DS-DBR laser in five different ways, distinguishing between the spectral regions probed by the laser and those not (the mode-hops). For the front pair contact used in this example, the mode-hop jump was 1.61 cm^{-1}. The numbers at the side of each bar give the probed wavenumber range. (c) Plot explaining the differing number of, and frequency range between, mode-hops under different scanning conditions. The dashed lines represent the boundaries between the longitudinal modes for a given supermode or front pair as a function of i_r and i_p, and the solid lines illustrate the five different tuning paths of (b). Every time a longitudinal mode is crossed by the scanning function, a mode-hop is observed. Adapted from Ward *et al.* [191].

Tuning path	i_r / mA	i_p / mA	Number of mode-hops	Average $\tilde{\nu}$ between mode-hops/ cm^{-1}	Total scanned $\tilde{\nu}$ range/ cm^{-1}	Effectively probed $\tilde{\nu}$ range/ cm^{-1}
1	$0-20$	0	5	0.29	9.81	1.76
2	$0-20$	$0-6$	3	1.23	9.73	4.90
3	0	$0-6$	1	1.64	4.89	3.28
4	$0-50$	0	17	0.26	32.02	4.65
5	$0-50$	$0-6$	16	0.48	33.85	8.09

Table 2.1: Summary of the different scanning conditions applied to the DS-DBR laser in Figures 2.5(b) and 2.5(c) and the resulting effects on the wavelength range probed. All used the same FP (5) with a constant front injection current.

measurements from the wavemeter and comparison of the absorption features with HITRAN simulations [14] allowed the transitions to be assigned. This in turn meant that mode-hops, which are jumps in the laser frequency resulting in gaps between continuous regions of recorded spectra, and the wavelength tuning range ($6365-6379$ cm^{-1}) could be identified.

Using the same methodology, five different operating conditions within the sub-band associated with one supermode (FP 5 in this case) were investigated by altering the relative amplitudes of the current ramps applied to the front, rear and phase sections; the resultant tuning characteristics are shown in Figure 2.5(b) and Table 2.1. When scanning just i_r across its full range (path 4), many mode-hops were observed and so only a small fraction of the overall range (4.7 cm^{-1} out of 32.0 cm^{-1}) was effectively accessible with the laser. Conversely, varying i_p alone (path 3) exploited the maximum tunability of one longitudinal cavity mode, and thus minimised the number of mode-hops and allowed access to a larger portion of a much narrower spectral window (3.3 cm^{-1} out of 4.9 cm^{-1}). When both i_p and i_r were varied (paths 2 and 5), intermediate performances were seen, depending on the relative extent to which i_p and i_r were tuned. These responses suggested that under the same i_r scanning regimes (*i.e.* similar total tuning ranges), a larger fraction of the spectrum was probed with a reduced number of mode-hops if i_p was also ramped at the same time. This behaviour can be rationalised by considering the longitudinal mode structure typical of a supermode [191], as shown in Figure 2.5(c), where the boundaries between consecutive longitudinal modes are plotted as dotted curves as a function of i_r and i_p and the different tuning paths along which the laser was driven are represented with arrows. As the currents are scanned, continuous wavelength tuning is observed when the path falls between these curves, but when a curve is crossed a mode-hop occurs [210].

It was noted that ramping i_f in addition to i_r and/or i_p had little effect on the spectral response. This may be due to fact that the selected front grating reflection is wider than the reflectivity curve of the overlapping supermode (Figure 2.3(b)), meaning high accuracy

Front pair	1	2	3	4	5	6	7
Mode-hop jump/ cm^{-1}	1.47	1.51	1.54	1.58	1.61	1.65	1.68

Table 2.2: Measured mode-hop jumps of the different supermodes (front pairs).

in the front grating tuning is unnecessary as the operating wavelength is principally defined by the rear and phase sections [190].

It was also noticed that the magnitude of the mode-hop jump was the same within a given supermode but varied between them, with the size of the mode-hop jump increasing as the FP increased (Table 2.2). This is because the length of the laser cavity is effectively altered on changing the FP as this adjusts the location of current injection into the front section [210]. The typical lengths of the different sections of the laser module reported in the literature - 500 μm for the rear, 500 μm for the gain, 100 μm for the phase and $0 - 300$ μm for the front (dependent on the FP selected) [191] - give FSRs of $1.10 - 1.32$ cm^{-1} for the different supermodes, which are comparable in terms of size and range to the mode-hop jumps observed experimentally.

In summary, modulating the injection currents of the different sections in this internal ramping mode allowed the laser to be scanned quasi-continuously over the $1563 - 1613$ nm range, but subject to the occurrence of mode-hops. These jumps in frequency of $\sim$1.7 cm^{-1} (determined by the geometry of the laser cavity) resulted in spectral gaps in the wavelength range probed. The number of mode-hops, and the wavelength range between them, varied depending on how the laser was scanned.

2.2.2.2 External ramping

In later work, modifications of the custom-built laser driver unit were undertaken to allow the application of external voltage ramps as well as those generated internally. As in the internal ramping mode of operation, this external ramp was applied simultaneously to the rear, phase and second front contact. This adaptation meant that voltage ramps of varying shapes, amplitudes and frequencies could be used to scan the injection currents for the different sections and thus scan the wavelength, or, alternatively, fixed injection currents could be applied giving fixed output wavelengths. Through the use of a 16-bit digital-to-analog converter (DAC), current step sizes of 0.125 μA in the front and phase sections, and 1.25 μA in the rear section, were achievable, corresponding to step sizes in wavelength as small as 1.5×10^{-5} nm (6×10^{-5} cm^{-1}, 2 MHz).

This ability to set fixed wavelengths of the DS-DBR (by fixing the injection currents of the different sections) meant that the laser was able to be discretely stepped, rather than

continuously scanned, across a wavelength range. This is a very useful property for the following reason: as seen in Section 2.2.2.1, if careful thought is not given to the current ramps selected when the laser is operated in a scanning mode, mode-hops may occur resulting in jumps in the laser output frequency, hence preventing access to certain spectral regions; however, when operated in a stepping mode, the entire wavelength range can be accessed by choosing appropriate fixed injection current settings.

LabVIEW [211] control of the DS-DBR was also developed so that the laser could be switched on and off remotely. The capability to set and change the fixed injection currents of the different sections via LabVIEW, thereby allowing the user to set the laser wavelength, was also established, as were programs that applied a sequence of pre-determined fixed currents or variable waveforms.

2.3 Demonstration of the DS-DBR Laser for Near-Infrared Spectroscopy

Whilst common in the telecommunications industry, DS-DBR lasers have never before been used to perform spectroscopic measurements. In this section, the first ever demonstrations of a DS-DBR as a laser source for near-IR spectroscopy, using both modes of operation reported in Section 2.2.2, are presented [202, 206].

2.3.1 Internal ramping mode

The results of Section 2.2.2.1 indicated that the laser could deliver mode-hop free scans over more than 2 cm^{-1} if the modulation settings for the front, rear and phase sections were carefully selected. In order to find these appropriate settings and provide an absolute frequency calibration for them, the experimental set-up described in Section 2.2.2.1 was used to perform direct absorption spectroscopy on CO_2. Approximately 80 combinations of settings giving consecutive, partially overlapping, mode-hop free spectral segments covering the two CO_2 combination bands over the $1563 - 1613$ nm DS-DBR wavelength range were found [202]. In each combination of settings, the FP contacts and i_f were fixed and the DS-DBR laser was scanned by ramping i_r and i_p. This was achieved by defining minimum and maximum values for i_r and i_p. Using a spectrum analyser and the known CO_2 transition frequencies, an absolute wavelength calibration was thus determined. The reliability and reproducibility of the DS-DBR meant these settings and calibrations could be used in future experiments.

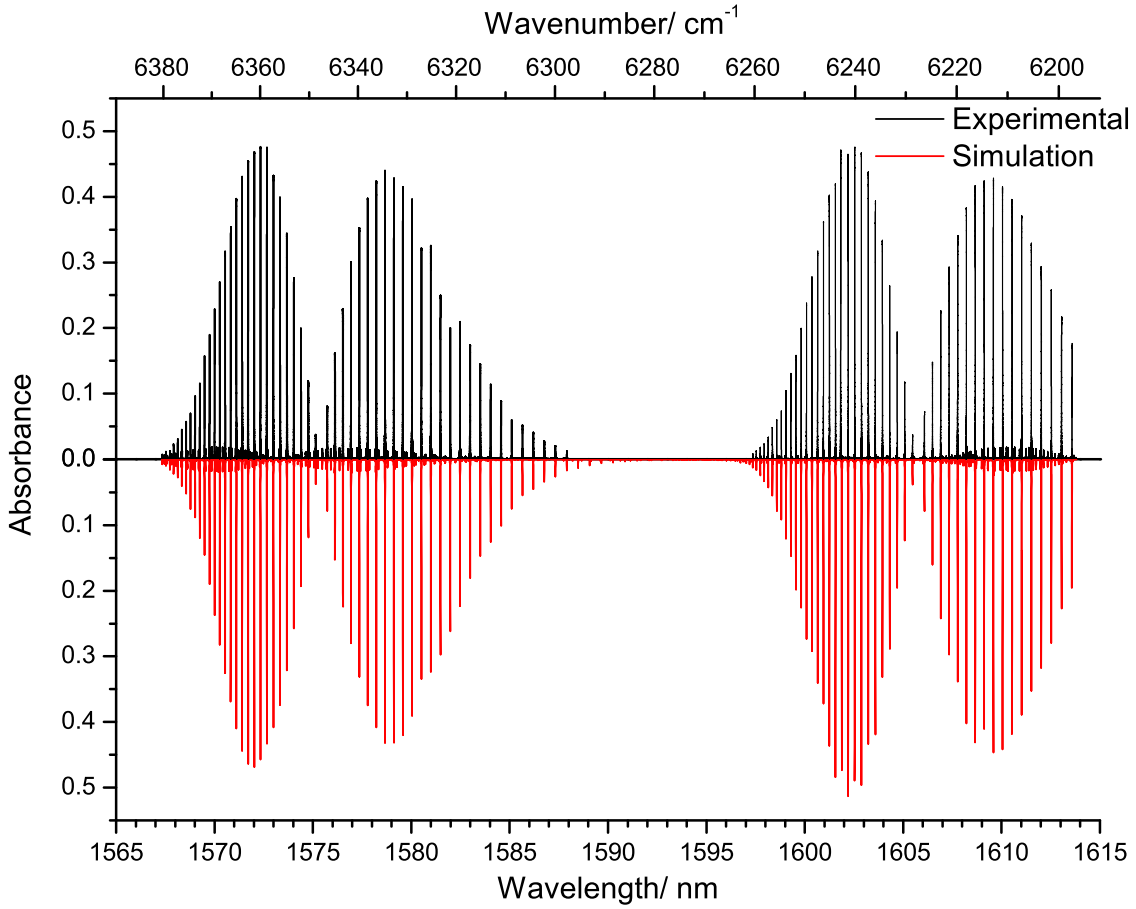

Figure 2.6: The experimentally recorded (upper) and HITRAN simulated (lower) [14] absorption spectrum of an 85 Torr sample of CO_2 across the $1563-1613$ nm spectral range of the DS-DBR ($l = 416$ cm).

The reproducibility of the DS-DBR was estimated by repeatedly turning the laser on and off and tracking the position of an absorption line. The absorption spectrum was recorded after a 2 s settling time following a switching event, and a frequency deviation as low as ± 7 MHz was measured over 10 min of uninterrupted lasing.

The CO_2 absorption spectrum across the whole $1563 - 1613$ nm range was reconstructed by stitching together the individually recorded scans and is given in Figure 2.6 along with a simulation based on values from the HITRAN database for the experimental conditions used [14]. The spectrum is dominated by two main ro-vibrational bands, which represent two of the four Fermi resonance components of the $3\nu_1 + \nu_3$ combination band mixing with other nearly degenerate bands exhibiting the same symmetry. Weaker transitions belonging to different combination bands and hot bands are also identifiable.

As well as offering this broadband coverage, the DS-DBR also supported high resolution spectroscopy, as exemplified by Figure 2.7 which shows expanded regions of Figure 2.6. Voigt profiles were fitted to the data points by fixing the Gaussian width at the expected Doppler width of 357 MHz and permitting other parameters to float. In the case of the

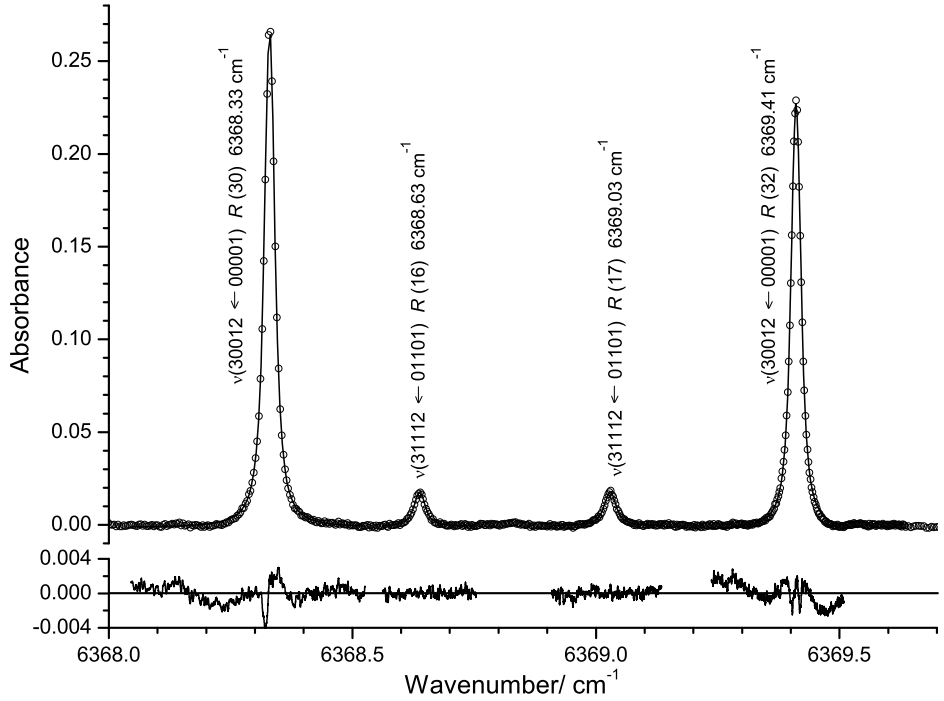

(a)

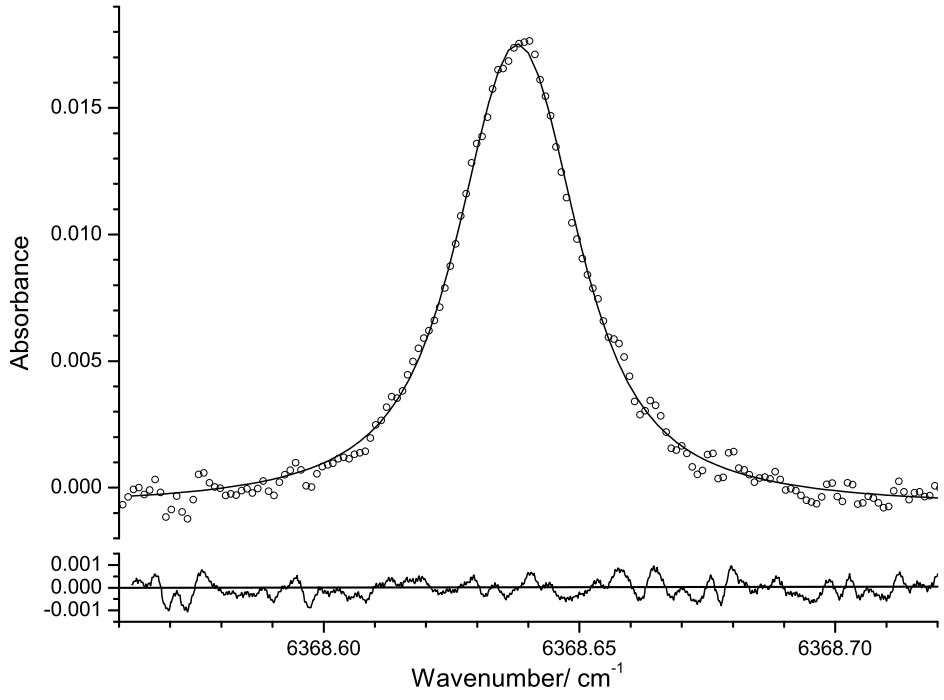

(b)

Figure 2.7: Expanded spectra of Figure 2.6 showing R branches in the $\nu(30012 \leftarrow 00001)$ and $\nu(31112 \leftarrow 01101)$ transitions of CO_2 around 1570 nm; transitions have been labelled following the nomenclature introduced in Section 2.2.2.1. The raw data (open circles) and Voigt fits (solid line) are shown in the upper trace, and the residuals between the two in the lower one. The number of experimental points has been reduced for clarity. In fitting the Voigt profiles, the Gaussian width was fixed at the expected Doppler width of 357 MHz and other parameters allowed to float. The returned Lorentzian widths agreed within 2% with the values predicted from the HITRAN database simulations.

$\nu(31112 \leftarrow 01101)$ $R(16)$ transition in Figure 2.7(b), the Voigt fit returned a goodness of fit R^2 value of 0.9939 and a Lorentzian width of 670 ± 4 MHz, which compared well with the value expected using the broadening coefficients from the HITRAN database of 680 ± 9 MHz. The area of the Voigt fit was also used to estimate the amount of CO_2 present in the multi-pass cell: the experimentally retrieved value of 85.4 ± 0.3 Torr was consistent with the pressure inside the cell measured using a baratron.

As a consequence of these absolute frequency calibrations, a current-wavelength reference table was produced. However, it was observed that the laser exhibited a non-linear wavelength-current dependency, as illustrated by the spectrum analyser trace in Figure 2.5(a). The degree of this non-linearity depended on whether the rear or phase section had a dominant role in the wavelength tuning and was further investigated using WMS.

The laser was scanned with a tuning path similar to that of path 2 in Figure 2.5(c), covering two CO_2 absorption lines within the same scan, namely the $R(20)$ and $R(22)$ transitions belonging to the $3\nu_1+\nu_3$ vibrational band at 6242.67 cm^{-1} and 6243.91 cm^{-1}, respectively. A fast modulation (1.3 kHz) was applied to either the phase or rear current ramp, with either a low or high modulation amplitude, A_m, set on the lock-in amplifier (*Stanford Research Systems*, SR830), and the signals demodulated at the second harmonic (Figure 2.8(a)). In each case, the pair of $2f$-WMS profiles returned a ratio of peak-to-peak amplitudes which differed greatly from the ratio of the experimentally measured direct absorbance values of 1.06. This unusual result can be ascribed to the aforementioned wavelength-current non-linearity, which causes the true modulation amplitude, a_m, to vary across the spectral region, thereby influencing the peak-to-peak amplitudes of the two WMS profiles to different extents, *i.e.* for a constant lock-in amplifier modulation amplitude of A_m in mV, there is a variation in the optical frequency modulation amplitude, a_m in cm^{-1}, with frequency across the scan, which skews the relative heights of the absorptions.

It was observed that the direction and speed with which a_m varied with wavelength across the spectral window, and hence the variation in the WMS signal amplitudes, depended on whether the fast modulation was applied to the phase or rear current and also on whether the modulation index, b (Equation 1.35), regime was low or high. This is summarised in Figure 2.8(b), where the measured peak-to-peak amplitudes of the pair of $2f$-WMS profiles are plotted as a function of b at each line position, as well as the theoretical trends expected for the $2f$-WMS Voigt profiles simulated for each modulation setting. These experimental and theoretical values agreed well for both of the transitions studied, but also highlighted the importance of evaluating and accounting for the contribution of modulation broadening to the spectral linewidth when conducting ratio measurements.

Although the wavelength-current non-linearity of the DS-DBR introduces complications in the retrieval of WMS signals due to the variation in a_m with wavelength, the DS-DBR

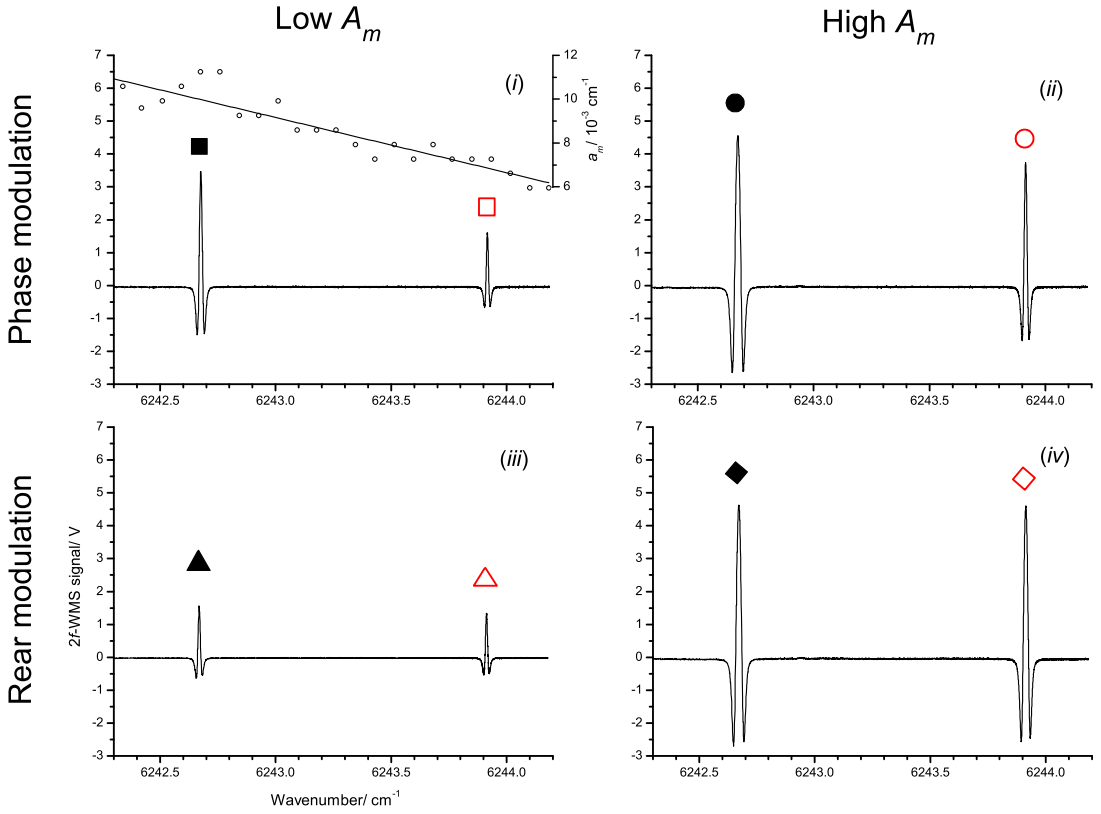

(a)

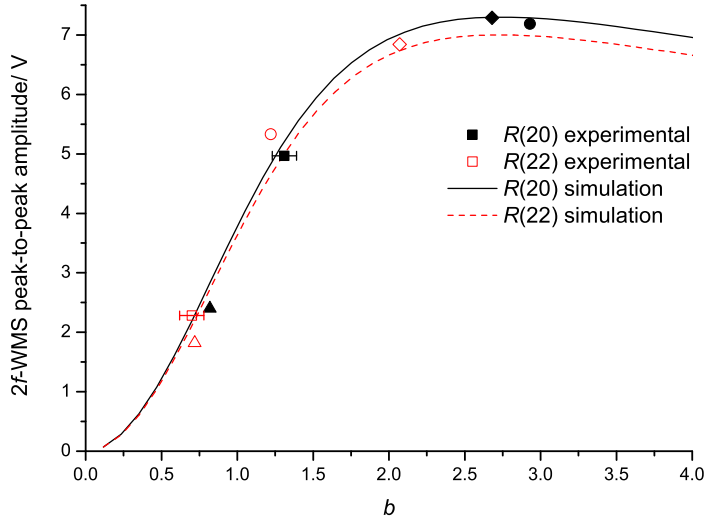

(b)

Figure 2.8: (a) $2f$-WMS spectra corresponding to the $R(20)$ (filled markers) and $R(22)$ (open markers) CO_2 transitions within the $3\nu_1 + \nu_3$ combination band at 6242.67 cm^{-1} and 6243.91 cm^{-1}, respectively, recorded under four different modulation settings. The wavelength range was scanned by means of a simultaneous modulation of i_p and i_r at 0.6 Hz and WMS conducted by superimposing a 1.3 kHz modulation to either the phase (*i*, *ii*) or rear (*iii*, *iv*) current inputs, at both low and high lock-in amplifier modulation amplitudes, A_m. The change in the magnitude of the optical frequency modulation amplitude, a_m, with wavelength for case (*i*) is also reported. The comparison between the experimentally measured and theoretically expected $2f$-WMS peak-to-peak amplitudes for the modulation settings in (a) are shown in (b).

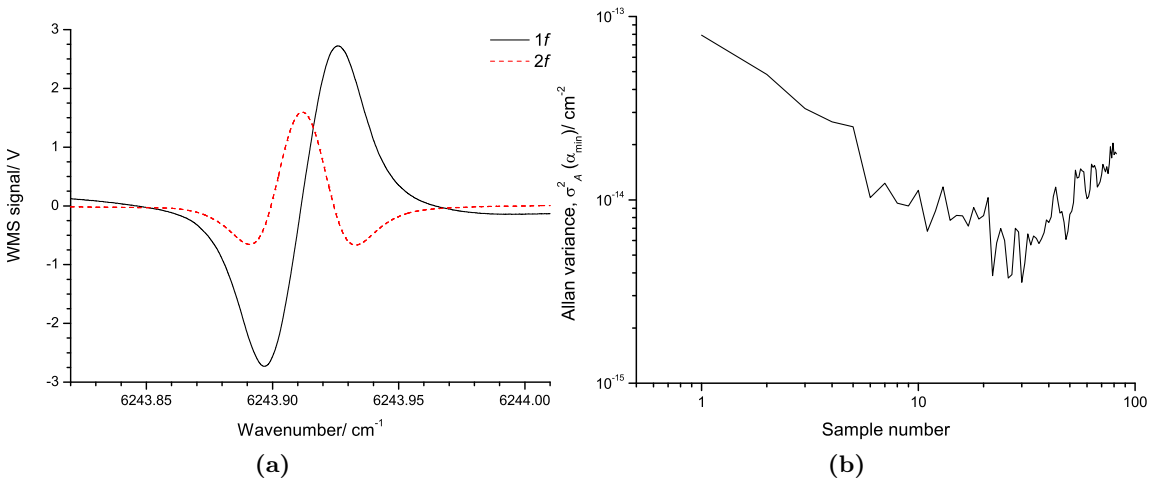

Figure 2.9: Further WMS investigations of the $R(22)$ transition at 6243.91 cm^{-1} using a calibrated mixture of 6% CO_2 in air at 74 Torr and path length of 416 cm. (a) $1f$- and $2f$-WMS signals for this absorption, highlighting the small RAM contribution to the baseline of the $1f$ profile. (b) Allan variance for the $2f$-WMS signal, with a spectrum recorded every 0.95 s.

does have the advantage of an effective independence between the wavelength and output power. This allows WMS to be conducted without large RAM distorting the profiles, raising the possibility of exploiting the intrinsically higher signals associated with $1f$-WMS: this is demonstrated by the near-zero offset of the baseline of the $1f$-WMS profile in Figure 2.9(a). An Allan variance analysis was carried out for the $2f$ detection scheme to examine the instrumental stability, yielding an optimal $\alpha_{\min}$ of 6.3×10^{-8} cm^{-1} measured over a 23 s acquisition time (Figure 2.9(b)). This sensitivity could be further improved by normalising the WMS signal to the instantaneous output power or by better stabilisation of the temperature of the system.

2.3.2 External ramping mode

When operated in the external ramping mode, fixed injection currents were applied to the different sections to give a fixed output wavelength, with each combination of fixed injection currents (referred to as 'settings' and expressed as (FP, i_f, i_r, i_p)) corresponding to one wavelength. This is demonstrated in Figure 2.10, which shows how the laser wavelength changes on varying i_f and i_r for a given FP and i_p. The discontinuities in wavelength indicate the boundaries of the different supermodes; each front pair effectively corresponds to just one supermode, apart from regimes where the injection currents are near their upper or lower limits when neighbouring supermodes are accessed instead [191, 201].

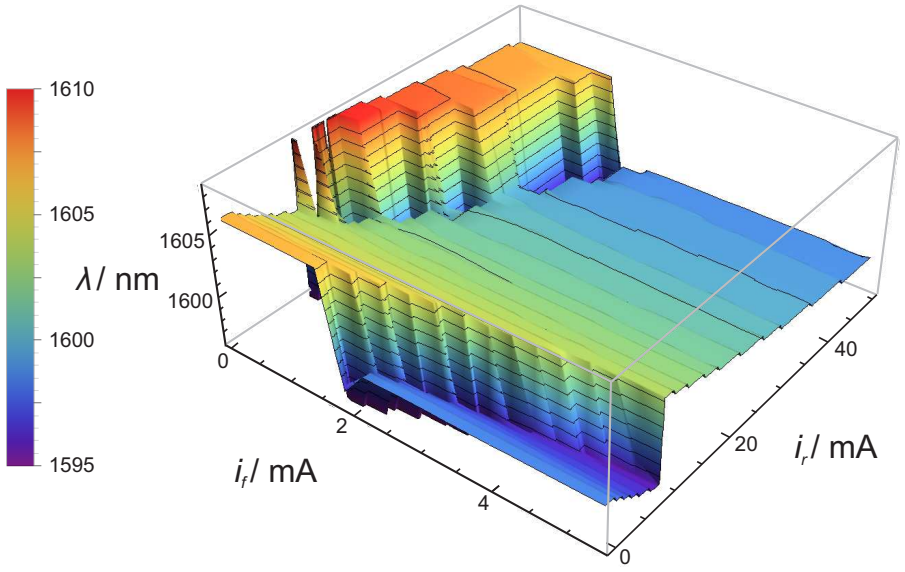

Figure 2.10: Output laser wavelength over the i_f-i_r plane for one front pair. Data recorded using FP 2, a fixed i_p of 0 mA and steps of 0.3 mA and 0.25 mA in i_f and i_r, respectively.

Hence, in order to step across a region with a certain step size to record spectra, all that is required is the selection of the appropriate settings which produce the necessary wavelengths. This must be done with care, however, to avoid mode-hops between the steps, which would result in larger wavelength jumps than intended. This is illustrated in Figure 2.11. In (a), the output wavelengths when changing i_r with a fixed FP = 2 and i_p = 0 mA are reported; (b) is similar but for various fixed values for i_p. Mode-hops are clearly present, indicated by the big jumps in wavelength on increasing i_r. These mode-hops can be explained by considering (c), which displays the longitudinal modes in each supermode as a function of i_r and i_p. On varying i_r at a fixed i_p, as was the case in (a) and (b) and is demonstrated by the dashed line, these longitudinal modes are crossed and at every crossing a mode-hop is observed. To avoid these, both i_p and i_r must be carefully selected such that subsequent points in a series of settings designed to step across a particular wavelength region follow a path between these longitudinal modes, as exemplified by the curved dotted lines. The results of such a methodology for one FP are shown in Figure 2.11(d) and for all FP in Figure 2.12.

A database of settings with their correlative wavelengths was thus created, from which a user simply has to select the DS-DBR settings which give the wavelengths of interest with the appropriate range and step size. Linear interpolation was used to estimate settings and wavelengths between calibrated points if higher resolution was required. The high degree of frequency reproducibility of the DS-DBR meant that such a table provided a long term reference source.

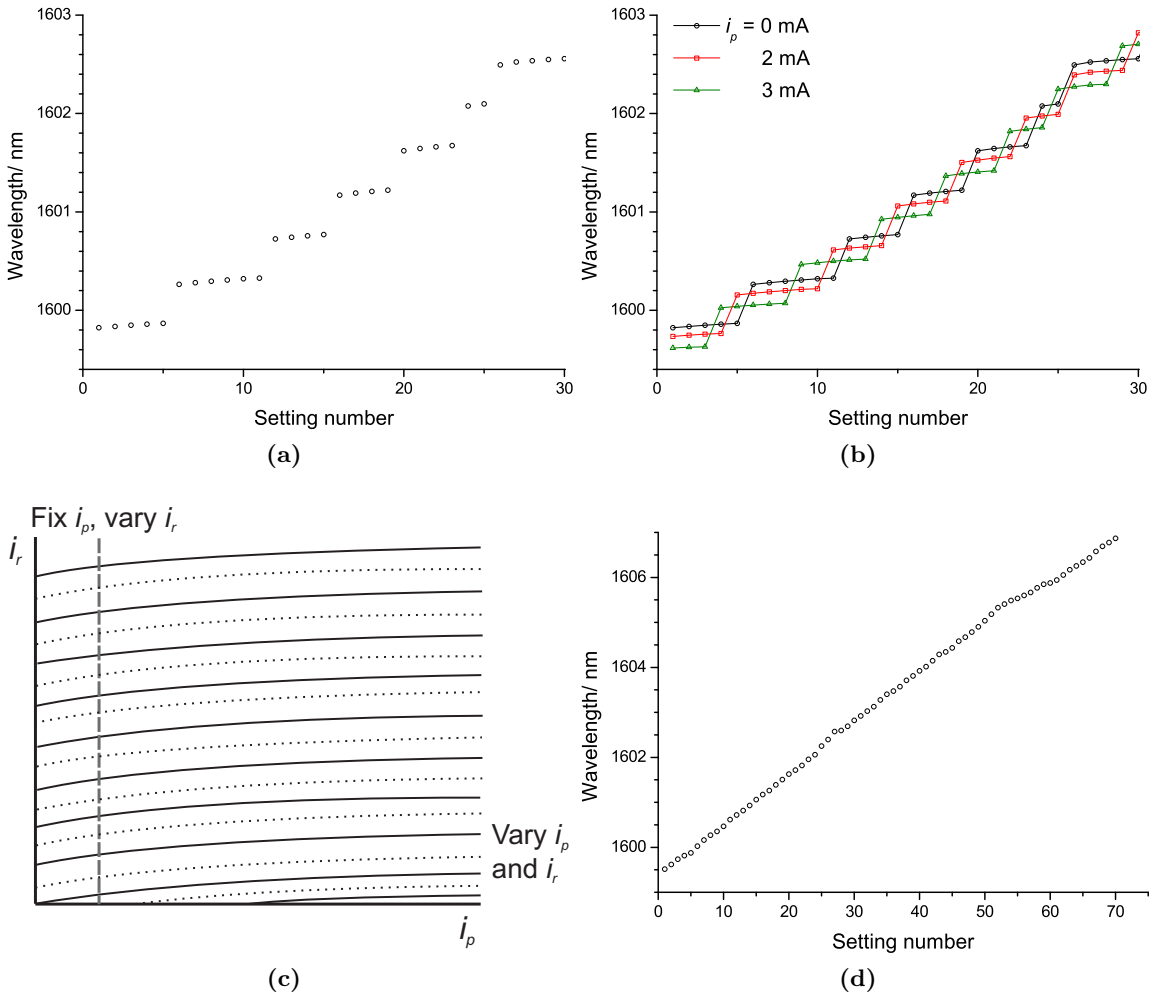

Figure 2.11: Selecting the DS-DBR settings when used in the external ramping mode for fixed wavelengths at fixed injection currents. In (a), the wavelengths of varying i_r with a fixed FP of 2 and i_p of 0 mA are reported; (b) is similar but for various fixed i_p. (c) illustrates the longitudinal modes (solid lines) in each supermode or FP (adapted from Ward *et al.* [191]). Every time a longitudinal mode is crossed, a mode-hop is observed, as occurs when i_p is fixed (dashed line). To avoid these, both i_p and i_r must be carefully selected to fall between the longitudinal modes (curved dotted lines). This method was used to select the settings in (d) and was repeated for each FP.

Wavelength reproducibility was investigated in two ways. Firstly, the laser output was injected into a 2.32 GHz spectrum analyser (*Melles Griot*, 13SAE906) and the short term frequency drifts seen on switching the device immediately off and on, or to different settings and back again, were measured: these were small in amplitude, ~ 20 MHz ($\approx 2\times10^{-4}$ nm). Secondly, the laser wavelength was recorded over time using a wavemeter (*Burleigh*, WA-1000) which had an error of ±0.001 nm (equivalent to ~ 120 MHz at these wavelengths). Each recorded wavelength was the average of 20 quickly taken (< 4 s), sequential wavemeter readings. The wavelengths at four different settings were logged throughout one afternoon and the following morning; these are summarised in Table 2.3 and the plot for the Settings 4

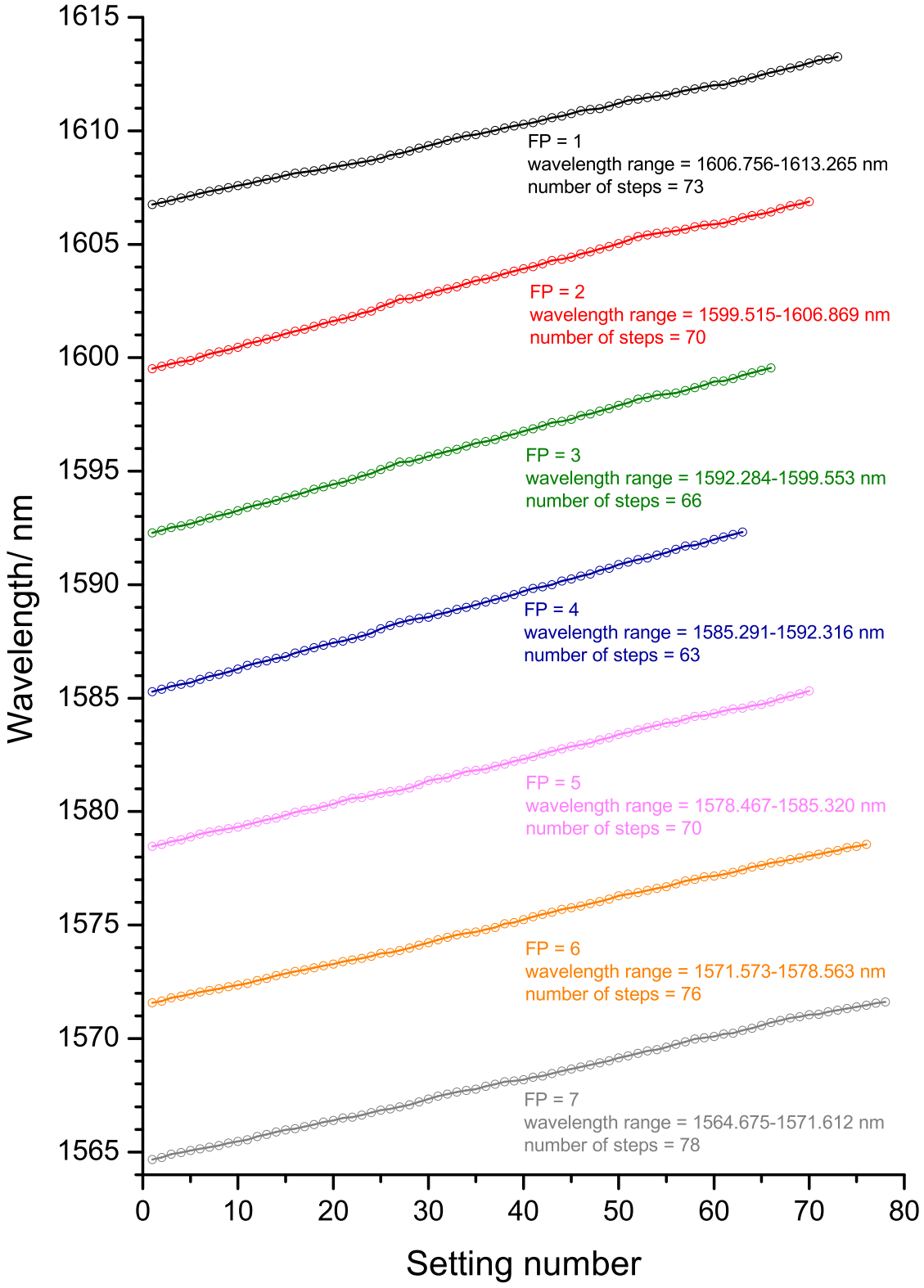

Figure 2.12: The results of using the methodology outlined in Figure 2.11 to find approximately 70 settings per FP covering ~ 7 nm in ~ 0.1 nm (12 GHz) steps, which overall spanned the entire $1563 - 1613$ nm DS-DBR wavelength range.

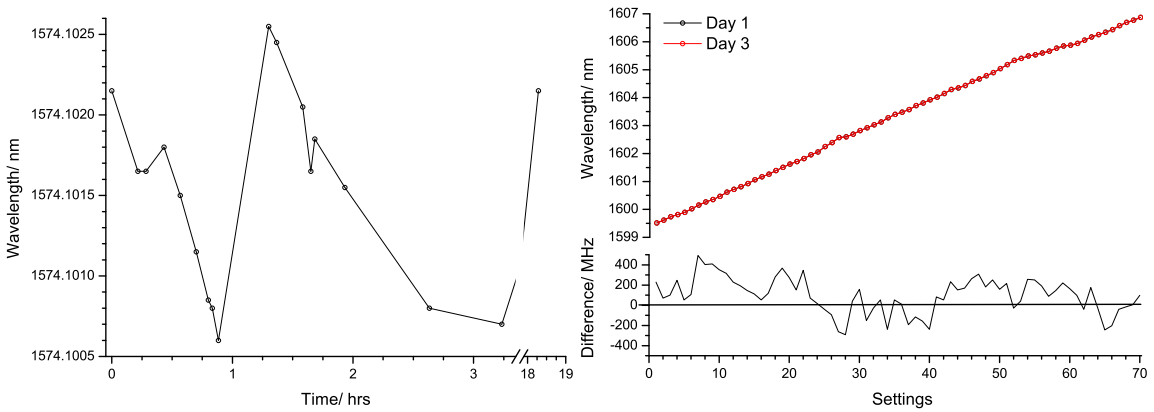

Figure 2.13: Wavelength stability studies of the DS-DBR over time at (a) one wavelength and (b) many wavelengths. In (b), the same series of settings covering FP 2 was applied to the DS-DBR two days apart, and the residual between the measured wavelengths shown in the lower trace. The average absolute residual was 167 MHz but the range observed implied a frequency reproducibility of ±400 MHz.

case shown in Figure 2.13(a). From these, a frequency drift of $\sim$ 80 MHz over several hours were observed, which is of a similar order of magnitude to the accuracy of the wavemeter. In addition, the wavelengths of a whole series of settings covering one FP were recorded two days apart and the difference between them calculated (Figure 2.13(b)). Further to these studies, spectra recorded two weeks apart using the same settings demonstrated a similar frequency shift as those seen in the short term studies [203]. All of these findings indicated that the DS-DBR offered both excellent short and long term wavelength stability.

The possibility of using the DS-DBR as a laser source for cavity enhanced spectroscopy was investigated by studying the output beam profile using a near-IR camera (*Electrophysics*, MicronViewer 7290A). The DS-DBR radiation exited the fibre via a fibre coupler (*Thorlabs*, F240APC-1550) and was then collimated using a 60 cm focal length, plano-convex lens (*Newport*) placed 3.4 cm after the fibre coupler. Images of the beam were recorded for all

Setting number	Settings (FP, i_f/ mA, i_r/ mA, i_p/mA)	Wavelength / nm	Frequency range/ MHz	Frequency drift/ MHz
1	(1, 3.8, 22.0, 2.8)	1608.7247±0.0008	324	89
2	(3, 1.6, 11.9, 4.7)	1595.8760±0.0006	283	75
3	(3, 4.9, 40.7, 2.2)	1592.4833±0.0007	296	85
4	(6, 1.8, 17.5, 4.9)	1574.1015±0.0006	236	73

Table 2.3: Investigating the wavelength drift of the DS-DBR laser with time, by monitoring the output wavelength for four different settings over three hours. The standard deviation of the wavelengths recorded over this time was taken as a measure of frequency drift of the laser.

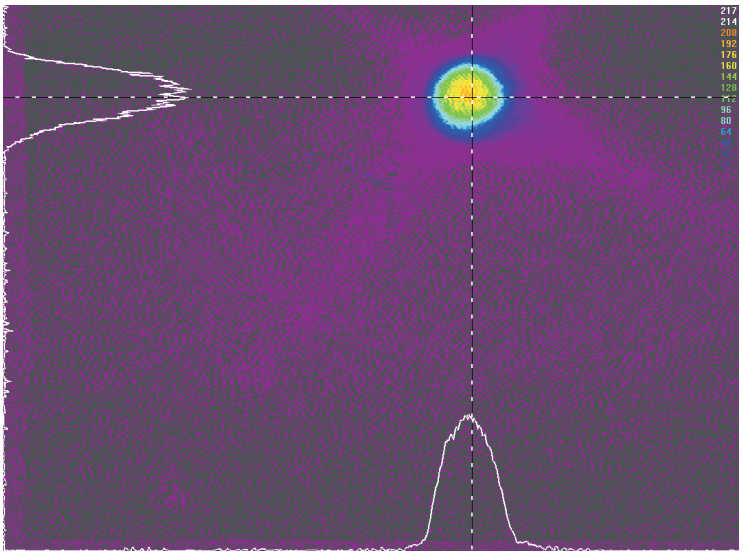

Figure 2.14: Camera image of Gaussian beam shape of the DS-DBR laser when operated in external ramping mode with fixed injection currents. In this example, FP = 2, λ = 1605.50 nm, $w_x = 0.55$ mm, $w_y = 0.51$ mm.

the different FPs and a 2D Gaussian fitted to find the spot sizes (radii) in the horizontal and vertical directions, w_x and w_y, respectively; an example of the camera image is given in Figure 2.14 and the calculated spot sizes summarised in Table 2.4. The beam waists were observed to be similar in both the x and y directions and for all the different FPs (as expected as all the light passed through the same single-mode fibre), with an overall average of $w_x = 0.52 \pm 0.03$ mm and $w_y = 0.51 \pm 0.03$ mm. These concurred with the spot sizes calculated using the knife-edge, beam profiling technique [212, 213], where a value for w_x of 0.54 ± 0.01 mm for the FP 2 case was found. Such a high quality, Gaussian beam profile implied that the DS-DBR laser radiation would couple well into a cavity in order to perform techniques such as CRDS.

FP	λ_p / nm	w_x / mm	w_y / mm	Ellipticity w_x/w_y
1	1607.75	0.54±0.05	0.52±0.04	1.03
2	1605.50	0.53±0.02	0.49±0.02	1.07
3	1593.41	0.53±0.03	0.51±0.03	1.02
4	1586.14	0.52±0.04	0.49±0.04	1.05
5	1579.01	0.57±0.06	0.55±0.05	1.03
6	1571.45	0.52±0.04	0.50±0.04	1.03
7	1564.68	0.47±0.01	0.46±0.01	1.02

Table 2.4: Table summarising the DS-DBR spot sizes in the horizontal (x) and vertical (y) directions for the different FP. Each reported value is the average of three recorded images.

2.4 Conclusions

In this chapter, near-IR laser sources were reviewed and the novel, broadband DS-DBR laser introduced. This widely tunable, single-mode laser source used a grating-based tuning mechanism to tune quasi-continuously over $1563 - 1613$ nm. The laser could be operated in either an internal or external ramping mode, the latter allowing the laser to be set at a fixed wavelength by injection of constant currents into the different DS-DBR sections.

The use of the DS-DBR as a useful spectroscopic laser source was demonstrated by performing measurements on the well-characterised ro-vibrational absorption spectrum of CO_2 in the near-IR. Operating the DS-DBR in the internal ramping mode, the CO_2 spectrum over the entire $1563 - 1613$ nm range was reconstructed from multiple, mode-hope free spectral segments which were individually probed by carefully selecting the appropriate current tuning. This experiment highlighted the major boon of the DS-DBR: that as well as being widely tunable over a large wavelength range, it is also able to perform spectroscopy at a high spectral resolution (a few MHz, limited in principle by the laser bandwidth). This opens up the possibility of performing high resolution work at widely separated wavelengths by sequential jumping between discrete spectral regions (valuable for monitoring multiple, spectrally separated, absorption features, from either one or more absorbers) as well as studying broadband absorbers with rotationally unresolved spectra spread over many wavenumbers. Furthermore, the use of the external ramping mode of operation allowed access to all wavelengths within the spectral bandwidth of the DS-DBR.

WMS was also performed on CO_2 samples by applying fast current modulation to either the phase or the rear section of the device; the non-linear wavelength-current relationship of the laser caused the modulation amplitude to vary across the spectral region accessed by the laser, introducing additional, but rectifiable, lineshape distortions, and higher than usual sensitivities for WMS were found (Allan variance measurements indicated an optimal $\alpha_{\min}$ of 6.3×10^{-8} cm^{-1} over 23 s). Additional studies showed that as well as presenting only small frequency drifts in the short term, the DS-DBR also offered long term wavelength stability allowing previously calibrated DS-DBR settings to be used confidently in the future.

In summary, the DS-DBR technology was demonstrated as an attractive laser source for spectroscopy, combining the favourable optical characteristics and high resolution capabilities of traditional near-IR devices with the wide tunability desirable for multi-species or broadband absorber detection. These advantageous attributes created a strong foundation upon which more complicated and sensitive spectroscopy could be based, such as translating the DS-DBR near-IR radiation to the mid-IR (Chapter 6) and, by virtue of the high beam quality observed, using the DS-DBR in cavity enhanced spectroscopy, which is the subject of the next chapter.

Chapter 3

Cavity-Based Spectroscopy in the Near-Infrared

Cavity-based spectroscopy has already been highlighted as a useful way of making sensitive spectroscopic measurements. This chapter reports on the development of a near-IR CRD spectrometer, which was initially tested using a conventional diode laser source. The DS-DBR laser, introduced and characterised in Chapter 2, was then coupled with the CRDS system and experiments performed on carbon dioxide to assess the efficacy of utilising this combination for widely tunable, high resolution, near-IR spectroscopy. CEAS was also performed with the DS-DBR, and the results compared with those from the CRDS studies. The framework for the CRD spectrometer developed here in the near-IR can easily be transferred to the mid-IR given a suitable radiation source and optical components, a concept which will be explored in Chapters 5 and 6.

3.1 Development of a CRD Spectrometer

In an optical cavity, the radiation confined inside the resonator reflects multiple times between the mirrors. Interference between these reflecting beams means that only certain frequencies of radiation are preserved by the cavity whilst others are rejected, producing standing waves for specific resonance frequencies. These standing waves are the eigenmodes of the resonator and are referred to as cavity modes. These modes depend upon the frequency of the input radiation and the length of the cavity, and fall into two different categories: longitudinal modes, which differ only in frequency to each other, and transverse modes, which differ in both frequency and their spatial intensity pattern (Section 1.2.2.1). CRDS is performed by bringing the laser into resonance with a cavity mode, which allows the light intensity in the cavity to increase, followed by a sudden disruption of the resonance

condition of the mode, which leads to the classic, exponential ring-down decay signal as light intensity leaks from the cavity [33, 65].

There are two ways that the cavity modes can be excited: by scanning either the laser wavelength or the cavity length. When using diode lasers, the former method can be achieved by applying a modulation to the laser injection current to tune the laser frequency periodically over more than one cavity FSR [214]; this approach has the advantage of simplicity, but comes at the cost of poor resolution of narrow spectral lines which only overlap with a few cavity mode frequencies. The latter technique is accomplished by affixing one of the cavity mirrors to a piezoceramic transducer (PZT) which changes length on application of a voltage ramp, so moving the mirror back and forth and modulating the cavity length [215]. The shape, frequency and amplitude of the applied waveform can be controlled, and the magnitude is often chosen such that each ramp corresponds to one FSR of the cavity to guarantee that at least one cavity mode is excited per stroke; this methodology is especially useful in cases where the laser frequency is not locked but may drift. However, in order to allow sufficient time for the light to couple into the cavity and the intensity of the modes to build up, the cavity should not be scanned over the linewidth of the cavity mode (Equation 1.39) faster than the ring-down time [33]. Thus a compromise between the frequency and amplitude of the cavity length modulation must be found. This technique of modulating the cavity length to generate the cavity modes was the preferred method in this work as it permitted the frequency to be scanned or stepped over a spectral region of interest.

In order to use cw lasers for CRDS, the requisite rapid interruption in the resonance condition can be realised by de-tuning the laser away from the resonance frequency or by using fast optical switches, such as electro-optic modulators (EOMs) or acousto-optic modulators (AOMs). Here, an AOM was employed to halt the injection of light into the resonator.

3.1.1 Hardware

The CRDS experimental set-up, using either a DL or the DS-DBR as the laser source, is illustrated in Figure 3.1 [206]. The DS-DBR has been described in Sections 2.2 and 2.3 and had an output power of 23 mW; the alternative laser source employed was a 1577 nm DFB laser diode (*NTT Electronics*, NLK1L5GAAA) with a quoted output power of 20 mW and a linewidth of 2 MHz, which was housed in a butterfly package mount (*Newport*, 744TEC) and controlled by commercial temperature (*Thorlabs*, TED200C) and current (*Thorlabs*, LDC205C) drivers. The light was passed through a fibre optic in-line isolator (*Newport*, F-ISO-D-2-P), which had a maximum isolation of 52 dB at 1550 nm, to avoid back reflection

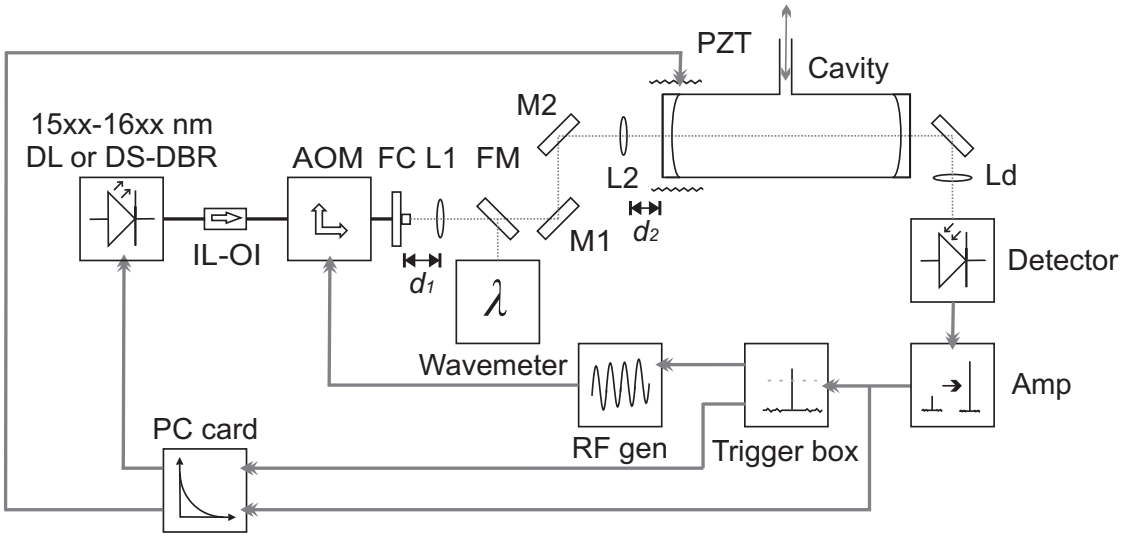

Figure 3.1: Experimental set-up for near-IR CRDS. IL-OI: in-line optical isolator; FC: fibre coupler; FM: flip mirror; L1, L2: collimating and mode-matching lenses, respectively; M1, M2: turning mirrors; Ld: focusing lens onto detector; Amp: variable gain, low noise current amplifier; RF gen: radio frequency generator to switch AOM. When using the DL, the cavity length was 47.0 cm with average mirror reflectivities of ~ 0.999; no beam collimation was required (*i.e.* no L1) but mode-matching was implemented by placing a 50 cm focal length lens 24 cm before the cavity. When using the DS-DBR laser, the cavity properties were measured as $L = 36.6$ cm and $R \sim 0.9999$; a 60 cm focal length lens was placed at L1 at a distance of $d_1 = 3.4$ cm after the fibre coupler to collimate the beam, and a 50 cm focal length lens at L2 at a displacement of $d_2 = 1.8$ cm before the cavity for mode-matching.

into the laser, and then through a polarisation maintaining (PM) fibre-coupled AOM (*Gooch & Housego*, T-M080-0.4C2J-3-F2P).

The AOM acted as the fast optical switch for the CRDS system. In an AOM, a laser beam interacts with a high frequency ultrasonic sound wave within an interaction medium, usually an optically polished block of glass or crystal [216]. The laser beam can be oriented with respect to the sound waves in such way as to induce reflection off the acoustic wavefronts by Bragg diffraction; this means that when a sound field is present, the beam is spatially deflected (1^{st} order diffracted beam), otherwise the light passes through the AOM without deviation (0^{th} order diffracted beam). The deflected beam can be controlled either by digital modulation, where the sound field, and hence the deflected beam, is switched on and off, or by analogue modulation, where the amplitude of the acoustic waves, and hence the intensity of the deflected beam, can be varied. Generally, the 1^{st} order beam is the one used in experiments as it can be switched on and off with a high extinction ratio (typically > 40 dB) and its intensity can be modulated between $0 - 85\%$ of the input beam. The acoustic waves are produced by a transducer, usually a fine wafer of lithium niobate, that is bonded onto the interaction medium and which vibrates when it is subject to a high frequency electrical signal. This signal is derived from a radio frequency (RF) driver, which

creates a high frequency carrier wave and is itself modulated by an analogue or digital input signal.

Here, the AOM was controlled by an 80 MHz RF generator (*Gooch & Housego*, A35080-10) and provided an extinction ratio in the 1st order beam of more than 50 dB with a rise-fall time ($10-90\%$) of 35 ns. As the 1st order beam was used as the output, only $\sim 30\%$ of the incident beam was transmitted by the AOM, giving a reduced power of 6.5 mW.

The output light from the AOM exited the fibre via a fibre coupler (*Thorlabs*, F240APC-1550). In the case of the DL, the output radiation was observed to be already collimated with a spot size of 1.36 mm and so a single lens (*Thorlabs*, LA5464-E), with a 50 cm focal length placed 24 cm before the cavity, was employed for mode-matching for optimal coupling of light into the cavity; for the DS-DBR, this radiation was collimated to a spot size of 0.54 mm by a 60 cm focal length, plano-convex lens (*Newport*, KPX119AR.18) placed 3.4 cm after the fibre coupler and then mode-matched using another plano-convex lens (*Thorlabs*, LA5464-E) with a 50 cm focal length placed 1.8 cm before the cavity.

Wavelength calibrations were performed as required by using a flip mirror placed before the cavity to send the laser light into a wavemeter (*Burleigh*, WA-1000), with an absolute accuracy of ± 0.001 nm, to correlate the DL currents or DS-DBR settings with wavelength.

Different cavities were used for the different laser sources. When using the DL, the cavity consisted of a pair of 25.4 mm diameter plano-concave mirrors placed 47.0 cm apart. The first of these mirrors had a 1.5 m radius of curvature and a quoted reflectivity of $R_1 \sim 0.999$, the second had a 1 m radius of curvature with a quoted reflectivity of $R_2 \sim 0.9994$ (*Newport*, 10CV00SR.70F). Such a configuration results in a FSR of 320 MHz and cavity beam waist of 0.48 mm at 1577 nm. When using the DS-DBR laser, the cavity was composed of a pair of 25.4 mm diameter plano-concave mirrors with 1.5 m radii of curvature (*REO*). These mirrors had a reflectivity of $R_{1,2} \sim 0.9999$ according to the manufacturer, and were designed for broadband reflectance over the range $1550-1650$ nm. The length of the cavity was 36.6 cm, corresponding to a FSR of 410 MHz and the beam waist at the cavity centre was 0.49 mm at 1565 nm.

For both cavities, the entrance mirror was mounted on a PZT (*Piezomechanik GmbH*, HPSt 150/20-15/12) so that cavity modes could be excited by applying a voltage ramp to the PZT to scan the cavity length. This PZT changed the cavity length by 0.08 μmV^{-1} and was controlled by a home-made high power PZT driver. The cavity also had several inputs for connections to a dry pump, gas samples and either a calibrated 10 Torr or 100 Torr capacitance manometer (*Oerlikon Leybold Vacuum*, Ceravac CTR 100, part numbers 230317 and 230316, respectively).

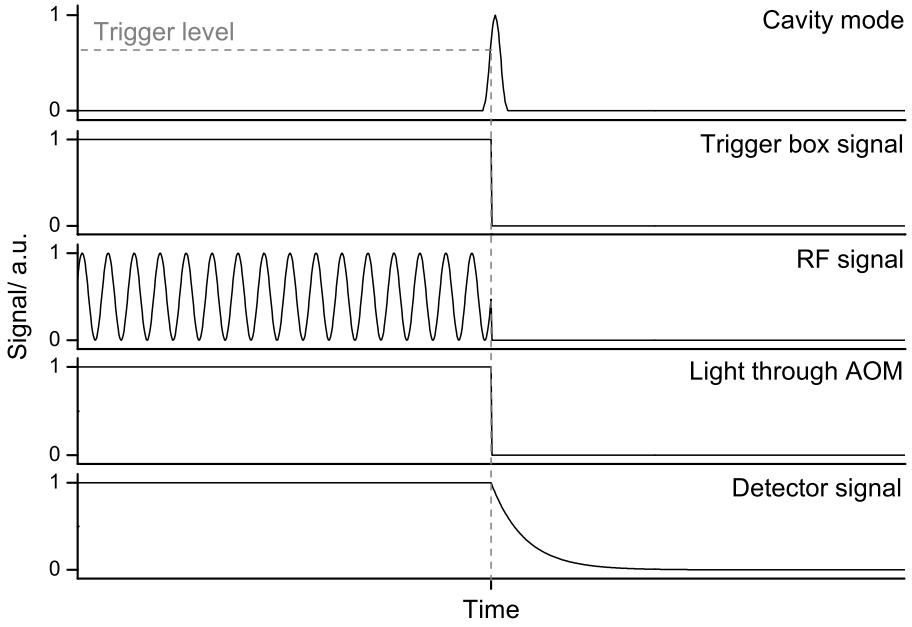

Figure 3.2: Explanation of the synchronisation of the different electronic components in the CRDS system. When a cavity mode was excited and the transmitted signal exceeded a set level, a custom-built trigger box was switched from on to off, which in turn stopped the production of the RF signal and the passage of light through the AOM (by the cessation of the deflection of light into the 1st order diffracted beam). Hence radiation was no longer injected into the cavity and the light in the cavity could ring-down.

The light exiting the cell was focused with a lens onto a fast InGaAs detector (*Thorlabs*, DET10C/M) with a 10 ns rise time. The signal was amplified with a variable gain, low noise current amplifier (*FEMTO*, DLPCA-200) set at a gain of 10^6 VA^{-1} with a bandwidth of 200 kHz when using the DL or at 10^5 VA^{-1} with a bandwidth of 400 kHz when using the DS-DBR.

This signal was fed into a custom-built trigger box with an input impedance of 5 MΩ. When the input signal exceeded a prescribed, set level (which could be altered), the trigger box produced an output TTL pulse and its reverse with an adjustable depth and width ($0.5 - 6$ ms). The reverse pulse was used to control the RF generator and hence the AOM light throughput. Therefore, when a cavity mode was excited and the transmitted signal surpassed a certain level, the discriminator box triggered the AOM to switch off and so allow the light in the cavity to ring-down (Figure 3.2). This decay was recorded using data acquisition (DAQ) cards, as described in the following section.

3.1.2 Software

In order to record and analyse the ring-down decays in real-time, DAQ cards connected to a computer were used. The ring-down was recorded using a 4-channel, 16-bit, 40 MSs^{-1}

PCI digitizer, with 512 MB memory, 50 Ω impedance and a programmable input voltage range of ±0.2 V or ±1 V (*Adlink*, PCI-9846D/512). The ±0.2 V input voltage range was used and data recorded at a $10 - 40$ MHz sampling rate, depending on the situation.

An additional PC DAQ card (*Adlink*, DAQ-2501) was used to create waveforms to scan the cavity length. This card had four analogue output (AO) channels with 12-bit resolution and an update rate of 1 MHz. One of these AO channels was used to generate a triangular waveform with an amplitude V_{amp} and frequency V_{freq} which was applied to the PZT via a high power piezo driver in order to scan the cavity length to generate cavity modes. Another AO channel was used to control the DL current driver and hence the DL wavelength. As the analogue output of the DAQ card covered a range of ±10 V at a 12-bit resolution (equivalent to a minimum step size of 5 mV), a 20:1 attenuator was also added to allow for the possibility of smaller output voltage steps (0.25 mV) which would give correspondingly smaller wavelength steps in order to perform high resolution spectroscopy.

Programs were written in LabVIEW to communicate with these cards and to analyse the data they acquired. Rapid determination of the exponential decay constants was achieved using an extension of the corrective successive integration method [212] known as linear regression of the sum (LRS) [217, 218]. This fitting routine was used to fit an exponential to a subsection of the collected data: the first few μs of data, t_{disc}, were discarded and an exponential fitted to the next several μs of data, t_{fit}, to find the RDT, where t_{disc} and t_{fit} were altered according to the experimental conditions. The RDT value measured was actually a combination of the true RDT and a contribution from the detector bandwidth [219]:

$$\tau_{\text{meas}}^2 = \tau_{\text{det}}^2 + \tau_{\text{act}}^2 \tag{3.1}$$

where τ_{meas} is the RDT recorded, τ_{det} is the contribution from the electronics (calculated using $\tau_{\text{det}} = 1/\pi\Delta f$ and the known bandwidth of the amplifier) and τ_{act} is the true RDT.

Two programs were written in order to perform experiments to assist in the retrieval of the RDTs and spectra. In the first, wavelength calibrations between the wavelength measured by the wavemeter and the output voltages of the DAQ card to the DL current driver, V_{mod}, or the DS-DBR settings were performed. In the second, cavity modes were simultaneously generated and monitored by applying a waveform to the PZT to scan the cavity length and continually recording the detector signal.

Ring-down traces were acquired as follows. On the detection of a cavity mode, the trigger box not only sent a reverse TTL pulse to the AOM to stop the injection of light into the cavity but also sent a TTL pulse to the computer to trigger the recording of the detector output by the PCI for a pre-determined period of time, t_{rec}. Two main LabVIEW programs were written to perform ring-down experiments:

Program One: *Recording ring-downs at a single wavelength.* The laser was set at the desired wavelength. In the case of the DL, this was done by manually adjusting the current to the appropriate value on the laser current driver; for the DS-DBR, one combination of settings corresponding to the target frequency was sent from the computer to the laser. Successive ring-downs were then recorded and fitted at this fixed wavelength until the program was instructed to stop by the user, at which point a plot of RDT against sample number was generated.

Program Two: *Recording CRD spectra across a wavelength range.* The laser was set at a series of required wavelengths in order to step over the spectral region of interest. In the case of the DL, this was accomplished by using one of the AO of the DAQ card to apply a step-function, voltage waveform, V_{mod}, to the laser diode controller to change the laser current and thus the wavelength; for the DS-DBR, this was achieved by sending a sequence of settings corresponding to known laser frequencies as determined in Sections 2.2.2.2 and 2.3.2. A desired number of ring-down events, n_{avg}, was recorded at each step. A plot of RDT against wavelength was thus created, using the known calibrations between V_{mod}/settings and wavelength. This could then be converted into an absorption spectrum by fitting a polynomial τ_0 baseline and calculating α using Equation 1.53, and a Voigt profile fitted either in *Origin* [220] or by using the Humlicek approximation [17].

Both of these programs were written with the capacity to be run in two different operational modes. In one of these modes, the data were analysed and the outcomes reported in real-time, so allowing the results of the experiment to be monitored as it progressed; in the other, all the data were recorded and saved before they were analysed, which allowed for shorter acquisition times.

Observation of the quality of the ring-downs and their associated fits led to the introduction of 'conditioning' criteria to filter the results [206, 221]. This removed anomalous results due to fitting exponential decays to non-ring-down events (*e.g.* instances when the trigger box was triggered by an abnormally large noise feature of the baseline, an electronic spike *etc.*), and also to discard RDTs calculated from poor data obtained from weak cavity modes. These criteria were:

1. The R^2 (coefficient of determination) value of the exponential fit had to exceed a certain value.
2. The calculated RDT had to lie within ± 3 standard deviations of the average of all the results.

Considering these, together with the effectiveness of the triggering on the cavity modes, an overall conversion efficiency of generated cavity modes into useful RDTs could be calculated.

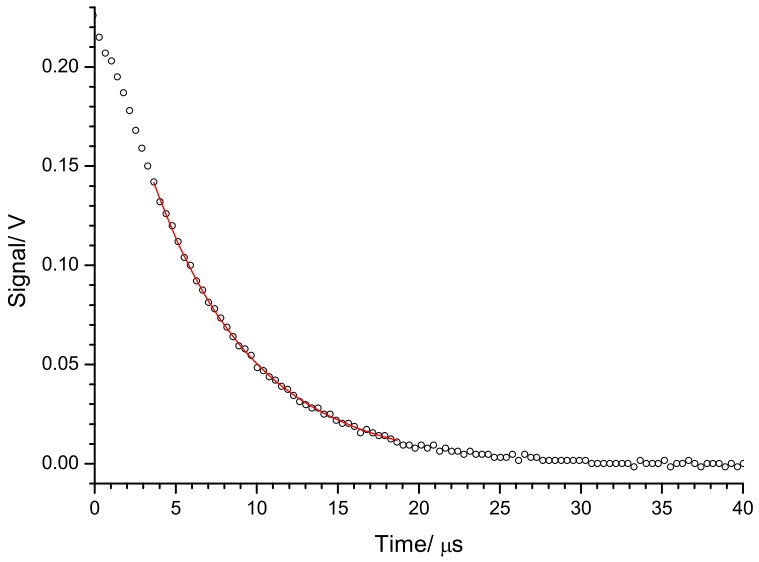

Figure 3.3: An example ring-down trace of the evacuated cavity at 1577.70 nm. The raw data are shown by the open circles; only a reduced number of data points are given for clarity. The exponential fit, shown by the solid line, was performed using $t_{\mathrm{disc}} = 3.5$ µs and $t_{\mathrm{fit}} = 15$ µs and returned a τ_{meas} value of 6.21 µs with an R^2 value of 0.9994.

Here in the near-IR, the high quality of the ring-downs recorded meant that most ($> 95\%$) RDTs were retained yielding a good conversion efficiency.

In these two programs, many parameters were available to be changed and set by the user. These included details on the DAQ card (sampling rate, voltage range), PCI card (sampling rate, voltage range, t_{rec}), PZT waveform (V_{amp}, V_{freq} and offset voltage of the piezo driver, V_{off}), trigger level of discriminator box, number of ring-downs to record per point (n_{avg}), settling time between laser steps to allow the laser temperature and current to stabilise (t_{sett}), fitting and analysis parameters (t_{disc}, t_{fit}, τ_{det}), conditioning criteria (minimum R^2 value) and wavelength calibrations (information on how λ varies with the DL V_{mod} or DS-DBR settings).

Using these programs, numerous CRDS experiments with the diode laser and DS-DBR in the near-IR were performed, as are now discussed.

3.2 Near-Infrared CRDS with Diode Laser Sources

In order to test the CRDS system and LabVIEW software, experiments were initially performed in the near-IR using the 1577 nm DFB DL. This began with the characterisation of the evacuated cavity and the inspection of the recorded data and fitted exponential.

An example of the ring-down trace for an empty cavity at 1577.70 nm is given in Figure 3.3. The first 3.5 µs of data were discarded and the next 15 µs fitted using the fast exponential

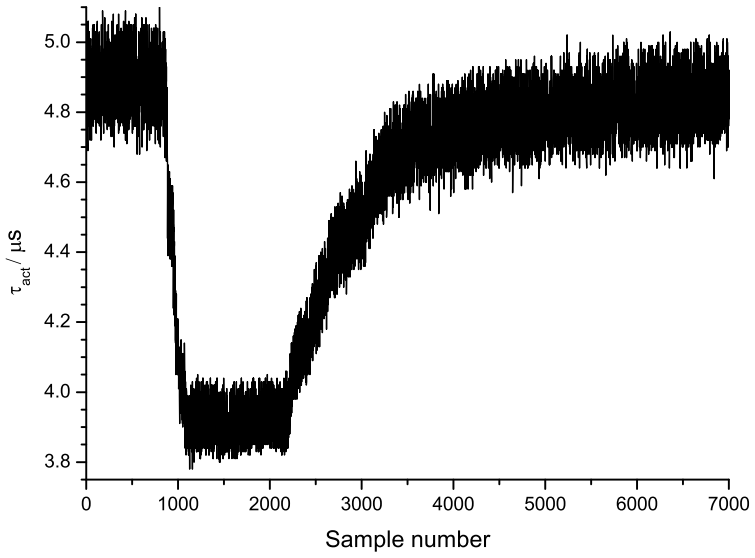

Figure 3.4: Change in RDT at a fixed wavelength (1577.26 nm) on filling an empty cavity with a 6.2 Torr sample of 20% CO_2 in air and then re-evacuating the cavity; data recorded over a period of 8 mins.

fitting algorithm described in Section 3.1.2. The fit returned a τ_{meas} value of 6.21 µs with an R^2 value of 0.9994. This corresponded to a true RDT, τ_{act}, of 6.00 µs, as found using Equation 3.1 to account for the contribution to the measured RDT from the electronics of $\tau_{\text{det}} = 1.6$ µs (from the known 200 kHz bandwidth of the amplifier). This in turn meant the optical cavity possessed an effective path length of 1.8 km and an average mirror reflectivity of 0.9997 at this wavelength.

The CRDS set-up was then assessed by conducting studies on the $\nu(31112 \leftarrow 01101)$ $P(19)$ transition of $^{12}CO_2$ at 1577.26 nm (6340.13 cm^{-1}) using a 20.3% mixture of CO_2 in air (transitions labelled using notation introduced in Section 2.2.2.1). Firstly, the DL was tuned to 1577.26 nm and many RDs at one wavelength were recorded, using Program One listed in Section 3.1.2. The cavity was originally placed under vacuum before adding 6.2 Torr of the calibrated CO_2 mixture; this caused the measured RDTs to decrease, as shown in Figure 3.4. The cavity was then re-evacuated so that the RDTs returned to their initial values. Using an average τ_0 value of 4.88 ± 0.08 µs measured before the addition of the CO_2 sample and an average τ value of 3.91 ± 0.06 µs recorded when the sample was present, α was estimated to be $1.70 \pm 0.11 \times 10^{-6}$ cm^{-1}. This is in very good agreement with the expected value of 1.71×10^{-6} cm^{-1} calculated by considering the pressures used.

CRD spectra of this transition were then recorded at various pressures of the CO_2 mixture by using Program Two described in Section 3.1.2 to measure the RDTs over the 1577.18 – 1577.31 nm wavelength range. A calibration curve between the voltage applied by the DAQ to the laser current driver and the laser wavelength reported by the wavemeter (*Burleigh*, WA-1000) was found and used to give the frequency scale. The experimental settings

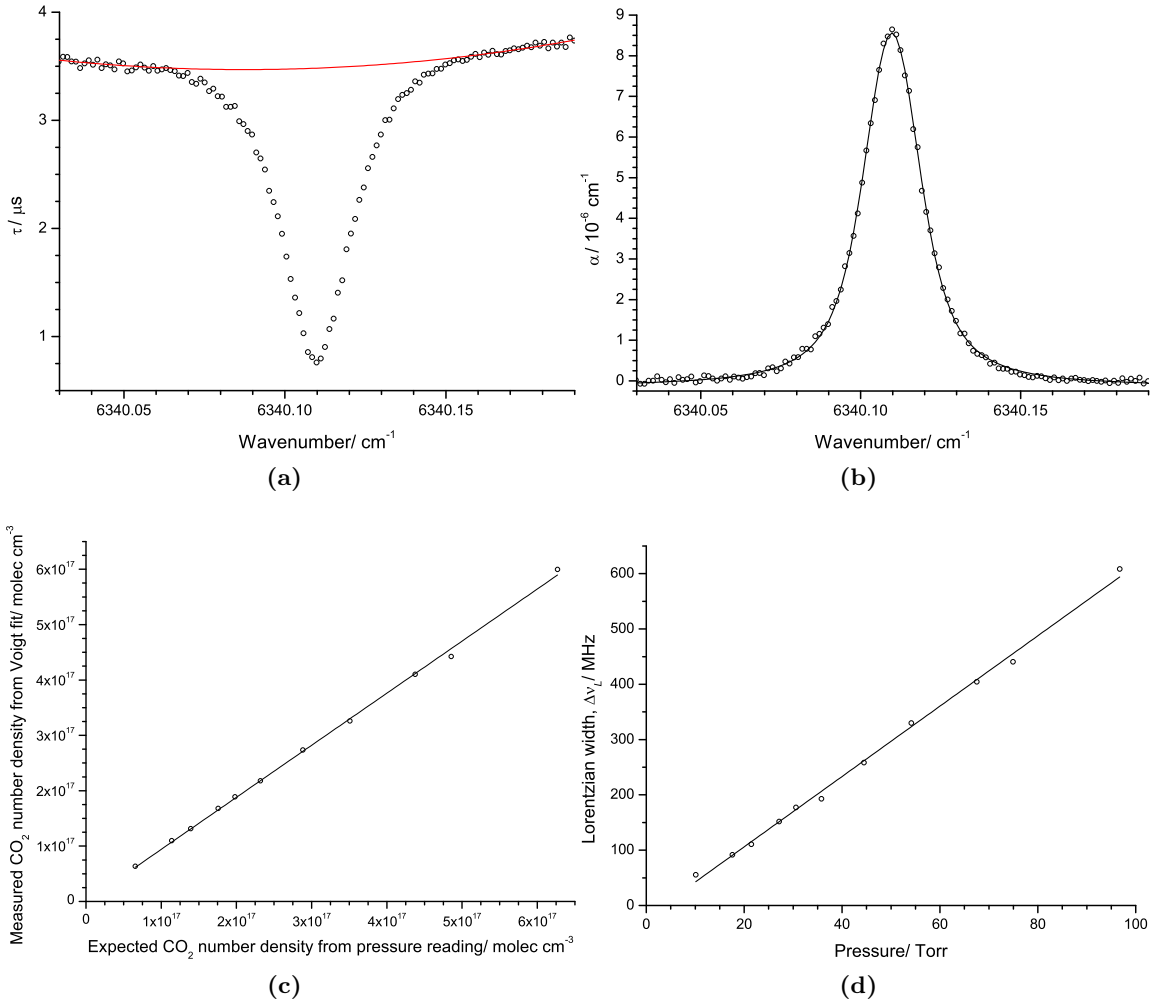

Figure 3.5: CRDS of the $\nu(31112 \leftarrow 01101)$ $P(19)$ CO_2 transition at 6340.13 cm^{-1} for a mixture of 20% CO_2 in air. (a) Initial RDT data across the absorption feature (open circles) with the fitted quadratic τ_0 baseline (solid line) recorded at 75 Torr. (b) The resultant CRD spectrum of the data in (a). (c) The linear relationship between the CO_2 concentrations calculated from the areas of the Voigt fits of the CRD spectra and the CO_2 concentrations expected from the measured pressures (10 – 100 Torr). (d) The variation in the Lorentzian widths of the fitted Voigt profiles with pressure.

employed were: DAQ card: ±10 V at 200 kHz update rate; PCI card: ±0.2 V at 40 MHz sampling rate with $t_{\text{rec}} = 50$ μs; PZT waveform: $V_{\text{amp}} = 7$ V, $V_{\text{freq}} = 12$ Hz, $V_{\text{off}} = 40$ V; spectra recording: $n_{\text{avg}} = 20$, $t_{\text{sett}} = 1$ s; fitting and analysis: $t_{\text{disc}} = 4$ μs, $t_{\text{fit}} = 40$ μs, $\tau_{\text{det}} = 1.6$ μs; conditioning criteria: minimum $R^2 = 0.9$. In this case, these settings were selected by direct experimentation, though a more systematic approach to finding the optimal experimental settings conditions was utilised in later work (Section 3.3 onwards). Each spectrum took 4 – 6 mins to be compiled. The recorded RDT data was converted into an absorption spectrum by fitting a quadratic τ_0 baseline to the results and calculating α using Equation 1.53; this is illustrated at 75 Torr by Figures 3.5(a) and 3.5(b), for which an α_{min} of 1.3×10^{-7} cm^{-1} was found; this sensitivity value is not as good as those usually

achieved by CRDS ($\sim 10^{-9}$ cm^{-1}), but this is understandable given the low reflectivity of the mirrors used (0.9997). A Voigt profile was then fitted using the Humlicek approximation [17] with the Gaussian width fixed at the predicted Doppler width of 354 MHz. A linear correlation, as expected, between the concentration of CO_2 calculated using the area of the Voigt fit and the measured pressures was observed, with a gradient of 0.941 and R^2 value of 0.9996 when the intercept was fixed at the origin (Figure 3.5(c)). A trend in increasing Lorentzian widths of the fitted Voigt profiles with increasing pressure was also seen (Figure 3.5(d)), with the calculated Lorentzian widths of $55-609$ MHz (6.4 MHzTorr^{-1}) comparing well with those expected of $62-591$ MHz (6.1 MHzTorr^{-1}) across this pressure range.

3.3 Near-Infrared CRDS with the DS-DBR Laser

By virtue of the favourable results from the preliminary investigations conducted using a conventional DL in the preceding section, it was concluded that the CRDS system and LabVIEW software developed worked well. The laser source was then replaced by the DS-DBR with the aim of creating a CRD spectrometer capable of performing high resolution spectroscopy across the $1563-1613$ nm wavelength range. The experimental set-up has been described previously (Figure 3.1, Section 3.1). In order to perform the CRDS measurements, the DS-DBR was stepped across the wavelength range of interest using the external ramping mode, as discussed in Sections 2.2.2.2 and 2.3.2.

3.3.1 Beam profiling and mode-matching

In order to efficiently couple the DS-DBR laser radiation into the cavity, the DS-DBR beam first needed to be collimated and then mode-matched to the lowest order resonator modes (Section 1.2.2.1, Appendix A). Using Equations 1.45 and 1.46, the beam waist at the cavity centre and the spot sizes at the mirrors for the DS-DBR optical cavity arrangement at the

Wavelength/ nm	1565	1615
w_0/ mm	0.4945	0.5023
$w_{1,2}$/ mm	0.5277	0.5361
f_2/ cm	98.90	102.16
d_2/ cm	2.30	0.76

Table 3.1: Properties of the DS-DBR optical cavity set-up over the wavelength range of the DS-DBR laser. The top half gives the values of the beam waists at the cavity centre and the spot sizes at the mirrors; the bottom half lists the exact solutions for the mode-matching optics assuming the incident laser beam has been collimated to a spot size of 0.54 mm.

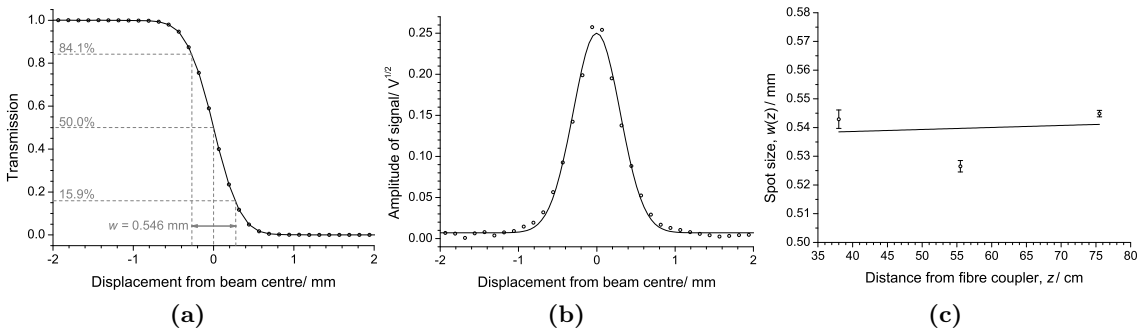

Figure 3.6: Finding the collimation optics, d_1 and f_1 of lens L1 in Figure 3.1, for the DS-DBR laser beam. The knife-edge, beam profiling technique was used to find the spot size, w, at a variety of distances from the laser fibre coupler for different values of d_1 and f_1 in order to determine those that collimate the beam. (a) Transmission plot and (b) Gaussian beam profile recorded using this method at a distance of 76 cm after the fibre coupler when $f_1 = 60$ cm, $d_1 = 3.4$ cm; in this example, $w = 0.546$ mm. The beam was judged to be sufficiently well collimated with $w = 0.54$ mm when $f_1 = 60$ cm, $d_1 = 3.4$ cm, as inferred from (c).

minimum and maximum wavelengths accessible with the laser were calculated (Table 3.1), indicating that the DS-DBR beam had to be collimated to a spot size greater than 0.53 mm in order to perform mode-matching. Collimation was achieved by use of a collimating lens with a focal length f_1 placed a distance d_1 after the laser fibre coupler (L1 in Figure 3.1). Different combinations of f_1 and d_1 were tried until a collimated beam was found.

The beam spot sizes were measured using the knife-edge, beam profiling technique [212, 213]. A beam blocker was gradually moved across the path of the laser beam and the decreasing detected signal recorded. A transmission plot was thus generated (Figure 3.6(a)) with the spot size equal to the distance between which the transmission falls from 84.1% to 15.9% [222]. This data could also be converted to a signal amplitude plot to observe the Gaussian beam profile (Figure 3.6(b)).

By re-iterating this procedure for various f_1 and d_1, it was deduced that a collimating lens with $f_1 = 60$ cm and $d_1 = 3.4$ cm was required. This produced a beam with a spot size of 0.54 mm (Figure 3.6(c)). This value could then be used to determine the focal length, f_2, and distance before the cavity, d_2, of the mode-matching lens (L2 in Figure 3.1), as outlined in Appendix A. This analysis gave exact solutions for f_2 and d_2 (Table 3.1). A range of different focal length lenses placed at a variety of distances were tested, and good data were observed when $f_2 = 50$ cm and $d_2 = 1.8$ cm; this mode-matching lens was thus employed for the remainder of the work in this chapter.

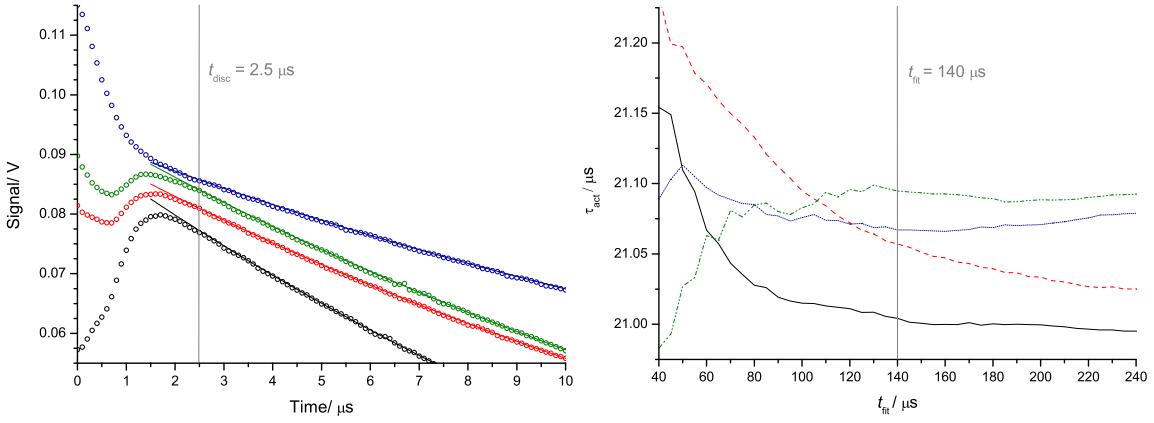

(a) Finding t_{disc} **(b)** Finding t_{fit}

Figure 3.7: Finding optimal (a) t_{disc} and (b) t_{fit} fitting parameters using four recorded ring-down traces. (a) Inspection of the data recorded at the beginning of the data acquisition revealed a delay between the trigger and the start of the ring-down: these non-ring-down points must be ignored in the exponential fitting. t_{disc} of 2.5 µs was judged as the minimum amount of data that needed to be removed to ensure only data pertaining to the true ring-down decay were used in the fitting procedure in all cases. A reduced number of raw data points (open circles) are shown for clarity, and the final fitted exponentials also plotted (solid lines). (b) Using this t_{disc} and the same examples, the RDT was calculated with increasing t_{fit}. The calculated RDT remained essentially constant in all cases when t_{fit} values greater than 140 µs were used, hence this value was chosen as the optimum value for t_{fit}.

3.3.2 Characterisation

The experimental and analysis settings employed throughout this, and the following section, were: DAQ card: ±10 V at 200 kHz update rate; PCI card: ±0.2 V at 10 MHz sampling rate with $t_{\mathrm{rec}} = 150$ µs; PZT waveform: $V_{\mathrm{amp}} = 4$ V, $V_{\mathrm{freq}} = 10$ Hz, $V_{\mathrm{off}} = 40$ V; amplifier gain: 10^5 VA^{-1}; fitting and analysis: $t_{\mathrm{disc}} = 2.5$ µs, $t_{\mathrm{fit}} = 140$ µs, $\tau_{\mathrm{det}} = 0.8$ µs (using $\tau_{\mathrm{det}} = 1/\pi\Delta f$ and the known 400 kHz bandwidth of the amplifier); conditioning criteria: minimum $R^2 = 0.9999$. The PZT amplitude modulation was set such that each ramp covered at least one FSR in the frequency domain, and the PZT frequency then chosen to give a fast acquisition rate while allowing sufficient time for the cavity modes to build in intensity, as discussed in Section 3.1. The optimal fitting parameters were determined by inspection of the raw data at the beginning of the data acquisition and the effect of varying t_{fit} on the RDT of the fitted exponential decay (Figure 3.7).

3.3.2.1 Cavity modes

Cavity mode transmission of the DS-DBR CRDS system was investigated using both the DS-DBR and the 1577 nm DFB DL, both emitting at 1577.5 nm and injected into exactly the same cavity after passing through identical optical components. Cavity modes

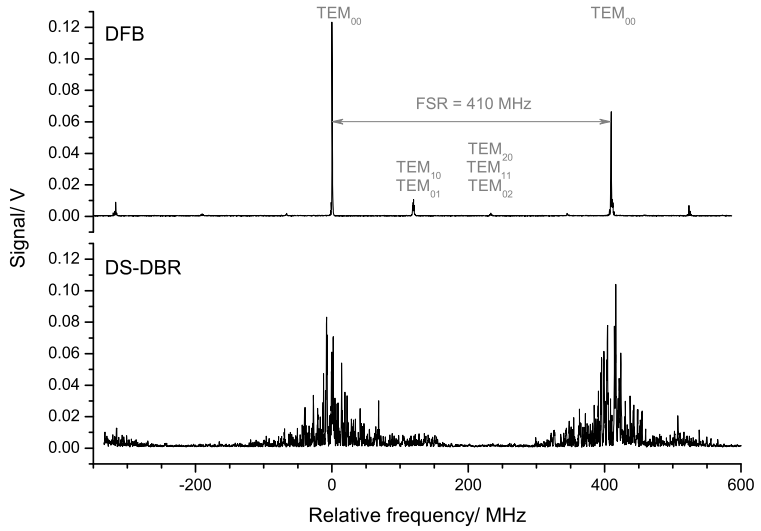

Figure 3.8: Cavity transmission of near-IR light at 1577.5 nm using a DFB diode laser and the DS-DBR. The gain of the amplifier was set 10 times larger for the recording of the DS-DBR data. The upper trace shows that a well-aligned CRDS cavity supporting predominantly TEM_{00} was achieved, though the use of the DS-DBR as a laser source resulted in much noisier cavity modes. Despite this, both laser sources gave similar RDTs for an evacuated cavity: 23.72 ± 0.10 μs for the DL and 23.45 ± 0.12 μs for the DS-DBR (discrimination level of trigger box altered accordingly).

were generated by scanning the PZT with a triangular waveform with an amplitude large enough to cover one FSR of 410 MHz in the frequency domain to ensure that at least one cavity mode was excited per ramp, and data were recorded over the up-ramp of the PZT modulation.

The upper trace in Figure 3.8 illustrates the sharp cavity modes (Lorentzian FWHM of 0.5 MHz, limited by the DL linewidth) observed when using the DFB diode laser. The regular spacing between the fundamental TEM_{00} modes and the presence of only small neighbouring transmissions implied that the cavity was well-aligned, thus guaranteeing that the discrimination level could be set such that the system was only triggered by the TEM_{00} modes. A good signal was obtained using a lower amplifier gain (10^4 VA^{-1}) than that required for the DS-DBR.

The lower trace in Figure 3.8 shows the transmission observed when using the DS-DBR. Although cavity modes with regular spacings were readily identifiable and the integrated areas under the modes were the same as those found in the DFB case (accounting for the different signal amplifications used), they were much noisier and broader (Lorentzian FWHM of 24 MHz) than those seen with the DFB. Similar quality cavity modes were also observed at other wavelengths using different front pair contacts. The fact that the cavity was well-aligned, as demonstrated by the DFB studies, indicated that the more chaotic structure of the cavity modes was not caused by the excitation of additional, higher order

modes, but instead was due to innate noise of the DS-DBR laser light itself or its coupling into the cavity.

RDTs at 1577.5 nm were recorded using both the DL and DS-DBR with analysis settings outlined above, except that in the case of the DL a τ_{det} of 0.6 µs was used, as the bandwidth of the amplifier at the 10^4 VA^{-1} gain setting was 500 kHz. In both cases, the trigger level of the discriminator box was set such that it was high enough so that only the most intense cavity modes would trigger an event to be recorded giving consistent RDTs, whilst still allowing for frequent triggering. In spite of the difference in the observed quality of the cavity modes, as seen in Figure 3.8, both laser sources gave similar RDTs for an evacuated cavity: 23.72 ± 0.10 µs for the DL and 23.45 ± 0.12 µs for the DS-DBR. This verification of the RDTs measured using the DS-DBR meant that it could be used to record CRD spectra despite its noisy cavity modes.

The exact source of the noise of the cavity modes observed with the DS-DBR is still unclear. On first sight, it might be supposed that the behaviour may be due to a difference in the linewidths of the lasers, with the DS-DBR linewidth being significantly greater than that of the DL, resulting in worse coupling of the DS-DBR output into the cavity; however, literature values estimate the linewidth of the DS-DBR to be $0.4 - 1.8$ MHz [194], *i.e.* smaller than the reported 2 MHz linewidth of the DL. Camera images and knife-edge measurements of the DS-DBR output (Sections 2.3.2 and 3.3.1) ruled out the possibility of poor beam shape or an excess of high order modes being a factor. The in-house built DS-DBR laser driver had comparable noise levels in its output currents as the commercial laser current driver used to power the DL, implying that the effect is not due to the power supply. The noise is also unlikely to be due to stimulated Brillouin scattering (SBS) [223] as the threshold powers for SBS given this fibre system are much higher than those used, and attenuating the power of the laser did not lead to any improvement. In addition, feedback from the rest of the system is improbable due to the presence of the optical isolator located directly before the laser. Nevertheless, it may be possible that there is some feedback at the laser facet (where the laser light is first coupled into the fibre) as an artifact of the manufacture process. Alternatively, and most probably, it is the laser-field phase noise intrinsic to the laser that results in rapid frequency fluctuations inside the laser linewidth, which in turn produce constructive or destructive interference when scanning the cavity as the instantaneous frequency falls inside or outside the mode, thereby converting the laser-field phase fluctuations into amplitude fluctuations giving noisy cavity modes [224]. Unfortunately, it is difficult to test either of these hypotheses for final confirmation of the root cause. It is worthy of note that similar, noisy cavity mode behaviour was also observed in other CRDS experiments with a different DFB diode laser (*Fitel*, FRL15DCWD-A81-19265-C) at 1556 nm using the same laser drivers and mounts as used for the 1577 nm

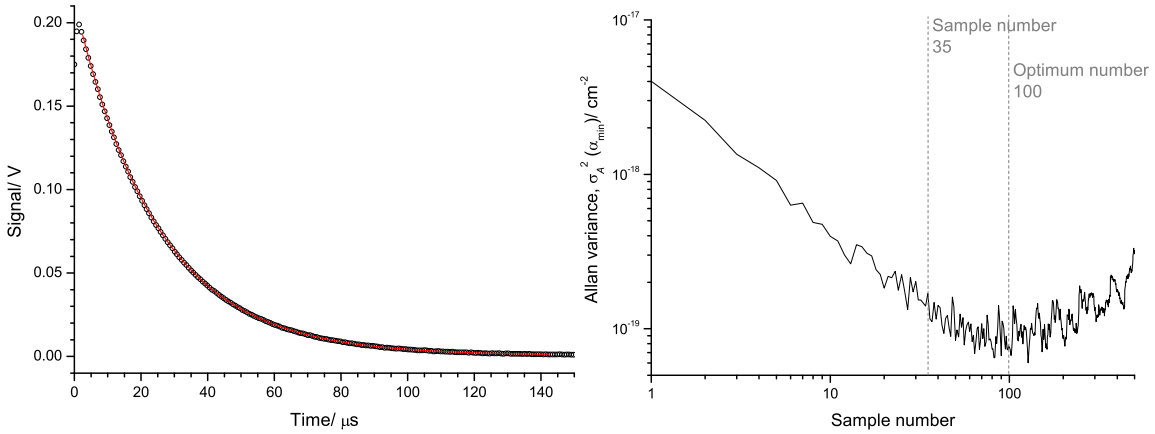

Figure 3.9: Ring-downs recorded at a single wavelength (1605.476 nm) of an evacuated cavity with the DS-DBR CRDS system. (a) Example ring-down trace with the raw data given by the open circles (only a reduced number of data points are shown for clarity) and the exponential fit by the solid line; this fit returned a τ_{act} value of 24.61 μs with an R^2 value of 0.999996. (b) Allan variance plot of the α_{min} values calculated from recorded sequential ring-downs under these conditions, each RDT taking ~ 0.2 s to acquire. Inspection of this plot indicated that an optimum number of ring-downs to record and average per point would be 100, giving an $\alpha_{\text{min}} = 2.8 \times 10^{-10}$ cm^{-1}. Also in the figure is given an indication of a higher detection limit ($\alpha_{\text{min}} = 4.1 \times 10^{-10}$ cm^{-1}) obtainable in a faster acquisition time (35 samples, ~ 7 s).

DFB DL above, which implies yet again that the cause is inherent to the laser itself or its fibre-coupling.

3.3.2.2 Ring-downs at a single wavelength

The DS-DBR wavelength was set at 1605.476 nm and 2200 ring-downs recorded of an evacuated cavity over a period of 7 mins using Program One described in Section 3.1.2; an example ring-down and its fit is given in Figure 3.9(a). The conditioning criteria stated above ($R^2 > 0.9999$, ± 3 standard deviations) were applied to remove anomalous results; however, the high quality of the recorded ring-downs meant that most RDTs were retained. Averaging all the filtered results gave $\tau_0 = 24.54 \pm 0.04$ μs, corresponding to an effective path length of 7.4 km and a geometric mean mirror reflectivity of 0.99995 at this wavelength.

The conditioned results of this data set were also used to construct an Allan variance plot [225], shown in Figure 3.9(b). The gradient of the Allan variance plot up to 20 s was equal to -1, indicating that the system was initially limited only by white shot noise. From this plot it was seen that the maximum sensitivity corresponded to an average of 100 RDTs, yielding an $\alpha_{\text{min}} = 2.8 \times 10^{-10}$ cm^{-1} over 20 s. It was considered, however, that an average of 35 RDTs, giving an $\alpha_{\text{min}} = 4.1 \times 10^{-10}$ cm^{-1} over 7 s, would be appropriate for the

recording of spectra to reduce the overall acquisition time, as the averaging procedure must be repeated at many points across a given wavelength range to build the spectrum.

3.3.2.3 Ring-downs across the DS-DBR wavelength range

The ability to record CRD spectra across the whole $1563 - 1613$ nm DS-DBR wavelength range using this set-up was then investigated. The cavity was filled with 80 Torr of N_2 and 35 RDTs were measured and averaged at 450 points across the wavelength range over a period of 45 mins. Figure 3.10(a) clearly demonstrates that the system is capable of acquiring such broadband spectra. No adjustment to the cavity alignment was made during the data collection, indicating that the cavity alignment and mode-matching was able to sustain cavity mode transmission across the entire 50 nm range.

Fluctuations in the RDT across the wavelength range were clearly observed and these are caused by a periodic variation in the mirror reflectivity, R, with wavelength; this was most obvious in the RDTs measured over smaller wavelength intervals as shown by the insets. 20% reductions in RDT over 0.06 nm in the wavelength domain were seen, which corresponded to a decrease in the effective path length of 1.6 km. This large variation in R over a small wavelength meant that a change in wavelength of less than just 0.01 nm (900 MHz) could result in a change in the RDT of 1 µs. Identical spectra recorded one hour apart displayed residuals of less than 1 µs at equivalent points, averaging to zero across the operating range. These residuals can thus be attributed to the highly varying R, the mechanical stability of the cavity and the wavelength reproducibility of the DS-DBR over time and on adjusting the settings. It was further noted that the RDT was susceptible to small changes in cavity alignment on evacuating, flushing or filling the cell.

As well as the $\sim$ 16 GHz (0.12 nm) periodic variation in R, a beating in R was also discernible with a frequency of $\sim$ 1100 GHz (9.5 nm). As R is the geometric mean of the reflectivities of the two individual mirrors, this beating can be explained by assuming that the reflectivity of each mirror, $R_n(\lambda)$, varies in wavelength with a slightly different periodicity; indeed, simulations indicated that a change in the period of $R_n(\lambda)$ as small as 1.5% would be enough to account for the beating observed (Figure 3.10(b)). Such minute changes in reflectivity between different mirrors is understandable given the unavoidable variations during the manufacturing process in each coating run due to subtle differences in surface roughness, interfacial imperfections (*e.g.* interface roughness, diffuse intermixing) between layers and thickness irregularities within the multi-layer stack [226].

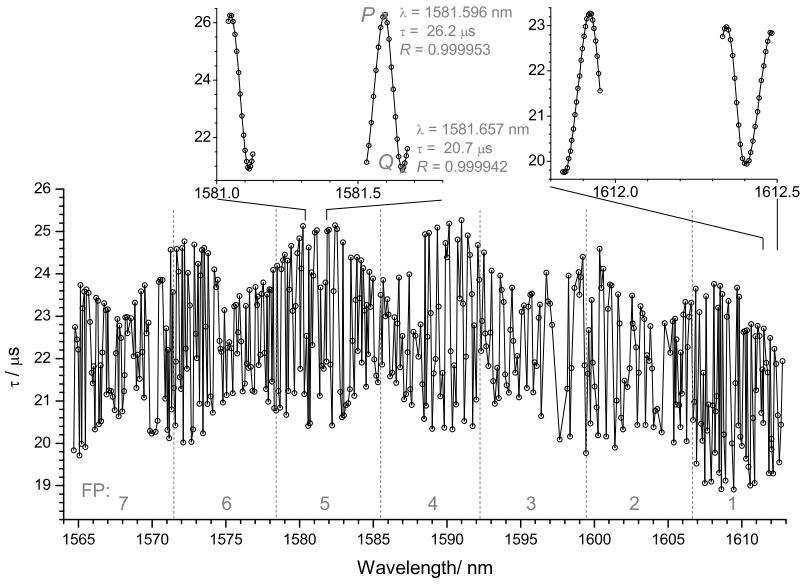

(a)

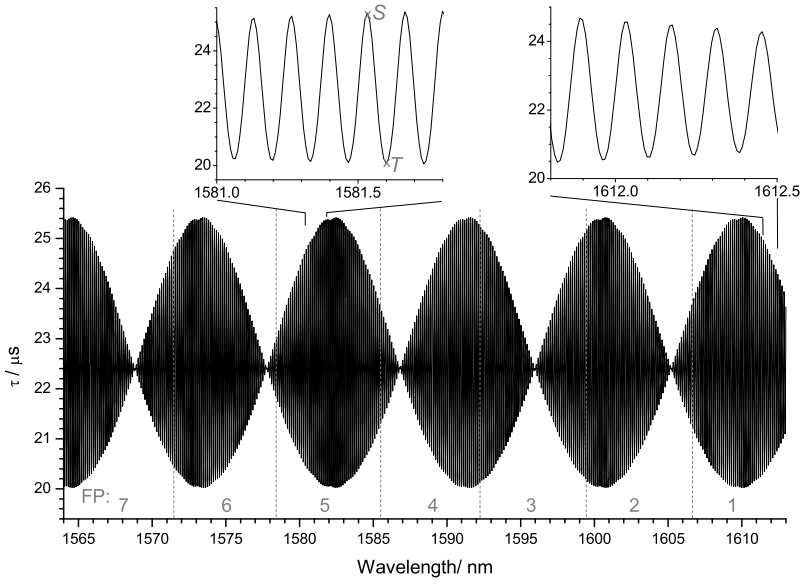

(b)

Figure 3.10: RDTs across the whole wavelength range of the DS-DBR. (a) Experimental results of averaging 35 RDTs at 450 points across 48 nm at 80 Torr of N_2. The range is divided into segments according to the different FPs (dashed lines). The insets show the RDTs measured at smaller wavelength intervals, indicating the large periodic variation in mirror reflectivity, R, with wavelength at a frequency of $\sim$ 16 GHz. Between points P and Q, a 20% reduction in RDT over 0.06 nm is observed. (b) Simulation of the RDTs assuming that the reflectivity of each mirror, $R_n(\lambda)$, varies in wavelength with a slightly different periodicity. The periods for R_1 and R_2 were set as 16.00 GHz and 16.24 GHz, respectively, *i.e.* a difference of 1.5%, and a central reflectivity of 0.9999455 used for both. The geometric mean, $R = \sqrt{R_1 R_2}$, as measured by the spectrometer, and the resultant τ were calculated across the spectral range, revealing beatings in τ of the order of $\sim$ 1100 GHz which are similar to those seen experimentally. The insets show that the $\sim$ 16 GHz periodic variations in R were also still present. However, this model does not account for the empirically observed general decrease in RDT with increasing wavelength, which may be due to a decreasing efficiency of the mode-matching or a fall in overall mirror reflectivity at longer wavelengths.

3.3.3 Spectroscopic measurements

Once characterised, the DS-DBR CRD spectrometer was used to perform spectroscopic studies on the narrowband absorber CO_2, using a variety of sources including air, a 5% calibrated mixture of CO_2 and breath samples.

In order to record these CRD spectra, the experimental conditions and fitting parameters as listed at the beginning of Section 3.3.2 were used. In addition, the number of RDTs averaged per point was set as $n_{\text{avg}} = 35$, as discussed in Section 3.3.2.2, and the settling time between points as $t_{\text{sett}} = 1 - 5$ s depending on the size of the intervening wavelength step. The DS-DBR was stepped across the spectral region of interest, as described in Sections 2.2.2.2 and 2.3.2. The wavelength changes for step sizes smaller than those that could be resolved by the wavemeter were estimated using linear interpolation between neighbouring points for which different wavelengths could be distinguished. This introduced inaccuracies in the frequency scale because the DS-DBR exhibits a non-linear wavelength-current relationship as seen in Chapter 2; however, these step sizes were considered small enough that a linear approximation in this case was valid.

3.3.3.1 Carbon dioxide in air

Firstly, studies were made of the $\nu(30013 \leftarrow 00001)$ $R(14)$ transition at 6238.77 cm^{-1} in 10 Torr of lab air. Using settings found in Section 2.3.2, spectra of τ against λ over the wavelength range $6238.699 - 6238.825$ cm^{-1} in 40 MHz steps were recorded over a period of 6 mins per spectrum. The periodic variations in R seen in Section 3.3.2.3 were observed in the baseline of the CRD spectra with the same frequency and magnitude; thus a 6^{th} order polynomial was used to fit a τ_0 baseline to the data before calculating α using Equation 1.53. A Voigt profile was then fitted to the absorption feature, fixing the Gaussian width as the Doppler width at 348 MHz. The data acquisition was repeated three times, one example of which is shown in Figure 3.11.

The fitted Voigt profile, together with data values reported in the HITRAN database [14], were used to estimate the concentration of CO_2 present in the lab air. Utilising both the area of the Voigt fit with the σ_{int} value, as well as the peak α_p data value with an estimate of the peak σ_p value (approximated using Equations 1.19 and 1.20), CO_2 concentrations of 622 ± 13 ppm and 604 ± 14 ppm, respectively, were returned from repeated and averaged measurements, which are typical values for indoor environments [227]. This implies that the quicker method of measuring only the α_p value at the line centre is a viable alternative to recording the whole spectrum; however, in employing this procedure care would be required to ensure the highly varying τ_0 baseline is fully accounted for by measuring this baseline prior to, and at regular intervals during, data acquisition.

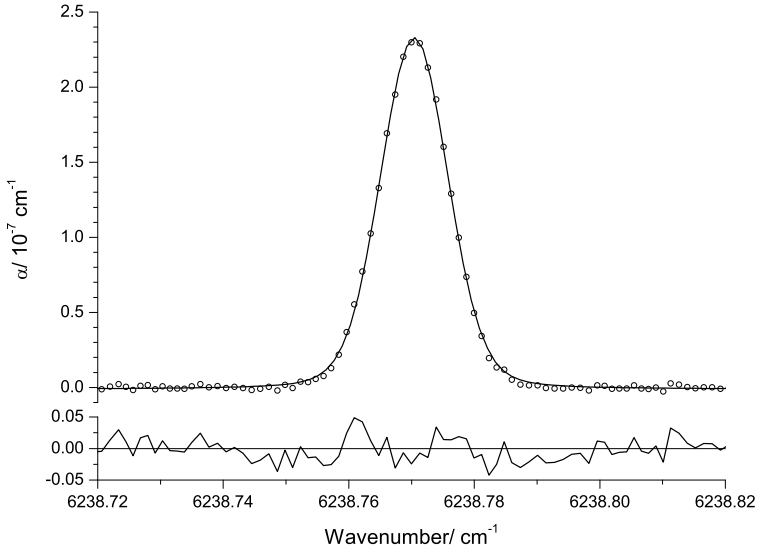

Figure 3.11: CRD spectrum of the $\nu(30013 \leftarrow 00001)$ $R(14)$ transition of $^{12}CO_2$ at 6238.77 cm^{-1} in 10 Torr of lab air. The raw data (open circles) and Voigt fit (solid line) are shown in the upper trace, and the residuals between the two in the lower one. In fitting the Voigt profile, the Gaussian width was fixed at the expected Doppler width of 348 MHz. For this case, the returned Lorentzian width was 62 ± 3 MHz (expected 57 MHz) and, by using the root mean square error value of the τ_0 baseline fit as $\Delta\tau^0_{\min}$, $\alpha_{\min}$ was estimated as 1.1×10^{-9} cm^{-1}.

Measurements of this transition were also conducted at increasing pressures in order to investigate the possibility of observing collisional, or Dicke, narrowing (Sections 1.1.2 and 5.3.2.1). This was suggested by the observation of small 'W' shaped residuals, characteristic of this narrowing phenomenon, between the data and Voigt fit, as seen in Figure 2.7(a). However, such studies proved inconclusive as fitting the data with Galatry profiles (which account for collisional narrowing) did not lead to significant improvements as residuals were not reduced.

3.3.3.2 Carbon dioxide in breath

One potential medical application of CO_2 detection is monitoring the deviations in the $^{13}CO_2/^{12}CO_2$ isotopic ratio in exhaled breath. Such changes can indicate metabolic activity associated with *Helicobacter pylori* (*H. pylori*) bacteria, which are present in the stomach and duodenum of over half of the global population [228]. While most carriers are asymptomatic, *H. pylori* can cause infections such as gastritis, peptic ulcers and stomach cancer [141]. The most reliable diagnosis of *H. pylori* infection is via a rapid urease test (RUT) of a biopsy of mucosa taken from the stomach [229, 230]. However, this is an invasive procedure, so non-invasive tests, such as the ^{13}C-urea breath test (UBT) [139, 231] are proving favourable alternative diagnostic tools in this area.

The UBT exploits the hydrolysis of urea ($CO(NH_2)_2$) to produce CO_2, H_2O and NH_3 by an enzyme called urease which is secreted by the *H. pylori* bacteria to neutralise the acidic environment of the stomach:

$$CO(NH_2)_2 + H^+ + 2H_2O \xrightarrow{\text{urease}} HCO_3^- + 2NH_4^+ \qquad \text{(Rn 3.1)}$$

$$HCO_3^- + H^+ \longrightarrow H_2O + CO_2 \qquad \text{(Rn 3.2)}$$

In the UBT, the ratio of the $^{13}CO_2/^{12}CO_2$ concentrations in the exhaled breath of a patient is measured before and 30 mins after the subject ingests a sample of ^{13}C-labelled urea [231]. If *H. pylori* bacteria are present, the ^{13}C-labelled urea is broken down by Reactions Rn 3.1 and Rn 3.2 to give $^{13}CO_2$ which is subsequently diffused into the bloodstream, transported to the lungs and then exhaled; hence enhanced levels of $^{13}CO_2$ in the breath of the patient after the administration of the ^{13}C-labelled urea indicates the presence of *H. pylori*. The change in the isotopic ratio, δ^{13}C, is given relative to a standard in parts per thousand (‰) by [97, 120]:

$$\delta^{13}C = \frac{R_{13/12} - R_{13/12,0}}{R_{13/12,0}} \times 1000‰ \qquad (3.2)$$

where $R_{13/12}$ and $R_{13/12,0}$ are the $^{13}C/^{12}C$ concentration ratios of the sample and the reference, respectively; in this case, these are the $^{13}CO_2/^{12}CO_2$ ratios measured in the exhaled breath samples after and before the ingestion of the ^{13}C-labelled urea, respectively. As an alternative, the internationally recognised Pee Dee Belemnite (PDB) standard of 0.0112372 can be used as the $R_{13/12,0}$ reference [73, 97]; the anomalously high $^{13}C/^{12}C$ ratio provided by this marine fossil ensures that most natural materials have a negative δ^{13}C in comparison.

Generally, positive UBT results, indicating the presence of *H. pylori*, are assigned to cases where $\delta^{13}C > 40‰$ and negative UBT results, implying the absence of *H. pylori* infection, are ascribed when $\delta^{13}C < 5‰$, though δ^{13}C as small as 2.4‰ have been reported to signify the existence of *H. pylori* [232]. The 'gold standard' accuracy required for UBTs has been agreed as 1‰.

Currently, the usual method to access the breath samples is by gas chromatography isotope ratio mass spectrometry (GC-IRMS) [233]. Despite achieving impressive sensitivities in δ^{13}C as low as 0.01‰ [234, 235], this technique suffers from several disadvantages, including the failure to distinguish between the $^{13}C^{16}O_2$ and $^{12}C^{16}O^{17}O$ isotopologues, and also between $^{12}C^{16}O_2$ and $^{14}N_2^{16}O$ [236]. In addition to its high cost, the apparatus is large, often off-site and cannot report results in real-time, preventing point-of-care diagnosis. Therefore other detection methods to analyse the breath samples have been proposed, including non-dispersive IR (NDIR) spectroscopy [237], opto-galvanic spectroscopy [238] and Fourier transform IR (FTIR) spectroscopy [236], as well as techniques based on laser

absorption spectroscopy such as photoacoustic spectroscopy (PAS) [239], direct homodyne spectroscopy [240], WMS [135, 241] and cavity-based spectroscopy [73, 142]. Although these optical absorption approaches are not yet able to obtain sensitivities competing with those achievable with GC-IRMS, they offer the prospect of economical, compact, real-time and point-of-care detection and are thus worthy of further investigation and development.

In order to utilise absorption spectroscopy for measuring the $^{13}CO_2/^{12}CO_2$ ratio in breath, suitable $^{12}CO_2$ and $^{13}CO_2$ transitions to monitor must be chosen. The CO_2 molecule has four normal vibrational modes: the IR inactive ν_1 symmetric stretching mode at 1338 cm^{-1}, the doubly degenerate ν_2 bending modes at 667 cm^{-1} and the ν_3 asymmetric stretching mode at 2349 cm^{-1}. Combination and overtone bands of these occur in the near-IR, with transitions of these bands at $\sim$ 1600 nm ($\sim$ 6200 cm^{-1}) being the most favourable for near-IR CO_2 sensing given that they are relatively free from absorptions of H_2O, a major component ($\sim 5\%$) in breath that can lead to unwanted spectroscopic interferences.

Several factors must be considered in order to select the appropriate $^{12}CO_2$ and $^{13}CO_2$ transitions, the first of which is the difference in the temperature dependence of the two transition intensities. This should be minimised to reduce the effect of environmental temperature fluctuations on the observed isotopic ratio. The intensity of an absorption signal corresponding to a rotational transition from state J depends on the Boltzmann population distribution [5]:

$$\frac{N_J}{N} = \frac{(2J+1)\mathrm{e}^{-hcE_J/k_BT}}{Q_r} \tag{3.3}$$

where N_J/N is the fractional population of the energy level with quantum number J, T is the absolute temperature, E_J is the rotational energy of the upper state J in cm^{-1} and Q_r is the rotational partition function (the contribution from the vibrational partition function has been neglected as the energy differences between vibrational levels are generally large compared to k_BT at room temperature). This indicates that by choosing $^{12}CO_2$ and $^{13}CO_2$ transitions which originate from rotational levels which are as close as possible in energy (ideally from levels with the same J), the susceptibility of δ^{13}C measurements to temperature variations is diminished. It can be shown that [118]:

$$\frac{\Delta\delta^{13}\mathrm{C}}{\Delta T} = \frac{hc\Delta E}{k_BT^2} \times 1000‰ \tag{3.4}$$

where ΔE is the difference in the ground state energies and $\Delta\delta^{13}\mathrm{C}/\Delta T$ is reported for a defined temperature. Transitions which exhibit similar absorption intensities are also desirable, as this avoids possible problems if the detector response is non-linear. Normally an additional criterion, that the selected $^{12}CO_2$ and $^{13}CO_2$ transitions must be within the $5-20$ GHz tuning range of a single scan of one DL to permit both features to be recorded

Isotopologue	Line centre / cm^{-1}	σ_{int} / $cm^2cm^{-1}molec^{-1}$	Ro-vibrational transition $\nu(\nu_1'\nu_2'l'\nu_3'r' \leftarrow \nu_1''\nu_2''l''\nu_3''r'')\ \Delta J(J'')$
$^{12}CO_2$	6228.598	7.296×10^{-27}	$\nu(31113 \leftarrow 01101)\ R(57)$
$*\ ^{12}CO_2$	6228.690	1.678×10^{-24}	$\nu(30013 \leftarrow 00001)\ R(0)$
$^{12}CO_2$	6228.727	1.320×10^{-26}	$\nu(40013 \leftarrow 10001)\ R(38)$
$*\ ^{13}CO_2$	6245.740	1.028×10^{-25}	$\nu(30012 \leftarrow 00001)\ R(4)$

Table 3.2: Line positions, integrated absorption cross-sections and transitions of the CO_2 features under investigation ($*$) and their neighbouring weaker lines [15].

simultaneously, is also employed. However, the broadband nature and fast switching capability of the DS-DBR means that this restriction need not be applied, allowing the best transitions to be chosen regardless of where they occur within the $1563 - 1613$ nm wavelength range.

Accordingly, $^{12}CO_2$ and $^{13}CO_2$ transitions with similar J, free from water lines and of similar intensity were selected for investigation and are listed in Table 3.2. These transitions correspond to different initial J levels of 0 and 4 for the $^{12}CO_2$ and $^{13}CO_2$ transitions, respectively, with a ΔE of 7.8 cm^{-1} [15] giving $\Delta\delta^{13}C/\Delta T = 0.128‰\ K^{-1}$ at 296 K; this means that ambient temperature fluctuations should not affect the measured $\delta^{13}C$ value significantly. Comparing the σ_{int} values for the two transitions listed in the HITRAN 2008 database [15], which account for the different isotopic abundances of 98.45% and 1.11% for the $^{12}CO_2$ and $^{13}CO_2$ molecules, respectively [242], the $^{13}CO_2/^{12}CO_2$ ratio of the areas or heights of the absorption signals of these two transitions, $r_{13/12}$, is 0.0613.

The absorption spectra expected for these transitions under the experimental conditions used were simulated to see the effect of neighbouring CO_2 lines (Figure 3.12). In the $^{12}CO_2$ case, tiny nearby transitions were observed to add to the shoulders of the target $^{12}CO_2$ absorption, while the $^{13}CO_2$ simulation indicated the presence of a significant baseline offset due to the wings of adjacent $^{12}CO_2$ transitions; these additional absorption features must therefore be accounted for in order to accurately extract the desired information from the transitions of interest.

Initially studies were performed using a $5.05 \pm 0.25\%$ calibrated mixture of CO_2 in 45% N_2 and 50% O_2 (*BOC*, 157837-L-C) before examining breath samples. Breath samples were collected in breath bags (*Fischer Analysen Instrumente GmbH*, 1.5 litres) and transferred to the cell without water removal or the filtration of aerosol particles. The cavity was filled with approximately 10 Torr of the sample under investigation, and CRD spectra were recorded of the $^{13}CO_2$ transition and then the $^{12}CO_2$ transition without changing the sample. Each spectrum was acquired over $4 - 10$ mins. A high order polynomial was used to fit a τ_0 baseline to the data and α calculated. For the $^{13}CO_2$ transition, a single Voigt

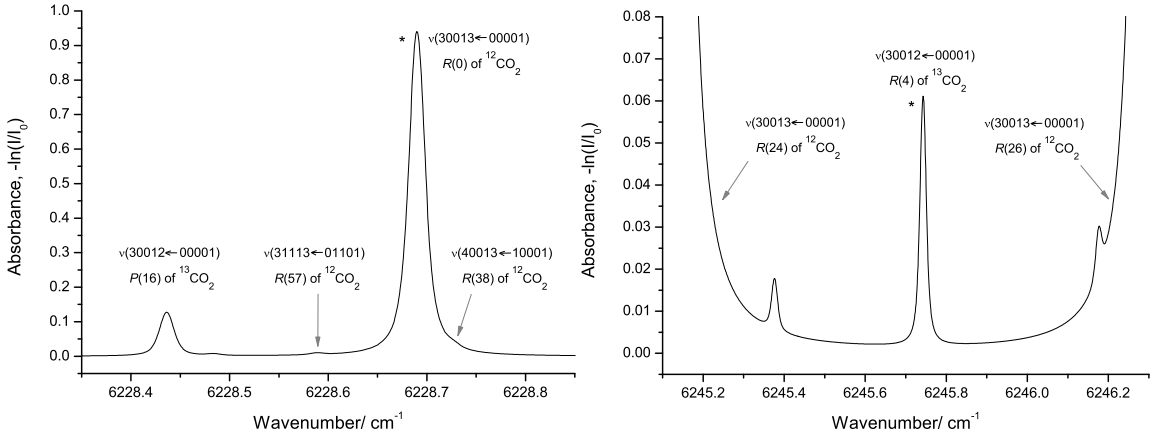

(a) $^{12}CO_2$ **(b)** $^{13}CO_2$

Figure 3.12: Simulated absorbances for the two selected CO_2 transitions for study ($*$) with their immediate neighbours, under conditions of 5% CO_2 in air at 50 Torr, 296 K in a 36.6 cm long cavity with mirrors of reflectivity $R = 0.9998$ using data from the HITRAN database [14]. In (b), the wings of the neighbouring $^{12}CO_2$ transitions result in a non-zero baseline for the $^{13}CO_2$ feature under investigation.

profile was fitted to the absorption feature; for the $^{12}CO_2$ transition, three Voigt profiles were fitted to account for the main transition and two neighbouring features. In fitting the Voigt profiles, the Gaussian widths were fixed at the Doppler widths of 348 MHz and 345 MHz for the $^{12}CO_2$ and $^{13}CO_2$ lines, respectively, and the baseline offsets fixed at zero. Two sets of spectra were recorded using the calibrated mixture, and three with the breath samples. Examples of the CRD spectra obtained for the different cases are given in Figure 3.13, in which small absorption features due to the weaker neighbouring transitions in the $^{12}CO_2$ spectra are clearly visible.

The amount of the CO_2 present in the samples was estimated using both the area of the Voigt fit and α_p data value. This latter approach, which was shown to be a viable technique in Section 3.3.3.1, was deemed preferable as it avoided any potential issues arising from the interference of the small, neighbouring transitions in the $^{12}CO_2$ case and also any possible inaccuracies in the wavelength calibration given the non-linear wavelength-current dependency of the DS-DBR present at a spectral resolution lower than that discernible with the wavemeter (Chapter 2). The results for both approaches are given in Table 3.3. Considering the results of using the preferred α_p analysis method, the calibrated mixture studies gave average CO_2 concentrations of $4.96 \pm 0.07\%$ and $4.85 \pm 0.05\%$ from the $^{12}CO_2$ and $^{13}CO_2$ transitions, respectively (errors reported based on the standard deviation of repeated measurements). These values are close to, and within the error of, the quoted $5.05 \pm 0.25\%$ of the calibrated mixture. For comparison, the breath studies reported average CO_2 concentrations of $3.81 \pm 0.02\%$ and $3.87 \pm 0.06\%$ using the $^{12}CO_2$ and $^{13}CO_2$ transitions, respectively (again, errors based on the variability of repeated measurements). $\alpha_{\min}$ values

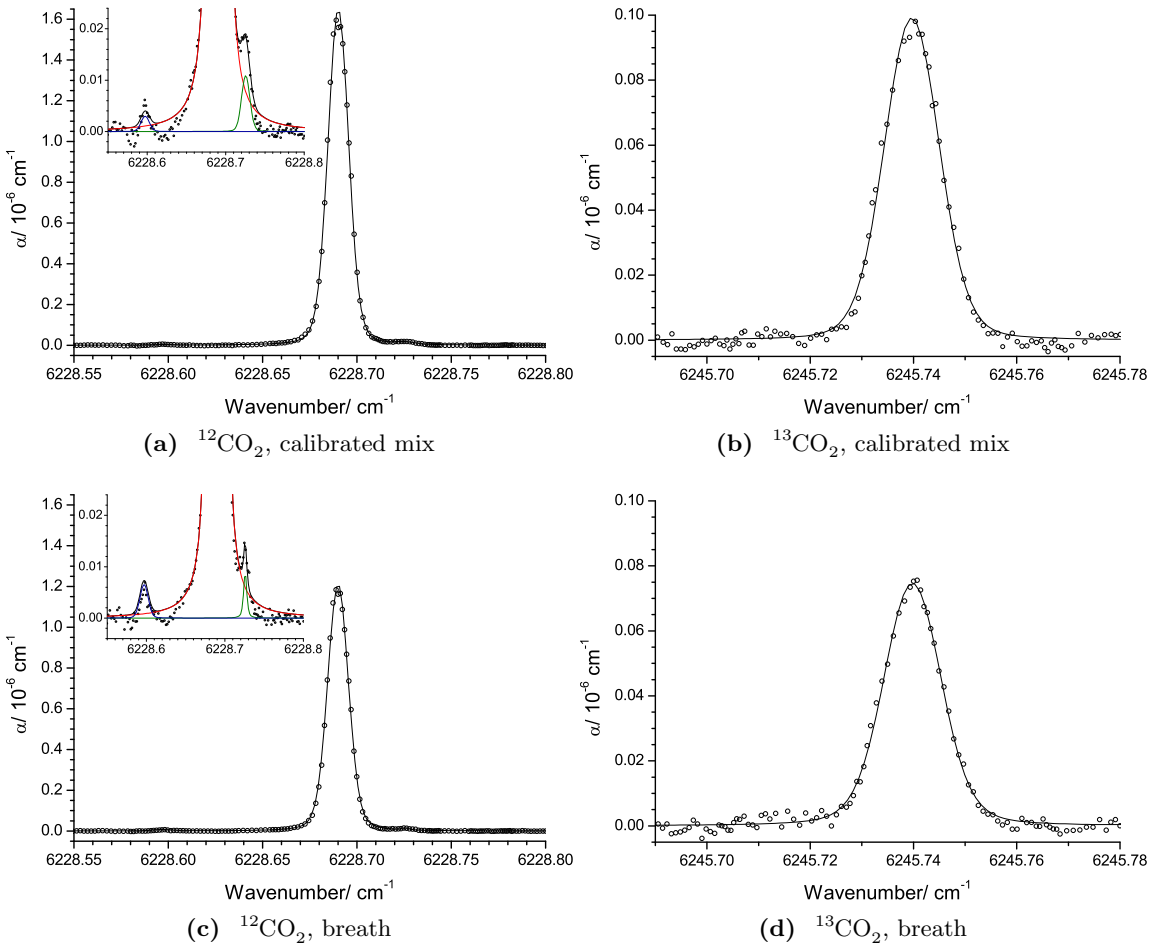

(a) $^{12}CO_2$, calibrated mix **(b)** $^{13}CO_2$, calibrated mix

(c) $^{12}CO_2$, breath **(d)** $^{13}CO_2$, breath

Figure 3.13: Examples of CRD spectra of the $\nu(30013 \leftarrow 00001)$ $R(0)$ $^{12}CO_2$ and $\nu(30012 \leftarrow 00001)$ $R(4)$ $^{13}CO_2$ transitions under investigation in both a $5.05 \pm 0.25\%$ CO_2 calibrated mixture ((a) and (b)) and breath samples ((c) and (d)) at ~ 10 Torr. The raw data are shown by the open circles and the total fit by the solid line. In fitting the Voigt profiles, the Gaussian widths were fixed at the expected Doppler widths and the baseline offsets fixed at zero, but other parameters were allowed to float with the Lorentzian widths expected to be in the range $60 - 70$ MHz. For the $^{12}CO_2$ transition of interest in (a) and (c), two neighbouring features were also fitted, as shown in the insets.

were estimated using the root mean square error (RMSE) of the fitted τ_0 baseline as the $\Delta\tau^0_{\text{min}}$ value in Equation 1.54 and found to be $\sim 1 - 2 \times 10^{-9}$ cm^{-1}. This is approximately $2 - 3$ times greater than the α_{min} estimated with the Allan variance study for $n_{\text{avg}} = 35$ in Section 3.3.2.2. Given that the mirror reflectivity, and thus RDT, change significantly with wavelength, and that these α_{min} values correspond to different wavelengths, this variation is unsurprising.

Table 3.3 also gives the $^{13}C/^{12}C$ ratio of the areas or heights of the $^{13}CO_2$ and $^{12}CO_2$ absorption signals, $r_{13/12}$. Again, considering the results of using the α_p analysis approach, these compare favourably with the expected value of 0.0613 from HITRAN: indeed, the $r_{13/12}$ for the calibrated mix compares very well but the breath sample one less so, which

Spectroscopic technique	Sample	Isotope	CO_2 conc. / %	$r_{13/12}$ Actual	% diff.	Accuracy
CRDS	Cal. mix	^{12}C	5.14 ± 0.10	0.0581 ± 0.0003	-5.2%	4.5‰
		^{13}C	4.87 ± 0.12			
Area Voigt fit	Breath	^{12}C	3.92 ± 0.05	0.0632 ± 0.0006	$+3.2\%$	10.2‰
		^{13}C	4.05 ± 0.02			
CRDS	Cal. mix	^{12}C	4.96 ± 0.07	0.0612 ± 0.0003	-0.1%	5.6‰
		^{13}C	4.85 ± 0.05			
α_p value	Breath	^{12}C	3.81 ± 0.02	0.0639 ± 0.0006	$+4.3\%$	9.9‰
		^{13}C	3.87 ± 0.06			
CEAS	Cal. mix	^{12}C	5.05 ± 0.11	0.0591 ± 0.0010	-3.5%	16.3‰
		^{13}C	4.88 ± 0.14			
Area Voigt fit	Breath	^{12}C	4.80 ± 0.09	0.0588 ± 0.0014	-4.0%	23.4‰
		^{13}C	4.61 ± 0.13			

Table 3.3: CRDS and CEAS results of studies of the $^{12}CO_2$ and $^{13}CO_2$ transitions listed in Table 3.2 performed using a $5.05 \pm 0.25\%$ calibrated CO_2 mixture (Cal. mix) and breath samples, with different breath samples used in the CRDS and CEAS experiments. Errors reported are the standard deviations of repeated measurements ($2-3$ spectra) and 'Conc.' means concentration. $r_{13/12}$ is the $^{13}C/^{12}C$ ratio of the areas or heights of the absorption signals of the two CO_2 transitions, and both the actual value calculated and its percentage difference (% diff.) compared to the HITRAN 2008 [15] value of 0.0613 are given. Accuracy is calculated as $SD(r_{13/12})/avg(r_{13/12}) \times 1000‰$, where avg and SD refer to the average and standard deviation, respectively.

may be due to a natural increased $^{13}CO_2/^{12}CO_2$ concentration ratio in the breath of the donor relative to the isotopic abundances assumed in the HITRAN database. An estimate of the precision with which the $\delta^{13}C$ could be reported was found by using the average, avg, and standard deviation, SD, of the $r_{13/12}$ values and a formula based on Equation 3.2 of $SD(r_{13/12})/avg(r_{13/12}) \times 1000‰$. The accuracies found were below 10‰, which is promising, but not as low as the 1‰ gold standard required for diagnostic purposes or the 0.22‰ reported in the literature for UBT precisions achievable via CRDS [142].

3.4 Near-Infrared CEAS with the DS-DBR Laser

As well as utilising the DS-DBR laser to perform CRDS, spectra were also recorded using CEAS. The set-up outlined in Section 3.1 was modified slightly in order to perform these CEAS measurements, with the final arrangement illustrated in Figure 3.14. The DS-DBR was scanned over the regions of interest via an external voltage ramp supplied by the computer, as discussed in Sections 2.2.2.2 and 2.3.2. Many cavity modes were excited simultaneously by the removal of the collimating and mode-matching lenses, off-axis injection of light into the cavity and the application of a high frequency (106 Hz), asymmetric

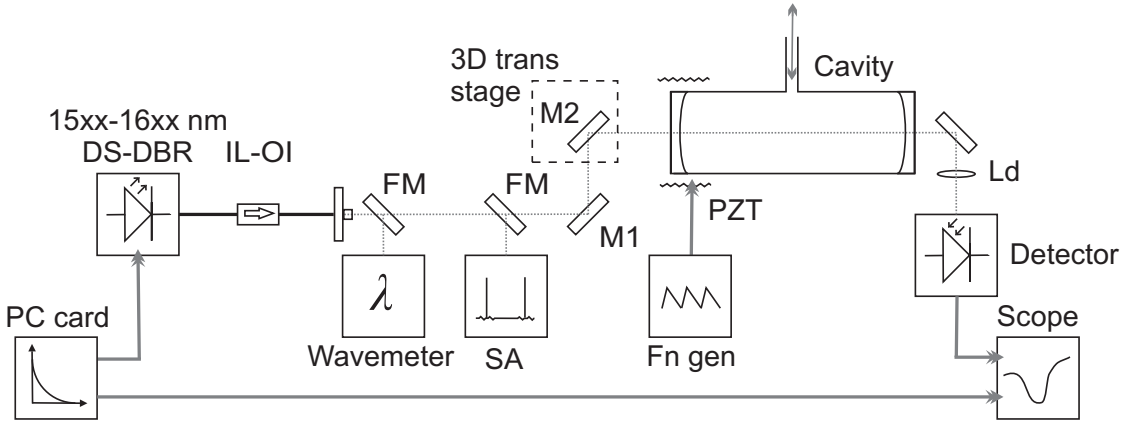

Figure 3.14: The experimental set-up for CEAS measurements. Cavity properties were measured as $L = 36.6$ cm, $R \sim 0.9999$. SA: spectrum analyser; FM: flip mirror; M1, M2: turning mirrors; Fn gen: function generator; Ld: focusing lens onto detector; Amp: variable gain, low noise current amplifier. M2 is mounted on a 3D translation stage to allow off-axis injection into the cavity.

triangular ramp to the PZT to jitter the cavity length. The laser was scanned across the desired wavelength ranges at 11 Hz and averaged 300 times to give smooth transmission spectra, each of which took approximately 30 s to acquire.

3.4.1 Carbon dioxide in breath

This CEAS set-up was used to study the same CO_2 transitions as those examined with CRDS in Section 3.3.3.2. Appropriate DS-DBR settings and voltage ramps were carefully selected to scan over the $^{12}CO_2$ and $^{13}CO_2$ transitions without mode-hops and were calibrated using a 2.32 GHz spectrum analyser (*Melles Griot*, 13SAE906) and the known transition frequencies. However, converting the CEAS measurements into absorption spectra was complicated by various factors.

Firstly, the ASE transmitted by the cavity had to be accounted for. In order to do this, the cavity was deliberately misaligned and the ASE signal was measured during the scans of the two different spectral regions: a small linear variation in ASE with wavelength was observed in both cases, with a different relationship for each. These varying ASE measurements were used as $I_{\text{base}}(\nu)$ in Equation 1.59 to calculate α.

The baseline, $I_0(\nu)$, was determined by recording spectra of the cavity filled with N_2 at the required pressure. Over the course of a day, the baselines of the two regions retained the same shape but their offsets were observed to decrease. Hence a function was fitted to the baseline data to reproduce its undulating shape (high order polynomials were necessary to accomplish this due to the highly variable mirror reflectivity across the regions of study,

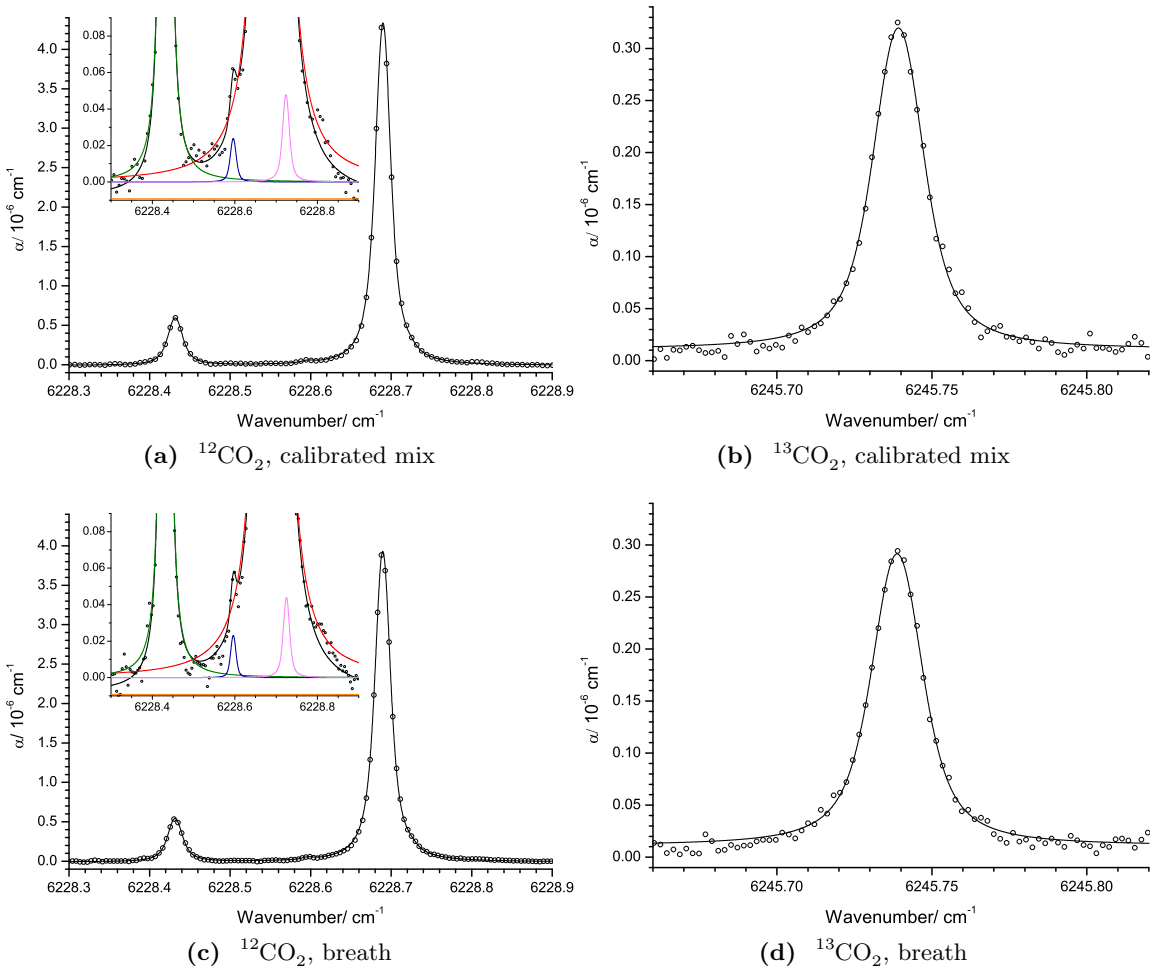

(a) $^{12}CO_2$, calibrated mix **(b)** $^{13}CO_2$, calibrated mix

(c) $^{12}CO_2$, breath **(d)** $^{13}CO_2$, breath

Figure 3.15: Examples of CEA spectra of the $\nu(30013 \leftarrow 00001)$ $R(0)$ $^{12}CO_2$ and $\nu(30012 \leftarrow 00001)$ $R(4)$ $^{13}CO_2$ transitions under investigation in both a $5.05 \pm 0.25\%$ CO_2 calibrated mixture ((a) and (b)) and breath samples ((c) and (d)) at ~ 50 Torr. The raw data are shown by the open circles and the total fit by the solid line; a reduced number of data points are shown for clarity. In fitting the Voigt profiles, the Gaussian widths were fixed at the expected Doppler widths. For the example calibrated mix $^{13}CO_2$ transition in (b), the CEAS study reported a CO_2 concentration (calculated from the Voigt fit area), Lorentzian width and α_{min} value of $4.88 \pm 0.11\%$, 379 ± 2 MHz (expected value 360 MHz) and 6.8×10^{-9} cm^{-1}, respectively.

as seen in Section 3.3.2.3) and this function then offset as appropriate to overlay the $I(\nu)$ data at the edges of the spectrum where no absorption by the features of interest occurred.

The fact that R varied greatly with wavelength introduced another problem: different values of R for the different scans were required to calculate α from Equation 1.59. These were found by performing measurements on samples of known CO_2 concentrations at various pressures, and R extracted from the gradient of the resultant plots of absorbance area against sample pressure. R was calculated as 0.9998696 for the $^{12}CO_2$ transition region corresponding to an effective path length of 2761 ± 7 m , with equivalent values of 0.9998705 and 2782 ± 23 m for the $^{13}CO_2$ case.

Finally, the actual fitting of the transitions themselves was difficult. In order to correctly fit the $^{12}CO_2$ transition, the three additional absorption features highlighted in Figure 3.12(a) needed to be fitted too; this was accomplished using a program called *PeakFit* [243]. A non-zero offset in the $^{13}CO_2$ case was required to account for the absorption wings of the strong, neighbouring $^{12}CO_2$ transitions (Figure 3.12(b)), which had become significant at the higher pressures used in the CEAS experiments; the extent of this offset was estimated using HITRAN simulations [14] and the baseline of the fit set accordingly.

Figure 3.15 gives examples of the CEA spectra recorded for the two $^{12}CO_2$ and $^{13}CO_2$ transitions for both the $5.05 \pm 0.25\%$ CO_2 calibrated mixture and breath samples. These were taken at ~ 50 Torr. In fitting the Voigt profiles, the Gaussian widths were fixed at the expected Doppler widths of 348 MHz and 345 MHz for the $^{12}CO_2$ and $^{13}CO_2$ lines, respectively, and the CO_2 concentrations calculated from the Voigt fit areas.

The areas of the Voigt fits, A_{12} and A_{13} for the $^{12}CO_2$ and $^{13}CO_2$ transitions, respectively, were used to find the $^{13}CO_2/^{12}CO_2$ ratio which could then be compared to that expected from HITRAN σ_{int} values [15]. However, manipulation of the integrated form of Equation 1.59 revealed that to find $r_{13/12}$, the different mirror reflectivities at the $^{12}CO_2$ and $^{13}CO_2$ transition wavelengths, R_{12} and R_{13}, respectively, had to be accounted for according to:

$$r_{13/12} = \frac{1 - R_{13}}{1 - R_{12}} \frac{A_{13}}{A_{12}} \tag{3.5}$$

The repeated and averaged results of all of these values are compared with those found from the CRDS experiments in Table 3.3. As expected, the reported accuracy is better in the CRDS case (by a factor of $2 - 3$) owing to this being an intrinsically more sensitive technique, as a time-domain (CRDS) measurement is less susceptible to intensity noise than an amplitude-domain (CEAS) one.

3.5 Conclusions

This chapter has described the development of a near-IR CRD spectrometer as well as providing demonstrations of its spectroscopic use by reporting the results of experiments conducted with the system using two different laser sources.

The software and hardware for the spectrometer have been outlined. In particular, two programs written in LabVIEW were discussed in detail: one of these programs was used to record ring-downs at a single, fixed wavelength, whereas the other measured ring-downs at many wavelengths for the acquisition of spectra. The CRDS set-up and programs were first tested by performing measurements using a traditional DFB diode laser source at 1577 nm, before the system was combined with the DS-DBR laser source introduced in Chapter 2.

Utilising the DS-DBR as the laser source for the CRD spectrometer, ring-downs were measured for an evacuated cavity across the whole wavelength range without the need for adjustments to the mode-matching or for cavity re-alignment. Measurements at the single wavelength of 1605.476 nm reported a τ_0 of 24.54 ± 0.04 µs, and an Allan variance analysis of these data implied an optimal α_{min} of 2.8×10^{-10} cm^{-1} over 20 s when filtering and averaging 100 ring-downs per point.

As an illustration of the DS-DBR CRDS system for high resolution spectroscopic applications, experiments were conducted on CO_2 at low pressures for a variety of samples and at a selection of wavelengths. Studies of the $\nu(30013 \leftarrow 00001)$ $R(14)$ transition at 1602.9 nm were used to determine the concentration of CO_2 present in lab air. Two other lines, the $\nu(30013 \leftarrow 00001)$ $R(0)$ $^{12}CO_2$ transition and the $\nu(30012 \leftarrow 00001)$ $R(4)$ $^{13}CO_2$ transition, were also studied in both calibrated CO_2 mixtures and breath samples, with the calculated concentrations from the calibrated mixture experiments in agreement with the reported values. These two transitions were studied owing to their potential use in the $^{13}CO_2/^{12}CO_2$ isotopic ratio analysis of breath samples to infer diseases associated with *H. pylori* bacteria, with promising initial results. If it were desired to further develop the use of this experimental system and the selected transitions to perform such measurements, this could be done quickly and simply by determination of the peak α_p data values of the absorption features, a method whose viability was ascertained in Section 3.3.3.1. This would involve recording τ and τ_0 values at just two frequencies corresponding to the top and bottom of the absorption feature by rapid switching of the DS-DBR between these well-defined frequency points, a feat made possible by the high sensitivity and wavelength reproducibility of the DS-DBR.

The DS-DBR was also used as a laser source for CEAS to study these same medically relevant CO_2 transitions in order to compare the two cavity-based techniques, with the reported accuracy being a factor of $2-3$ times better in the CRDS case.

In summary, this chapter proved the DS-DBR can be combined favourably with CRDS for gas monitoring applications. High resolution spectra with high sensitivities are achievable, and the wide tunability of the DS-DBR across 50 nm renders the possibility of multi-species detection or the investigation of broadband absorbers. Additionally, the high reliability and reproducibility of the output wavelength selection allows for the sequential jumping between discrete spectral regions, which is valuable for probing many, spectrally widely separated, absorption features, and also for repeating measurements over extended periods of time.

The framework for the CRD spectrometer developed in this chapter in the near-IR can easily be transferred to the mid-IR, given appropriate optical components and radiation sources. Possible mid-IR laser sources are reviewed in the following chapter, and the combination of mid-IR light and this CRDS system is then investigated in Chapters 5 and 6.

Chapter 4

Laser Light Sources in the Mid-Infrared

When absorption spectroscopy is used for gas sensing, the dual requirements of high sensitivity and selectivity can be achieved using two different approaches: firstly, by using sensitive detection techniques such as phase sensitive detection and path length enhancement and, secondly, by using the mid-IR region of the spectrum where absorption cross-sections are relatively high. This chapter outlines the main mid-IR laser sources available, including some of the benefits and drawbacks of each, before concentrating on difference frequency generation (DFG), which is the technique employed to make mid-IR light for the work presented in this thesis. The theory of DFG is discussed in depth and the experimental DFG system developed in this work is introduced and characterised.

4.1 Mid-Infrared Laser Light Sources

As discussed in Section 1.1.3, sensitivity for gas sensing can be optimised by monitoring the strong, fundamental absorption features of a species present in the mid-IR region ($2.5-12$ μm). There are several mid-IR sources available, each of which has its own advantages and disadvantages and hence would be the preferred choice in different situations [244–246]. The main possibilities are outlined below and their respective wavelength ranges summarised in Figure 4.1.

Colour centre lasers

Colour centre lasers [247] work by optically pumping certain colour centres in the alkali halides to produce pulsed and cw lasers tunable over the range $2-3.5$ μm. Despite providing

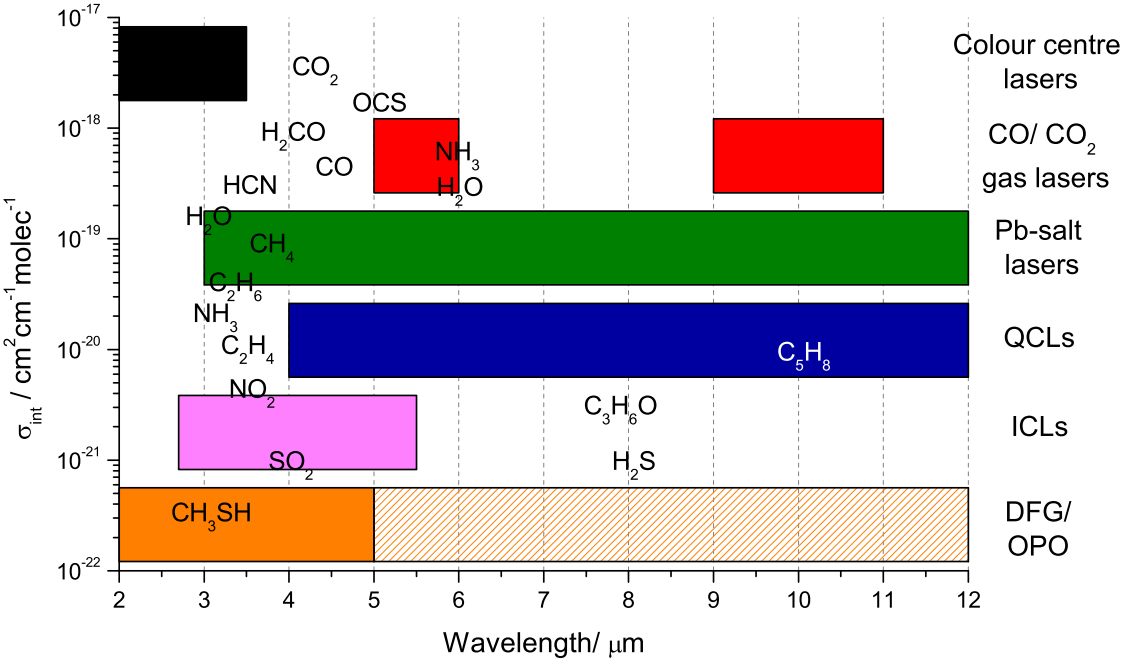

Figure 4.1: A comparison of the wavelength ranges covered by various mid-IR laser sources, together with the absorption strengths of a selection of medically important gaseous species. The hatched area indicates spectral ranges where DFG/OPO operation has been demonstrated but with a reduced efficiency.

high output powers (up to several W) with linewidths of the order of MHz, these sources suffer from a limited mid-IR spectral range and the requirement for liquid N_2 cooling.

CO and CO_2 gas lasers

CO ($5-6$ μm) [248] and CO_2 ($9-11$ μm) [249] lasers use gas mixtures as the gain media which are electrically pumped via a gas discharge. They have high output powers but only offer a stepwise tunability across the wavelength range (with steps of the order of $1-2$ cm^{-1} when operated in cw mode) due to the inherent line-tuning of the laser. To solve this, the laser radiation is usually electro-optically modulated with a tunable microwave source in a CdTe or GaAs crystal to create laser sidebands, allowing ∼50% of the wavelengths within the lasing range to be accessible.

Pb-salt lasers

IV-VI semiconductor lasers [48, 184], also known as lead-salt lasers, are similar to the more familiar GaAs near-IR semiconductor lasers and consist of a crystal of a Pb-salt semiconductor such as $Pb_{1-x}Sn_xSe$. They have a broad IR coverage of $3-30$ μm [24] as well as a narrow laser linewidth. Generally, low powers (∼ 1 mW) and the need for cryogenic cooling have prohibited their usage in any potential portable gas analysers. However, major advances have led to improvements in the mid-IR. DFBs, DBRs and ECDLs are now

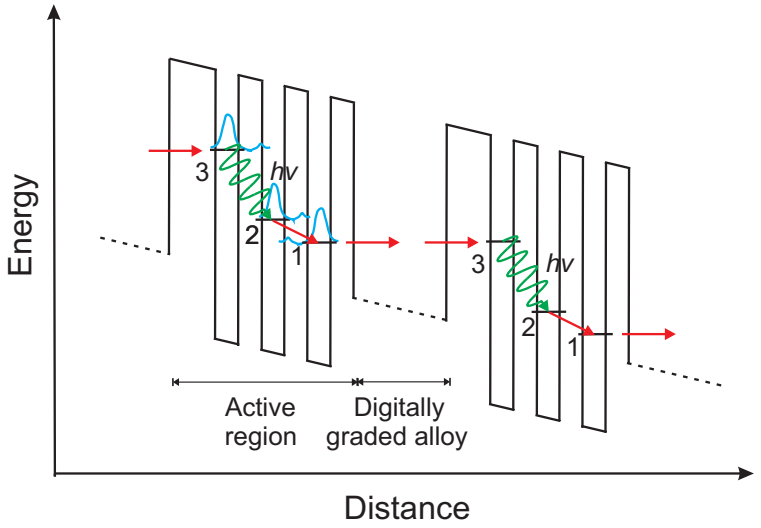

Figure 4.2: An explanation of the lasing scheme of a QCL. The active regions, comprising a series of three quantum wells, are separated by a digitally graded alloy, whose effective conduction band edges are represented by the dashed lines. An electron is injected into level 3, falls to level 2, emitting the lasing photon as it does so, and then relaxes to level 1. It then tunnels to a neighbouring set of identical quantum wells and the process is repeated. The electron thus cascades down the potential gradient as it crosses the structure, emitting a photon at each active region. Adapted from Faist *et al.* [250].

available, and offer higher temperature operation, greater spectral tunability (wide tuning of $\sim$ 100 nm and fine tuning of $\sim$ 20 cm^{-1} have been reported) and larger power outputs (up to $\sim$ 0.5 W of cw power).

Quantum cascade lasers (QCLs)

Quantum cascade lasers (QCLs) [27, 81, 250–253] are unipolar semiconductor devices consisting of periodic heterostructures, such as multiple GaAs/AlGaAs heterojunctions, which are engineered such that several quantum wells are present within each conduction band and that the energy of the coupled square well potentials decrease on moving across the device. Molecular beam epitaxy is used to deposit the semiconductor layers with thicknesses nearly equal to the de Broglie wavelength of the material (*e.g.* $\sim$ 25 nm in GaAs), allowing for the formation of the quantum wells by an analogous process to the simple particle in a box system with energy levels determined by the layer thickness. Figure 4.2 illustrates how a QCL works, as first constructed and demonstrated by Faist *et al.* in 1994 [250]. An electron is injected into the upper excited level (3), falls to a lower level (2), emitting the lasing photon at a wavelength corresponding to the energy gap as it does so, and then relaxes to the ground state (1). This relaxation from level 2 to 1 occurs over a much shorter time scale than the radiative transition between levels 3 and 2, as the energy difference between levels 1 and 2 is designed to be approximately equal to that of an optical phonon; this creates the required population inversion between levels 3 and 2 [250]. After relaxing to the ground state, the narrow barrier thickness between the neighbouring quantum wells

(< 5 nm) means the electron then tunnels through to, and is injected into the upper excited state of, the next quantum well. The process is repeated such that the electron cascades down through a staircase of quantum wells, emitting a photon of a precise wavelength at each step. The fact that one electron engenders the emission of many photons leads to relatively high laser output powers (up to 100 mW). Furthermore, this electronic cascade of transitions between intersubband states means the emitted wavelength of QCLs is not determined by the band gap properties of the semiconductor material (as is the case for traditional telecom diode lasers), but rather by the layer thickness. Hence, by modification of the quantum well depth, *i.e.* the thickness of the semiconductor layers, a wide range of wavelengths are accessible.

Initially, QCLs were operated in a pulsed fashion by application to the laser chip of a rapid, top-hat current pulse. Depending on the temporal duration of this applied pulse, either inter- [254] or intra- [255] pulse mode lasing could be achieved. As improvements in technology to efficiently remove the build up of heat in the active regions of the laser have been made, QCLs operating in the cw regime have been also developed [256]. Whereas pulsed QCLs have relatively low spectral resolutions ($\sim$ 250 MHz) due to spectral broadening caused by frequency chirping, cw QCLs have narrower linewidths and are also easier to use in terms of optics and electronics.

QCLs exhibit favourable characteristics in terms of wavelength coverage ($4-12$ µm), ease of use, compactness, output power (up to tens of W [253]), linewidth, operating temperature (for both pulsed and cw modes) and wavelength tunability (DFB QCL: $\sim$ 10 cm^{-1}; EC QCL: $\sim$ 300 cm^{-1}). Indeed, many companies now offer a range of QCLs [257, 258], and high power ($10-100$ mW), room temperature cw DFB QCLs with $\sim$ 1 MHz linewidths and continuous frequency tuning ranges of $\sim$ 10 cm^{-1} for wavelengths between $4.3-9.5$ µm are commercially available [258]. Further advances are continually being made too, especially with regards to improvements in the operating temperatures required for cw operation [259, 260], though further development of room temperature, cw QCLs operating at short wavelengths ($3-5$ µm) is still required. The advent of EC QCLs has been of particular significance, as these lasers are not restricted by thermal tuning and can thus scan broad spectral ranges, with tuning ranges of $100-500$ cm^{-1} at longer wavelengths ($8-11$ µm) having been reported [261, 262]. Broadband coverage has also been achieved by the stacking of active regions with different optical energies which emit at different wavelengths within a single QCL [263], as well as by using arrays of DFB QCLs [264, 265].

All of these attractive properties of QCLs have ensured their swift incorporation into a variety of real world applications and they are now utilised in a wide range of research fields, including atmospheric and trace gas sensing [76, 104], breath analysis [160], plasma diagnostics [266] and reaction kinetics [123]. However, QCLs are still mainly high current

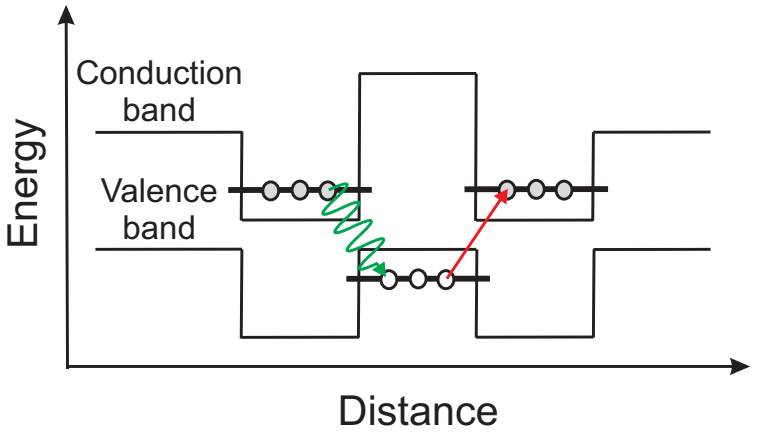

Figure 4.3: An explanation of the lasing scheme of an ICL. The electrons are initially trapped in a well in the conduction band but then radiatively combine with holes in the valence band. The addition of a field gradient causes the electrons to tunnel back into the conduction band, resulting in a 'W' movement of the electrons across the device and their return to the beginning of the process in anticipation of the next lasing transition. Adapted from Huang *et al.* [267].

devices and consequently need a large heat dissipation, necessitating some type of cooling (typically water cooling); such large power requirements may also limit their ability for field deployment. Furthermore, the absence of commercially available room temperature cw QCLs at wavelengths shorter than 4.3 μm, along with the complications arising from non mode-hop free tuning, has placed some constraints on their use in spectroscopy.

Interband cascade lasers (ICLs)

Since their proposal by Yang in 1995 [268], interband cascade lasers (ICLs) [269–272] have undergone substantial development and have demonstrated many positive attributes. They have a similar structure to QCLs, with thin layers of semiconductor deposited together, but make use of a type II alignment of the conduction and valence bands of the GaSb-based material system, resulting in electrons being confined in one material and holes in the other and may consist of a semi-metallic band overlap at the boundary between the electron and hole injector regions. In contrast to a QCL, where the lasing transition occurs between two levels within the conduction band (intraband), the lasing transition in an ICL involves the recombination of electrons from the conduction band with holes in the valence band (interband). On application of a field gradient, the electrons then tunnel back into the conduction band, ready for the next lasing transition. This behaviour means the electrons move in a 'W' shape across the active region, as shown in Figure 4.3.

ICLs emit in the important $2.7 - 5.5$ μm spectral window [273] and also have low threshold currents and high output powers. The use of cryogenically cooled ICLs for trace gas sensing applications has already been demonstrated [111]. Advances in this class of semiconductor lasers continue [267, 272, 274], with a current emphasis on developing their

room temperature cw operation [270, 271, 275–277]. Indeed, a thermoelectrically cooled cw ICL operating at 264 K was recently reported [269], and such lasers are now beginning to become commercially available [278, 279]. However, these lasers are still limited by their high temperature sensitivity caused by significant non-radiative losses, and the large financial investment they represent.

Type I quantum well DFB lasers

Progress has also been made in extending the wavelength range of DFB lasers using a type I quantum well arrangement into the mid-IR [280]. Single-mode, GaSb-based lasers with highly strained GaInAsSb quantum wells were limited in their emission up to 2.8 μm [281] until the introduction of the quinternary alloy AlGaInAsSb as a new barrier and waveguide material, which allowed the conduction and valence band energies to be adjusted independently. Such quantum well lasers have demonstrated pulsed mode operation at 3.26 μm at room temperature [282], cw operation at 3.06 μm at 20°C [283] and most recently cw operation up to around room temperature at $3 - 3.5$ μm with mode-hop free tuning of 8.5 nm and output powers ~ 1 mW [284]. However, these laser devices are still very much at an early developmental stage.

Non-linear optics (NLO)

In contrast to the direct laser radiation devices outlined above, mid-IR light can also be generated by non-linear optical processes, which convert near-IR radiation inputs to the mid-IR. There are two main ideas based on non-linear optics (NLO) in order to generate mid-IR radiation: optical parametric oscillators (OPOs) and difference frequency generation (DFG). Both exploit a second order non-linear optical effect concerning laser light at three different frequencies, ω_1, ω_2 and ω_3, which are also known as the pump, signal and idler radiation, respectively, with $\omega_1 > \omega_2 > \omega_3$ and $\omega_1 = \omega_2 + \omega_3$, that occurs inside a suitable non-linear crystal under appropriate phase matching and environmental conditions. NLO is one of the few ways cw, tunable, $2 - 5$ μm laser light can be generated, and has the additional benefit that any favourable properties of the near-IR sources (*e.g.* room temperature operation, precise wavelength resolution, compactness, narrow linewidths and continuous, rapid tunability) are translated into the mid-IR. Depending on the input frequencies and the crystal material selected, radiation over the whole $2 - 12$ μm region can be produced.

In OPOs [285], the non-linear crystal is placed inside an optical cavity. The pump radiation, ω_1, is injected into it generating both the signal and idler radiation at ω_2 and ω_3. OPOs can either be singly resonant (where only ω_2 is in resonance with the cavity), doubly resonant (with both ω_2 and ω_3 in resonance) or even triply resonant (all three frequencies

in resonance) [24]. The presence of the cavity allows the ω_2 and/or ω_3 fields to build up to large values giving high powers (several W), but the wide bandwidth of the radiation (typically > 3 GHz) makes it unsuitable for high resolution studies. Although cw OPOs can operate at wavelengths up to ~ 4.5 μm with smooth, mode-hop free tuning of up to 60 GHz [286, 287], their prohibitive cost, critical alignment and onerous maintenance somewhat limit their use and tend to confine them to laboratory studies.

In DFG, the pump and signal laser light rays, ω_1 and ω_2, respectively, are passed through the appropriate dielectric medium to create the idler radiation with frequency $\omega_3 = \omega_1 - \omega_2$. DFG-based sources offer narrow linewidths and wide, rapid and continuous wavelength tunability. However, low crystal conversion efficiencies tend to lead to low output powers of the order μW-mW (though this can be improved by the use of a waveguide architecture in the crystal), which can be extremely inhibiting when attempting to combine DFG mid-IR radiation with certain spectroscopic techniques, especially given the typically poorer detectors and optical components in this spectral region compared to those available in the near-IR, visible and UV. In addition, in order to achieve the full output tunability the phase matching requirements in the non-linear crystal must be considered. But it is this wide, continuous wavelength tunability, including wavelengths not accessible by other laser sources, that is the major advantage of DFG. Since DFG was first used by Pine in 1974 at $2.2 - 4.2$ μm [288], advances in non-linear optical materials and pumping lasers have extended the spectral coverage obtainable by DFG-based mid-IR laser sources; of particular significance was the work accomplished by the Laser Science Group at Rice University (Houston) in 1991 [289, 290].

As DFG was the technique implemented in this work to produce mid-IR radiation, the following section is dedicated to a more detailed discussion on its background theory. The actual DFG experimental set-up used in this thesis is then described and characterised in Section 4.3.

4.2 Difference Frequency Generation

4.2.1 Non-linear optics (NLO)

Optics is the study of the properties and behaviour of light, including its interactions with matter. At the low light intensities encountered in nature, the optical properties of materials are observed to be invariant to the intensity of the incident radiation. However, as the light intensity increases, additional, non-linear interactions between the radiation and matter begin to manifest themselves. NLO describes the behaviour of light in such

extremes, as occurs when non-linear media, whose dielectric polarisation responds non-linearly to the electric field of the radiation, are subjected to high intensity light with electric field strengths comparable to those of interatomic electric fields. In such situations, the optical properties of the material become dependent on the characteristics and intensity of the radiation. Although sufficiently intense light sources required to study NLO have only been developed within the last century with the advent of the laser, this relatively new scientific discipline has already been the subject of extensive research and many books [174, 291–293].

In general, during the interaction of light with a dielectric material, the oscillating electric field of the radiation disturbs the atomic electron density distributions in the medium, leading to instantaneous charge displacements and induced electric dipole moments. The induced electric polarisation of the material, $P(t)$, when it is subjected to an applied electric field, $E(t)$, is given by:

$$P(t) = \chi^{(1)}E(t) + \chi^{(2)}E^2(t) + \chi^{(3)}E^3(t) + \dots \tag{4.1}$$

$$= \underbrace{P^{(1)}(t)}_{P^L(t)} + \underbrace{P^{(2)}(t) + P^{(3)}(t) + \dots}_{P^{NL}(t)} \tag{4.2}$$

where χ are the electric susceptibility constants of the material, which indicate the ability of the dipoles within the substance to respond to the polarising electric field.

In the limit of low intensity radiation, only the first term of Equation 4.1 is required to accurately represent the induced polarisation, so the polarisation is observed to depend linearly on the applied electric field strength with a proportionality constant equal to the linear susceptibility constant, $\chi^{(1)}$. In the case of strong optical fields, however, the contributions from the higher order terms to the overall polarisation must also be accounted for, necessitating the use of the full version of Equation 4.1. This non-linear response engenders new components in the polarisation of the material, $P^{NL}(t)$, at frequencies not present in the incident radiation, and these in turn create new frequency components in the electromagnetic field. The process of how this new light is generated can be described by Maxwell's relations, resulting in the following wave equation (assuming the material is non-magnetic and devoid of free charges and currents):

$$\nabla^2 E(t) - \frac{n^2}{c^2}\frac{\partial^2 E(t)}{\partial t^2} = \frac{4\pi}{c^2}\frac{\partial^2 P^{NL}(t)}{\partial t^2} \tag{4.3}$$

In this work, only the quadratic contribution to the non-linear polarisation, $P^{(2)}(t)$, and its resultant second order non-linear optical interactions, will be considered.

4.2.1.1 Units for NLO

In this thesis, the Gaussian system of units [174] has been adopted unless otherwise stated. In this system, mechanical properties are measured in cgs units, *i.e.* cm for distance, g for mass and s for time. The fundamental unit is one of charge, known as the statcoulomb, and the unit of electric potential is the statvolt. However, literature adopting this convention seldom explicitly quotes the units of electrical quantities, but instead just states that the value is given in electrostatic units (esu). When using the Gaussian unit system, the vectors for the electric field, electric displacement field, magnetic induction, magnetic intensity, polarisation and magnetisation all have the same dimensions of statcoulomb cm^{-2}, also equivalent to one gauss, and the units of the susceptibilities $\chi^{(1)}, \chi^{(2)}$ and $\chi^{(3)}$ are none, $\mathrm{cm\,statvolt}^{-1}$ and $\mathrm{cm}^2\mathrm{statvolt}^{-2}$, respectively.

There are two different conventions when using the MKS (SI) unit system. In the first [294], Equation 4.1 becomes:

$$P(t) = \epsilon_0(\chi^{(1)}E(t) + \chi^{(2)}E^2(t) + \chi^{(3)}E^3(t) + \ldots) \tag{4.4}$$

and the units of $\chi^{(1)}, \chi^{(2)}$ and $\chi^{(3)}$ are none, mV^{-1} and $\mathrm{m}^2\mathrm{V}^{-2}$, respectively.

In the second convention, Equation 4.1 is written as:

$$P(t) = \epsilon_0(\chi^{(1)}E(t)) + \chi^{(2)}E^2(t) + \chi^{(3)}E^3(t) + \ldots \tag{4.5}$$

with the units for $\chi^{(1)}, \chi^{(2)}$ and $\chi^{(3)}$ now equal to none, CV^{-2} and CmV^{-3}, respectively.

4.2.2 Second order NLO

The equation for the electric field of an electromagnetic wave travelling in the z direction through an isotropic medium is given by:

$$E(z,t) = E_0\cos(kz - \omega t) \tag{4.6}$$

$$= A\mathrm{e}^{\mathrm{i}(kz-\omega t)} + A^*\mathrm{e}^{-\mathrm{i}(kz-\omega t)} \tag{4.7}$$

where E_0 is the electric field amplitude, k is the propagation wavevector, ω is the angular frequency and A is the complex field amplitude equal to $E_0/2$. If the electric field of the light incident on the dielectric material has two distinct frequency components, ω_1 and ω_2 with $\omega_1 > \omega_2$, so that it can be expressed as:

$$E(t) = E_1\mathrm{e}^{-\mathrm{i}\omega_1 t} + E_2\mathrm{e}^{-\mathrm{i}\omega_2 t} + c.c. \tag{4.8}$$

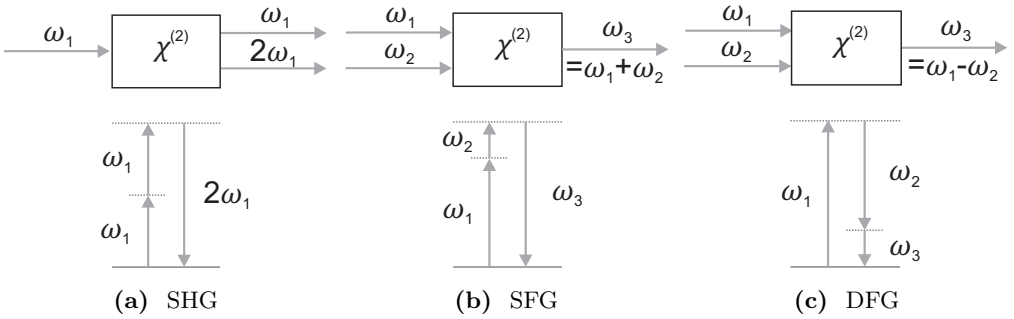

Figure 4.4: The interaction schematics and energy level descriptions for the second order non-linear processes of (a) SHG, (b) SFG and (c) DFG.

where $E_m = A_m \mathrm{e}^{\mathrm{i}k_m z}$ and *c.c.* represents the complex conjugates, then the second order contribution to the non-linear polarisation is given by:

$$\begin{aligned} P^{(2)}(t) &= \chi^{(2)} E^2(t) \qquad (4.9) \\ &= \chi^{(2)} E_1^2 \mathrm{e}^{-2\mathrm{i}\omega_1 t} + c.c. \\ &\quad + \chi^{(2)} E_2^2 \mathrm{e}^{-2\mathrm{i}\omega_2 t} + c.c. \\ &\quad + 2\chi^{(2)} E_1 E_2 \mathrm{e}^{-\mathrm{i}(\omega_1+\omega_2)t} + c.c. \qquad (4.10) \\ &\quad + 2\chi^{(2)} E_1 E_2^* \mathrm{e}^{-\mathrm{i}(\omega_1-\omega_2)t} + c.c. \\ &\quad + 2\chi^{(2)} (E_1 E_1^* + E_2 E_2^*) \end{aligned}$$

where the four different processes involved are:

1. Second harmonic generation (SHG) $P(2\omega_1) = \chi^{(2)} E_1^2 \mathrm{e}^{-2\mathrm{i}\omega_1 t}$ (4.11)
   $P(2\omega_2) = \chi^{(2)} E_2^2 \mathrm{e}^{-2\mathrm{i}\omega_2 t}$ (4.12)
2. Sum frequency generation (SFG) $P(\omega_1+\omega_2) = 2\chi^{(2)} E_1 E_2 \mathrm{e}^{-\mathrm{i}(\omega_1+\omega_2)t}$ (4.13)
3. Difference frequency generation (DFG) $P(\omega_1-\omega_2) = 2\chi^{(2)} E_1 E_2^* \mathrm{e}^{-\mathrm{i}(\omega_1-\omega_2)t}$ (4.14)
4. Optical rectification (OR) $P(0) = 2\chi^{(2)}(E_1 E_1^* + E_2 E_2^*)$ (4.15)

Each of these source terms of the form $P(\Omega)$ drives a field component at frequency Ω. Hence the three processes of SHG, SFG and DFG result in four new, non-zero frequency components of the polarisation and hence light at four new frequencies: $2\omega_1$, $2\omega_2$, $\omega_1+\omega_2$ and $\omega_1-\omega_2$. These are illustrated in Figure 4.4. Conversely, OR creates a static field inside the non-linear crystal.

In reality, only one of these interactions occurs efficiently on the irradiation of a non-linear material by light with two different optical frequencies. Which process is dominant is determined by how well the experimental requirements unique to each non-linear interaction, referred to as the 'phase matching conditions', are satisfied.

Of these various second order non-linear optical effects, the one of particular interest in this work is DFG due to its ability to produce mid-IR light. Thus the remainder of this chapter is devoted to further theoretical and experimental discussions of this process.

4.2.2.1 Second order non-linear susceptibility

Though not explicitly emphasised in the preceding derivations, the electric field and induced polarisations are actually vectorial quantities, varying over three-dimensional space. The second order non-linear susceptibility is in fact a third rank tensor, $\chi^{(2)}_{ijk}$, where i, j, k refer to the Cartesian components of the field x, y, z. The form of this tensor is restricted by various symmetry properties of the non-linear optical material [293]. In situations where the dispersion of $\chi^{(2)}$ can be neglected, such as when the frequencies of interest are in the material's transparency region and far from absorption resonances, Kleinman's symmetry can be employed which allows the susceptibility's indices to be permuted freely without permuting the corresponding frequencies. This yields a contracted notation for $\chi^{(2)}$:

$$d_{il} = \frac{1}{2}\chi^{(2)}_{ijk} \tag{4.16}$$

where the two indices jk are distilled into the one index l according to:

jk:	11	22	33	23, 32	31, 13	12, 12
l:	1	2	3	4	5	6

Thus $\chi^{(2)}$ can now be written in the simpler form of a 3×6 matrix allowing the second order polarisation leading to DFG to be expressed as:

$$\begin{pmatrix} P_x(\omega_3) \\ P_y(\omega_3) \\ P_z(\omega_3) \end{pmatrix} = 4 \begin{pmatrix} d_{11} & d_{12} & d_{13} & d_{14} & d_{15} & d_{16} \\ d_{21} & d_{22} & d_{23} & d_{24} & d_{25} & d_{26} \\ d_{31} & d_{32} & d_{33} & d_{34} & d_{35} & d_{36} \end{pmatrix} \cdot \begin{pmatrix} E_x(\omega_1)E_x(\omega_2) \\ E_y(\omega_1)E_y(\omega_2) \\ E_z(\omega_1)E_z(\omega_2) \\ E_y(\omega_1)E_z(\omega_2) - E_z(\omega_1)E_y(\omega_2) \\ E_x(\omega_1)E_z(\omega_2) - E_z(\omega_1)E_x(\omega_2) \\ E_x(\omega_1)E_y(\omega_2) - E_y(\omega_1)E_x(\omega_2) \end{pmatrix} \tag{4.17}$$

where $\omega_3 = \omega_1 - \omega_2$. The values of the coefficients vary between different dielectric materials, and any additional symmetry properties of the utilised medium can impose further limitations on the susceptibility d_{il} tensor. For example, lithium niobate ($LiNbO_3$), one of the most commonly used materials for DFG and that used in this work, belongs to the

crystallographic point group C_{3v} which reduces the d_{il} tensor to:

$$d_{il} = \begin{pmatrix} 0 & 0 & 0 & 0 & d_{31} & -d_{22} \\ -d_{22} & d_{22} & 0 & d_{31} & 0 & 0 \\ d_{31} & d_{31} & d_{33} & 0 & 0 & 0 \end{pmatrix} \tag{4.18}$$

with $d_{22} = 5.0 \times 10^{-9}$, $d_{31} = -10.4 \times 10^{-9}$ and $d_{33} = -64.9 \times 10^{-9}$, all in units of cm statvolt^{-1} [293, 295, 296]. Only certain matrix coefficients are accessible experimentally depending on the polarisations of the electric fields applied. So, by knowing the magnitudes of the different d_{il} components, the most efficient polarisation scheme which maximises the effective value of the non-linear susceptibility constant and hence the amount of new light generated, can be found. The value of the effective non-linear susceptibility constant for the adopted interaction geometry is referred to as d_{eff}.

4.2.3 Difference frequency generation (DFG)

DFG has been the focus of a range of books [24, 297] and journal reviews [244, 245, 298], and has also played an important role in spectroscopy [299]. It involves passing two electromagnetic waves with frequencies ω_1 and ω_2, known as the pump and signal radiations, respectively, through an appropriate dielectric medium to create light with a new frequency, ω_3, called the idler radiation, where $\omega_3 = \omega_1 - \omega_2$ and $\omega_1 > \omega_2 > \omega_3$. Figure 4.4(c) provides an interpretation of this process at a quantum level: the excitation caused by the pump radiation to the highest energy level is succeeded by two photon decays back to the ground state, the first of which is via stimulated emission caused by the signal radiation; conservation of energy means the final decay photon must have frequency ω_3.

In the ideal case, when the non-linear material is lossless, ω_3 is absent from the incident radiation, ω_1 is undepleted by the non-linear process (so A_1 is effectively constant) and the input beams are cw, collimated and monochromatic, then the DFG interaction of the coupled wave equation (Equation 4.3) can be assigned a trial solution of the form:

$$E_3(z,t) = A_3(z)\mathrm{e}^{\mathrm{i}(k_3 z - \omega_3 t)} + c.c. \tag{4.19}$$

which represents a plane wave travelling in the $+z$ direction with frequency ω_3. The wavevector, k_3, and linear refractive index, n_3, of the idler radiation are defined as:

$$k_3 = \frac{n_3 \omega_3}{c} \tag{4.20}$$

$$n_3 = \sqrt{\epsilon_r(\omega_3)\mu_r(\omega_3)} \tag{4.21}$$

where $\epsilon_r(\omega_3)$ and $\mu_r(\omega_3)$ are the relative permittivity and permeability, respectively, of the material at frequency ω_3. The former describes the resistance encountered when forming an electric field in a material, and the latter is approximately equal to one for most naturally occurring substances at optical frequencies and is assumed to be unity in this work. The amplitude of the non-linear polarisation driving the wave equation for DFG can be written as:

$$P_3(z,t) = 4d_{\text{eff}}A_1A_2^*\text{e}^{\text{i}[(k_1-k_2)z-\omega_3 t]} + c.c. \tag{4.22}$$

By using this as the P^{NL} term, substituting in Equation 4.19, replacing ∇^2 with $\text{d}^2/\text{d}z^2$ (as the interaction only occurs along the z axis) and applying the slowly varying amplitude approximation (where it is assumed A_3 varies only slowly over the crystal length), then the wave equation (Equation 4.3) becomes:

$$\frac{\text{d}A_3}{\text{d}z} = \frac{8\pi\text{i}d_{\text{eff}}\omega_3^2}{k_3c^2}A_1A_2^*\text{e}^{\text{i}\Delta kz} \tag{4.23}$$

where Δk is termed the wavevector mismatch which for DFG is:

$$\Delta k = k_1 - k_2 - k_3 \tag{4.24}$$

As the intensity of each wave is designated as the magnitude of the time-averaged Poynting vector with a value of:

$$I_m = \frac{n_m c}{2\pi}\left|A_m\right|^2 \tag{4.25}$$

where $m = 1, 2, 3$, then the integration of Equation 4.23 over the length of the dielectric crystal, L_{crys}, allows the amplitude of the resultant idler radiation to be determined. The idler intensity is thus equal to:

$$I_3 = \frac{512\pi^5 d_{\text{eff}}^2}{n_1n_2n_3\lambda_3^2 c}I_1I_2L_{\text{crys}}^2\text{sinc}^2\left(\frac{\Delta kL_{\text{crys}}}{2}\right) \tag{4.26}$$

where λ_3 is the idler wavelength in a vacuum, given by $\lambda_3 = 2\pi c/\omega_3$, and $\text{sinc}x = \text{sin}x/x$. Hence the conversion efficiency varies with Δk via the $\text{sinc}^2(\Delta kL_{\text{crys}}/2)$ factor, as illustrated in Figure 4.5. The $\text{sinc}^2(\Delta kL_{\text{crys}}/2)$ term is known as the phase mismatch factor and forms the basis of the phase matching conditions required for efficient DFG to take place, as discussed in the following section.

4.2.4 Phase matching

The phase relationship between the interacting waves determines the direction of power flow between the propagating fields, and as such affects the efficiency of a non-linear conversion process. So in order for the two incident optical fields to interact efficiently to generate the

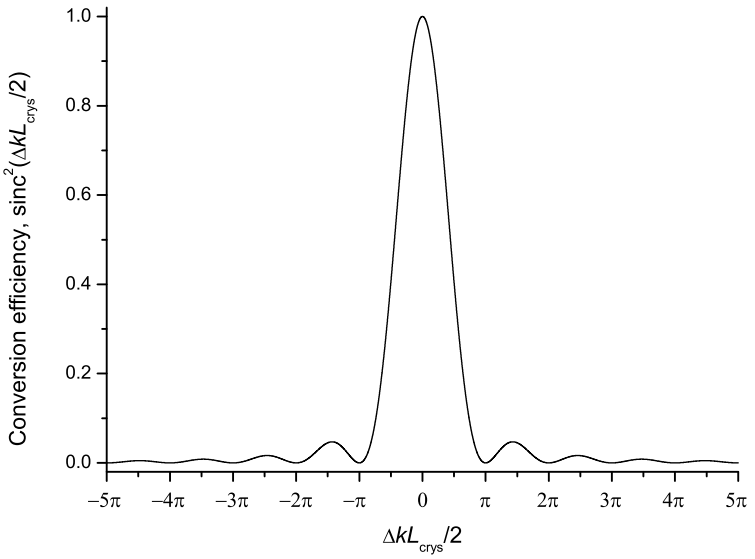

Figure 4.5: Conversion efficiency curve for non-linear interaction processes, including DFG, under the plane wave approximation. The maximum conversion efficiency occurs when $\Delta k = 0$; minima occur at $\Delta k = 2m\pi/L_{\text{crys}}$ where m is a non-zero integer.

new one, a phase matching condition must be fulfilled: this condition is that the wavevector mismatch must equal zero, *i.e.* $\Delta k = 0$. Such perfect phase matching corresponds to the maximum of the conversion efficiency curve and a maximum in the generated radiation intensity, as demonstrated in Figure 4.5.

A dramatic decrease in the conversion efficiency is seen when this condition is not satisfied. This is due to the varying phase relationship of the interacting waves along the direction of propagation caused by the frequency dependence of the propagating waves' phase velocities induced by chromatic dispersion. Minima in the conversion efficiency occur when a relative phase shift of $m\pi$, where m is a non-zero integer, is accumulated on the passage of the waves through the medium. The distance over which such a phase shift occurs is known as the coherence length, L_c:

$$L_c = \frac{\pi}{\Delta k} \tag{4.27}$$

Unfortunately, the perfect phase matching condition of $\Delta k = 0$ is impossible to achieve. This is because of an effect known as normal dispersion, which causes the refractive index to increase with frequency for most materials. In the case of DFG, where $\omega_1 > \omega_2 > \omega_3$, this means that $n_1 > n_2 > n_3$. Hence the wavevector mismatch for DFG (Equation 4.24), which can be expressed as:

$$\Delta k = \frac{n_1\omega_1}{c} - \frac{n_2\omega_2}{c} - \frac{n_3\omega_3}{c} \tag{4.28}$$

cannot equal zero as required for perfect phase matching. This can be proved by contradiction: substitution of $\Delta k = 0$ and $\omega_1 - \omega_2 = \omega_3$ into Equation 4.28 gives $\omega_1/\omega_3 = (n_3 - n_2)/(n_1 - n_2)$, a statement which is not possible as the left hand side is positive but the right hand side is negative. However, two experimental methods have been developed to

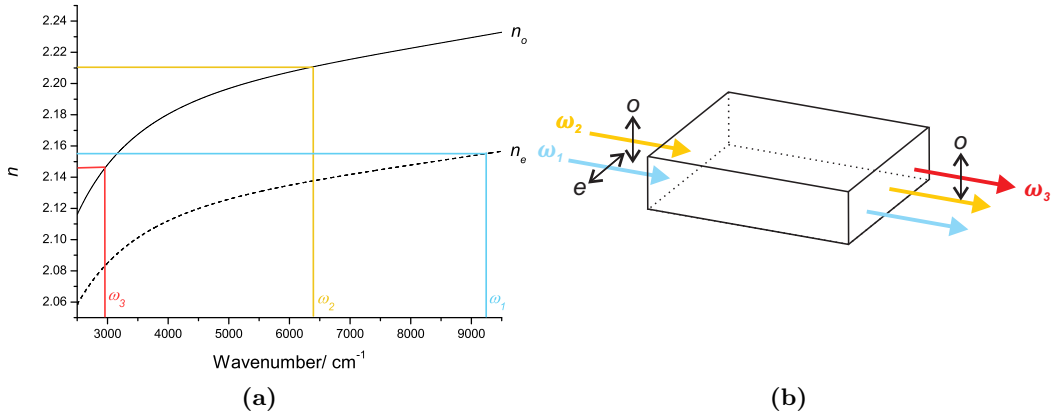

Figure 4.6: BPM for DFG using congruent $LiNbO_3$, a negative uniaxial crystal with $n_o > n_e$ as shown in (a) (refractive indices calculated at 24.5°C [300]). The highest frequency ω_1 wave is set as e-polarised so that it experiences the lower refractive index, n_e, and a type I scheme, with the other two waves being o-polarised, adopted as this maximises the d_{eff} value. (b) depicts this combination of polarisations of the interacting waves.

overcome this problem to maximise the DFG process: birefringent phase matching (BPM) and quasi phase matching (QPM).

4.2.4.1 Birefringent phase matching (BPM)

Birefringence is the dependence of the refractive index on the polarisation direction of the optical radiation. For example, uniaxial crystals, such as $LiNbO_3$, exhibit two different refractive indices: an ordinary refractive index, n_o, when the light is polarised perpendicularly to the plane containing the propagation wavevector and the optical c axis (axis of rotational symmetry) of the material, and an extraordinary refractive index, n_e, when it is parallel. Uniaxial crystals can either be positive, with $n_e > n_o$, or negative, $n_o > n_e$.

In BPM [301], the polarisation of the highest frequency wave (ω_1) is chosen such that is experiences the lowest of its possible refractive indices, while the other two waves are assigned polarisations following either the type I or type II phase matching scheme. In type I interactions, the highest frequency polarisation is orthogonal to both polarisations of the other two frequencies; for type II interactions, the lowest two frequencies are orthogonally polarised to each other. Normally the scheme which accesses the largest possible d_{eff} component of the susceptibility tensor is chosen. The refractive indices of the three waves are controlled by either tuning the crystal temperature as according to the Sellmeier equation [300, 302, 303] or by altering the angle between the direction of propagation of the incident light beam and the optical c axis of the crystal [304]. Figure 4.6 illustrates the use of BPM for DFG using congruent $LiNbO_3$.

In the early days of NLO, BPM was the dominant phase matching strategy adopted. However, it suffers from several drawbacks. BPM cannot be implemented if the material is not birefringent, which includes all isotropic crystals, or if the material has insufficient birefringence to counterbalance the normal dispersion of the linear refractive indices over the frequency range of interest. Furthermore, limitations on the polarisations enforced by the different phase matching strategies make some of the coefficients of the non-linear susceptibility d_{il} tensor unattainable. In particular, the d_{33} component, which is often larger than the other coefficients and so would be especially useful to exploit (as is the case with $LiNbO_3$), cannot be accessed as this would require all the interacting waves to be polarised in the same direction, a feat not possible with BPM.

4.2.4.2 Quasi phase matching (QPM)

As an alternative, the phase matching technique of QPM can be utilised, as employed in this thesis. This approach was proposed even before BPM [305, 306], though BPM was the first to be widely implemented.

In QPM [298, 307], the phase of the non-linear polarisation is periodically reset to maintain a coherent build up of the non-linear interaction. This rephasing is achieved by regularly inverting the orientation of one of the crystalline axes of the material, and hence the sign of its second order non-linear susceptibility constant, $\chi^{(2)}$, over the distance in which it interacts with the propagating waves. The effect of normal dispersion means the wavevector mismatch deviates from the perfect phase matching condition of $\Delta k = 0$; in QPM, the non-zero Δk is compensated for by introducing an additional wavevector, k_g, which ensures a continuous build up of the generated radiation over the crystal length.

Figure 4.7 demonstrates the variation in the intensity of the generated light with distance for cases of perfect phase matching, no phase matching and QPM. When the phase matching condition is fully satisfied, so $\Delta k = 0$, energy from the incident optical fields is efficiently transferred to the generated wave and its intensity increases quadratically with propagation distance. In contrast, when the non-linear interaction is strongly dephased, so $\Delta k \neq 0$, the amplitude of the generated field oscillates over the crystal length. However, if a QPM scheme is adopted such that the sign of the non-linear susceptibility constant is inverted every mL_c, where m is an odd integer, then the phase of the polarisation wave is shifted by π and the interaction is essentially rephased at each reversal, resulting in a monotonic power flow into the generated radiation.

QPM can be described mathematically as follows, assuming that the pump source is cw and undepleted and by applying the plane wave approximation. The evolution of the DFG field is described by the slowly varying wave equation (Equation 4.23) which can be integrated

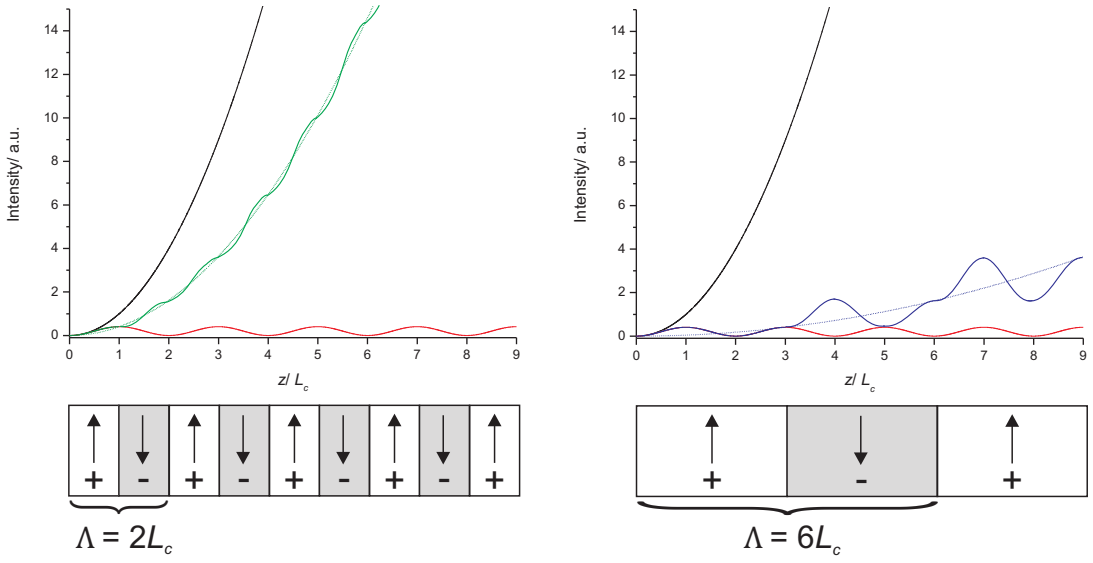

(a) $m = 1$ **(b)** $m = 3$

Figure 4.7: The effect of QPM on the intensity of the generated radiation as a function of propagation distance, z, given in units of L_c. The two extreme regimes of perfectly phase matched (black) and mismatched (red) are shown, in addition to two QPM schemes with different orders: (a) $m = 1$ (green) and (b) $m = 3$ (blue). The modulation period of the inversion of the sign of the susceptibility, known as the poling period and given by $\Lambda = 2mL_c$, is illustrated in the lower parts of the figures for the two cases.

over the crystal length to give:

$$A_3(L_{\text{crys}}) = \Gamma \int_0^{L_{\text{crys}}} d(z) \mathrm{e}^{\mathrm{i}\Delta k z} \mathrm{d}z \tag{4.29}$$

where $\Gamma = 8\pi \mathrm{i}\omega_3^2 A_1 A_2^* / k_3 c^2$ and $d(z)$ represents the (possibly) spatially varying non-linear susceptibility. For a uniform medium, $d(z)$ is simply a top-hat function of length L_{crys} and depth d_{eff}, resulting in the expression for the idler intensity previously found (Equation 4.26). However, if the variation in the non-linear susceptibility of the material is a periodic reversal of its sign such that $d(z)$ can be expressed as a symmetric square wave modulation from $+d_{\text{eff}}$ to $-d_{\text{eff}}$ with a period Λ (Figure 4.8), then $d(z)$ can be written as the well-known Fourier series for a square wave function:

$$d(z) = \sum_{m=-\infty}^{\infty} d_m \mathrm{e}^{-\mathrm{i}k_m z} \tag{4.30}$$

where Λ is known as the poling period, $k_m = 2m\pi/\Lambda$ for the m^{th} spatial harmonic and d_m is the corresponding Fourier coefficient given by:

$$d_m = \frac{2d_{\text{eff}}}{m\pi} \sin\left(\frac{m\pi}{2}\right) \tag{4.31}$$

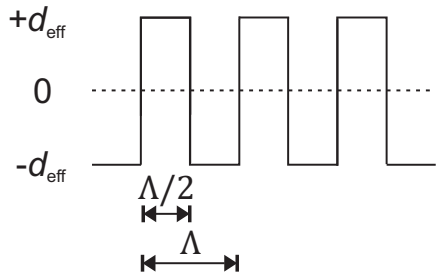

Figure 4.8: The d coefficient plotted as a function of distance in a QPM crystal.

which is equal to zero for all even values of m and has a magnitude of $2d_{\text{eff}}/m\pi$ for all odd orders. Equation 4.30 can be substituted into Equation 4.29 and the resultant expression integrated. Assuming one Fourier component of the QPM grating is sufficiently closer to Δk than the others such that it dominates the summation, this integration yields:

$$A_3(L_{\text{crys}}, m) = \Gamma L_{\text{crys}} d_m \mathrm{e}^{\mathrm{i}\Delta k_{\text{QPM}} L_{\text{crys}}/2} \text{sinc}(\Delta k_{\text{QPM}} L_{\text{crys}}/2) \tag{4.32}$$

where the effective wavevector mismatch for QPM-DFG is:

$$\Delta k_{\text{QPM}} = k_1 - k_2 - k_3 - k_m \tag{4.33}$$

$$= 2\pi \left(\frac{n_1}{\lambda_1} - \frac{n_2}{\lambda_2} - \frac{n_3}{\lambda_3} - \frac{m}{\Lambda} \right) \tag{4.34}$$

Equations 4.31 and 4.33 indicate that the use of QPM alters the wavevector mismatch and the non-linear susceptibility constant from their values for perfect phase matching in a homogeneous medium: the phase matching condition is shifted to $\Delta k = k_m$ and the effective d coefficient is reduced by a factor of $2/m\pi$ so the conversion efficiency falls by a factor of $(2/m\pi)^2$ and the average growth rate of the generated radiation intensity is lower than that for a perfectly phase matched interaction (Figure 4.7). The QPM order, m, refers to the number of coherence lengths after which the intensity build up begins and is related to the poling period by:

$$\Lambda = 2mL_c \tag{4.35}$$

Usually, m is chosen to be one as it gives the largest d_m value, but higher order interactions can be useful in situations where small L_c are required in order to generate short wavelength radiation, as small poling periods are difficult to manufacture [308].

The main advantage of QPM is its ability to access the larger coefficients of the non-linear susceptibility tensor. However, the requirement for poling periods of the order of microns presents fabrication challenges: poling periods of $\sim$ 30 μm are needed to generate 3 μm radiation, and even smaller poling periods (as low as 5 μm) are required to create shorter wavelength light.

Material	Chemical formula	Acronym	Operating wavelengths/ μm	PM method	Example reference
Lithium niobate	$LiNbO_3$	PPLN	$1.5 - 5$	QPM	[311, 312]
Lithium tantalate	$LiTaO_3$	PPLT	$0.4 - 4.5$	QPM	[308, 313]
Potassium titanyl phosphate	$KTiOPO_4$	PPKTP	$2 - 5$	QPM	[314]
Potassium titanyl arsenate	$KTiOAsO_4$	PPKTA	$2.4 - 4.5$	QPM	[315]
Zinc germanium phosphide	$ZnGeP_2$	ZGP	$3.8 - 8$	BPM	[316, 317]
Cadmium selenide	CdSe	CdSe	$2 - 5.5$, $8 - 12$	BPM	[318]
Silver selenogallate	$AgGaSe_2$	AgSe	$2.7 - 12$	BPM	[319]
Silver thiogallate	$AgGaS_2$	AGS	$2 - 11$	BPM	[320]
Gallium arsenide	GaAs	GaAs	$2.3 - 12$	QPM	[321, 322]
Gallium selenide	GaSe	GaSe	$3.3 - 19$	BPM	[323–325]

Table 4.1: Summary of the key materials used for DFG mid-IR generation [244, 245, 285].

Initially, the periodically poled materials were produced by forming a stack of thin crystal slices where every other layer was inverted by 180° to reverse the crystal's optical axis [309]. Contemporary techniques make use of electric field poling methods, in which a periodic electrode is lithographically etched onto the surface of the crystal and then subjected to a large electric field ($\sim 10 - 100$ kV mm^{-1}), inverting the sign of the susceptibility in the domain of the electrode [310]. Despite advances in the manufacturing processes, it is still hard to create perfectly homogeneous regions within the periodically poled materials, and any imperfections in the QPM grating may decrease its conversion efficiency [307].

Nonetheless, several periodically poled non-linear crystals are now commercially available owing to their well established fabrication technologies and the relatively low cost of the required materials. Periodically poled lithium niobate (PPLN) was the first widely used ferroelectric oxide crystal and remains the most popular today, though others such as periodically poled lithium tantalate (PPLT), potassium titanyl phosphate (PPKTP) and potassium titanyl arsenate (PPKTA) are also used. These four crystals represent the most mature quadratic non-linear materials and each of them can be pumped at 1 μm by advanced solid-state lasers, allowing for the generation of light in the $2 - 4.5$ μm range. For longer wavelengths, more unusual materials, in conjunction with more uncommon pump sources emitting above 2 μm, are required, though many of these substances are not suitable for QPM as the introduction of periodic poling into the material is too difficult, meaning BPM must be implemented instead. Table 4.1 summarises some of the main materials available.

PPLN is often used for QPM-DFG applications as it is transparent over the $0.3 - 5.5$ μm range and its d_{33} component is the largest of the ferroelectric oxide crystals [244, 298]. Furthermore, relatively long PPLN crystals are available and it has a high photorefractive damage threshold which can be increased by magnesium oxide doping [326].

4.2.5 Conversion efficiency

In previous sections, it has been assumed that the interacting waves are plane waves, with wavefronts taking the form of infinite, planar, equiphase surfaces perpendicular to the direction of propagation. The use of a plane wave as the trial solution to the wave equation for a DFG process (Equation 4.19) resulted in a conversion efficiency dependent on Δk and dominated by a sinc^2 term, with a maximum at $\Delta k = 0$ (Equation 4.26, Figure 4.5).

In reality, laser sources tend to have Gaussian beam profiles, as discussed in Section 1.2.2.1 and Appendix A [10, 166]. When focused Gaussian beams interact with a non-linear material, the irregular longitudinal and transverse phase distributions of these waves introduce departures from the traditional collinear plane wave situation. As the properties of the wavefronts vary with the distance travelled in the propagation direction, and also differ from those of a plane wave, it can be presumed that the optimal phase matching condition is no longer $\Delta k = 0$ [327].

A variety of mathematical approaches for the treatment of DFG interactions using focused Gaussian beams have been proposed [314, 328–330], but the formalism offered by Borri *et al.* [331] as a generalisation of the theory of Chu and Broyer [332] is adopted here. This model uses the first MKS unit system as outlined in Section 4.2.1.1 (though expressions in alternative unit systems are also available [289]) and gives the output idler power as:

$$P_i = \frac{32\pi^2 d_{\text{eff}}^2}{\epsilon_0 c n_i \lambda_i^2 (n_s\lambda_p + n_p\lambda_s)} L_{\text{crys}} P_p P_s \times h(\xi, \sigma, \mu, \alpha, L_{\text{crys}}) \tag{4.36}$$

where P is the power, the subscripts p, s and i refer to the pump, signal and idler radiations, respectively, and h is the focusing function, with other variables and constants as previously designated in the Nomenclature. The focusing function is defined as:

$$h(\xi, \sigma, \mu, \alpha, L_{\text{crys}}) = \frac{\mathrm{e}^{-\alpha L_{\text{crys}}/2}}{4\xi} \int_{-\xi}^{\xi}\int_{-\xi}^{\xi} \frac{\mathrm{e}^{-\mathrm{i}\sigma(\tau-\tau')+\alpha L_{\text{crys}}(\tau+\tau')/4\xi}}{1+\tau\tau'-\mathrm{i}\frac{1+\mu^2}{1-\mu^2}(\tau-\tau')}\mathrm{d}\tau\mathrm{d}\tau' \tag{4.37}$$

where α is the absorption coefficient of the material at λ_i and the dimensionless quantities ξ, μ and σ are given by:

$$\xi = \frac{L_{\text{crys}}}{b} \tag{4.38}$$

$$\mu = \frac{n_s\lambda_p}{n_p\lambda_s} \tag{4.39}$$

$$\sigma = -\pi b\left(\frac{n_p}{\lambda_p} - \frac{n_s}{\lambda_s} - \frac{n_i}{\lambda_i} - \frac{1}{\Lambda}\right) \tag{4.40}$$

$$= -\frac{b}{2}\Delta k_{\text{QPM}} \tag{4.41}$$

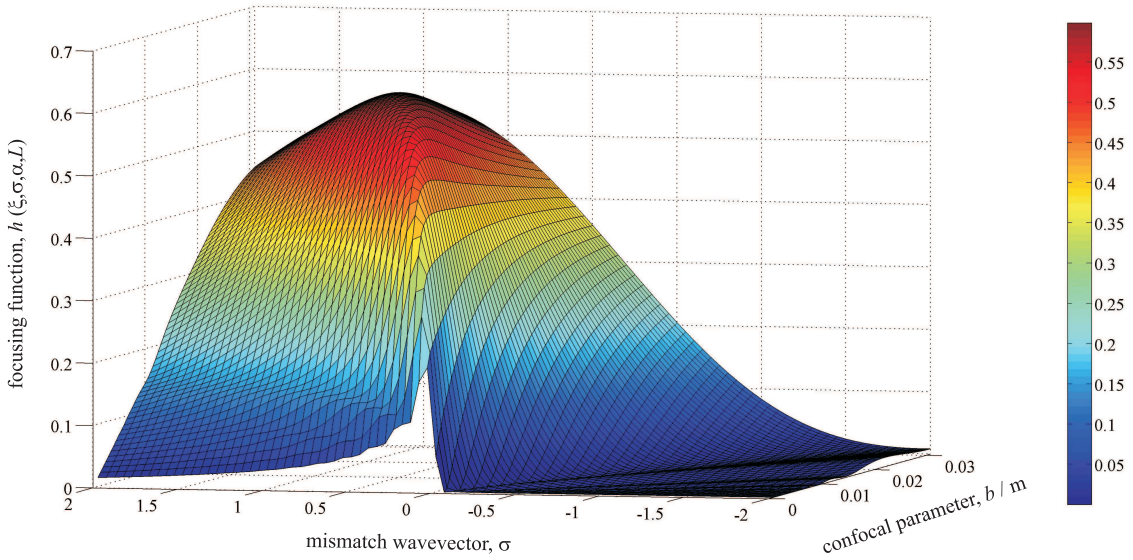

(a) 3D plot

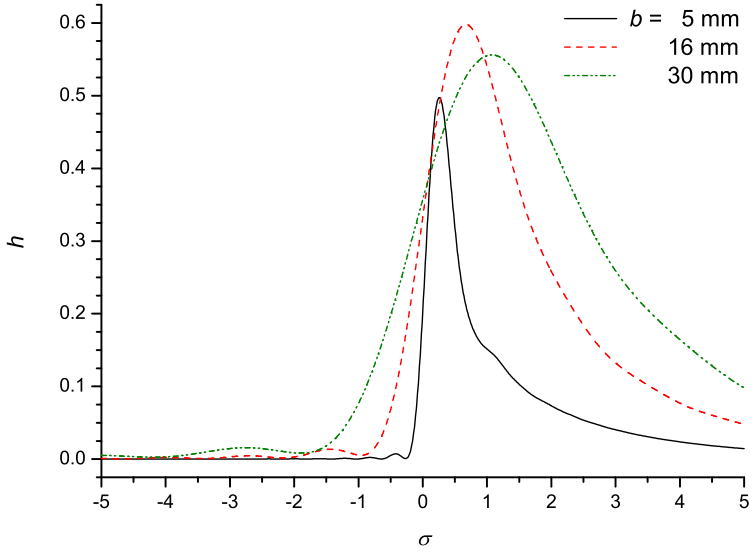

(b) Cross-sections

Figure 4.9: An example numerical evaluation of the focusing function, h, as a function of the mismatch parameter, σ, and the confocal parameter, b, for experimental conditions of $\lambda_p = 1064.32$ nm, $\lambda_s = 1558.49$ nm, $L_{\text{crys}} = 40$ mm and $\alpha = 0.001$ cm^{-1}. (a) 3D plot reproduced from Ciaffoni [333]. (b) Cross-sections of h at selected values of b.

and where b is the confocal parameter (Figure A.2) and can be regarded as the longitudinal extent of the region in which the waves interact in the crystal.

Equation 4.41 relates the phase mismatch parameter, σ, to the more conventional wavevector mismatch, Δk_{QPM}. Simulations of h can be performed in order to find the values of b and σ that maximise h and hence the idler output power (Figure 4.9). In performing such calculations, the temperature dependence of the refractive indices, crystal length and

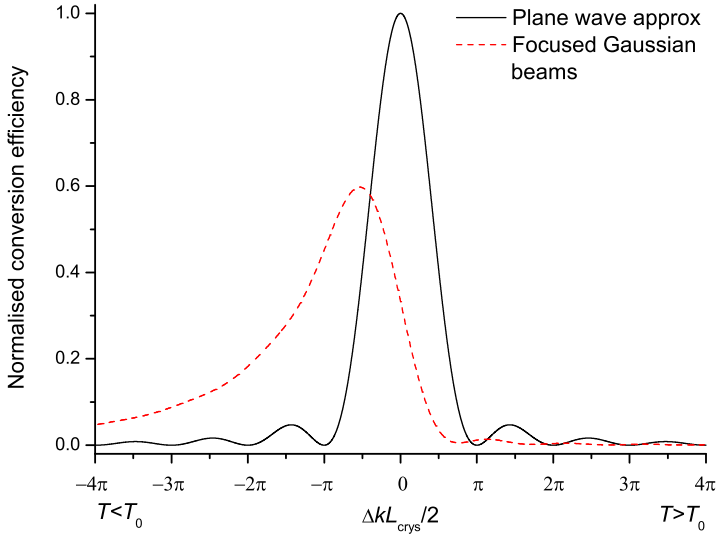

Figure 4.10: The conversion efficiency curves for the collinear plane wave and focused Gaussian wave regimes. Increasing $\Delta k L_{\text{crys}}/2$ also corresponds to increasing temperature, T, and decreasing signal wavelength, λ_s, as can be deduced from Equation 4.28 and knowledge of the temperature dependence of n (Equation 4.44). T_0 represents the theoretical temperature at which the DFG interaction is optimised for the plane wave approximation.

poling period must be taken into account [302, 334]. It is found that, regardless of the value of b, the peak of h always occurs at a positive value of σ, which differs from the normal phase matching condition of $\sigma = 0$. This is highlighted in Figure 4.9(b), which also shows that the highest possible value of h can only be reached by one value of b, b_{opt}, and deviations from this value change the shape of the efficiency curve. This optimum case is a compromise between using tightly focused beams, which enhances the field intensity at the centre of the crystal but at the cost of reducing the interaction distance (*e.g.* $b = 5$ mm), and having a softer focus, which ensures a longer, but weaker, interaction between the waves (*e.g.* $b = 30$ mm).

The optimal focusing condition occurs when the confocal parameters for each field are identical and equal to this optimal b value, *i.e.* $b_p = b_s = b_i = b_{\text{opt}}$. The beam waist, w_0, for each beam can be related to this confocal parameter by:

$$b_{\text{opt}} = \frac{2\pi n_m \omega_{0,m}^2}{\lambda_m} \tag{4.42}$$

where $m = p, s, i$. Thus the best focusing scheme for the incident beams can be found using beam propagation studies and ray transfer matrix analysis (Appendix A) to give beam waists at the centre of the crystal corresponding to the b_{opt} value, so maximising h and the DFG conversion efficiency.

Figure 4.10 is a comparison of the conversion efficiencies of the plane wave and Gaussian beam schemes. It is seen that with focused Gaussian beams, the maximum obtainable

conversion efficiency value is lower than that achievable under the plane wave approximation and that this occurs at negative Δk values. Furthermore, an asymmetric broadening of the profile is observed when $\Delta k < 0$, meaning a greater range of temperatures and wavelengths provide an acceptable conversion efficiency.

In situations when the beams are weakly focusing and diffraction effects can be neglected, the near field approximation can be applied such that $\xi \to 0$ and so $h \to \xi$. Equation 4.36 can thus be reduced to [288, 289, 335]:

$$P_i = \frac{4\omega_i^2 d_{\text{eff}}^2}{\pi\epsilon_0 c^3 n_p n_s n_i} \frac{L_{\text{crys}}^2}{w_{0,s}^2 + w_{0,p}^2} P_p P_s \tag{4.43}$$

which again follows the first MKS unit system convention as outlined in Section 4.2.1.1.

4.3 Experimental QPM-DFG Systems

Since their first experimental demonstration [288], a huge variety of DFG-based mid-IR laser sources have been reported, driven by demand from a wide range of applications and made feasible by the availability of new lasers and improved non-linear materials.

In order to efficiently produce mid-IR radiation by DFG, careful consideration must be given to the non-linear material and laser sources to be used. The optimal choices for these will vary depending on the experimental priorities and the requirements of any potential applications, and concern properties such as output power, operating wavelengths and spectral tunability. High output powers are often desirable for sensitive spectroscopic studies, which can be achieved by using powerful laser input sources and materials with large non-linear conversion efficiencies; however, pump depletion may limit the maximum output intensity and the use of very high pump intensities can lead to the occurrence of other, competitive non-linear processes [336]. At least one input laser is usually selected to be widely tunable to yield a broad spectral coverage in the mid-IR; this then requires a periodically poled crystal with several different poling periods on multiple tracks, along with a mechanism for its temperature tuning, to allow access to the full potential wavelength range. Additionally, the spectral linewidth of the DFG output is a convolution of the pump and signal linewidths, which has implications for high resolution spectroscopic work in which narrow linewidths are essential.

In this work, radiation at ~ 3 μm was desired for the reasons outlined in Section 1.1.3. PPLN was selected as the mixing crystal as it is the best dielectric medium for this wavelength range. Commercial telecom-type diode lasers, using optically pumped amplifiers to boost their typically low power outputs, were initially chosen as the radiation sources,

rather than more powerful dye or Nd:YAG lasers, as this meant a relatively inexpensive, compact and tunable DFG system could be created; however, the use of different laser sources was also explored in later work (Section 5.4, Chapter 6).

Two possible PPLN-based QPM-DFG strategies that can be used to generate light at 3.3 μm are a free-space system using bulk PPLN [94, 337, 338] or a fibre-coupled system using a waveguide PPLN module [312, 339–341]. Using a bulk PPLN crystal has the advantages of being able to utilise high total input powers ($0.1 - 3$ W) and the ability to change the poling period of the multi-grating crystal to give wide mid-IR tunability (> 200 nm), but such schemes typically achieve only low conversion efficiencies ($0.01 - 0.05\%$ $W^{-1}cm^{-1}$) and hence low idler powers ($10 - 400$ μW). In waveguide systems, however, higher conversion efficiencies are possible ($1 - 40\%$ W^{-1}) [342] as the interacting fields are overlapped more efficiently, allowing greater output powers to be generated (up to 15 mW) [341]. A fibre-coupled system is also flexible, portable and more robust. On the other hand, the fixed poling period of the waveguide PPLN crystal results in a narrow mid-IR wavelength range (~ 20 nm), so limiting the detection of species to a smaller spectral window. In addition, the beam quality of the mid-IR light tends to be poor [343] with far field diffraction patterns and 'Airy like' rings [341] due to the presence of wavefront aberration [344], which is a problem when it is desired to combine this radiation with optical cavities.

One of the aims of this thesis was to use the mid-IR produced by DFG as a laser source for CRDS; another was to obtain an extended mid-IR wavelength coverage. Considering these objectives and the factors outlined above for the two different QPM-DFG strategies, a free-space system using a bulk PPLN multi-grating crystal was deemed preferable in order to achieve a high beam quality to aid in the fulfilment of the CRDS requirement for high efficiency coupling into a single mode of an optical cavity, and also to offer the desired wavelength flexibility via a range of possible poling periods.

4.3.1 Free-space QPM-DFG set-up

The experimental set-up of the QPM-DFG free-space system to generate mid-IR is shown in Figure 4.11. Most of the work for its design and development has already been reported [333], though it is summarised again here.

The signal laser source was either a 1560 nm pigtailed DFB diode laser or the DS-DBR laser; the use of the latter is discussed fully in Section 6.1. The 1560 nm DL (*JDS Uniphase*, CQF474/708-19220) offered a wavelength range of $1558.5 - 1561.5$ nm via temperature and current tuning and a linewidth of 1 MHz, with an output power at the end of a PM fibre of 23 mW. It was housed in a butterfly package mount (*Newport*, 744TEC) and controlled by commercial temperature (*Thorlabs*, TED200C) and current (*Thorlabs*, LDC205C) drivers.

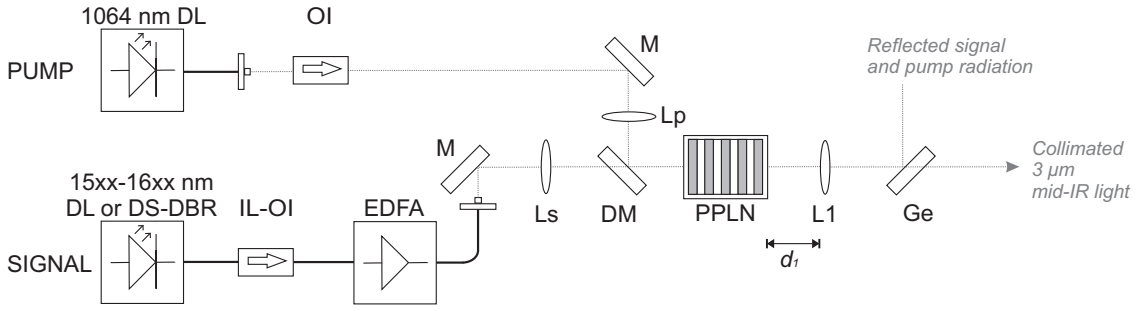

(a) Schematic

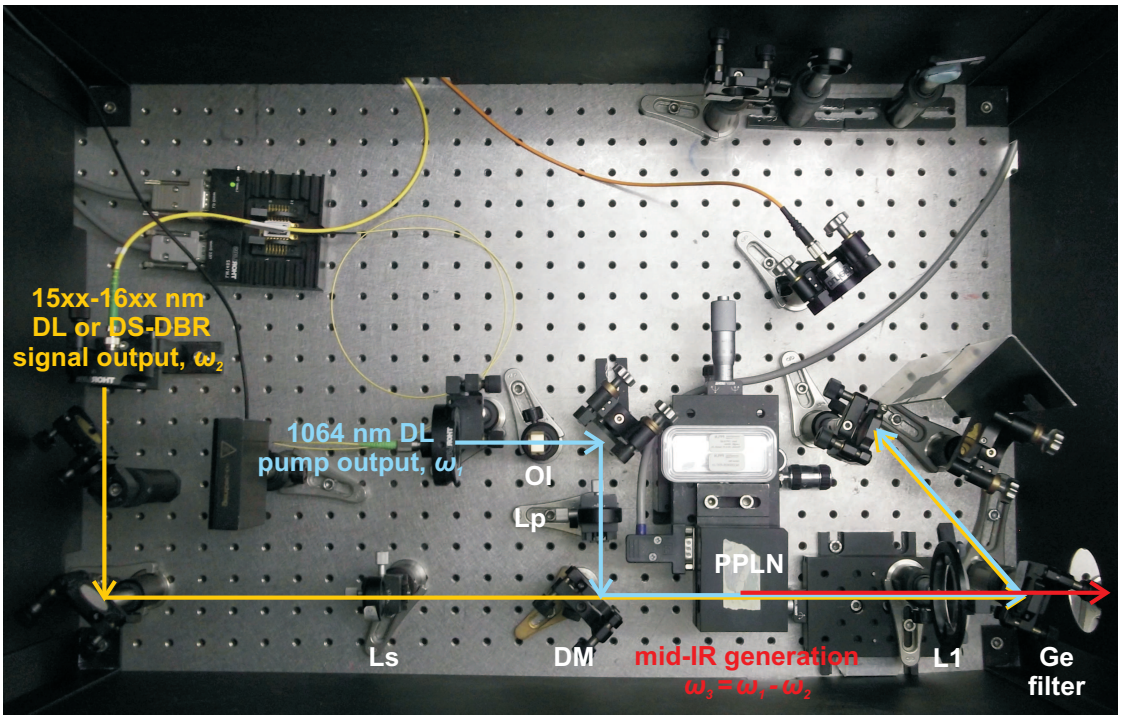

(b) Photo

Figure 4.11: A (a) schematic and (b) photo of the experimental set-up for the mid-IR DFG free-space system. The 15xx − 16xx nm signal light from either a DL (or DS-DBR, see Chapter 6) is combined with the 1064 nm pump radiation in the PPLN crystal to generate mid-IR light. The remaining pump and signal radiation is reflected by the germanium filter into a beam dump or wavemeter, leaving a ray of mid-IR light. OI: optical isolator; IL-OI: in-line optical isolator; Ls, Lp, L1: lenses; DM: dichroic mirror; d_1: distance between PPLN and L1.

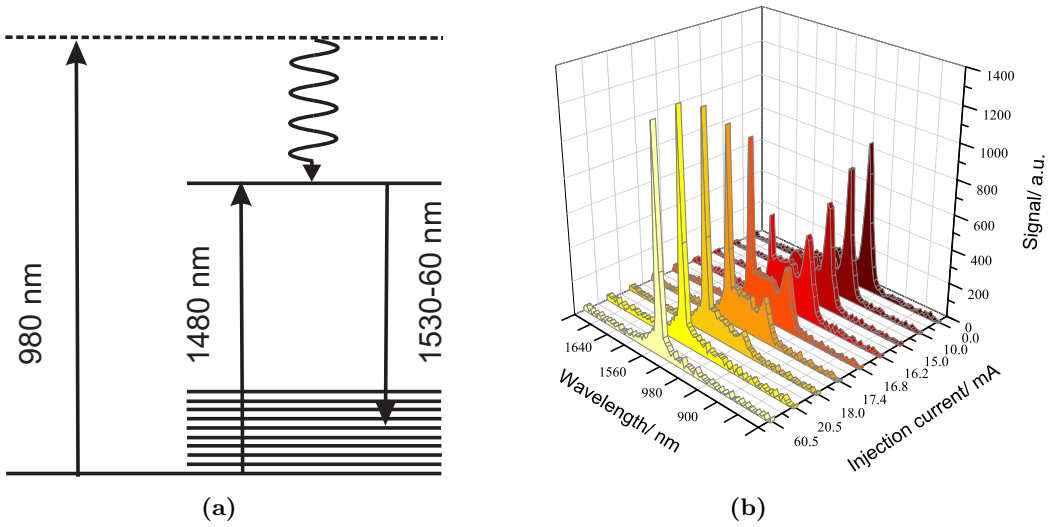

Figure 4.12: (a) The energy level diagram for an EDFA pumping scheme. (b) The output of the EDFA seeded at 1560 nm as a function of injection current of the input signal radiation.

This light passed through a double stage fibre optic in-line isolator (*Newport*, F-ISO-D-2-P), which had a peak isolation of 52 dB at 1550 nm and an operating bandwidth of $1520 - 1580$ nm, to avoid back reflection into the laser, and then entered an erbium doped fibre amplifier (EDFA).

A fibre amplifier is an optical amplifier which uses an optical fibre as a gain medium. Generally, the signal to be amplified co-propagates with light from a pump laser (which is at a significantly different wavelength to the signal input) through the fibre core, though some fibre amplifiers work using a counter-propagation pumping scheme [345] or a mixture of the two [346–348]. The pump laser excites the dopant ions into a higher energy level from which they decay via stimulated emission triggered by a photon at the signal wavelength, thereby causing new photons to be emitted at this wavelength travelling in the same direction with the same phase: thus the signal radiation is amplified. In the case of an EDFA, the gain medium is a glass fibre doped with rare earth erbium ions and two pump lasers operating at 980 nm and 1480 nm are used to amplify signals in the 1550 nm region. The energy level diagram can be depicted as a quasi-three-level system (Figure 4.12(a)). The high powers of the pump lasers are able to amplify a weak input signal to output intensities of $10 - 30$ dBm ($10 - 1000$ mW). However, as well as amplifying the signal radiation, light produced by spontaneous emission is also amplified. This generates incoherent, broadband, randomly polarised optical radiation called amplified spontaneous emission (ASE), which increases the noise and decreases the amplifier gain. The gain and noise level depend strongly on the power of the signal input, pump laser power, fibre length and erbium ion density, but it has

been demonstrated that, if supplied with sufficient pump power, the EDFA can operate in a saturation regime with maximum gain and a suppressed noise level [349].

Here, a C-band EDFA (*Nuphoton Technologies*, NP2000-C4-PR-B25-1200-FCA-01) was used. It was designed to give saturated output power in the $1530 - 1560$ nm region of up to 400 mW for input powers of less than 25 mW, though it was found experimentally that a threshold input power of 1.5 mW was required and that the signal was only amplified to ~ 250 mW. Investigations into the performance of the EDFA were conducted by dispersing the output beam using a diffraction grating and measuring the results with an IR camera (*Electrophysics*, MicronViewer 7290A) [333]. On increasing the injection current (and hence the power and wavelength) of the 1560 nm input radiation, a change was seen in the spectral width and peak height of the output: the ASE and 980 nm pump 'spike' were diminished and the output at the desired signal wavelength was increased and narrowed (Figure 4.12(b)).

The pump source was a single-mode fibre-coupled 1064 nm DL (*Lumics*, LU1064M150) with a linewidth of 30 MHz, spectral coverage of ± 1 nm and an output power of 140 mW. The laser module was installed in a 14 pin butterfly laser diode mount (*Thorlabs*, LM14S2) with commercial temperature (*Thorlabs*, TED200C) and laser (*Thorlabs*, LDC205B) controllers. However, this device suffered from poor continuous tunability, with only narrow (~ 1 GHz) mode-hop free spectral windows. Because of this, the pump radiation was kept at a constant wavelength of 1064.3 nm and tuning in the mid-IR achieved by varying the wavelength of the signal laser; this allowed access to idler wavelengths between $3342.5 - 3356.4$ nm ($2979.4 - 2991.7$ cm^{-1}). The pump radiation was passed through a 48 dB optical isolator (*OFR*, IO-2.5-1064-VLP) and then directed and focused by several optical elements onto the PPLN. In other, later experiments, this pump laser was occasionally replaced with a higher power (500 mW), single-mode Nd:YAG laser (Section 5.4).

The PM fibres which guided the signal and pump laser outputs were connected to suitable fibre couplers held in rotation mounts which were adjusted to optimise the polarisation axes for difference frequency mixing. Both beams were focused using anti-reflection (AR) coated, plano-convex lenses with focal lengths and distances chosen to maximise spatial overlap along the PPLN crystal and so also the DFG conversion efficiency, as discussed in Section 4.2.5; details are given in Table 4.2 [333].

The two input beams were combined with a dichroic mirror (*Edmund Optics*) and their precise overlap established before entering the PPLN crystal. The AR coated, 4 cm long PPLN crystal (*Stratophase*, OPO3-40) contained 8 tracks, each with cross-sectional dimensions of 0.5×0.5 mm^2, with grating periods ranging from $29.5 - 31.5$ µm in 0.25 µm steps. The crystal was mounted in a temperature stabilized oven (*HC Photonics*, TC038) which allowed the temperature to be tuned in steps of 0.1°C and controlled the crystal temperature via resistive heating to within ± 0.5°C of that set. The crystal and oven were fixed on a

Radiation	λ/ nm	w_{far}/ mm	w_0/ µm	f/ mm	d/ mm
p	1064.32	1.2	35	119	111
s	1558.49	1.8	42	148	140
i	3356.60	1.8	42	71	61

Table 4.2: Results for the optimal focusing optics for the pump and signal beams into the PPLN crystal. The values of the collimated spot sizes for the beams before the focusing optics, w_{far}, were measured with an IR camera. The mathematical simulations of h for these experimental conditions, calculated using Equation 4.37, are shown in Figure 4.9 and returned a maximum value of $h = 0.6$ at $b = 16$ mm. For this value of b, the beam waists, w_0, required at the centre of the PPLN crystal for the pump and signal beams were deduced using Equation 4.42, and the idler beam waist set equal to the maximum of these. The strength and positions of the lenses (Ls and Lp in Figure 4.11) needed to focus the beams to these beam waists were calculated using ray transfer matrix analysis (Appendix A). f and d refer to the focal length and distance before the crystal, respectively [333].

3D translation stage with micrometer controls in order to allow selection of the appropriate PPLN track and to ensure that the beams passed fully though this track.

The three beams exiting the PPLN crystal were collected by a 50 mm diameter, calcium fluoride (CaF_2) plano-convex lens (*Crystran*, CAF50LENS135) with a focal length of 13.5 cm. By setting the distance d_1 in Figure 4.11(a) as 12.80 cm, a collimated idler beam of spot size 1.80 mm was generated (Section 5.2.2). An AR coated Ge filter (*Edmund Optics*, 62643), with a transmittance of 73% at 3.2 µm, reflected the pump and signal radiation into a wavemeter (*Burleigh*, WA-1000), allowing the vacuum wavelengths of the signal and pump lasers to be monitored, leaving the mid-IR radiation ready for study or experimental use.

The mid-IR light was measured by focusing the radiation with a CaF_2 lens (*Crystran*) onto a 2-stage thermoelectrically cooled HgCdZnTe photodiode (MCZT-PD) detector, optimised for the $3 - 4$ µm spectral range and with a 1 mm^2 active area, which was coupled with a low bandwidth (100 kHz) pre-amplifier (*Vigo Systems*, PVI-2TE-4/VPDC-0.1l).

4.3.2 PPLN parameters: poling period and temperature

The values of the PPLN temperatures and poling periods (at the reference temperature of 25°C) required for DFG at the wavelength ranges of the laser sources used in this work were found by solving Equation 4.34 for the case of perfect phase matching. The pump wavelength was fixed at 1064.3 nm and the signal wavelength varied over $1555 - 1615$ nm, representing the range accessible with the DFB and DS-DBR lasers used as signal sources in this thesis. The results, shown in Figure 4.13, indicated that poling periods in the range $29.85 - 30.7$ µm and PPLN temperatures of $25 - 85$°C would be necessary to access the full potential idler wavelength range of $3100 - 3400$ nm. However, due to the limited, defined

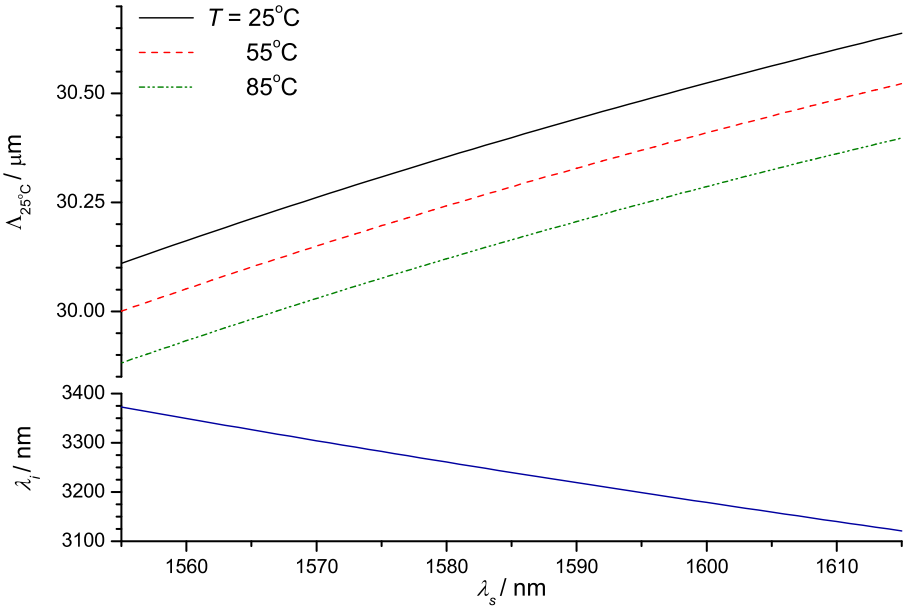

Figure 4.13: Calculated idler wavelengths and the required poling periods for optimal DFG efficiency at various PPLN temperatures over the range of signal wavelengths accessible in this work, $\lambda_s = 1555 - 1615$ nm, at fixed $\lambda_p = 1064.3$ nm.

poling periods of the PPLN crystal, only Λ of 30.00 μm, 30.25 μm and 30.50 μm could actually be used, though this still provided enough flexibility for good mid-IR generation. In order to perform these calculations, the temperature dependence of the refractive indices and the length of the poling period had to be taken into account. The extraordinary refractive index for $LiNbO_3$ at wavelength λ_m (where $m = p, s$ and i for the pump, signal and idler radiations, respectively) and temperature T is given by the Sellmeier equation [302]:

$$n_m^2 = a_1 + b_1 f + \frac{a_2 + b_2 f}{\lambda_m^2 - (a_3 + b_3 f)^2} + \frac{a_4 + b_4 f}{\lambda_m^2 - a_5^2} - a_6 \lambda_m^2 \tag{4.44}$$

where the a and b coefficients are listed in Table 4.3 and $f = (T - 24.5)(T + 570.82)$ with T in °C. The true length of the poling period, Λ, at the temperature T is related to its length at the reference temperature of 25°C, $\Lambda_{25°C}$, by [334]:

$$\Lambda = \Lambda_{25°C} \left[1 + \alpha(T - 25) + \beta(T - 25)^2\right] \tag{4.45}$$

where $\alpha = 1.54 \times 10^{-5}$ K^{-1}, $\beta = 5.3 \times 10^{-9}$ K^{-2} and T is once again in °C.

When the 1560 nm DFB laser was used as the signal source, the 30.00 μm poling period was employed. The optimum PPLN temperature was determined by performing temperature tuning experiments, where the mid-IR power generated was measured as a function of crystal temperature for constant λ_p and λ_s. These powers were found by converting the voltage signal of the mid-IR radiation recorded with the MCZT detector, which had a known responsivity of 9.02 ± 1.80 μWV^{-1} at 3.3 μm with 1 MΩ impedance. The results

Parameter	Value	Parameter	Value
a_1	5.35583	b_1	4.629×10^{-7}
a_2	0.100473	b_2	3.862×10^{-8}
a_3	0.20692	b_3	-0.89×10^{-8}
a_4	100	b_4	2.657×10^{-5}
a_5	11.34927		
a_6	0.015334		

Table 4.3: The a and b coefficients for the Sellmeier equation (Equation 4.44) to describe the temperature dependence of the extraordinary refractive index in $LiNbO_3$ [302].

of such a temperature tuning curve for $\lambda_p = 1064.295$ nm and $\lambda_s = 1560.244$ nm are shown in Figure 4.14(a). The shape of the curve resembled the conversion efficiency curve calculated for focused Gaussian beams (Figure 4.10), and indicated that the optimum crystal temperature, T_{opt}, necessary for maximum DFG conversion efficiency was 83.1°C with a temperature acceptance bandwidth of 7°C (FWHM). It was also found that for the $1558.5 - 1561.5$ nm signal wavelength range, $T_{\text{opt}} = 78.6 - 86.2$°C. These temperatures are approximately 15°C higher than those predicted by solving Equations 4.34, 4.44 and 4.45 for perfect phase matching.

The experimental results of Figure 4.14(a) were translated into the Δk domain and then compared with those of a theoretical curve simulated using Equation 4.36 for the same experimental conditions (Figure 4.14(b)). The experimental maximum did not occur in the negative $\Delta k_{\text{QPM}} L_{\text{crys}}/2$ region as predicted by theory, but instead at a displacement of $+9.5\ \Delta k_{\text{QPM}} L_{\text{crys}}/2$ units. This positive shift is a common feature among such tuning curves [333, 340] and is possibly due to the inaccuracies in the quoted poling period of the PPLN crystal and/or a misreporting of the true crystal temperature by the thermistor. Indeed, in order to shift the experimental peak position to overlay that of the simulation, a decrease in $\Lambda_{25^\circ\text{C}}$ of just 70 nm is required, which is of the same order of magnitude as the uncertainty in the grating as reported by the manufacturer (±10 nm). There is also a big discrepancy in the peak height between the theoretical and experimental results. This is likely to be caused by non-ideal spatial and spectral beam qualities, inefficient spatial overlap within the PPLN crystal and disparities between the numerically estimated optimal values for b and w_0 and those actually used. However, such magnitude deviations from the expected idler powers are commonly observed (references in Table 4.4).

4.3.3 Output power

The pump and signal powers incident on the PPLN crystal were measured as 66 mW and 213 mW, respectively, using a power meter (*Gentec-EO*, SOLO 2). These input powers

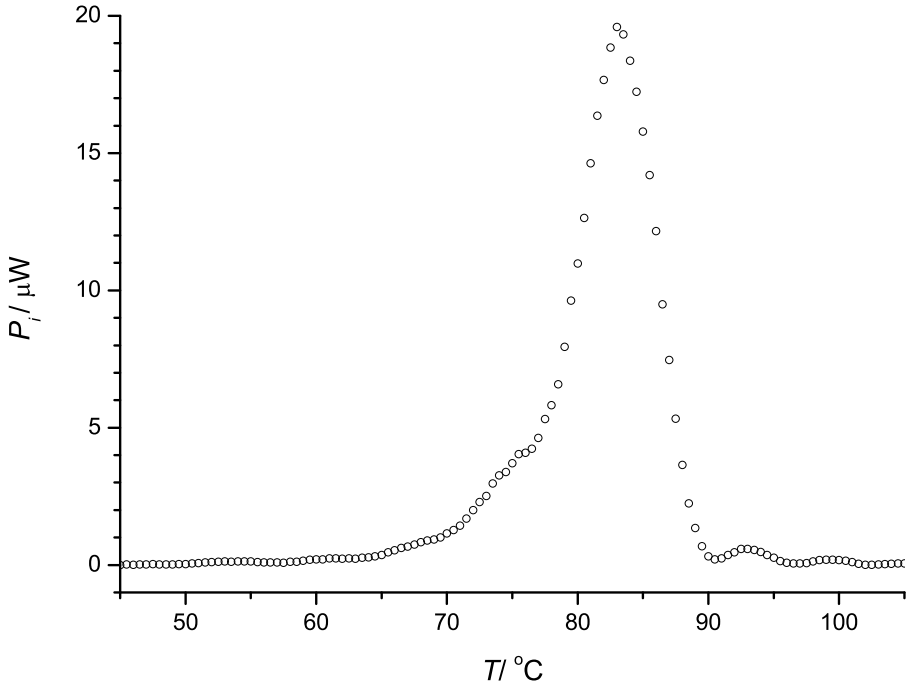

(a) Experimental data

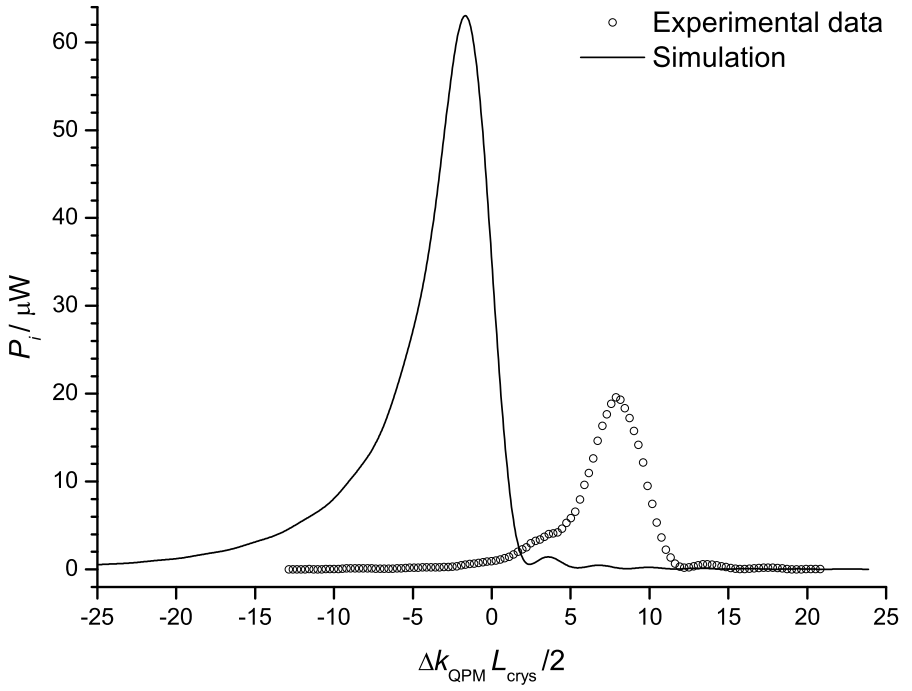

(b) Experimental data and simulation

Figure 4.14: (a) Temperature tuning curve recorded at $\lambda_p = 1064.295$ nm, $\lambda_s = 1560.244$ nm and $\Lambda = 30.00$ µm, indicating an optimal crystal temperature of 83.1°C. (b) Translation of this experimental data into the Δk domain for comparison with the theoretical simulation.

Pump	λ_p / nm	P_p / mW	Signal	λ_s / nm	P_s / mW	λ_i / µm	P_i / µW	L_{crys} / mm	η / % $W^{-1}cm^{-1}$	Reference
DBR+YDFA	1083	600	ECDL	840	25	3.8	12	20	0.040	[352]
DBR+YDFA	1064	800	DFB+E/YDFA	1550	260	3.4	220	19	0.056	[353]
DBR+YDFA	1083	1600	DFB+EDFA	1561	500	3.5	640	19	0.042	[19]
ECDL	808	20	Nd:YAG	1064	660	3.4	27	50	0.041	[94]
DL	850	78	Nd:YAG+YDFA	1064	3830	4.2	170	40	0.014	[331]
Nd:YAG	1065	217	DFB	1560	50	3.4	19	30	0.057	[354]
ECDL+YDFA	1050	550	EFL	1560	3900	3.2	3500	50	0.033	[311]
ECDL+MOPA	820	980	Nd:YAG	1064	180	3.4	280	50	0.035	[148]
Ti:sapphire	827	200	Nd:YAG	1064	400	3.7	48	40	0.015	[355]
ECDL	820	3.5	Nd:YAG	1064	1700	3.6	10	50	0.034	[338]
DBR	1064	74	DFB+EDFA	1560	229	3.3	29	40	0.043	[333]
DBR	1064	66	DFB+EDFA	1560	213	3.3	19.6	40	0.035	$*$

Table 4.4: A comparison of the conversion efficiencies for reported free-space QPM-DFG systems in the 3−4 µm region from 2000-present. The references are ordered chronologically with $*$ referring to this work. YDFA: ytterbium doped fibre amplifier; MOPA: master oscillator power amplifier; EFL: erbium fibre laser.

predicted a theoretical mid-IR power of 63 µW for this DFG set-up, estimated using Equation 4.36 with $h = 0.59$, as associated with the optimum focusing conditions adopted in this experiment, and $d_{\text{eff}} = d_{33}(2/\pi)M_{ij} = 14.4$ pmV^{-1}, as resulting from a first order QPM interaction accessing the PPLN d_{33} coefficient (Equation 4.31), where $d_{33} = 27.2$ pmV^{-1} [293] and $M_{ij} = 0.85$ is the Miller factor for the DFG process using these pump and signal lasers [94, 350, 351].

Experimentally, the effective mid-IR power generated was measured as 19.6 µW. This indicated an overall DFG conversion efficiency of 0.035% $W^{-1}cm^{-1}$, calculated according to:

$$\eta = \frac{P_i}{P_p P_s L_{\text{crys}}} \times 100\% \tag{4.46}$$

which is a typical performance for this configuration (Table 4.4), though this power output is still much lower than that offered by some other available mid-IR sources (Section 4.1).

4.4 Conclusions

In this chapter, various mid-IR laser sources were discussed and the technique chosen to generate mid-IR light in this work, DFG, explored in depth. In order for efficient DFG conversion to take place, phase matching conditions must be satisfied; this can be realised experimentally by the methods of BPM or QPM, with the latter requiring the use of periodically poled materials, such as PPLN, in which the phase of the non-linear polarisation is periodically reversed in order to maintain a coherent build up of the non-linear interaction.

The experimental free-space QPM-DFG system using a bulk PPLN crystal which was constructed in this work was then described and characterised. The system provided tens of μW of power across the $3.1-3.4$ μm wavelength range at a conversion efficiency of 0.035% $W^{-1}cm^{-1}$, which is a typical performance for such a free-space arrangement. This radiation was used to perform the mid-IR spectroscopy chronicled in the remainder of this thesis.

Chapter 5

CRDS and QPM-DFG for Mid-Infrared Spectroscopy

By marrying the use of the mid-IR region of the spectrum and enhanced detection techniques, highly sensitive spectrometers, capable of multi-component detection and high selectivity, can be constructed. Whilst there are many examples in the literature of using mid-IR light from a range of different sources with a variety of spectroscopic techniques for gas sensing applications, there are relatively few examples involving the coupling of mid-IR radiation into an optical resonator. This chapter therefore begins with a review of the current state of cw cavity-based mid-IR spectroscopy before reporting on the 3 μm diode laser-based DFG CRD spectrometer created in this work by combining the mid-IR radiation source described in Section 4.3 with the CRDS system developed in Section 3.1. The results of its use in spectroscopic studies of methane, deuterium and acetone are presented, demonstrating its suitability for sensitive trace gas sensing. Having established this viability, further enhancements to increase the sensitivity of the system were then sought, and the alterations made in order to achieve this objective are reported and the improved set-up characterised.

5.1 Cavity-Based Mid-Infrared Spectroscopy

The literature is rife with examples illustrating the use of all the different mid-IR laser sources outlined in Section 4.1 with a whole range of different spectroscopic techniques, from simple direct absorption measurements to heterodyne methods or the use of multi-pass cells. However, there are comparatively few cases documented where the very long path lengths afforded by optical cavities are coupled with mid-IR light to perform spectroscopy. Presumably this is because such a feat is difficult given the typically low input

powers, relatively poor mirrors and noisy detectors available at these wavelengths, especially compared to those obtainable in the near-IR. Nevertheless, the potential benefits of the intrinsically higher levels of sensitivity and selectivity offered in the mid-IR, as discussed in Section 1.1.3, make this a strategy worthy of investigation. Some of the major examples of the successful coupling of mid-IR radiation and cavity-based spectroscopy are described below and summarised in Table 5.1.

CEAS is perhaps the easiest cavity-based method to implement, and has been favourably combined with various QCL sources by Tittel and co-workers. For example, a liquid N_2 cryogenically cooled cw DFB QCL operating at 5.2 μm with ~ 20 mW power was coupled into a cavity with an effective path length of 0.67 km to perform CEAS on nitric oxide (NO) [356–358]. The laser frequency was tuned over $1918 - 1923$ cm^{-1} in 0.5 cm^{-1} steps by modulating the laser current and a NO detection limit of 10 ppb with a 15 s integration time achieved, though this was reduced to 2 ppb when the CEAS was combined with wavelength modulation. This laser source has recently been used in real-time, simultaneous monitoring of NO and CO_2 in exhaled breath [359]. Tittel and co-workers have also used other QCLs to detect NO by CEAS. These TEC cw DFB QCLs, which required additional water cooling to access the total tuning range, operated at 5.5 μm with output powers of 30 mW and were used to measure NO at 1835.6 cm^{-1} [360] and 1828.0 cm^{-1} [361] with detection limits of 3.2 ppb in 1 s and 3.6 ppb in 4 s, respectively, though the former detection limit was lowered when $2f$-WMS was integrated into the CEAS system.

Miller *et al.* have used a liquid N_2 cryogenically cooled cw DFB ICL to perform CEAS for formaldehyde (H_2CO) detection, with the aim of using the system for spacecraft and indoor air monitoring [362]. A H_2CO transition at 2832.485 cm^{-1} was studied at 50 Torr and yielded a detection limit of 150 ppb for a 3 s acquisition time. An OPO has also been used as a mid-IR laser source for CEAS by Harren and co-workers [74, 363]. This powerful (1.2 W) and tunable ($3 - 4$ μm) radiation source allowed ethane (C_2H_6) to be measured with a sensitivity of 50 ppt over a 0.25 s integration time at 2996.9 cm^{-1}, as well as permitting other species, such as H_2O, CH_4 and acetone ($(CH_3)_2CO$), to be observed. The last of these is a broadband absorber and was studied by tuning the laser wavelength over $2967 - 2973$ cm^{-1} to obtain a detection limit of 100 ppb with a 0.4 s integration period.

Another, lower power, type of tunable mid-IR laser source, based upon DFG, has been combined with CEAS by Grilli *et al.* [339]. In this case, a waveguide PPLN module was used to generate 260 μW of 3.2 μm light, tunable over 35 cm^{-1}, via DFG with two near-IR diode laser sources, and this light was used to perform CEAS to monitor ethene (C_2H_4) at low pressures (~ 2 Torr), achieving a sensitivity of $\alpha_{\min}(BW) = 1.6 \times 10^{-8}$ cm^{-1}Hz$^{-1/2}$. Such a device has applications in urban and industrial air monitoring. This DFG system has also been used in another resonant cavity technique, PS-CRDS, monitoring the same

ethene isotopologues at 3081 cm^{-1} and reporting a τ_0 of 5.09 ± 0.08 µs and an α_{min} of 1.4×10^{-7} cm^{-1} in 4 mins [364].

CRDS is a more challenging cavity-based technique, but this too has been used in conjunction with mid-IR laser sources. Mürtz and co-workers have used CO overtone lasers to perform CRDS at different regions in the mid-IR. Their first CO overtone laser operated between $2.6 - 4.1$ µm with output powers of $40 - 200$ µW and was used to study $^{13}CH_4$ [105, 119], ethane [146] and formaldehyde [99] at 3048.3 cm^{-1}, 3000.3 cm^{-1} and 2853.4 cm^{-1}, respectively. τ_0 values of $6 - 12$ µs were reported and studies were conducted on calibrated mixtures, ambient air and breath samples, though in the latter case a cooling trap was used to remove unwanted species. Investigations of the $^{13}CH_4/^{12}CH_4$ isotopic ratio were conducted by measuring the $^{13}CH_4$ and $^{12}CH_4$ transitions at 3048.3 cm^{-1} and 2947.8 cm^{-1}, respectively, yielding a CH_4 detection limit of 105 ppt over 20 s and an isotopic ratio accuracy of 11‰ [120]. The second CO overtone laser covered the $4.8 - 5.5$ µm wavelength range and the frequency modulated sidebands used provided powers at $10 - 40$ µW. The combination of this laser with CRDS achieved higher τ_0 values ($\sim$ 32 µs) and has been used to detect carbonyl sulphide (OCS) at 2039.0 cm^{-1} with a 7 ppt in 0.4 s detection limit in calibrated mixes, ambient air and breath samples [365], ^{14}NO and ^{15}NO at 1874.9 cm^{-1} with a 7 ppt in 70 s detection limit in exhaled nasal breaths [366] and ^{13}CO at 2012.2 cm^{-1} with a 7 ppb in 0.8 s detection limit in exhaled breath samples [367].

Paldus *et al.* have demonstrated the use of a QCL as a light source for CRDS [368]. A liquid He cooled cw DFB QCL operating at 8.5 µm with 16 mW power was used to monitor a transition of ammonia (NH_3) at 1177 cm^{-1}. The QCL could be tuned over 15 nm by means of temperature modulation, and the QCL CRDS set-up reported a τ_0 of 0.929 ± 0.002 µs. Different concentrations of NH_3 in N_2 were studied at standard temperature and pressure (stp), achieving α_{min} values of 1.8×10^{-8} cm^{-1} for single shot measurements and 1×10^{-9} cm^{-1} by averaging 600 spectra, yielding a NH_3 detection limit of 0.25 ppb in 1 s. Popp *et al.* have combined CRDS with an OPO laser source for ethane detection at 2990 cm^{-1} [369]. The $2.4 - 3.8$ µm, 200 mW radiation source was coupled into the 0.52 m cavity with a τ_0 of 13 µs. The spectrometer was tested by monitoring the stepwise reduction in the concentration of ethane in N_2 from 75 ppb to 0 ppb with flowing samples at a constant pressure of 75 Torr. An α_{min} of 1.2×10^{-9} cm^{-1} was observed in a 16 s integration time, corresponding to an ethane detection limit of 300 ppt in 16 s.

Ethane has also been investigated with CRDS using mid-IR light generated by QPM-DFG. Stry *et al.* produced 27 µW of radiation tunable over $3 - 3.6$ µm by mixing light from an ECDL ($794 - 820$ nm) and a Nd:YAG ring laser (1064 nm) in a bulk PPLN crystal, and coupled this into an optical cavity with $\tau_0 = 11.22 \pm 0.04$ µs, obtaining a sensitivity of 1×10^{-8} cm^{-1} over a 2 s integration period [94]. A $1f$ lock-in technique was also employed

to frequency stabilise the cavity resonances to the laser frequency. Studies of 100 ppb of ethane in N_2 at stp were performed at 3000 cm^{-1} with a 150 MHz resolution, and a detection limit of 1 ppb over a 2 s acquisition time attained. This system was improved in later work by the addition of an amplifier to the pump diode laser and the replacement of the signal source with a higher power Nd:YAG laser [148]. This resulted in an increase in the mid-IR power to 280 µW, which in turn lowered the ethane detection limit to 270 ppt in 1 s and the sensitivity to 8×10^{-9} $cm^{-1}Hz^{-1/2}$. A different ethane transition at 2983 cm^{-1} was measured and experiments on breath samples conducted, taking into account the presence of water.

Alternative resonant cavity-based methods have also been performed in the mid-IR. One such example is OF-CEAS [36], in which the laser is passively locked to the optical cavity resonance frequency to permit a greater intensity build up inside the cavity. The laser light is injected into a tilted confocal cavity and scanned through many cavity resonances. Part of the light is allowed to return to the laser from the resonator and this feedback, which is frequency selected by the cavity, forces the laser to emit at the cavity resonance frequency with a narrower laser linewidth, provided certain intensity and optical phase conditions are satisfied. Thus the coupling of light into the resonator is more efficient and the light intensity transmitted by the cavity is far larger than for normal CEAS. Conventional OF-CEAS uses a three-mirror V-shaped cavity [370], where a linear cavity is folded around a central mirror through which the laser beam is introduced at a non-normal angle of incidence, hence spatially decoupling the optical feedback beam from other reflections off the first cavity mirror. Romanini *et al.* have used this technique with RT cw DFB QCLs operating at 4.5 µm [371] and 5.6 µm [372]. In the first instance, the QCL was wavelength tuned by control of the laser temperature to study the nitrous oxide (N_2O) transition at 2242 cm^{-1} at low (50 mbar) pressures, achieving an $\alpha_{\min}$ of 3×10^{-9} cm^{-1} for 1 s averaging of spectra composed of 100 independent points, which corresponded to a N_2O detection limit of 35 ppt. CO_2 was also observed in this wavelength range with a 15 ppb detection limit. In the second case, formaldehyde was studied at 1769 cm^{-1}. The compact and transportable device displayed mode-hop free wavelength tuning over $1763 - 1770$ cm^{-1} and an $\alpha_{\min}$ of 1.6×10^{-9} cm^{-1} for one scan (0.1 s, 100 data points). Allan variance studies indicated an optimal integration time of 12 s would result in a detection limit of 5 ppt, limited by the development of small fringes which prevented the further reduction in the rms noise level at integration times greater than several tens of seconds. Hamilton and Orr-Ewing [104] have also used a cw DFB QCL and a V-shaped optical cavity to perform OF-CEAS, this time at 7.8 µm. Simultaneous measurements of CH_4 and N_2O in ambient air were recorded with a resolution of 0.014 cm^{-1} and an $\alpha_{\min}$ of 5.5×10^{-8} cm^{-1} for 1 s averaging achieved. More recently, Bergin *et al.* [373] have demonstrated that a two-mirror linear cavity is also a viable geometry for OF-CEAS. With this configuration, the field directly reflected from the coating of the first cavity mirror was not found to adversely affect the optical feedback

locking scheme. No feedback attenuation optics were needed at the power of the laser used and the unadjusted feedback rate yielded a frequency locking range smaller than one cavity FSR. This simpler arrangement has the advantages that it requires one less cavity mirror than a V-cavity, thereby lowering cavity losses, and, as all modes have a node at each mirror, there is no variation in the power build up of odd and even modes. A 3 mW, cw DFB QCL operating at -10°C was coupled into the two-mirror linear optical cavity and OF-CEAS performed at 5.5 μm. An $\alpha_{\min}$ of 2.4×10^{-8} cm^{-1} was achieved by averaging over 1 s, a value limited by etalon fringing. Spectroscopic measurements of NO were performed, with investigations into the temporal stability of the instrument indicating that an NO detection limit of 5 ppb in 2 s was feasible.

Another, more complex resonant cavity method, NICE-OHMS, has also been combined with both QCL and DFG-based mid-IR sources. Taubman *et al.* locked a 8.5 μm DFB QCL to a high finesse optical cavity to achieve natural laser linewidth narrowing down to 5.6 Hz [374]. This laser light was combined with NICE-OHMS to study a N_2O transition at 1175.0 cm^{-1} at low (∼mTorr) pressures, attaining a sensitivity of 9.7×10^{-11} cm^{-1}Hz$^{-1/2}$ limited by the MCT detector utilised. More recently, $2.8 - 4.8$ μm light generated by DFG has also been combined with NICE-OHMS [375]. Restricted to the $3.0 - 3.4$ μm wavelength range by the reflectivity profiles of the cavity mirrors, transitions of CH_4 circa 3120 cm^{-1} at very low (∼μTorr) pressures were studied. In the Doppler broadened regime, a sensitivity of 2×10^{-7} cm^{-1}Hz$^{-1/2}$ was reported, though this was reduced to 6×10^{-9} cm^{-1}Hz$^{-1/2}$ when wavelength modulated NICE-OHMS was used to investigate sub-Doppler Lamb dips.

A yet more complicated and expensive technique, cavity enhanced direct frequency comb spectroscopy (CE-DFCS), has also been used in conjunction with mid-IR laser sources. Foltynowicz *et al.* have used a 400 mW OPO, together with CE-DFCS, to create a spectrometer which has a central wavelength tunable between $2.8 - 4.8$ μm and a simultaneous spectral coverage range of $100 - 300$ nm, depending on the central wavelength chosen, with a 800 MHz resolution [376, 377]. At this resolution, a sensitivity of 5.4×10^{-9} cm^{-1}Hz$^{-1/2}$ for 6000 points was achieved, corresponding to 6.9×10^{-11} cm^{-1}Hz$^{-1/2}$ per spectral element. Absorptions from ethyne (C_2H_2), N_2O and CH_4 were observed at stp between $2525 - 2740$ cm^{-1}, and hydrogen peroxide (H_2O_2) at 630 Torr over $2597 - 2740$ cm^{-1} was measured with a detection limit of 8 ppb in 1 s, though this increased to 130 ppb in the presence of 3% H_2O.

De Natale and co-workers have been developing spectrometers using mid-IR produced by DFG coupled with a range of cavity-based techniques. The initial DFG design consisted of mixing $848 - 855$ nm pump radiation from a master/slave diode laser system with 1064.5 nm fibre amplified signal radiation from an Nd:YAG laser in a bulk PPLN crystal to generate 172 μW of power over $4.15 - 4.35$ μm [331]. This was used to study a $^{17}O^{12}C^{16}O$

transition at 2340.77 cm^{-1} using cavity enhanced saturated-absorption spectroscopy, with the resulting sub-Doppler Lamb dips providing useful information pertaining to the line centre frequency. The system was improved by the addition of a fs Ti:sapphire optical frequency comb synthesiser (OFCS), which phase locked the pump and signal lasers of the DFG source to two near-IR teeth of the optical comb [378]. The benefits of such a strategy are two-fold: as well as improving the accuracy of the reported wavelengths, it enhances the spectrometer sensitivity because results can be averaged for longer without the problem of slow laser drift. In later work, an $830 - 870$ nm ECDL was used as the signal source generating 20 μW of mid-IR radiation at 4.5 μm within a single-pass DFG scheme [379]. This mid-IR radiation was frequency referenced using the OFCS and CRDS performed on the $^{13}CO_2$ transition at 2231.8 cm^{-1}. An effective path length of 15 km and a τ_0 of 25 μs were obtained. By measuring 256 CRD events over 60 s, a $\Delta\tau_0/\tau_0$ of $\sim 1\%$ was found, indicating that the locking of the pump and signal lasers of the DFG set-up to the OFCS not only allowed measurements to be made with accurate absolute frequencies, but also with very high sensitivities. The mid-IR power was further increased to $80 - 300$ μW when the ECDL was used to seed a cw ring Ti:sapphire laser; when coupled into an optical cavity, this provided a short term absorption sensitivity of 1.3×10^{-11} $cm^{-1}Hz^{-1/2}$ in a measurement time of 100 μs [380]. This radiation was then used to perform saturated-absorption cavity ring-down (SCAR) spectroscopy on the 2343.66 cm^{-1} $^{17}O^{12}C^{16}O$ transition with precise absolute frequency measurements and a sensitivity of 1.1×10^{-9} cm^{-1} over a 12 min acquisition time [40]. A huge advance was then made when intracavity DFG [332] was used to produce an extremely powerful (up to 30 mW) cw tunable mid-IR laser source at $3.9 - 4.6$ μm [381]. This was achieved by placing the MgO-doped PPLN crystal inside the Ti:sapphire laser cavity itself. This also resulted in a Gaussian beam profile with a near TEM_{00} mode. The mid-IR laser source was still phase locked to the OFCS for absolute frequency stabilisation and was used in both CRD and SCAR spectroscopy giving $\alpha_{\min}$ values of 10^{-9} $cm^{-1}Hz^{-1/2}$ and 10^{-10} $cm^{-1}Hz^{-1/2}$, respectively [382, 383]. 33 ro-vibrational transitions in the ν_3 $^{14}C^{16}O_2$ band over $2190 - 2250$ cm^{-1} were studied at a high resolution (1 kHz) and absolute frequencies measured with an uncertainity of $0.7 - 4.8$ MHz. SCAR was also used to measure $^{14}C^{16}O_2$ at 2209.11 cm^{-1} with a detection limit of 43 parts per quadrillion (10^{15}, ppq) over a 1 hr averaging time, which has applications in radiocarbon dating and the detection of hazardous materials [101].

There are also several reports of the use of mid-IR cavity-based spectroscopy in a range of different applications. One of the principal fields of use has been in environmental sensing, where this concept has been implemented in such diverse situations as atmospheric trace gas detection [93, 104, 385–387], indoor environmental monitoring [388, 389] and industrial applications, the latter including combustion studies [390], detection of explosives [121] and the measurement of vehicle exhaust emissions [391, 392]. In addition, breath sensors

Spectroscopic technique	Laser source	Wavelength range/ μm	Frequency studied/ cm^{-1}	Power / mW	$\alpha_{min}(BW)$ / $cm^{-1}Hz^{-1/2}$	Molecule	Detection limit / integration time	Reference
CEAS	QCL	5.2	1920.7	20	3×10^{-7} *	NO	10 ppb/ 15 s	[358]
CEAS + 2f-WMS	QCL	5.5	1835.6	30	3×10^{-7} *	NO	0.7 ppb/ 1 s	[360]
CEAS	ICL	3.5	2832.5	12	8×10^{-7} *	H_2CO	150 ppb/ 3 s	[362]
CEAS	OPO	3.0 – 4.0	2996.9	1200	5×10^{-11}	C_2H_6	50 ppt/ 0.25 s	[74, 363]
CEAS	DFG	3.2 – 3.3	3081.0	0.26	2×10^{-8}	C_2H_4	160 ppb/ 31 s	[339]
CRDS	CO laser	2.6 – 4.1	3000.3	0.10	2×10^{-9}	C_2H_6	100 ppt/ 5 s	[146]
CRDS	CO laser	2.6 – 4.1	2947.8	0.10	8×10^{-9}	CH_4	105 ppt/ 20 s	[120]
CRDS	CO laser	2.6 – 4.1	2853.4	0.10	7×10^{-9}	H_2CO	2 ppb/ 2 s	[99]
CRDS	CO laser	4.8 – 5.5	2039.0	0.04	7×10^{-11}	OCS	7 ppt/ 0.4 s	[365]
CRDS	QCL	8.5	1177.0	16	3×10^{-9}	NH_3	0.25 ppb/ 1 s	[368]
CRDS	OPO	2.4 – 3.8	2990.1	200	5×10^{-9}	C_2H_6	300 ppt/ 16 s	[369]
CRDS	DFG	3.0 – 3.6	3000.3	0.027	1×10^{-8}	C_2H_6	1 ppb/ 2 s	[94]
CRDS	DFG	3.3 – 3.4	2989.0	0.016	2×10^{-8}	CH_4	50 ppb/ 6 s	[384] †
OF-CEAS	QCL	4.5	2239.8	15	3×10^{-9}	N_2O	35 ppt/ 1 s	[371]
OF-CEAS	QCL	5.6	1769.5	70	5×10^{-11}	H_2CO	60 ppt/ 0.1 s	[372]
OF-CEAS	QCL	7.8	1275.0	4	6×10^{-9}	CH_4	8 ppb/ 1 s	[104]
OF-CEAS	QCL	5.5	1824.3	3	5×10^{-9}	NO	5 ppb/ 2 s	[373]
PS-CRDS	DFG	3.2 – 3.3	3081.0	0.26	6×10^{-7}	C_2H_6	1 ppm/ 240 s	[364]
NICE-OHMS	QCL	8.5	1175.0		1×10^{-10}	N_2O		[374]
NICE-OHMS	DFG	2.8 – 4.8	3120.0		2×10^{-7}	CH_4		[375]
CE-DFCS	OPO	2.8 – 4.8	2658.9	400	5×10^{-9}	H_2O_2	8 ppb/ 1 s	[377]
SCAR + OFCS	DFG	3.9 – 4.5	2209.1	30	1×10^{-10}	$^{14}C^{16}O_2$	43 ppq/ 1 hr	[101, 382]

Table 5.1: Key examples of cavity-based mid-IR spectroscopic studies reported in the literature, using a variety of mid-IR laser sources and a range of cavity-based techniques. 'Frequency studied' refers to the actual wavelength at which the measurements for the target molecule were taken, * indicates the value was not given in the paper but calculated from reported results, † refers to this work and ppt and ppq are parts per trillion (10^{12}) and parts per quadrillion (10^{15}), respectively. Other acronyms are listed in the Nomenclature.

for ethane [393], formaldehyde [394] and acetone [160] based on such arrangements have been proposed. Mid-IR cavity-based spectroscopy has been employed in high resolution spectroscopic studies to investigate fundamental lineshape and molecular properties, such as the lineshape parameters of deuterium [395], the absorption line centres of ethene [396] and the intermolecular interactions in heavy water [397]. Plasma diagnostics [27, 95, 398] and surface studies [399] have been other areas of research utilising these methods.

The above discussion highlights that whilst a number of examples exist illustrating the use of different mid-IR laser sources with different cavity-based techniques, there are few accounts in the literature of using mid-IR radiation generated by DFG to perform CRDS: the two major ones being those reported by Stry *et al.* in 2002 [94, 148] and by de Natale and co-workers from 2009-present [40, 101, 380–383]. In the remainder of this chapter, the results of work combining DFG-generated mid-IR light with CRDS to create a 3 μm DFG CRD spectrometer are presented. The design and development of this device is described and the results of its use in spectroscopic studies of various molecules reported, thereby demonstrating its potential as a useful tool to study atmospheric, environmental or medical gases of interest.

5.2 Experimental Set-Up of a DFG-Based CRD Spectrometer

5.2.1 Combining the QPM-DFG and CRDS systems

A mid-IR CRD spectrometer was created by combining the all DL-based, free-space QPM-DFG set-up described in Section 4.3 with the CRDS system developed in Section 3.1, as shown in Figure 5.1 [384]. This radiation source meant that the spectrometer operated over a 3342.5 − 3356.4 nm (2979.4 − 2991.7 cm^{-1}) spectral range, and as such different cavity mirrors to those previously used were required. In this case, the cavity was composed of a pair of 25.4 mm diameter, zinc selenide (ZnSe) plano-concave mirrors with 1 m radii of curvature (*NovaWave Technologies*). These mirrors were AR coated on the plane side and HR coated on the curved side with a quoted reflectivity of $R \sim 0.9998$ at 3300 nm. The first mirror was mounted on the PZT, as before. The length of the cavity was 77 cm, corresponding to a free spectral range of 195 MHz.

In coupling together the separately developed DFG and CRDS entities, it was found that the relative positioning of the EDFA and AOM components of the two systems was important. The input voltage signal to, and hence throughput of, the AOM is shown in Figure 5.2(a): once triggered by the detection of a cavity mode, the AOM switched off so that no more signal radiation could pass through it. A similar profile was also desired for the near-IR

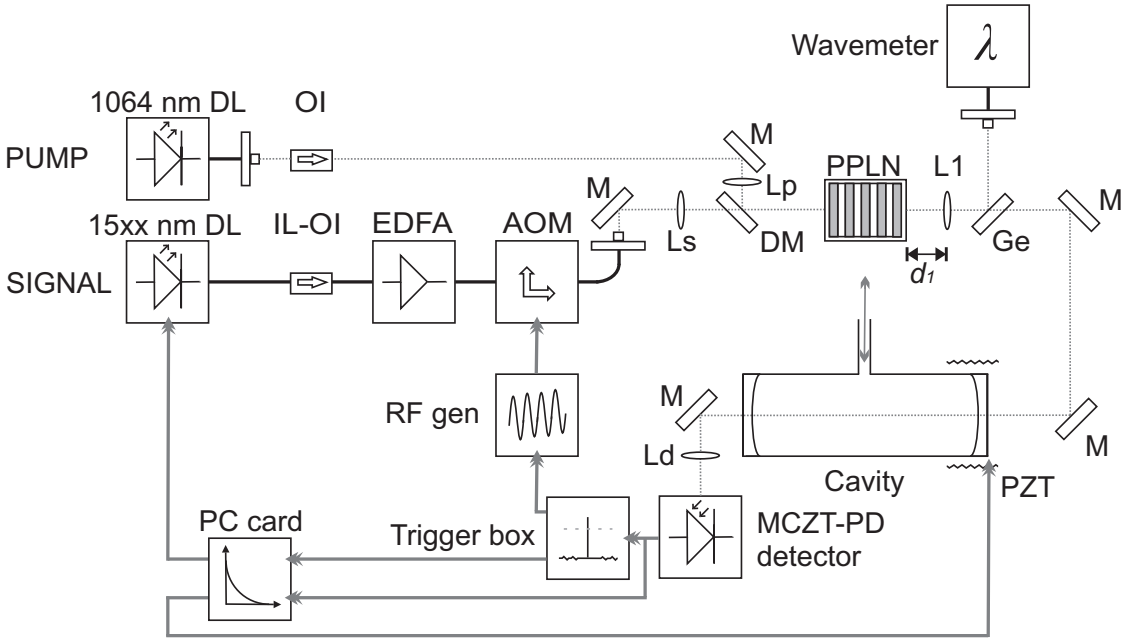

(a) Schematic

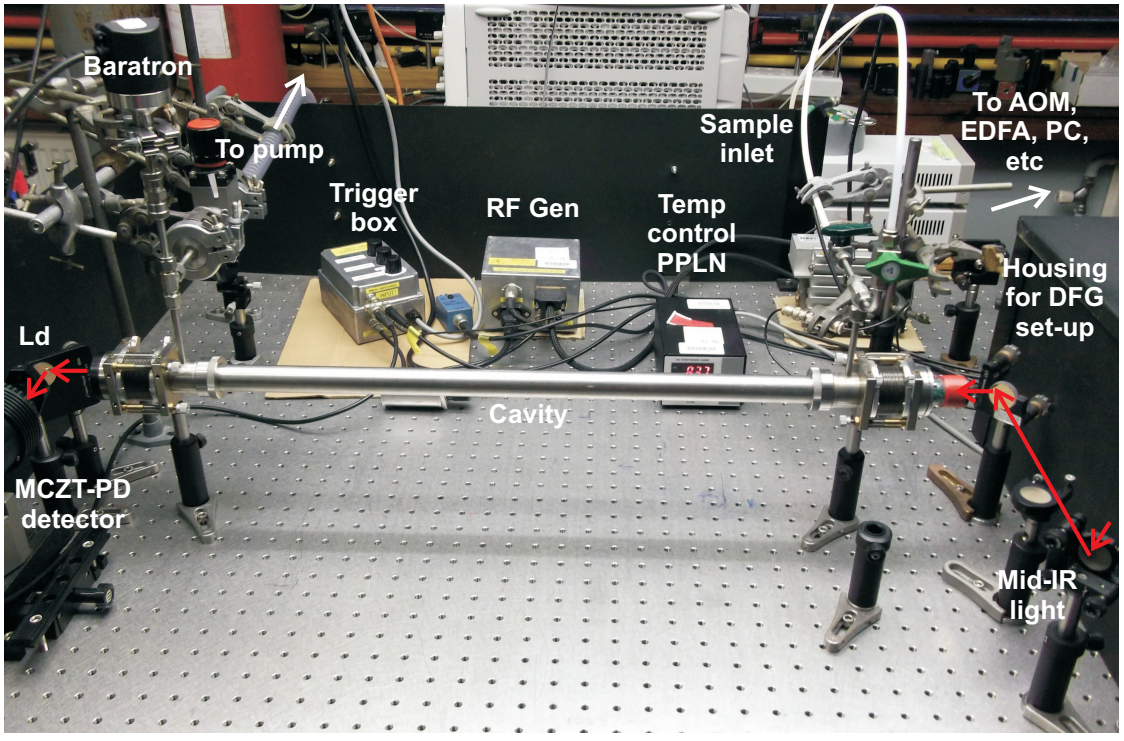

(b) Photo

Figure 5.1: A (a) schematic and (b) photo of the experimental set-up for the mid-IR DFG free-space system combined with the CRD spectrometer. The mid-IR light generated by QPM-DFG of two near-IR diode lasers is injected into an optical cavity composed of mirrors of reflectivity $R = 0.9996$ and length $L = 0.77$ m. RF gen: radio frequency generator to switch AOM; MCZT-PD detector: HgCdZnTe photodiode detector.

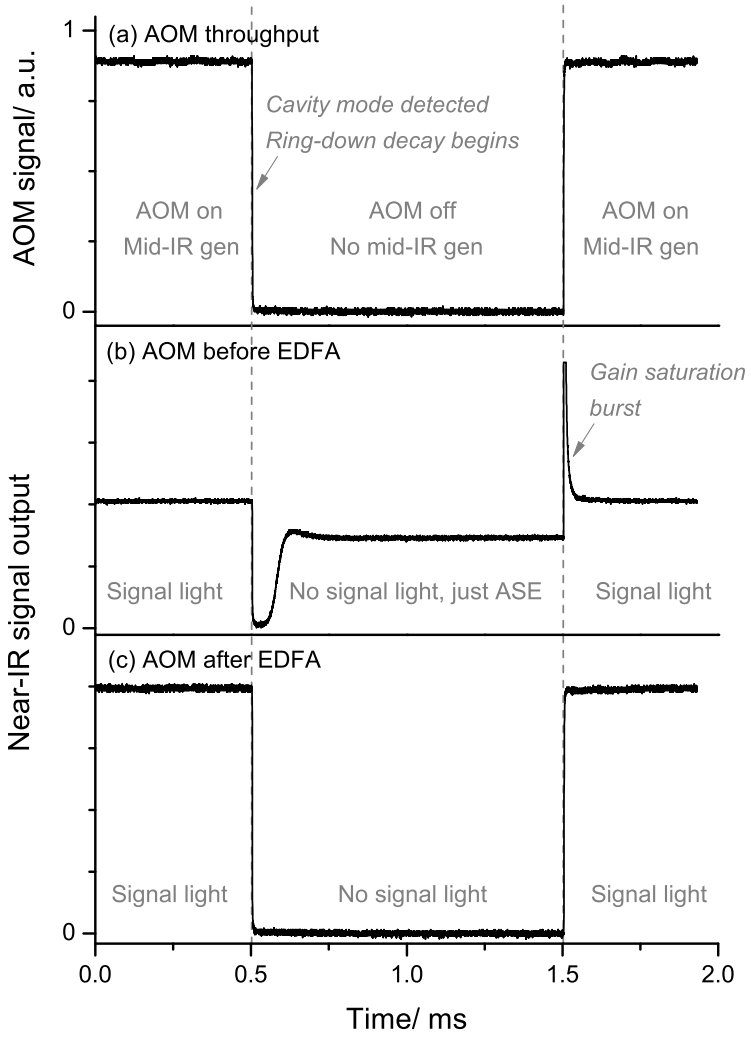

Figure 5.2: The amount of signal radiation available for mid-IR generation as the AOM is switched on and off when the AOM is placed (b) before and (c) after the EDFA.

radiation exiting the fibre coupler, as this would thus prevent the generation of further mid-IR light and so allow ring-downs to be recorded.

Initially, the AOM was placed before the EDFA so that when the AOM was triggered the EDFA would cease to be seeded and would only emit ASE which could not be used in mid-IR generation. This was the preferred configuration because it would give higher mid-IR powers as the signal radiation available for mid-IR generation would not be reduced by passing it through the AOM. However, it became apparent that this arrangement was unworkable (Figure 5.2(b)) due to gain saturation of the EDFA [400]. This is where the gain of the amplifier does not instantly adjust to the required level, and so on a sudden increase in the EDFA input power, such as that caused by the AOM switching back on after a ring-down event, the gain reduces to the appropriate level only after a certain, finite response time of the EDFA. This response time is of the order of μs or greater [400, 401], which is comparable to the RDTs that were to be recorded. This phenomenon created

large, decaying bursts of the seeded EDFA output power of the signal radiation, which in turn resulted in large spikes in the generated mid-IR. These spikes led to the re-triggering of the system which prevented the AOM from remaining on for a sufficient length of time to allow enough mid-IR to couple into the cavity to generate cavity modes.

To avoid this effect, it was therefore decided to place the AOM after the EDFA. This meant that there was a continuous seeding of the EDFA, and so a constant output of amplified signal radiation. This radiation was then passed through the AOM and when the AOM was triggered to switch off, its passage was stopped (Figure 5.2(c)). However, this arrangement lowered the amount of signal radiation available for mid-IR generation and hence the ultimate level of mid-IR power. Indeed, inserting the AOM at this position caused the power of the signal radiation incident on the PPLN crystal to drop from 213 mW (Section 4.3.3) to 112 mW. At the wavelengths used to perform the experiments with CH_4 in Section 5.3.1 and their associated optimal PPLN properties ($T_{\text{crys}} = 84.3°\text{C}$, $\Lambda = 30.00$ µm), this resulted in a final mid-IR output power of 15.8 µW with a conversion efficiency of 0.053% $W^{-1}cm^{-1}$.

Unless otherwise specified, the following settings were used in the experiments conducted in this chapter: DAQ card: ±10 V at 200 kHz update rate; PCI card: ±0.2 V at 20 MHz sampling rate with $t_{\text{rec}} = 50$ µs; PZT waveform: $V_{\text{amp}} = 6$ V, $V_{\text{freq}} = 10$ Hz, $V_{\text{off}} = 60$ V; fitting and analysis: $t_{\text{disc}} = 1.5$ µs, $t_{\text{fit}} = 40$ µs, $\tau_{\text{det}} = 1.6$ µs (using $\tau_{\text{det}} = 1/2\pi BW$, as according to the manufacturer's specifications, and the known bandwidth of the detector); conditioning criteria: minimum $R^2 = 0.95$. The PZT amplitude and frequency were chosen following the same reasoning as that discussed in Section 3.1, and the optimum fitting parameters determined using the same procedures as implemented in Section 3.3.2.

In order to tune the mid-IR radiation over a region of interest for the acquisition of spectra, the frequency of the signal radiation was changed whilst keeping the pump wavelength constant, as discussed in Section 4.3.1. This meant that wavelength calibrations correlating the V_{mod} from the DAQ into the DL current driver with the signal wavelength were needed in order to step across the required mid-IR spectral range with the desired resolution. When recording spectra, the number of RDTs averaged per point was set as $n_{\text{avg}} = 100$ (Section 5.2.3) and the settling time between points as $t_{\text{sett}} = 2$ s.

5.2.2 Beam profiling and mode matching

A suitable collimating lens, L1, with focal length f_1 placed a distance d_1 after the PPLN crystal, as shown in Figure 5.1(a), was required. Beam profiling techniques like those employed in Section 3.3.1 were once again used, and it was found that a 50 mm diameter, CaF_2 plano-convex lens (*Crystran*, CAF50LENS135) with a $f_1 = 13.5$ cm placed at $d_1 =$

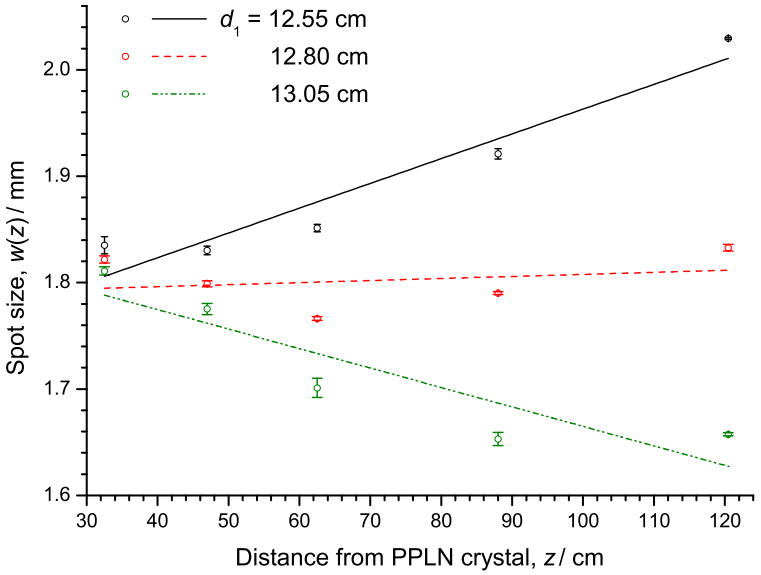

Figure 5.3: Profiles of the width of the mid-IR light beam with increasing distance from the PPLN crystal for different displacements, d_1, of the 13.5 cm focal length collimating lens. A collimated beam with spot size $w = 1.80 \pm 0.03$ mm was observed when $d_1 = 12.80$ cm.

12.80 cm after the PPLN crystal collimated the idler beam to a spot size of 1.80 ± 0.03 mm (Figure 5.3).

At 3345.676 nm (2988.933 cm^{-1}), the beam waist at the cavity centre was calculated as $w_0 = 0.7198$ mm and the spot sizes at the mirrors as $w_{1,2} = 0.9178$ mm. Using the collimated spot size of 1.80 mm and the mode-matching analysis of Appendix A, it was found that optimal mode-matching could be achieved by placing a lens with focal length $f = 73.52$ cm at a distance $d = 37.12$ cm before the cavity. However, it was discovered that the cavity alignment and beam quality were good enough for efficient cavity coupling without the need for mode-matching, as discussed in Section 5.2.3. As it was desired not to decrease the already low power levels in the mid-IR, this circumstance was very beneficial as it meant that it was possible to minimise the distance travelled by the mid-IR light before entering the cavity, thereby reducing power dissipation, and also to avoid the introduction of any additional lenses into the optical beam path, which would decrease the light intensity even when using optics made of CaF_2 which has a relatively high transmission at 3 μm.

5.2.3 Characterisation

An example of the observed cavity modes is shown in Figure 5.4. The regular spacing between the modes, and the relative lack of neighbouring modes of smaller intensity, ensured that the system was only triggered by the fundamental TEM_{00} modes. The average signal height of these cavity modes above the detector baseline varied between $2 - 10$ mV,

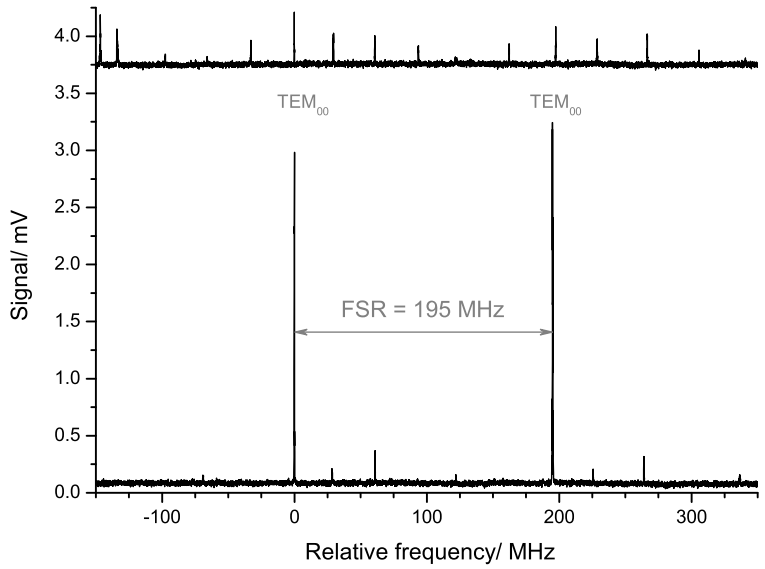

Figure 5.4: Cavity transmission of the mid-IR light on scanning the PZT at two different degrees of optical cavity alignment. The upper trace corresponds to a poor cavity alignment, while the lower one to a well-aligned CRDS cavity supporting predominantly TEM_{00} modes. The traces have been offset for clarity.

corresponding to powers of $0.04 - 0.18$ μW. The trigger level of the discriminator box was set such that it was high enough so that only the most intense cavity modes would trigger an event to be recorded in order to give consistent RDTs, but low enough to allow frequent triggering.

The pump and signal wavelengths were set at 1064.289 nm and 1560.795 nm, respectively, generating mid-IR light at 3345.653 nm (2988.95 cm^{-1}). This light was coupled into the cavity filled with N_2 at a pressure of 6 Torr, and 3015 ring-downs recorded over 3 mins. These were then fitted with the LRS fitting routine described in Section 3.1.2 and τ_0 found using Equation 3.1; an example of such a ring-down and fit is shown in Figure 5.5(a).

In these experiments, it became clear that two important factors had to be considered. The first one was the effectiveness of the triggering on the cavity modes. Cavity modes were generated on both the up and down ramp of the PZT modulation, so as the PZT waveform had a frequency of 10 Hz and an amplitude equivalent to one FSR in the spectral domain to ensure at least one cavity mode per ramp was produced, the theoretical cavity mode trigger rate was 20 Hz. However, the system was not triggered continuously on every cavity mode at this expected rate, but at a reduced rate of 16.8 Hz, *i.e.* only 84% of the cavity modes triggered the detection system to record ring-downs. Additionally, as discussed in Section 3.1.2, the poor quality of some of the cavity modes led to the requirement for conditioning criteria to filter the results. Here, it was decided to discard results with R^2 values of the exponential fit lower than 0.95 and those with an RDT outside the ±3 standard deviation range of the overall average. Considering these two factors together, a total conversion

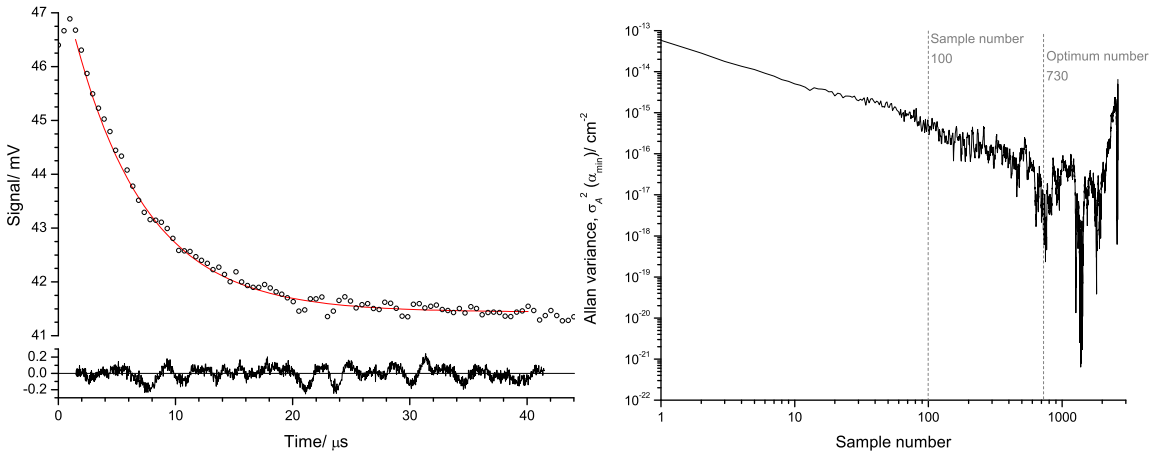

Figure 5.5: Ring-downs recorded of 6 Torr of N_2 at a single wavelength (3345.653 nm). (a) An example of a ring-down trace with the raw data given by the open circles (only a reduced number of data points are shown for clarity) and the exponential fit by the solid line; the residuals between the two are given in the lower plot. The fitting routine only used data recorded $1.5 - 41.5$ μs after the trigger and returned a τ_0 of 6.14 μs, indicating a mirror reflectivity of 0.9996 and effective path length of 1.84 km. (b) An Allan variance plot of the $\alpha_{\min}$ values calculated from recorded sequential ring-downs under the same conditions over 3 mins. The results were filtered so that only ring-downs whose fits had an $R^2 > 0.95$ were used. Inspection of this plot indicated that an optimum number of ring-downs to record and average per point would be 730, giving a detection limit in the RDT of $\sim 10^{-9}$ s and $\alpha_{\min}$ of $\sim 10^{-9}$ cm^{-1}; however, this would necessitate a long recording time per point. Hence in order to record spectra, 100 ring-downs per point, with a detection limit in the RDT of $\sim 10^{-8}$ s ($\alpha_{\min}$ of $\sim 10^{-8}$ cm^{-1}) taking ~ 6 s per point, was used.

efficiency of 73% of the generated cavity modes into useful RDTs was achieved. Complete conversion was not possible owing to the low and varying mid-IR power levels entering the cavity caused by the fluctuations in both the crystal temperature (due to the oven warming cycles) and in the temperature of the lab environs on the time scale of $5 - 10$ mins.

The filtered results of this data set were used to construct an Allan variance plot [225], shown in Figure 5.5(b). From this plot it was seen that the maximum sensitivity corresponded to an average of 730 RDTs. It was judged, however, that an average of 100 RDTs, would be more appropriate for the recording of spectra to reduce the total acquisition time.

This data set was also used to estimate the $\alpha_{\min}$ for this system either when recording at one wavelength (using the optimal number of RDTs to average of 730) or when taking spectra (100 RDTs average per point). Applying the conditioning criteria outlined above to groups of 730 of this data set and averaging the results, it was found $\tau_0 = 6.065 \pm 0.003$ μs (1σ), yielding an $\alpha_{\min} = 2.9 \times 10^{-9}$ cm^{-1} over 44 s ($\alpha_{\min}(BW) = 1.9 \times 10^{-8}$ cm^{-1}Hz$^{-1/2}$). For groups of 100, $\tau_0 = 6.07 \pm 0.03$ μs (1σ) giving $\alpha_{\min} = 2.8 \times 10^{-8}$ cm^{-1} over 6 s ($\alpha_{\min}(BW) = 6.9 \times 10^{-8}$ cm^{-1}Hz$^{-1/2}$). Using this value of $\tau_0 = 6.07$ μs, the mirror reflectivity was calculated as $R = 0.9996$. It is worthy of note that this optimal $\alpha_{\min}$ of 2.9×10^{-9} cm^{-1} is worse than

that found in Section 3.3.2.2 when using the near-IR DS-DBR CRD spectrometer of 2.8×10^{-10} cm^{-1} ($\alpha_{\min}(BW) = 1.3 \times 10^{-9}$ cm^{-1}Hz$^{-1/2}$); this is because lower reflectivity mirrors were used in the mid-IR compared to the near-IR due to commercial availability restrictions, and as a consequence only smaller τ_0 values were achievable with correspondingly worse results for $\alpha_{\min}$ (Equation 1.54).

5.3 Spectroscopic Measurements with the DFG-Based CRD Spectrometer

In order to demonstrate the use of this DFG CRD spectrometer, studies on methane, deuterium and acetone were conducted to illustrate different favourable characteristics of the system. The absorption cross-sections of these compounds over the wavelength range of the spectrometer are shown in Figure 5.6.

As a first validation of the DFG CRDS system, studies of the narrowband absorber methane (CH_4) at 3346 nm were performed. CH_4 was chosen as it has highly resolved and well-assigned spectral features. It is also of medical interest. Typical concentrations of CH_4 in breath vary from ambient air levels to 30 ppm [149] and it has also been shown that breath CH_4 can be used as a biomarker for colonic fermentation and intestinal problems such as irritable bowel syndrome [150, 152]. In fact, laser spectroscopic techniques have already been developed for the measurement of CH_4 in breath [88, 144]. In addition, CH_4 is an important molecule for environmental studies as it is a potent greenhouse gas [26]. Knowledge of the ratios of its isotopologues allows information about its sources and sinks, and thus the global CH_4 budget, to be inferred [118, 406], with δ^{13}C values (Equation 3.2) of different CH_4 sources and sinks varying between -10‰ and -80‰ [120, 407, 408]. It is considered necessary to be able to measure this isotopic ratio with a precision of $0.1 - 1$‰ for atmospheric research [118, 409], and thus a highly sensitive instrument is required.

Next, the DFG CRD mid-IR spectrometer was used to study deuterium (D_2) so to appraise the capability of the system to perform high resolution spectroscopy. Particular D_2 transitions at certain pressures ($\sim 100 - 7,600$ Torr [23, 410]) display Dicke narrowing [395, 411, 412], and the D_2 feature monitored in this work demonstrated this effect over the range of pressures investigated ($100 - 450$ Torr). Such collisionally narrowed absorption features must be fitted with more complex lineshapes, such as Galatry profiles, rather than the usual Gaussian or Voigt functions; thus a spectrometer used to take these measurements would need to have a sufficiently high wavelength resolution and sensitivity, as well as an accurate frequency calibration, in order to distinguish and assess these differences in the absorption lineshapes. D_2 is also a useful molecule to study as the experimental data collected can be compared with the outputs of theoretical simulations in order to test theories

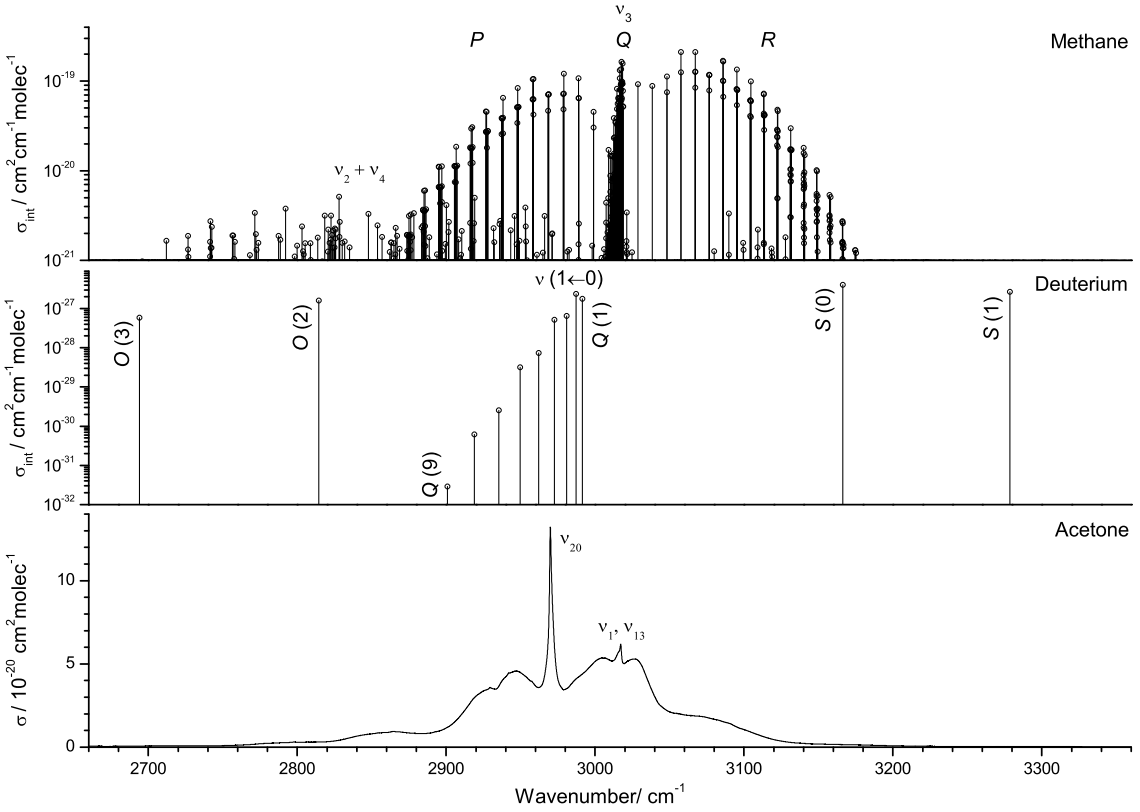

Figure 5.6: Absorption cross-sections of the three molecules studied in this work across the 3 µm region: σ_{int} values of the narrowband absorbers CH_4 and D_2 are shown, whereas σ values are given for the broadband absorber acetone. The CH_4 σ_{int} values reported are from the HITRAN database [15]; the major features observable correspond to the P, Q and R branches of the fundamental $\nu_3(F_2)$ vibrational transition, though absorptions due to other combination bands are also present in this range, such as the F_1 and F_2 symmetry bands of the $\nu_2 + \nu_4$ transition. The D_2 linestrengths and positions are the results of simulations performed by Kassi *et al.* [402] and correspond to the electric quadrupole transitions of the fundamental vibrational band, $\nu(1 \leftarrow 0)$, of D_2, comprising of O, Q and S branches ($\Delta J = -2, 0$ and $+2$, respectively). The acetone σ values are estimated from the 1 ppm-meter, 760 Torr, 296 K absorption spectrum reported in the PNNL database [403] and corroborated by work by Harrison *et al.* [404], with the band centred at 2972 cm^{-1} caused by the $\nu_{20}(B_2)$ CH_3 degenerate stretching mode and the feature at 3019 cm^{-1} by the $\nu_1(A_1)$ and $\nu_{13}(B_1)$ CH_3 degenerate stretches [405].

and algorithms which have been developed to model the effects of collisional broadening or to predict the spectroscopic parameters of transitions (*e.g.* line centres, linestrengths, pressure shift coefficients, *etc.*). Once validated, the results of these models could be utilised to provide useful information in spectral regions inaccessible by current experiments to aid in tasks such as the astrophysical search of D_2 lines [402].

Finally, investigations into the broadband absorber acetone ($(CH_3)_2CO$) were conducted. Measurements of broadband absorbers are fundamentally more difficult than those of narrowband absorbers due to the problems in finding a τ_0 value (as this must now be measured separately rather than by simply selecting a τ_0 value from the τ spectrum at a nearby wavelength at which no absorption occurs) and due to the fact that there is often no clear

absorption feature to fit (so estimates of the σ values, rather than σ_{int}, must be used to calculate sample concentrations). It was desired to test the ability of the DFG CRDS system to measure broadband absorbers, and acetone was chosen due to its medical relevance: acetone concentrations present in breath can be used monitor the levels of ketones in blood [413, 414]. In the case of type 1 diabetes, for example, the onset of ketoacidosis is accompanied by increased levels of both blood ketones and breath acetone [415–417], with healthy subjects exhibiting acetone breath concentrations of $0.35 - 0.85$ ppm (accepted value of 0.49 ppm) [82] compared to the $0.80 - 3.97$ ppm levels seen in diabetic patients [158].

5.3.1 Methane

CH_4 is a stereotypical spherical top molecule with tetrahedral symmetry and thus belongs to the T_d point group which consists of the irreducible representations A_1, E, F_1 and F_2. It has nine normal modes of vibration [418]: a non-degenerate stretch $\nu_1(A_1)$, a doubly degenerate bend $\nu_2(E)$, a triply degenerate stretch $\nu_3(F_2)$ and a triply degenerate bend $\nu_4(F_2)$, with fundamental frequencies of 2917 cm^{-1}, 1533 cm^{-1}, 3019 cm^{-1} and 1306 cm^{-1}, respectively [419]. A simple group theoretical analysis of the transition dipole moment integral (Section 1.1.1) reveals that the only IR active fundamental vibrational transitions from the ground vibrational A_1 state are those of the $\nu_3(F_2)$ and $\nu_4(F_2)$ modes. This evaluation is further complicated, though, by the fact that vibrational transitions are simultaneously accompanied by rotational ones, which perturb the genuine vibrational motion of the system. This means the degeneracy of the vibrational state is lifted by a first order Coriolis interaction and other, higher order ro-vibrational effects [420], which results in the splitting of a ro-vibrational transition into several components.

The upper and lower states of CH_4 transitions are listed in HITRAN [14, 15] with global quanta, V, of (ν_1 ν_2 ν_3 ν_4 n C^*), where ν_i is the quantum number for the i^{th} vibrational mode, n is a multiplicity index and C^* is the symmetry, and with local quanta, Q, of (J C α F), where J is the quantum number associated with the total angular momentum excluding nuclear spin, F is the quantum number associated with the total angular momentum including nuclear spin, C is the ro-vibrational symmetry of the state ($= A_1, A_2, E, F_1$ or F_2) and α is a counting integer for levels of the same J and C, incremented in order of increasing energy [14, 421].

5.3.1.1 Results

CRD spectra of CH_4 were recorded at 2989 cm^{-1}, sourcing the CH_4 from a variety of samples. λ_p was set at 1064.292 nm and λ_s scanned between $1560.740 - 1560.862$ nm, generating mid-IR light over the range $3345.38 - 3345.94$ nm ($2988.7 - 2989.2$ cm^{-1}) covering

Line centre / cm^{-1}	σ_{int} / cm^{2}cm^{-1}molec^{-1}	Rotational transition ($J'C'\alpha' \leftarrow J''C''\alpha''$)
2988.795	1.1×10^{-19}	(2 A_1 4 $\leftarrow$ 3 A_2 1)
2988.933	6.4×10^{-20}	(2 F_1 9 $\leftarrow$ 3 F_2 1)
2989.033	6.4×10^{-20}	(2 F_2 11 $\leftarrow$ 3 F_1 1)

Table 5.2: Line positions, integrated cross-sections, rotational levels and symmetry labels of the $P(3)$ transitions of the fundamental $\nu_3(F_2)$ band of CH_4 studied [14]. The degeneracy of the $\nu_3 = 1$ excited vibrational level is lifted by the Coriolis interaction and therefore the $P(3)$ transition is split into several components. The initial and final states contributing to each component are labelled using the nomenclature (J C α), where J is the quantum number associated with the total angular momentum excluding nuclear spin, C is the ro-vibrational symmetry of the state and α is a counting integer for levels of the same J and C, incremented in order of increasing energy.

three strong CH_4 transitions, details of which are given in Table 5.2. Studies were carried out at pressures of 25 Torr or lower, as at higher pressures the absorptions due to these features were sufficiently large to result in substantial decreases in both the RDTs and cavity transmission. Using low pressures also had the advantage of isolating the features under investigation from interferences from water. The second of these lines, at 2988.933 cm^{-1}, was studied in detail as its lower absorption cross-section allowed a greater range of pressures to be examined without reducing the RDT below that which could be measured.

Spectra of τ against λ_i were recorded using Program Two of Section 3.1.2 and the conditions stated above in Section 5.2.1. A τ_0 baseline was fitted to the data and α calculated using Equation 1.53. A Voigt profile was then fitted to the absorption feature, fixing the Gaussian width as the Doppler width at 277 MHz; the broadening contribution from the narrow laser linewidths (< 10 MHz) was negligible and hence not included.

Firstly, a calibrated 7.5 ppm mixture of CH_4 in air (*CK GAS*, Order Ref 15205) was tested. The cavity was filled with several different pressures of the sample between $2 - 4$ Torr, and CRD spectra recorded of the 2988.933 cm^{-1} CH_4 line in steps of 34 MHz; these spectra took between $10 - 15$ mins to record. The areas of the fitted Voigt profiles were used to estimate the concentration of CH_4 present in the cell using the σ_{int} reported in the HITRAN database [14], and these calculated concentrations were then compared with those expected. The results of these experiments are shown in Figure 5.7. The returned Lorentzian contributions to the linewidths of the fitted Voigt profiles at each pressure were observed to be similar to the values predicted from the broadening coefficients reported in HITRAN. For example, for the spectrum recorded at 3.2 Torr (Figure 5.7(a)), a fitted Lorentzian width of 34 ± 8 MHz was found compared to the expected value of 17 ± 4 MHz; this discrepancy may be due to minor laser frequency instabilities over the acquisition time period or the cumulative effect of slight miscalibrations of each frequency step due to the inaccuracies in the wavemeter

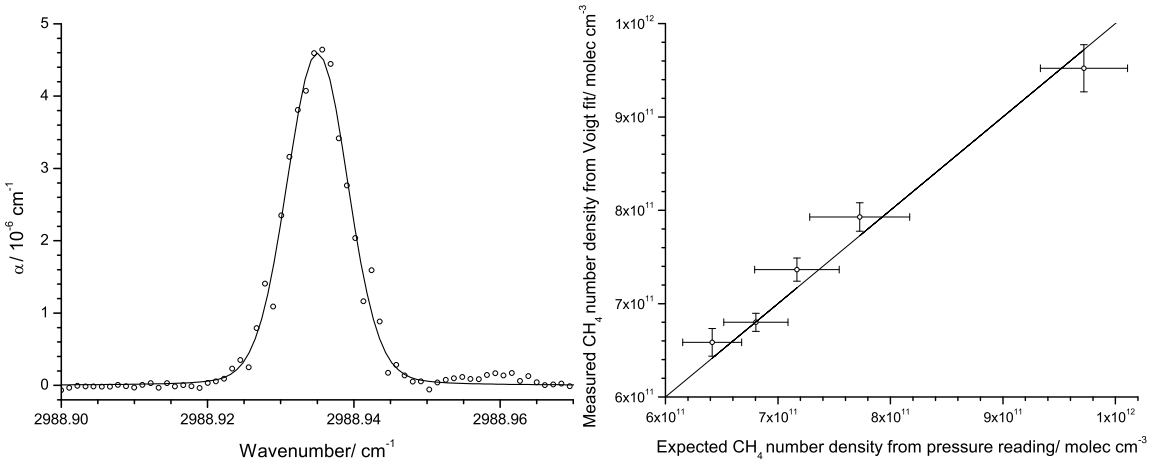

Figure 5.7: CRDS results of the 2988.933 cm^{-1} CH_4 line of a 7.5 ppm calibrated mixture of CH_4 in air. (a) is an example of a spectrum recorded at 3.2 Torr, with the raw data given by open circles. From the Voigt fit (solid line), the concentration of CH_4 in the sample was calculated, and a fitted Lorentzian width of 34 MHz found. This was repeated at several pressures between $2-4$ Torr, with the resulting CH_4 concentrations shown in (b) as open circles, where the y-error bars are calculated from the error in the area of the Voigt fit, and the x-error bars from the change in pressure inside the cell during the spectra acquisition period. The average of these results gave a concentration of CH_4 of 7.59 ± 0.16 ppm. Also shown in (b) is a straight line through the origin with a unitary gradient (solid line), to emphasise how well the expected and calculated concentrations compare.

used to perform the wavelength calibrations. A good agreement between the calculated and expected concentrations was also observed. These experimental results gave an average concentration of CH_4 of 7.59 ± 0.16 ppm (the quoted error is the standard deviation of the repeated measurements). Using the $\alpha_{\min}$ of 2.8×10^{-8} cm^{-1} calculated in Section 5.2.3, the expected sensitivity for this CH_4 line at 3 Torr is 50 ppb, which is comparable with the experimental error found.

To illustrate the use of the DFG CRDS system to a medical situation, two samples of breath were analysed in order to calculate the CH_4 concentration present. These samples were collected in breath bags (*Fischer Analysen Instrumente GmbH*, 1.5 litres) and then transferred to the cell without water removal or the filtration of aerosol particles. One sample was from a known non-methane producer; this sample was studied at five different pressures between $3-5$ Torr in an undiluted form. The other sample was from a known methane producer; in order to avoid overlarge absorbances and to ensure continuous triggering, this sample was diluted with N_2 within the cell in an approximate 1:4 ratio, and four different pressures of this mix between $3-4$ Torr studied. CRD spectra with a resolution of 34 MHz were recorded of the 2988.933 cm^{-1} CH_4 line, and the fitted Voigt profiles used to estimate the concentration of CH_4. Examples of these spectra, each taking between $10-15$ mins to record, are shown in Figure 5.8.

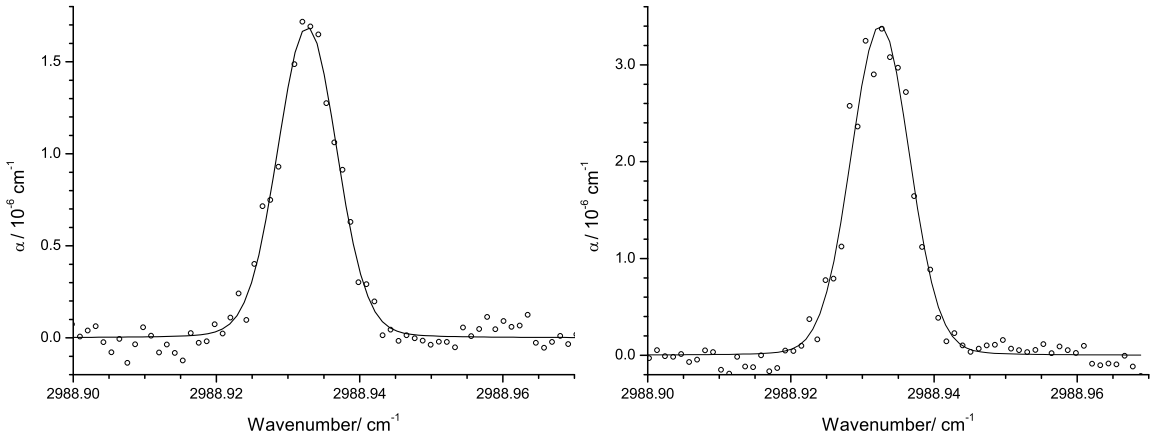

Figure 5.8: CRD spectra of the 2988.933 cm^{-1} CH_4 line in breath samples at 4 Torr. (a) is an undiluted sample from a non-methane producer; (b) is a diluted sample from a methane producer. Both sets of data (open circles) have been fitted with Voigt profiles (solid lines). From these fits, the CH_4 levels of the two different subjects were calculated as 2.3 ppm and 29.5 ppm, respectively. The Lorentzian widths of 27 MHz and 21 MHz for the two plots compared well with the values expected using the broadening coefficients from the HITRAN database [14] of 20 MHz and 21 MHz, respectively.

Averaging the calculated concentrations from these spectra, a CH_4 concentration of 2.26 ± 0.10 ppm for the non-methane producer and 29.4 ± 1.0 ppm for the methane producer were found. These concentrations were in line with the results expected from previous studies of these subjects using CEAS of the $2\nu_3$ band of CH_4 at 1.65 µm [203].

5.3.1.2 Discussion

To place these results in context, they must be compared with other, similar spectroscopic studies in the mid-IR. As seen in Section 5.1, there are very few examples in the literature of coupling mid-IR light produced by DFG into a cavity to perform CRDS: the two major ones being those reported by Stry *et al.* in 2002 [94, 148] and by de Natale and co-workers from 2009-present [40, 101, 380–383]. Of these, the work by Stry *et al.* is most comparable to that presented here; a summary of the results from both studies is given in Table 5.3. Stry *et al.* [94] used DFG of a diode laser and a frequency-stabilised Nd:YAG laser to generate 27 µW of mid-IR radiation at 3.3 µm, which was then used in CRDS by modulating the laser frequency at 100 Hz, yielding a RDT acquisition rate of 100 Hz. An $\alpha_{\min}$ of 10^{-8} cm^{-1} over a 2 s integration time was reported, and the spectrometer used to measure ethane with detection limits of 1 ppb at 100 mbar of a calibrated 100 ppb mixture of ethane in N_2. This is a similar $\alpha_{\min}$ to the one found in the CH_4 studies of this work [384], which employed a cavity whose τ_0 was half of that reported by Stry *et al.* and used cavity length modulation at 10 Hz to generate cavity modes, with a nominal RDT acquisition rate of

Property	Stry *et al.*	This study
$\tilde{\nu}_i$/ cm^{-1}	3000	2989
Signal laser type	Nd:YAG	DFB-DL+EDFA
λ_s/ nm	1064	1560
P_s/ mW	660	112
Pump laser type	ECDL	DBR-DL
λ_p/ nm	808	1064
P_p/ mW	20	66
P_i/ µW	27	16
L_{crys}/ cm	5	4
η/ % W^{-1}cm^{-1}	0.041	0.053
L/ cm	53	77
Cavity mirrors	$R = 0.9998$ at 3.3 µm for both	
τ_0/ µs	11.22	6.07
$\Delta\tau^0_{\text{min}}$/ µs	0.04	0.03
α_{min}/ cm^{-1}	1×10^{-8}	3×10^{-8}
Cavity mode scanning method	Wavelength (via λ_s)	Cavity length
Cavity mode scan rate/ Hz †	100	10
RDT acquisition rate/ Hz	100	20 ‡
n_{avg} per point	500	100 $*$
t_{int}/ s	2	6
Step size/ MHz	150	34

Table 5.3: A comparison of the key DFG and CRDS properties from Stry *et al.* [94] and this study [384]. † refers to the rate at which the laser current (Stry *et al.*) or the PZT component (this study) were scanned. In this work, the value reported for the RDT acquisition rate (‡) is the nominal RDT acquisition rate (the effective acquisition rate was 16.8 Hz, as discussed in Section 5.2.3) and n_{avg} ($*$) is the number of RDTs recorded per point before the conditioning criteria were applied (which reduced the actual number of RDTs averaged to $80 - 95$).

20 Hz. Another significant difference between the two studies was the approach to the analysis of the exponential decays. In Stry *et al.*, each data point represented the mean value of five measured decay times, which were themselves the result of an average of 100 decay events. In this work, an exponential decay was fitted to each ring-down event and the resulting RDTs from these fits averaged. It can be concluded from these comparisons that the performance of this spectrometer is consistent with that developed by Stry *et al.* and reaches the expected sensitivities for such a configuration. Whilst the spectrometer developed in this work does not match the very high detectivities achieved by de Natale and co-workers, this is unsurprising as it does not incorporate an OFCS and is consequently less sensitive; however, such an omission means that this system has the advantages of being considerably less complex and expensive.

5.3.2 Deuterium

Due to its homonuclear nature, ordinary electric dipole allowed absorption cannot be used to investigate the fundamental vibration-rotation energy levels of the D_2 molecule [422]. Instead, Raman scattering spectroscopy [410, 411, 423–425], electric quadrupole absorption spectroscopy [395, 402, 426, 427] or electric field induced absorption spectroscopy [422] must be used. As these processes are about a million times weaker than ordinary dipole absorptions [422], it is necessary to utilise high concentrations of D_2, sensitive spectroscopic techniques or both in order to study these transitions. Furthermore, in consequence of its low mass and small size, the spectroscopy of D_2 is additionally complicated by the observation of Dicke narrowing in the IR region at atmospheric and lower pressures. In order to complement the experimental work undertaken, many computational studies have also been conducted [402, 412, 427–429]. Here, electric quadrupole absorption spectroscopy has been used to investigate the collisional narrowing of a D_2 transition at 3.3 μm.

5.3.2.1 Dicke narrowing

The effect of Dicke, or collisional, narrowing [21–23, 430] on the widths of spectral lines was initially postulated in 1953 [22] before its first experimental observation in the quadrupole spectrum of H_2 in 1963 [431]. It refers to the narrowing of the Doppler broadening of a spectral line due to elastic, velocity changing collisions between the absorbing species and other particles. Due to the detailed balance principle, these collisions favour the transfer of large velocities to smaller ones, leading to a reduction in the range of velocities associated with the molecules in the sample. This results in a narrowing of the molecular velocity distribution and hence also in the spectral Doppler distribution [23], which is manifested as a taller and narrower overall observed profile.

Dicke narrowing occurs in situations when the pressure is high enough so that a significant number of these elastic, velocity changing collisions occur within the dephasing time of the system, but also when the combination of the molecular mass, pressure and pressure broadening coefficients of the target transition means that the lineshape has a substantial contribution from the Doppler broadening mechanism and is not dominated by the pressure broadening caused by phase changing collisions, *i.e.* $\Delta\nu_D > \Delta\nu_L$. As $\Delta\nu_D \propto m^{-1/2}$ (Equation 1.13) and $\Delta\nu_L \propto \gamma p$ (Equation 1.10), Dicke narrowing is thus more likely to be observed when studying the transitions of lighter molecules with small pressure broadening parameters at lower pressures. For IR transitions of typical molecules at room temperature, this corresponds to pressures of 100 Torr or less [21].

There are two major models which quantitatively describe the narrowing effects of the velocity perturbing collisions on the lineshape, depending upon whether the collisions are

treated as hard or soft [21]. When the collisions are considered to be hard, such as when the mass of the perturber is much greater than that of the absorber, the velocity probability distribution after every collision is assumed to be Maxwellian, so that the velocity of each particle following the collision is independent of its velocity before. The lineshape obtained from this hard collision model is described by the Rautian profile [21].

However, in the soft collision limit, which is most appropriate for light perturbers, the effects of individual collisions are assumed to be negligible so that the final velocity is strongly correlated to the velocity prior to the collision. Hence it is only after the cumulative action of many collisions that a random velocity distribution is attained, at which point the molecular dynamics may then be modelled using Brownian motion. This soft collision model for velocity changes, with the assumption that velocity changing collisions are statistically independent of state changing collisions, gives rise to the Galatry profile [20], which can be written as [21, 432]:

$$N(x,y,z) = \frac{1}{\sqrt{\pi}}\mathrm{Re}\left[\int_0^\infty \exp\left\{-\mathrm{i}x\tau - y\tau + \frac{1}{2z^2}\left(1 - z\tau - \mathrm{e}^{-z\tau}\right)\right\}\mathrm{d}\tau\right] \tag{5.1}$$

where the dimensionless variables x, y and z are given by:

$$x = \frac{(\nu - \nu_0) - \delta p}{\Delta\nu'_D} \tag{5.2}$$

$$y = \frac{\gamma p}{\Delta\nu'_D} \tag{5.3}$$

$$z = \frac{k_B T}{2\pi c m \Delta\nu'_D D} \tag{5.4}$$

$$= z_0 p \tag{5.5}$$

In Equations 5.2-5.5, all the frequencies are in wavenumbers, δ is the line shift per unit pressure, $\Delta\nu'_D$ is the 1/e Doppler half-width related to $\Delta\nu_D$ (Equation 1.13) by $\Delta\nu'_D = \Delta\nu_D/2\sqrt{\ln 2}$, m is the molecular mass, D is the optical diffusion coefficient in $\mathrm{cm^2 s^{-1}}$ and other variables and constants are as listed in the Nomenclature. z is termed the standardised narrowing parameter and is related to the effective frequency of the velocity changing collisions within the soft collision approximation. As such, z scales with pressure as shown in Equation 5.5, where:

$$z_0 = \frac{k_B T}{2\pi c m \Delta\nu'_D D_0} \tag{5.6}$$

In this equation, the inverse pressure dependence of D has been removed to yield the pressure-independent optical diffusion coefficient, D_0, which is a function of temperature and some constants related to the gas species [429]. It is worthy of note that this optical diffusion coefficient, D, is similar, but not identical, to the conventional mass diffusion

coefficient, D_m, which also has units of cm^2s^{-1} and is approximated by [433]:

$$D_m = 2.6280 \times 10^{-3} \sqrt{\frac{T^3}{M_r}} \frac{1}{p\phi^2} \tag{5.7}$$

where M_r is the relative molecular mass, ϕ is the molecular diameter in Å and p has units of atm.

5.3.2.2 Results and discussion

CRD spectra of the D_2 electric quadrupole $\nu(1 \leftarrow 0)$ $Q(2)$ transition at 2987.29 cm^{-1} were recorded at a variety of pressures ($70 - 460$ Torr). Pure D_2 (*BOC*, 299917-AH) was used, and λ_p set at 1064.302 nm, T_{crys} at 84.5°C and λ_s stepped over the wavelength range $1560.396 - 1560.433$ nm in order to generate mid-IR light between $3345.38 - 3345.94$ nm ($2987.20 - 2987.35$ cm^{-1}) to cover the transition of interest.

In these experiments, very large absorbances were observed, corresponding to small τ_{act} values. Whilst using the single exponential decay model of Equation 1.49 and extracting τ_{act} from τ_{meas} using Equation 3.1 is a suitable method to find τ_{act} if $\tau_{\text{act}} > \tau_{\text{det}}$, it becomes less viable as the magnitude of τ_{act} approaches that of τ_{det}, as was the case in these measurements. In such situations, an alternative fitting function which better models the ring-down is required. Such a function can be created by taking the convolution of the exponential decay of the laser light with the (assumed) exponential decay originating from the response of the electronics of the system; this yields a sum of two weighted exponential decays. Hence, in these D_2 studies, the signal intensity, $I(t)$, at a time t was fitted with the double exponential decay model:

$$I(t) = \frac{S\tau_{\text{det}}}{\tau_{\text{det}} - \tau_{\text{act}}} \left(\tau_{\text{det}} e^{-(t-t_{\text{off}})/\tau_{\text{det}}} - \tau_{\text{act}} e^{-(t-t_{\text{off}})/\tau_{\text{act}}} \right) + S_0 \tag{5.8}$$

where S and S_0 are the amplitude and offset constants associated with the signal, respectively, τ_{act} and τ_{det} represent, as before, the true RDT and the contribution to the measured RDT from the electronics, respectively, and t_{off} is the time offset. This last constant ensures that the point $t = 0$ corresponds to the time when the cavity mode activated the trigger box and so the true start of the cavity ring-down, and thus is set equal to $-t_{\text{disc}}$. In fitting this function to the recorded data, values of $t_{\text{disc}} = 1.5$ µs and $t_{\text{fit}} = 40$ µs were used as before, and fixed values of $\tau_{\text{det}} = 1.6$ µs and $t_{\text{off}} = -t_{\text{disc}} = -1.5$ µs were also utilised.

In addition to averaging a given number of RDTs at every point in the spectrum, a series of sequential spectra of the same sample were also averaged. This methodology was employed to average out any thermo-mechanical drifts which may have occurred during the total data

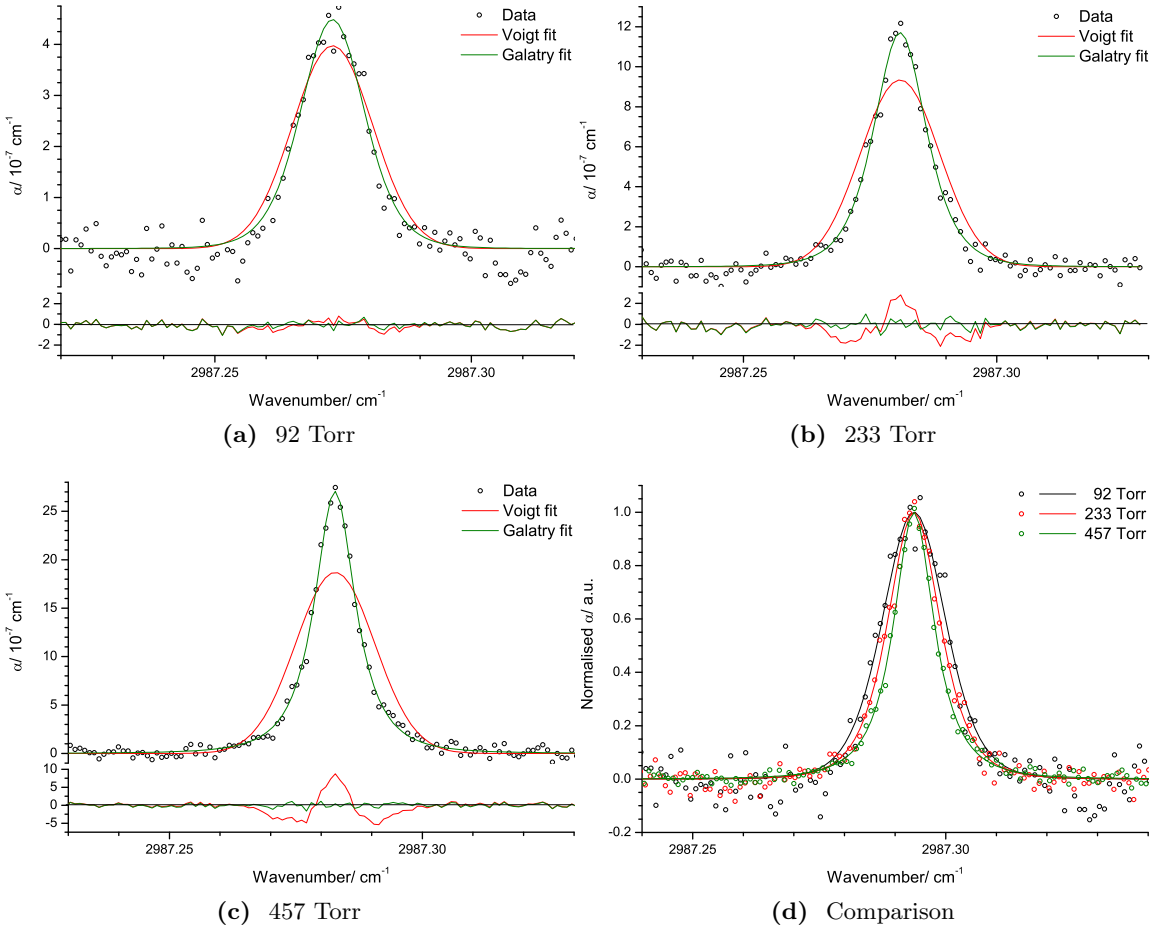

(a) 92 Torr **(b)** 233 Torr

(c) 457 Torr **(d)** Comparison

Figure 5.9: (a)-(c) Example absorption spectra of the $\nu(1 \leftarrow 0)$ $Q(2)$ D_2 transition under investigation at increasing pressures. The raw data are shown by the open circles and the Voigt and Galatry fits by the solid red and green lines, respectively; also given are the residuals between the two different fits and the data. In fitting the Voigt and Galatry profiles, the Gaussian width was fixed at the expected Doppler width of 554 MHz and the offset at zero; other parameters, including z, were allowed to float. A characteristic 'W' shape in the Voigt fit residual is clearly seen, indicating the occurrence of Dicke narrowing, and this becomes more pronounced at higher pressures; in contrast, the Galatry fit residual is much smaller and flatter showing that this profile is a better model for the lineshape. (d) Comparison of the normalised absorption data and Galatry fits for these plots in order to illustrate the effect of Dicke narrowing on the transition lineshape as pressure increases. The plots have also been shifted to the 2987.293 cm^{-1} zero pressure line position [402].

acquisition time [434, 435]. The RDT was evaluated and averaged $n_{\text{avg}} = 10$ times at 127 points across the spectral range with a settling time between points of $t_{\text{sett}} = 0.2$ s, and then 10 RDT spectra averaged with a settling time of 7 s between spectra. This procedure took ~ 40 mins.

These two ideas, of extracting τ_{act} using the double exponential fitting model of Equation 5.8 and of averaging sequentially recorded RDT spectra, were combined with Program Two of Section 3.1.2 to obtain spectra of τ against λ_i. A τ_0 baseline was fitted to the data, using

Take	Pressure / Torr	Line centre / cm^{-1}	HWHM / cm^{-1}	Area / cm^{-2}	z	R^2
1	73.7	2987.281	0.00838	0.667×10^{-8}	0.229	0.9348
2	91.7	2987.273	0.00759	0.748×10^{-8}	0.412	0.9311
3	104.6	2987.275	0.00665	0.913×10^{-8}	0.509	0.9690
4	136.3	2987.289	0.00721	1.069×10^{-8}	0.529	0.9744
5	176.5	2987.272	0.00663	1.405×10^{-8}	0.629	0.9730
6	192.3	2987.275	0.00604	1.476×10^{-8}	0.624	0.9815
7	232.6	2987.281	0.00622	1.703×10^{-8}	0.695	0.9845
8	264.2	2987.287	0.00563	1.976×10^{-8}	0.858	0.9809
9	251.3	2987.278	0.00674	1.902×10^{-8}	0.676	0.9874
10	310.2	2987.282	0.00553	2.251×10^{-8}	0.916	0.9885
11	369.1	2987.269	0.00523	2.689×10^{-8}	1.027	0.9943
12	456.8	2987.284	0.00486	3.408×10^{-8}	1.251	0.9936

Table 5.4: Results of Galatry fits to the recorded data of the $\nu(1 \leftarrow 0)$ $Q(2)$ transition of D_2 at various pressures ($70 - 460$ Torr). In fitting the Galatry profiles, the Gaussian width was fixed at the expected Doppler width, $\Delta\nu_D$, of 554 MHz and the offset at zero, whilst other parameters were allowed to float. The line centres reported have been corrected for the -0.002 cm^{-1}amagat^{-1} pressure shift for this transition [424, 436]; the average of these zero pressure line positions is 2987.279 ± 0.006 cm^{-1}. R^2 is the coefficient of determination and indicates how well the Galatry curve fits the data points.

either a linear (pressures < 300 Torr) or cubic (> 300 Torr) polynomial, and α calculated using Equation 1.53. It is noteworthy that this process of averaging the τ spectra and then converting this average to an α spectrum gave the same result as transforming the individual τ spectra to α spectra before averaging these α spectra. As the former method was easier to implement, this technique was adopted.

Examples of the absorption spectra recorded at different pressures are given in Figure 5.9. These were fitted using both a Voigt and Galatry profile, and in both cases the vertical offset was set at zero and the Gaussian width at the expected Doppler width of 554 MHz whilst allowing other parameters, including the Galatry z narrowing parameter, to float. A 'W' structure is clearly observed in the residuals of the Voigt fits which is indicative of Dicke narrowing, and this residual structure becomes more pronounced at higher pressures as this narrowing effect becomes more significant. In comparison, the Galatry profile provides a much better fit for the recorded data as the residuals are smaller and unstructured.

Table 5.4 summarises the results of the Galatry fits of the data recorded at various pressures, and some of these properties are displayed in Figure 5.10. From these plots and data, it was possible to calculate values for the line centre, σ_{int} and D_0 of 2987.279 ± 0.006 cm^{-1}, $2.29 \pm 0.03 \times 10^{-27}$ cm^{2}cm^{-1}molec^{-1} and 1.20 ± 0.05 cm^{2}amagat s^{-1}, respectively, where an amagat is a unit of number density defined as the number of ideal gas molecules per unit volume at 1 atmosphere of pressure and 0°C [433].

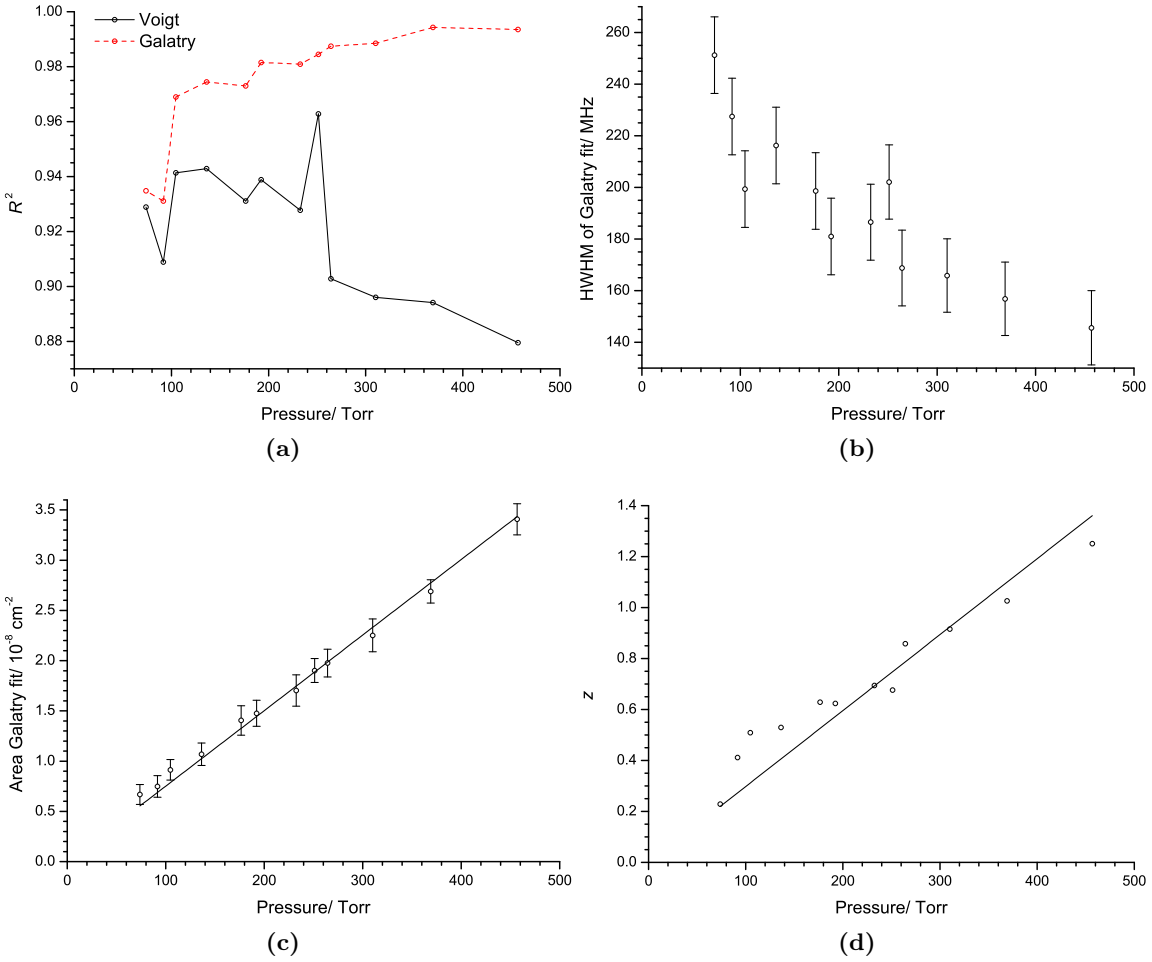

Figure 5.10: Plots concerning the Galatry fits to the data of the $\nu(1 \leftarrow 0)$ $Q(2)$ transition of D_2 at various pressures. (a) The appropriateness of using a Galatry, rather than Voigt, profile is indicated by the goodness of fit parameter, R^2, for the different experimental data sets: as pressure increases, the Voigt fit becomes increasingly worse whereas the Galatry fit remains good. (b) The reduction in the HWHM of the Galatry fit as pressure increases, signifying the increasing effect of Dicke narrowing. The error bars were estimated from the frequency resolution of the fit returned by the in-house developed Galatry fitting routine [437]. (c) The gradient of the plot of the area of the Galatry fit against pressure allows an estimate of σ_{int} to be found; using a linear fit with the intercept fixed at the origin, σ_{int} was calculated as $2.29 \pm 0.03 \times 10^{-27}$ $\text{cm}^2\text{cm}^{-1}\text{molec}^{-1}$. (d) By considering Equations 5.5 and 5.6, the slope of the line of best fit of a plot of z against pressure can be used to find D_0; fixing the intercept of the linear fit at the origin, D_0 was estimated as 1.20 ± 0.05 $\text{cm}^2\text{amagat}\,\text{s}^{-1}$.

There are several recorded observations of Dicke narrowing for different D_2 transitions in the IR in the literature; the results of these experimental studies which pertain to the $\nu(1 \leftarrow 0)$ $Q(2)$ transition under investigation here are given in Table 5.5, along with the reported results of simulations. The findings of this work with regards to the line centre, σ_{int} and D_0 are consistent with those measured or calculated previously. Though the line centre found in this work is 0.014 cm^{-1} lower than that predicted by Kassi *et al.* [402], this is of the order of the 0.01 cm^{-1} error associated with the wavemeter used for frequency

Reference	Technique	Light source	Line centre / cm^{-1}	D_0 / $cm^2 amagat\, s^{-1}$	σ_{int} / $cm^2 cm^{-1} molec^{-1}$
Brannon *et al.*, 1968 [422]	Electric field induced absorption spectroscopy	Carbon arc lamp, quartz iodine tungsten filament lamp	2987.268 ± 0.020		
McKellar and Oka, 1978 [426]	Electric quadrupole absorption spectroscopy	DFG: 488/515 nm Ar^+ laser (pump), tunable dye laser (signal), $LiNbO_3$	2987.2955 ± 0.0040		
Jennings *et al.*, 1986 [423]	Raman spectroscopy	Ar-ion laser	2987.289 ± 0.007		
Smyth *et al.*, 1987 [411]	Raman spectroscopy	Kr-ion laser (pump), tunable ring dye laser (probe)		0.967 ± 0.022 ‡	
Forsman *et al.*, 1992 [410]	Raman spectroscopy	Ar-ion laser (pump), tunable dye laser (probe)		0.955 ± 0.032 ∗	
Gupta *et al.*, 2007 [427]	Simulation		2987.288		
Komasa *et al.*, 2011 [428]	Simulation		2987.2934		
Kassi *et al.*, 2012 [402]	Simulation		2987.2934		2.378×10^{-27}
This work, 2013	Electric quadrupole absorption spectroscopy	DFG: 1064 nm DL (pump), 1560 nm DL (signal), PPLN	2987.279 ± 0.006	1.20 ± 0.05	$2.29 \pm 0.03 \times 10^{-27}$

Table 5.5: Data for the $\nu(1 \leftarrow 0)$ $Q(2)$ transition of D_2 reported in the literature and found in this work. All line centres have been corrected for pressure induced shifting so represent the zero pressure line positions. D_0 values reported are for $Q(2)$ transitions in pure D_2 samples measured at 25.4°C (‡) and 30.2°C (∗), and compare well with the literature value of the mass diffusion coefficient of pure D_2 at rtp of 0.950 $cm^2 amagat\, s^{-1}$ [411, 433].

Mode	Approximate type of mode	Symmetry	$\tilde{\nu}$/ cm^{-1}
ν_1	CH_3 degenerate stretch	A_1	3019
ν_2	CH_3 symmetric stretch	A_1	2937
ν_{13}	CH_3 degenerate stretch	B_1	3019
ν_{14}	CH_3 symmetric stretch	B_1	2937
ν_{20}	CH_3 degenerate stretch	B_2	2972

Table 5.6: IR active fundamental vibrational modes of acetone over the 3.3 μm region [405].

calibrations. Of greater significance, however, is the very good agreement between the calculated σ_{int} and this first experimental measurement of it. Yet most importantly of all, the fact that Dicke narrowing was clearly observed on the D_2 $\nu(1 \leftarrow 0)$ $Q(2)$ transition, with the features better fitted by Galatry rather than Voigt profiles, has demonstrated the capability of the DFG CRDS system to perform high resolution spectroscopy.

5.3.3 Acetone

Acetone belongs to the C_{2v} point group and due to its relatively large, bulky size has a greater number of, and more complex, vibrational modes than those of smaller absorbers such as CH_4. These manifest themselves as broad, congested IR absorption features meaning that acetone is classified as a broadband absorber. Its rotational spectrum is particularly complicated by the internal rotation of the two methyl groups and their interaction with each other and the rigid-body rotation of the rest of the molecule [438]. There are 24 vibrational modes of acetone [405]; the IR active bands centred over the 3 μm region which are shown in Figure 5.6 are listed in Table 5.6.

Single wavelength studies, similar to those performed in Section 3.2, were conducted. A 5.37 ± 0.27 ppm calibrated mixture of acetone in N_2 (*BOC*, 166668-AK-C) was used. The pump and signal wavelengths were set as 1064.304 nm and 1560.035 nm, respectively, and T_{crys} at 81.7°C, generating mid-IR radiation at 3349.299 nm (2985.70 cm^{-1}).

There were two important issues that needed to be addressed in order to carry out these experiments. One was that, because acetone is a broadband absorber, it was necessary to record a separate τ_0 value with the same cavity conditions and alignment as those used for the sample measurements. The other was that the cavity mirror alignment altered slightly with large changes in the cell pressure ($\sim$ 100 Torr). In order to overcome these problems, the RDTs were recorded as follows. An evacuated cell was flushed and then filled with approximately 90 Torr of N_2, at which point τ_0 was measured. The cavity was then flushed with the acetone sample, maintaining a constant, similar pressure inside the

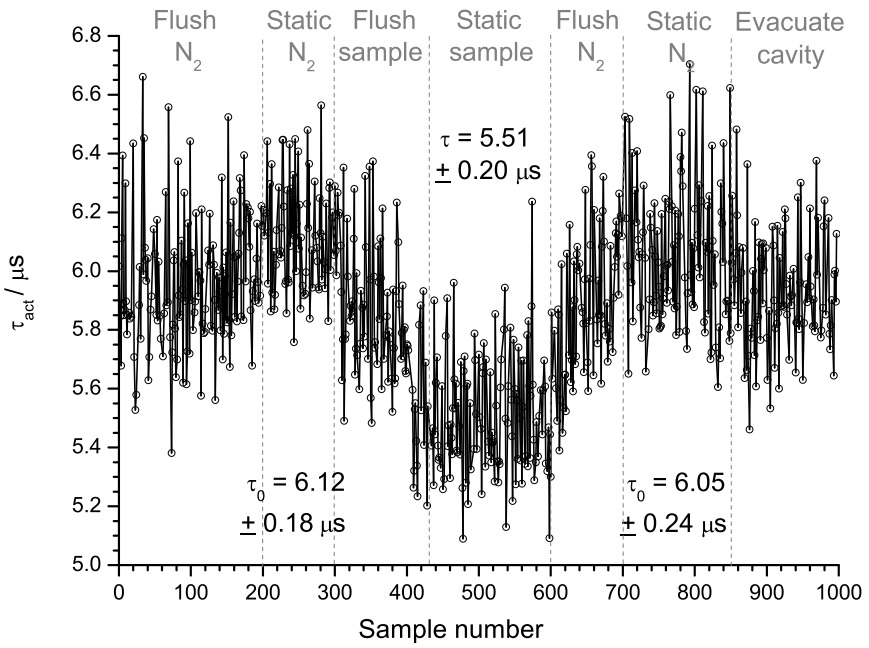

Figure 5.11: Change in RDT recorded using the mid-IR CRD spectrometer at a single wavelength (2985.70 cm^{-1}) on filling the cavity with approximately 90 Torr of a 5 ppm calibrated mixture of acetone in N_2. The independent axis gives the number of RDTs recorded, approximately one every 0.5 seconds. τ_0 was measured by filling the cavity with $\sim$ 90 Torr of N_2. The cell was then flushed and filled with the sample to $\sim$ 90 Torr, observed as a reduction in the RDT. After a period of time, the cavity was re-flushed with N_2 and a post-sample τ_0 recorded. By measuring the RDT with and without the sample, and estimating the absorption cross-section of acetone for this wavelength from the PNNL data [403], the acetone concentration was calculated; for this example, a concentration of 5.34 ppm was found.

cell, before filling with $\sim$ 90 Torr of the calibrated mix. τ was recorded while holding this stationary sample of acetone inside the cavity. Afterwards, the cell was flushed and re-filled with $\sim$ 90 Torr N_2 in order to measure a post-sample τ_0 to check that no significant changes in the background RDT had occurred, before evacuating the cavity ready for the next experiment. An example of this procedure is shown in Figure 5.11, and the results of repeated runs summarised in Table 5.7. The acetone concentration calculated from the average of the experimental results (5.26 ± 0.08 ppm) agreed well with that quoted by the manufacturer (5.37 ± 0.27 ppm) for this 5 ppm mixture.

Following on from these single wavelength studies, it was desired to determine the optimum wavelength in order to perform acetone measurements in breath. This selection is dependent on two criteria: the chosen wavelength must be one at which acetone absorbs strongly but is also free from absorbances due to other species present in the sample. The two strongest absorption features of acetone as determined from the experimental PNNL data (Figure 5.6) [403], which occur at 2970 cm^{-1} and 3017 cm^{-1} and correspond to the $\nu_{20}(B_2)$ and $\nu_1(A_1)/\nu_{13}(B_1)$ vibrational modes, respectively, were identified as regions of interest owing to their large and distinct absorption profiles; this latter point was significant as it

Cal. mix	Take	p / Torr	τ_0/ µs Before	τ_0/ µs After	τ / µs	α / cm^{-1}	Acetone conc. / ppm
5 ppm	1	91.8	6.13 ± 0.20	6.06 ± 0.21	5.49 ± 0.17	6.34×10^{-7}	5.34
	2	89.0	6.12 ± 0.18	6.05 ± 0.24	5.51 ± 0.20	6.05×10^{-7}	5.26
	3	89.6	6.14 ± 0.20	6.07 ± 0.18	5.53 ± 0.20	6.00×10^{-7}	5.18
							5.26 ± 0.08

Table 5.7: Results of the single wavelength studies of the 5.37 ± 0.27 ppm calibrated mixture of acetone in N_2 at 2985.70 cm^{-1}. All experiments were performed at sample pressures of approximately 90 Torr. τ_0 values were recorded before and after the introduction of the sample into the cavity, with those measured before used to calculate the absorption. An estimate of the absorption cross-section of acetone at this wavelength ($\sigma = 3.96 \times 10^{-20}$ cm^{2}molec^{-1}) from the PNNL data [403] was used to find the concentration of acetone. An average of the results of the acetone concentration in terms of ppm for the calibrated mixture was then computed (value at base of 'Acetone conc./ ppm' column); this agreed well with the expected value.

allowed for the potential of recording spectra over a wavelength range to observe changes in absorbance and therefore fit the spectral feature. Simulations of the absorbance of acetone at concentrations of 1 ppm and 5 ppm in a breath-like matrix (2% H_2O in air) at 100 Torr for these two ranges are shown in Figure 5.12, using the 1.84 km effective path length found in Figure 5.5(a) in Section 5.2.3 and data from the HITRAN 2004 [14] and PNNL [403] databases. It can be seen that in both regions the absorbance by acetone is appreciable, but the 2970 cm^{-1} feature was judged preferable for study as acetone absorbs more strongly here and it suffers less from interference by other absorbing species.

On fixing the pump laser wavelength at 1064.3 nm, it was calculated that a signal laser source operating at 1556.2 nm and 1567.7 nm would be required to monitor the features at 2970 cm^{-1} and 3017 cm^{-1}, respectively. Furthermore, in order to scan over the FWHM of the absorption features, it was also determined that the signal source in both cases needed a tunability of ±0.3 nm about the central wavelength. Thus whilst the 3017 cm^{-1} feature was accessible using the DS-DBR as the signal source, the preferred absorbance at 2970 cm^{-1} was not.

As such, a DFB diode laser (*Fitel*, FRL15DCWD-A81-19265-C) centred at 1556.2 nm with a 1 MHz linewidth and 40 mW output power was purchased. This was substituted for the *JDSU* 1560 nm diode laser previously used as the signal source (Sections 4.3, 5.2 and 5.3.1, Figure 5.1(a)) and T_{crys} altered accordingly in order to maximise the generation of mid-IR radiation at the new wavelength of 2970 cm^{-1}. Although light of a similar power to earlier experiments was produced, noisy cavity modes were observed which were broader and lower in peak amplitude than expected (Figure 5.13). This effect was similar to the behaviour seen earlier when the DS-DBR was used as a near-IR light source for CRDS (Section 3.3.2.1). These previous studies with the DS-DBR had revealed, however, that

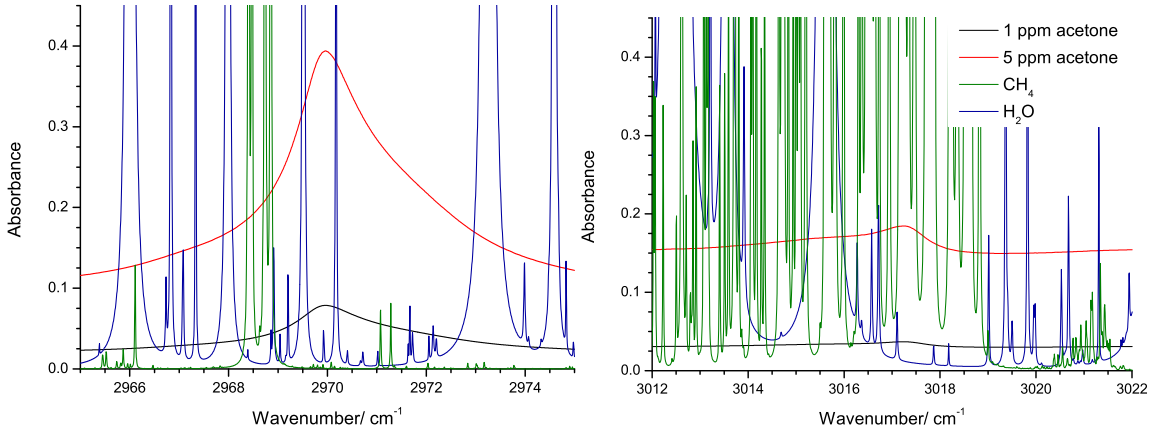

(a) 2970 cm^{-1} **(b)** 3017 cm^{-1}

Figure 5.12: Simulations using HITRAN 2004 [14] and PNNL [403] data of the expected absorbances of 1 ppm and 5 ppm acetone in breath (2% H_2O in air) over the 2970 cm^{-1} and 3017 cm^{-1} regions, using the measured effective path length of the CRDS system of 1.84 km.

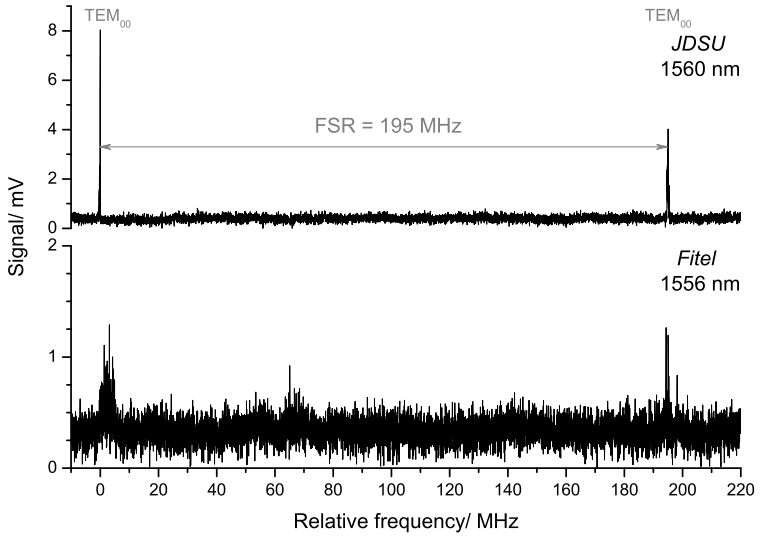

Figure 5.13: Cavity transmission of mid-IR light using two different DFB diode lasers as the signal radiation source. The same cavity, cavity scanning conditions and pump radiation source (λ_p = 1064.298 nm) were used in both cases, as well as the different optimum T_{crys} required for the different wavelengths. From Equation 1.39, the cavity modes for this mid-IR system were predicted to have widths of $\Delta\nu_{\text{mode}}$ = 25 kHz. In the upper trace, the *JDSU* 1560 nm DL was used as the signal source with λ_s = 1559.896 nm and T_{crys} = 83.5°C to generate 15.0 µW of mid-IR light at 2985.181 cm^{-1}; strong, sharp cavity modes (Lorentzian FWHM of 0.3 MHz, limited by the DL linewidth) were observed which could be discriminated by the trigger box and so used to record RDTs. In the lower trace, the *Fitel* 1556 nm DL was used as the signal source with λ_s = 1556.323 nm and T_{crys} = 70.6°C yielding 13.5 µW of mid-IR light at 2970.463 cm^{-1}; much wider, noisier and weaker cavity modes (Lorentzian FWHM of 5.5 MHz) were now seen, which were too small for the trigger box to detect.

the noisy cavity modes could still be used to report accurate RDTs. But whereas in the case with the DS-DBR in the near-IR an amplifier could be used to boost the signal of the weak, noisy cavity modes so they could be detected by the trigger box and hence activate the system, this was not possible with the *Fitel* 1556 nm DL in the mid-IR because the signal had already been pre-amplified by the detection module; this action had introduced a large τ_{det} ($\sim$ 1.6 µs) relative to τ_{act} ($\sim$ 6 µs) thereby making a significant contribution to τ_{meas} (Equation 3.1), and any further increase in τ_{det} would have led to an even greater uncertainty in τ_{act} found. So although the *Fitel* laser linewidth was nominally 1 MHz, its bandwidth was sufficiently large compared to that of the *JDSU* laser that high quality modes could not be observed in the mid-IR; the reduced height of these modes meant they could no longer be distinguished by the trigger box and hence no ring-downs could be recorded. This highlights a significant problem when buying commercial products where only minimal specifications are provided.

5.4 Improving the DFG-Based CRD Spectrometer

5.4.1 Alterations

Towards the end of this work, two major changes were made to the DFG-based CRD spectrometer in order to increase its sensitivity levels and improve its performance. The first was to substitute the pump DL used heretofore with a more powerful (500 mW), single-mode Nd:YAG laser (*Laser Quantum*, Forte-S 1064 500 mW) in order to maximise the amount of mid-IR radiation generated (Equation 4.36). This laser was not fibre-coupled, but the collimated beam output had a Gaussian beam profile with a spot size of 1.1 mm, which was similar to the 1.2 mm value measured after the fibre coupler of the DL used earlier. Additionally, the typical operating wavelength of the YAG laser was observed to be 1064.525 nm, which was slightly higher than the usual 1064.300 nm output of the pump DL employed before. However, simulations indicated that this change in λ_p by +0.2 nm only required an increase in T_{crys} of $0.1 - 0.4$°C compared to values found previously over the $1560 - 1615$ nm signal wavelength range. A comparison of the mid-IR power levels attained with the different pump radiation sources is given in Table 5.8.

In contrast to the manufacturer's specification, the YAG was not observed to exhibit exclusively single-mode behaviour, but fluctuated between single- and multi-mode behaviour with time. This effect was monitored using a spectrum analyser with a FSR of 10 GHz (*Melles Griot*, 13SAE046) and an oscilloscope (*LeCroy*, Waverunner 6100A, 1 GHz, 10 GSa/s), as shown in Figure 5.14. It was noted that drifts between the two different behaviours was most prominent after the laser was initially switched on, and that the

Pump	λ_p / nm	P_p / mW	Signal	λ_s / nm	P_s / mW	Λ / µm	T_{crys} / °C	λ_i / nm	P_i / µW	η / % W^{-1}cm^{-1}	Section
DBR	1064.295	66	DFB + C-band EDFA	1560.800	112	30.00	84.3	3345.69	15.8	0.053	4.3.3 5.2.1
YAG	1064.527	214	DFB + C-band EDFA	1560.748	117	30.00	84.5	3348.22	73.4	0.073	5.4.1

Table 5.8: A comparison of the mid-IR radiation generated using the DBR DL and YAG as the pump laser. Both the pump and signal powers are those measured incident on the PPLN, *i.e.* in the case of P_p, after the OI, and for P_s, after the IL-OI, EDFA and AOM.

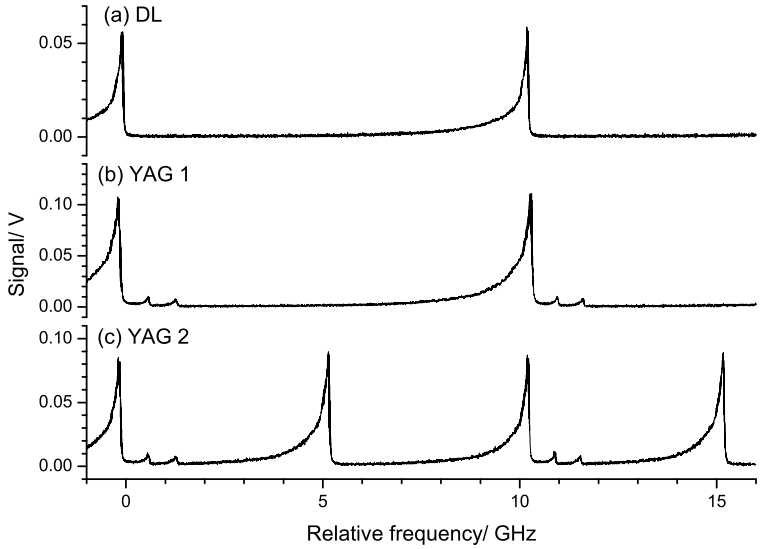

Figure 5.14: Transmission spectra of the 10 GHz, 1064 nm spectrum analyser when seeded with light from (a) the 1064 nm DL and (b), (c) the Nd:YAG laser. In (a), single-mode behaviour of the DL is observed, whereas the YAG laser alternates between (b) single-mode and (c) multi-mode behaviour with time; these two traces were recorded 2 mins apart.

severity of the multi-mode behaviour also varied. In general, once fully warmed, the laser displayed periods of single-mode behaviour lasting between $10 - 30$ mins. Hence, to ensure experimental data was only recorded during these times of desired single-mode behaviour, the waste pump radiation reflected by the Ge filter (Figure 5.1(a)) was injected into the spectrum analyser and the result constantly monitored to inspect the YAG performance.

In addition to changing the pump radiation source, a new detector and amplification system was also installed. This new detector was a 4-stage thermoelectrically cooled HgCdZnTe photodiode (MCZT-PD) detector, optimised for detection at 3.4 µm, which was coupled with a 20 MHz pre-amplifier (*Vigo Systems*, PVI-4TE-3.4/MIPDC-F-20); full details are listed in Table 1.1. The high bandwidth of this detection module meant that a custom-built variable gain, variable low pass filter amplifier could be used in conjunction with the detector to enhance the output signal with a corresponding small increase in response time, whilst still being faster overall than the previously utilised PVI-2TE-4/VPDC-0.1l

Gain		τ_{det}/ µs
15 dB	×5.6	0.55
20 dB	×10.0	0.55
25 dB	×17.8	0.53
30 dB	×31.6	0.52
35 dB	×56.2	0.52
40 dB	×100.0	0.51
45 dB	×177.8	0.51
50 dB	×316.2	0.50
55 dB	×562.3	0.49

Table 5.9: A table of the gain settings and associated τ_{det} of the new detector and amplification system, using the 500 kHz low pass filter on the amplifier.

detection module. Table 5.9 gives the gain settings accessible with this amplifier, as well as the measured τ_{det} of this combined new detector and amplifier system when using the 500 kHz low pass filter on the amplifier.

5.4.2 Characterisation

The pump and signal wavelengths were set at 1064.527 nm and 1560.742 nm, respectively, generating mid-IR light at 3348.250 nm (2986.64 cm^{-1}). This light was coupled into an evacuated cavity and cavity modes with the new system (using a gain setting of 25 dB and a low pass filter of 500 kHz on the amplifier) were observed; an example is shown in Figure 5.15. 960 ring-downs were then sequentially recorded over 4.5 mins, which were fitted with the LRS fitting routine described in Section 3.1.2 and τ_0 extracted using Equation 3.1 with $\tau_{\text{det}} = 0.53$ µs; an example of such a ring-down and fit is shown in Figure 5.16(a).

Again, it was noted that the effectiveness of the triggering on the cavity modes, and the requirement for conditioning criteria to filter the results, were significant factors in the overall conversion of cavity modes into valid RDTs. Here, results were discarded if the R^2 values of their exponential fits were lower than 0.95 or the RDT was outside the ±3 standard deviation range of the overall average.

The filtered results of this data set were used to construct an Allan variance plot [225], shown in Figure 5.16(b). From this plot it was seen that the maximum sensitivity corresponded to an average of 537 RDTs, with $\tau_0 = 5.9840 \pm 0.0007$ µs (1σ), yielding an α_{min} of 6.4×10^{-10} cm^{-1} over 151 s ($\alpha_{\text{min}}(BW) = 7.8 \times 10^{-9}$ cm^{-1}Hz$^{-1/2}$). This is better than the optimal α_{min} of 2.9×10^{-9} cm^{-1} attained by averaging 730 RDTs over 44 s ($\alpha_{\text{min}}(BW) = 1.9 \times 10^{-8}$ cm^{-1}Hz$^{-1/2}$) found using the previous pump laser and detection system in Section 5.2.3.

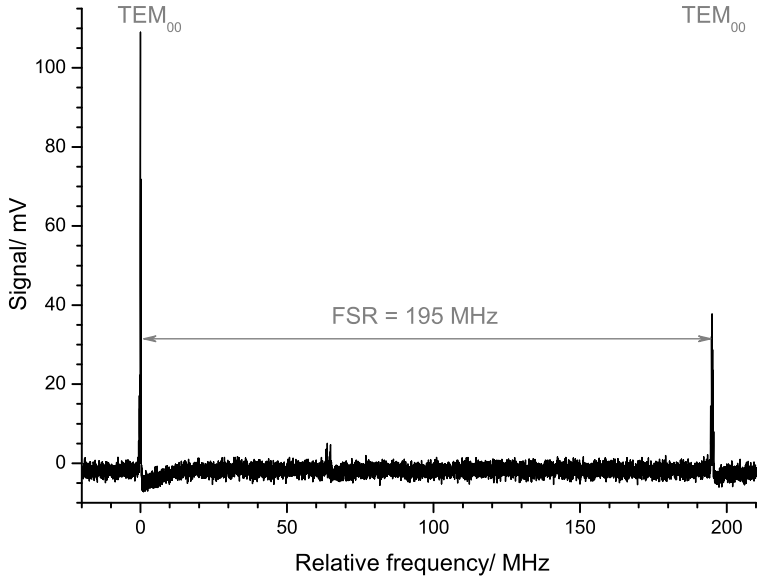

Figure 5.15: Cavity transmission of the mid-IR light on scanning the PZT of the improved DFG-based CRD spectrometer, in which the pump radiation source was replaced with a more powerful YAG laser and a new detector and amplification system utilised, with the amplifier settings at 25 dB gain and 500 kHz low pass filtering. Once again, a well-aligned CRDS cavity, supporting predominantly TEM_{00} modes, was achieved.

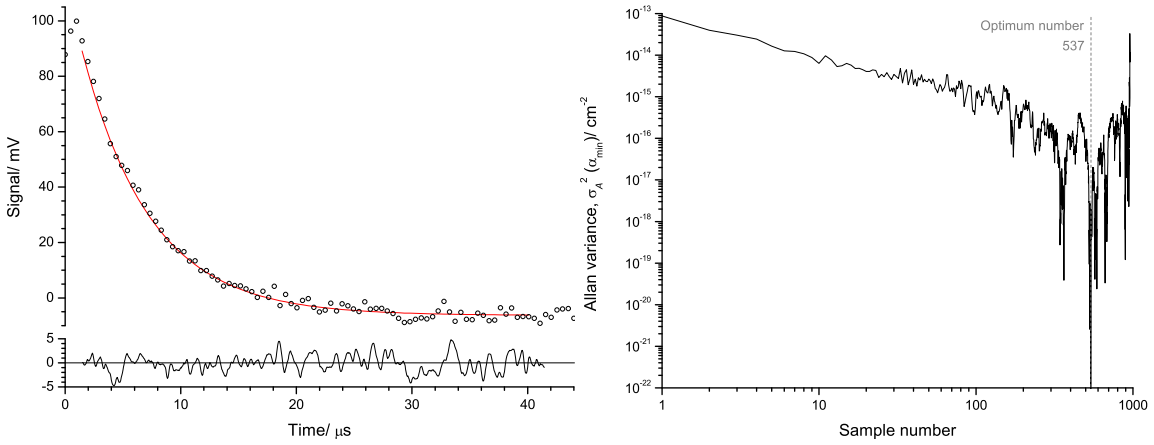

(a) **(b)**

Figure 5.16: Ring-downs recorded of an evacuated cavity at a single wavelength (3348.250 nm). (a) An example of a ring-down trace with the raw data given by the open circles (only a reduced number of data points are shown for clarity) and the exponential fit by the solid line; the residuals between the two are given in the lower plot. The fitting routine only used data recorded $1.5 - 41.5$ μs after the trigger and returned a τ_0 of 6.03 μs, indicating a mirror reflectivity of 0.9996 and effective path length of 1.81 km. (b) An Allan variance plot of the $\alpha_{\min}$ values calculated from sequentially recorded ring-downs under the same conditions over 4.5 mins. The results were filtered so that only ring-downs which had fits with $R^2 > 0.95$ were used. Inspection of this plot indicated that an optimum number of ring-downs to record and average per point would be 537, giving an $\alpha_{\min}$ of 6×10^{-10} cm^{-1}.

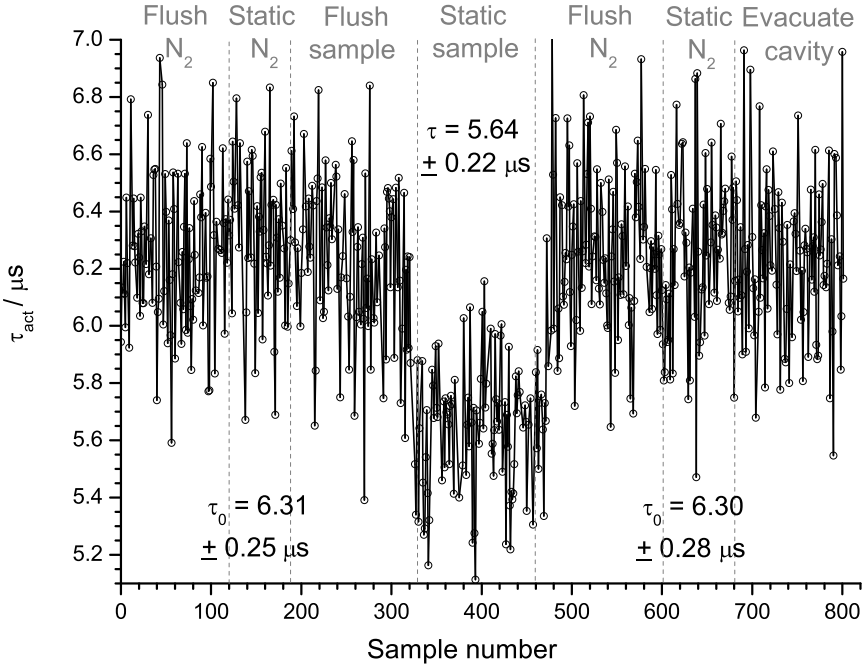

Figure 5.17: Change in RDT recorded using the improved mid-IR CRD spectrometer at a single wavelength (2985.70 cm^{-1}) on filling the cavity with approximately 90 Torr of a 5 ppm calibrated mixture of acetone in N_2, following the same procedure as that described in Section 5.3.3. For this example, the acetone concentration was calculated as 5.30 ppm.

5.4.3 Spectroscopic measurements

In order to test this improved mid-IR spectrometer, single wavelength studies of the 5.37 ± 0.27 ppm calibrated mixture of acetone in N_2 were repeated. The pump and signal wavelengths were set as 1064.525 nm and 1560.510 nm, respectively, and T_{crys} at 81.8°C, generating mid-IR radiation at 3349.299 nm (2985.70 cm^{-1}). The same methodology as outlined in Section 5.3.3 was applied; an example of one of the experimental runs is shown in Figure 5.17, and the results from four different trials are given in Table 5.10. Once again, the acetone concentration calculated from the average of the experimental results (5.24 ± 0.06 ppm) compared favourably with that specified by the manufacturer (5.37 ± 0.27 ppm), and also agreed well with the value found using the previous CRD spectrometer set-up (5.26 ± 0.08 ppm).

5.5 Conclusions

The combination of mid-IR light generated by QPM-DFG (Chapter 4) with CRDS (Chapter 3) is an attractive strategy for gas sensing spectroscopic applications and in this chapter, it has been demonstrated that an all DL sourced DFG-based CRD spectrometer at 3 μm is a viable and useful technique for such a purpose.

Cal. mix	Take	p / Torr	τ_0/ µs Before	τ_0/ µs After	τ / µs	α / cm^{-1}	Acetone conc. / ppm
5 ppm	1	87.4	6.32 ± 0.24	6.26 ± 0.25	5.64 ± 0.25	5.85×10^{-7}	5.18
	2	86.5	6.26 ± 0.23	6.31 ± 0.25	5.69 ± 0.24	5.82×10^{-7}	5.21
	3	90.8	6.31 ± 0.25	6.30 ± 0.28	5.64 ± 0.22	6.21×10^{-7}	5.30
	4	83.4	6.17 ± 0.26	6.23 ± 0.27	5.63 ± 0.23	5.71×10^{-7}	5.30
							5.24 ± 0.06

Table 5.10: Results of the single wavelength studies of the 5.37 ± 0.27 ppm calibrated mixture of acetone in N_2 at 2985.70 cm^{-1} found using the improved DFG-based CRD spectrometer. The τ_0 values measured after the introduction of the sample into the cavity were used to calculate the absorption, and an estimate of the absorption cross-section of acetone at this wavelength ($\sigma = 3.96 \times 10^{-20}$ cm^{2}molec^{-1}) from the PNNL data [403] was used to find the concentration of acetone. An average of these results was then computed (value at base of 'Acetone conc./ ppm' column).

Light from a 1560 nm diode laser, amplified by an EDFA, was mixed with 1064 nm radiation from another diode laser in a bulk PPLN crystal to generate mid-IR light with powers of $10 - 20$ µW. This light was injected into a 77 cm long cavity with mirror reflectivities of 0.9996 to give cavity modes which were used to perform CRDS. On flushing the cavity with N_2, a τ_0 of 6.07 µs with a standard deviation of 0.03 µs was measured, implying a minimum detectable absorption coefficient of 2.8×10^{-8} cm^{-1} over 6 s ($\alpha_{\min}(BW) = 6.9 \times 10^{-8}$ cm^{-1}Hz$^{-1/2}$) when filtering and averaging 100 ring-downs per point. Allan variance analysis indicated an optimal $\alpha_{\min}$ of 2.9×10^{-9} cm^{-1} by averaging 730 RDTs over 44 s ($\alpha_{\min}(BW) = 1.9 \times 10^{-8}$ cm^{-1}Hz$^{-1/2}$). Such sensitivities are comparable with the only other similar study reported in the literature, that of Stry *et al* [94].

The use of the DFG CRDS system for spectroscopic applications was illustrated by performing experiments on a variety of molecules. Initially, the mid-IR CRD spectrometer was used to investigate the narrowband absorber CH_4 at low pressures (< 25 Torr). Studies of the ($2\ F_1\ 9 \leftarrow 3\ F_2\ 1$) $P(3)$ transition in the fundamental $\nu_3(F_2)$ band at 2988.933 cm^{-1} were used to find the concentration of CH_4 present in a 7.5 ppm calibrated mixture of CH_4 in air and in breath samples from both methane and non-methane producers. The results, 7.59 ± 0.16 ppm, 29.4 ± 1.0 ppm and 2.26 ± 0.10 ppm, respectively, correlate well with the anticipated concentrations. The Lorentzian widths of the Voigt fits of the spectra were also of the order expected given the pressure regimes used. The optimal $\alpha_{\min}$ of 2.9×10^{-9} cm^{-1} implied a detection limit of 5 ppb over 42 s for the same conditions.

The spectrometer was then used to study the $\nu(1 \leftarrow 0)\ Q(2)$ transition of D_2 at 2987.29 cm^{-1} to assess the ability of the system to perform high resolution spectroscopy. The absorption profile of this transition was measured at various pressures ($70 - 460$ Torr) and was observed to narrow as pressure increased due to Dicke narrowing. This was clearly demonstrated

by the characteristic 'W' feature seen in the residuals between the data and Voigt fits, which became more apparent at increased pressures. Instead, the lineshapes were more accurately represented by Galatry profiles, which accounted for the collisional narrowing. The fact that the system could detect these differences in lineshape demonstrated its capacity for high resolution work. From these measurements, a σ_{int} value for this transition of $2.29 \pm 0.03 \times 10^{-27}$ cm^{2}cm^{-1}molec^{-1} was also found, which was in very good agreement with that predicted by theoretical calculations of 2.378×10^{-27} cm^{2}cm^{-1}molec^{-1}.

Measurements of acetone were also conducted in order to assess the capability of the DFG CRD spectrometer to detect broadband absorbers. Single wavelength studies at 2985.70 cm^{-1} of a 5.37 ± 0.27 ppm calibrated mixture of acetone in N_2 were carried out by recording τ_0 and τ values at this wavelength with the cavity filled with ~ 90 Torr of N_2 and the sample, respectively. The calculated concentration of 5.26 ± 0.08 ppm compared favourably with the expected value.

Finally, two modifications to enhance the sensitivity of the DFG-based 3 μm CRD spectrometer were made: a 500 mW Nd:YAG laser was substituted for the pump radiation source in order to boost the amount of mid-IR power, and a new detector and amplification unit, capable of recording data faster with larger amplification gains, was emplaced. These amendments led to an improvement in the maximum sensitivity achievable with the spectrometer, with Allan variance measurements signifying a new optimal α_{min} of 6.4×10^{-10} cm^{-1} over 151 s ($\alpha_{\text{min}}(BW) = 7.8 \times 10^{-9}$ cm^{-1}Hz$^{-1/2}$). The spectroscopic utility of this system was then tested by repeating the single wavelength studies at 2985.70 cm^{-1} of the 5 ppm calibrated mixture of acetone in N_2; this time, an acetone concentration of 5.24 ± 0.06 ppm was calculated.

The results of all these experiments indicate that the DFG CRD spectrometer is capable of measuring high resolution spectra with high sensitivity. However, whilst the DLs used in the DFG system used here offer many advantages, they only cover a small spectral range. Replacing the 1560 nm diode laser with the widely tunable DS-DBR laser of Chapter 2 would evidently allow a larger range of mid-IR radiation to be generated ($3000 - 3200$ cm^{-1}), and this use of the DS-DBR as the signal laser for DFG, and the combination of the resultant mid-IR radiation with optical cavity techniques, is the subject of the following chapter.

Chapter 6

Combining the DS-DBR Laser with QPM-DFG for Mid-Infrared Spectroscopy

Throughout this thesis, it has been emphasised how a broadband, cavity-based spectrometer in the mid-IR would be a sensitive and selective approach for gas sensing. Three distinct elements, each addressing one of these separate aspects, have been studied and developed in this work: the widely tunable DS-DBR laser (Chapter 2), the CRD spectrometer (Chapter 3) and the QPM-DFG system for the generation of mid-IR light (Chapter 4). Some of these components have already been successfully paired: the DS-DBR laser has been combined with the CRD spectrometer for near-IR CRDS (Section 3.3) and the mid-IR radiation produced by the DFG system has been coupled into a cavity to perform mid-IR CRDS (Chapter 5). In this final experimental chapter, the last remaining permutation, namely the use of the broadband DS-DBR laser with the QPM-DFG system, is explored. The applicability of this arrangement for high resolution, mid-IR spectroscopy over an extended wavelength range is demonstrated by the use of this radiation for direct absorption spectroscopic studies of methane and methanethiol, and also for WMS for the former species. Then, as a culmination of all that has gone before, the chapter concludes with work performed to unite all three disparate entities to achieve the goal of creating a DS-DBR sourced, DFG-based mid-IR cavity-based spectrometer.

6.1 Using the DS-DBR Laser as the Signal Source for QPM-DFG

The work presented in this chapter was conducted using the QPM-DFG experimental set-up described in Section 4.3.1 and illustrated in Figure 4.11, with the DS-DBR laser replacing the DL as the signal source [205]. For the work performed in Section 6.2, in order to access the whole mid-IR spectral coverage possible given the different and extended signal wavelength range provided by the DS-DBR, one further change was required: an alternative EDFA covering the telecommunications L-band. This EDFA (*Nuphoton Technologies*, NP2000-L1-PR-B25-1200-FCA-01) was designed to give saturated output power in the $1568 - 1603$ nm region of up to 26 dB, but as only one of the pump lasers could be used, the signal power was only amplified to 63 mW. All other elements and particulars of the system, however, remained the same. Using this L-band EDFA, up to 2.6 μW of mid-IR radiation was generated, resulting from a conversion efficiency of 0.016% $W^{-1}cm^{-1}$, which was a typical performance for this configuration [311, 331, 354].

As before, the wavelength of the pump DL was fixed at 1064.3 nm and mid-IR wavelength tuning achieved by scanning the signal laser. The $1563 - 1613$ nm spectral range of the DS-DBR meant that this set-up had the potential of generating cw mid-IR radiation between $3130 - 3330$ nm ($3000 - 3200$ cm^{-1}). In order to scan across the entire mid-IR frequency range obtainable with this signal and pump laser combination, the physical properties of the PPLN, namely its poling period and temperature, also had to be considered, as discussed previously. The calculations of Section 4.3.2, which are summarised in Figure 4.13, revealed that to access all the possible wavelengths of the DS-DBR DFG system, two different poling periods (*i.e.* tracks in the PPLN crystal) of 30.25 μm and 30.50 μm, together with temperatures in the range of $25 - 85°C$, were required [439]. All of the initial work presented here was conducted with just half of the wavelength range available, so only one track with $\Lambda = 30.25$ μm was used. However, the temperature of the crystal still needed to be tuned as the DS-DBR was scanned to ensure generation of a significant level of mid-IR power.

By finding the optimum crystal temperature, T_{opt}, for various signal wavelengths, a relationship between these two parameters was determined (Figure 6.1(b)) which allowed T_{opt} to be estimated and implemented for every spectrum recorded; this calculated relationship was observed to work well experimentally, giving optimal conversion and high mid-IR powers, at all the wavelengths studied in this work, which can be attributed to the sufficiently spread nature of the data points used in its computation. Figure 6.1(a) shows an example of one temperature tuning curve recorded for pump and signal wavelengths of 1064.288 nm

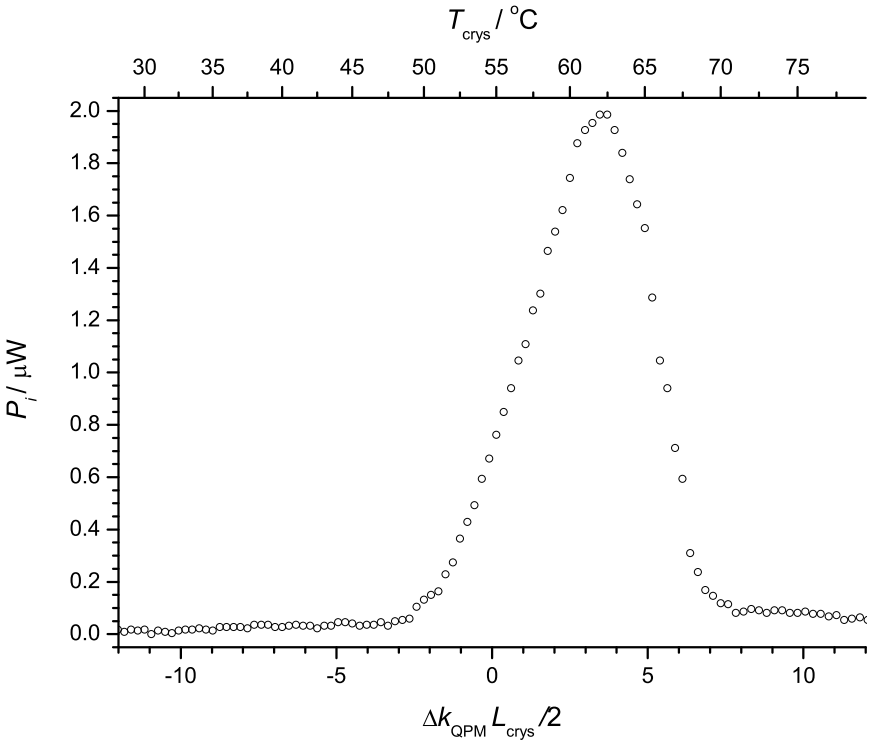

(a) An example temperature tuning curve for 3264.61 nm idler radiation. The experimental data was translated into the $\Delta k_{\mathrm{QPM}} L_{\mathrm{crys}}/2$ domain using the Sellmeier equation (Equation 4.44) [302].

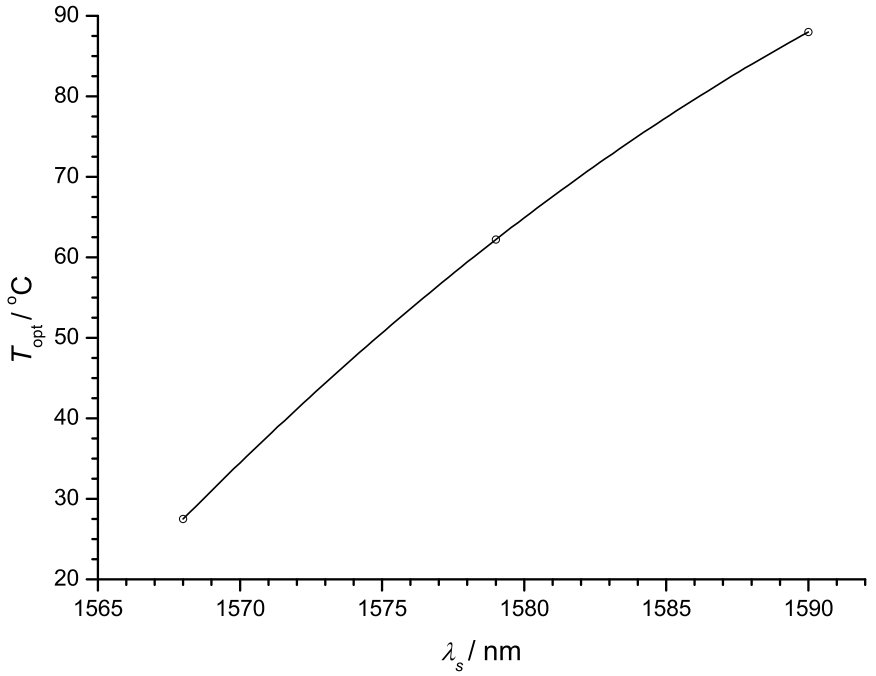

(b) Calibration curve of the optimal PPLN crystal temperature, T_{opt}, with signal wavelength for the $\Lambda = 30.25$ µm PPLN track. Data are shown as open circles and the quadratic fit ($T_{\mathrm{opt}} = -87025.45995 + 107.5671895\lambda_s - 0.033194205\lambda_s^2$) as a solid line.

Figure 6.1: Temperature tuning curves recorded of the mid-IR light generated by the QPM-DFG set-up when using the DS-DBR as the signal radiation source.

and 1579.081 nm, respectively, translated into the $\Delta k_{\mathrm{QPM}} L_{\mathrm{crys}}/2$ domain. This plot possesses the usual asymmetry observed for QPM tuning curves with focused Gaussian beams [127, 244]. However, it is noteworthy that the maximum does not occur in the negative $\Delta k_{\mathrm{QPM}} L_{\mathrm{crys}}/2$ region as predicted by theory (Section 4.2.5). This positive shift is a common feature among such tuning curves [333, 340] and is possibly due to the inaccuracies in the quoted poling period of the PPLN crystal. Indeed, in order to shift the peak position of Figure 6.1(a) to the negative region, a decrease in Λ of just 29 nm is required which has the same order of magnitude as the uncertainty reported by the manufacturer of the PPLN crystal ($\pm$10 nm). The FWHM of the temperature tuning curve in Figure 6.1(a) is 4.5 in the $\Delta k_{\mathrm{QPM}} L_{\mathrm{crys}}/2$ domain and 9.5°C (centred at 62.3°C) in the temperature domain.

6.2 Non-Cavity-Based Mid-Infrared Spectroscopy Using the Combined DS-DBR Laser and QPM-DFG System

The set-up outlined in Section 6.1 was used in single-pass direct absorption experiments on both narrowband and broadband absorbers, namely CH_4 and methanethiol (CH_3SH), respectively [205]. WMS was also performed on CH_4.

To record spectra across the wavelength range of interest, the internal scanning mode of the DS-DBR, as described in Sections 2.2.2.1 and 2.3.1, was employed. The reliability and reproducibility of the DS-DBR meant the mode-hop free scan settings and absolute wavelength calibrations performed using CO_2 in Section 2.3.1 were able to be used in these experiments to generate a mid-IR frequency scale. In all of these studies, the scan rate of the DS-DBR was set at 1.3 Hz and a fast oscilloscope (*Agilent*, MSO8104A Infiniium, 1 GHz, 4 GSa/s) utilised for data acquisition.

6.2.1 Methane

As expected given the mechanism of the DFG process, the properties of the DB-DBR in the near-IR were transposed to the mid-IR. This included favourable characteristics such as a good quality beam shape, but also less advantageous attributes like the occurrence of mode-hops on scanning the laser frequency. These mode-hops are jumps in frequency of ~ 1.7 cm^{-1} (determined by the laser cavity geometry) which result in gaps between continuous regions of recorded spectra and the number of mode-hops, as well as the wavelength range between them, varies depending on how the laser is scanned (Section 2.2.2.1).

This translation of the modulation characteristics of the DS-DBR laser observed in the near-IR to the mid-IR was confirmed by absolute frequency measurements of the absorption lines

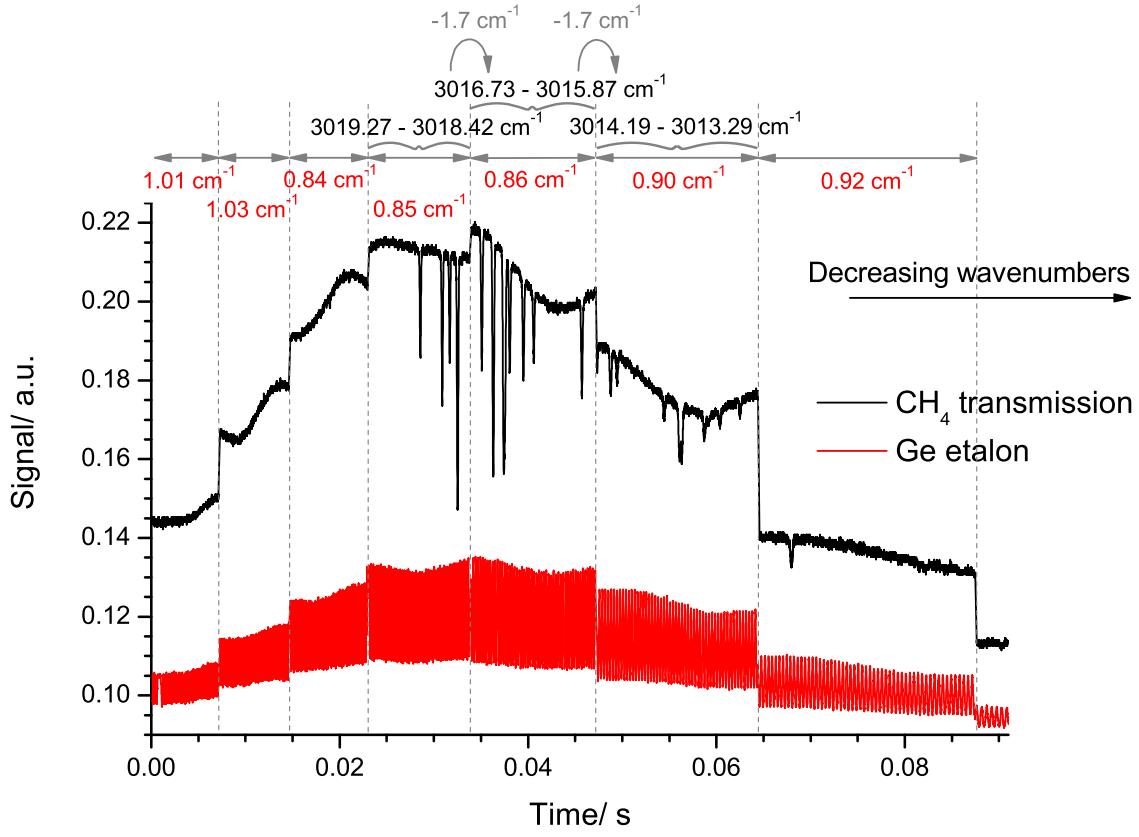

Figure 6.2: The CH_4 transmission spectrum (upper, black) and corresponding 500 MHz Ge etalon trace (lower, red) on scanning the DS-DBR; traces have been offset for clarity. The scan settings used in this case result in the presence of mode-hops, indicated by dashed vertical lines. The Ge etalon allowed the spectral ranges of the mode-hop free regions to be determined (red numbers). Absolute wavelength calibrations were possible for those segments containing CH_4 peaks (black numbers) which allowed the size of the mode hops to be estimated (grey values).

of CH_4 (*BOC*, CP grade, 99.995%) and relative frequency measurements using a 500 MHz Ge etalon, as illustrated in Figure 6.2. The DS-DBR was scanned over a large wavelength range (18.4 cm^{-1}) which encompassed several mode-hops. Relative frequency calibration was possible using the Ge etalon for all of the mode-hop free regions in the spectrum, but absolute calibration was only feasible for those regions containing CH_4 transitions. The size of the mode-hop jump for the scan settings used here was calculated as 1.7 cm^{-1}, a value which depends on the front pair selected.

It is notable that the overall intensity variation of the spectrum strongly resembles the shape of the conversion efficiency curve of Figure 6.1(a). In this case, however, the PPLN was set at one temperature and the wavelength scanned. The temperature was chosen in order to optimise the signal at the central wavelength of the spectrum, so the conversion efficiency, and hence signal, at the wings is lower. From Figure 6.2, the FWHM for the conversion efficiency in the frequency domain was estimated as 8.6 cm^{-1}, which corresponded to 3.7 in

the $\Delta k_{\mathrm{QPM}} L_{\mathrm{crys}}/2$ domain. This is larger, as expected, than the FWHM predicted by the plane wave approximation for this case (2.8 in the $\Delta k_{\mathrm{QPM}} L_{\mathrm{crys}}/2$ domain).

6.2.1.1 Direct absorption spectroscopy

The pump laser wavelength, λ_p, was set at 1064.289 nm. The signal wavelength, λ_s, was scanned by applying 40 mode-hop free scan settings (as found in Section 2.3.1 [202]) to the DS-DBR, covering a range of $1567.3 - 1588.0$ nm, along with their corresponding optimal T_{crys}, $26.3 - 83.2$°C, over a period of 5.5 hours. The resultant idler radiation of $3016 - 3096$ cm^{-1} was passed through a 10 cm long glass cell with CaF_2 windows filled with 0.18 Torr of CH_4 and 6 Torr of humid air. Each spectrum was averaged over five scans, each scan taking 0.8 s to acquire.

The overall CH_4 direct absorbance spectrum, formed by stitching together these 40 individual spectra, is shown Figure 6.3(a). The major absorption lines correspond to the Q and R branches of the fundamental $\nu_3(F_2)$ transition of CH_4, centred at 3015 cm^{-1} (transitions labelled using notation introduced in Section 5.3.1). Figure 6.3(b) is a horizontally expanded version of Figure 6.3(a) and Figure 6.3(c) shows an example of a Voigt fit to one of the absorption lines.

For comparison, a simulation of the expected absorbance for the experimental conditions is included as the lower plots in Figures 6.3(a) and 6.3(b). This simulation was calculated using data from the HITRAN 2004 database [14] and is composed of two parts: firstly, the contribution from the 10 cm cell filled with 0.18 Torr CH_4 and 6 Torr moist air, and, secondly, the absorption by 1% H_2O in air at 760 Torr over a 90 cm long open path. This last part corresponds to the absorption which took place before the radiation entered the cell and was required to account for the broadened H_2O absorption lines present in the spectrum. The simulation is in good agreement with the recorded data in terms of both the positions and intensities of the absorption features.

The Voigt fitting of the (6 A_2 8 $\leftarrow$ 6 A_1 1) $Q(6)$ transition in Figure 6.3(c) also returned good fitting parameters. The Gaussian width was fixed at the expected Doppler width of 280 MHz, and the fitted value for the Lorentzian width found to be 46 ± 1 MHz. Considering the pressures of CH_4 and buffer present in the sample, the expected Lorentzian width due to pressure broadening using values from the HITRAN database [14] was 30 ± 6 MHz.

While the frequency calibration was excellent at the low wavenumbers recorded at the beginning of the data acquisition period (Figure 6.3(b)), small drifts in the frequency calibration were observed at higher wavenumbers which were recorded at later times. These drifts were not always of the same magnitude, nor even in the same direction. For example,

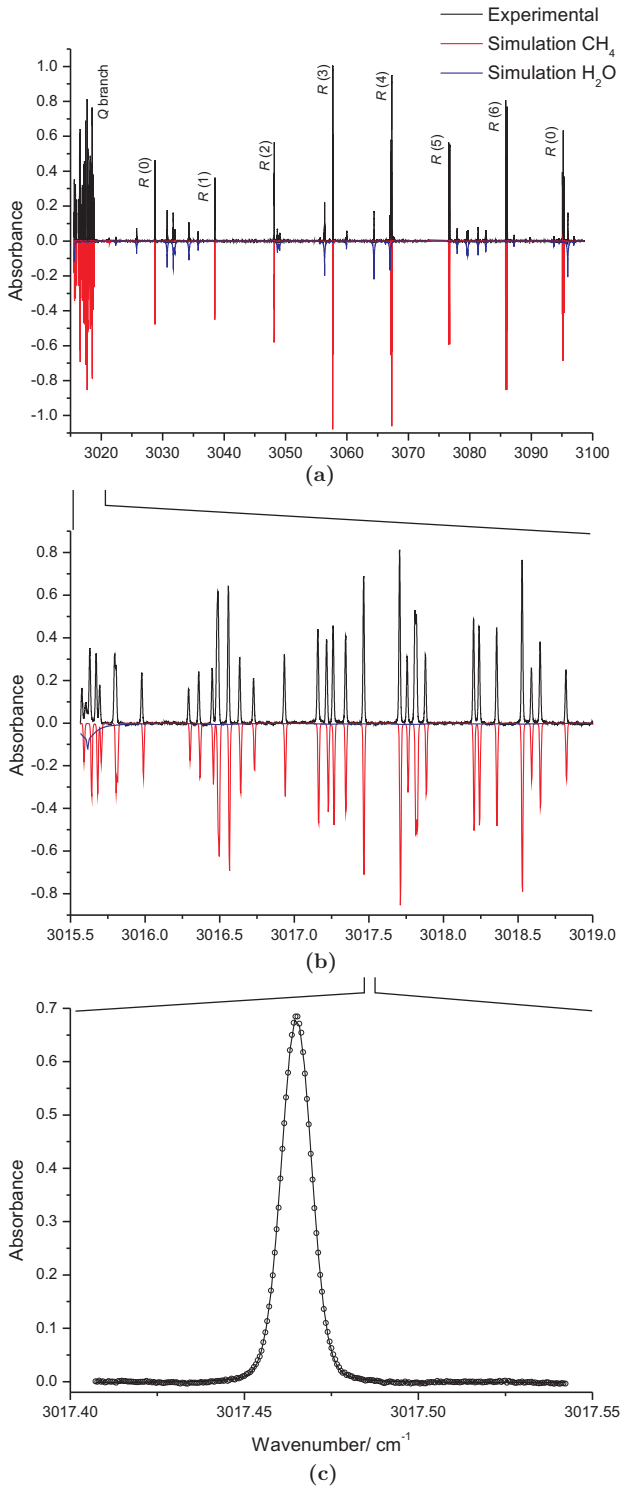

Figure 6.3: CH_4 direct absorption spectra. (a) The CH_4 direct absorption spectrum across the entire frequency range of $3016 - 3096$ cm^{-1}. (b) A zoom in of this in the $3015.5 - 3019.0$ cm^{-1} region. The absorption lines correspond to the Q and R branches of the fundamental $\nu_3(F_2)$ transition. In (a) and (b), the lower traces are simulations calculated using HITRAN 2004 data composed of two parts: firstly, absorption due to 1% H_2O in air at 760 Torr over a 90 cm long open path and, secondly, absorption by 0.18 Torr CH_4 and 6 Torr moist air in a 10 cm long cell. (c) An example of a Voigt fit (solid line) to the data (open circles), using the 3017.47 cm^{-1} (6 A_2 8 $\leftarrow$ 6 A_1 1) $Q(6)$ transition. A reduced number of data points are displayed for clarity.

a drift in frequency of +0.01 cm^{-1} was observed at the transitions centred at 3057.7 cm^{-1} and of +0.02 cm^{-1} at 3076.7 cm^{-1}. These offsets might have been due to a drift in the wavelength of the pump laser with time, a problem which could be rectified by constant monitoring of λ_p during spectra acquisition. However, it is worth emphasising that these drifts of ~ 0.02 cm^{-1} were small relative to the range of wavenumbers covered by the entire spectrum (83 cm^{-1}).

6.2.1.2 Wavelength modulation spectroscopy

Further spectroscopic studies were conducted on the four $R(5)$ absorption lines in the ν_3 vibrational band at 3076.7 cm^{-1} using $2f$-WMS (Section 1.2.1.1). T_{crys} was set at 71.2°C. Both the rear and phase injection currents, i_r and i_p, respectively, of the DS-DBR were ramped in order to scan λ_s, covering a wavelength range of $3076.5 - 3076.8$ cm^{-1} in the mid-IR. This light was passed through a 46.5 cm long aluminium box with CaF_2 windows containing 12 mTorr of CH_4 in 12.1 Torr of N_2; the composition of this sample was confirmed by fitting Voigt profiles to the direct absorption spectrum. Although four absorption features were seen in this wavelength range, only the features at 3076.68 cm^{-1} and 3076.73 cm^{-1} were examined in detail as they had the property of having almost the same linestrength, and so approximately the same amplitude in the direct absorption spectrum.

A lock-in amplifier (*Stanford Research Systems*, SR830) was used to encode the detected signal at a 1.3 kHz modulation frequency and afterwards to demodulate it at the second harmonic ($n = 2$) of the reference frequency. A lock-in time constant of 1 ms was used and spectra were averaged over 10 scans.

The novel property of performing WMS using the DS-DBR laser, as seen in Section 2.3.1, is the ability to modulate either i_r or i_p. WMS spectra were recorded for both possibilities, and in both cases at low and high amplitudes of the modulating signal as defined by the lock-in amplifier, A_m. The resultant data are shown in Figure 6.4(a). Although these two absorptions should be the same size as each other in all of these WMS spectra (as they have very nearly the same height and width in the direct absorption spectrum), they plainly are not. This is due to the fact that for a fixed lock-in amplifier modulation amplitude, A_m in mV, there is a variation in the optical frequency modulation amplitude, a_m in cm^{-1}, with frequency across the scan, which distorts the relative heights of the transitions; the same behaviour was observed when using the DS-DBR to conduct WMS in the near-IR (Section 2.3.1). This yet again illustrates that the performance and properties of the DB-DBR in the near-IR have been translated to the mid-IR via the DFG process.

This behaviour was investigated further by recording the signal from a 2.32 GHz spectrum analyser (*Melles Griot*, 13SAE906) monitoring the near-IR light output from the DS-DBR

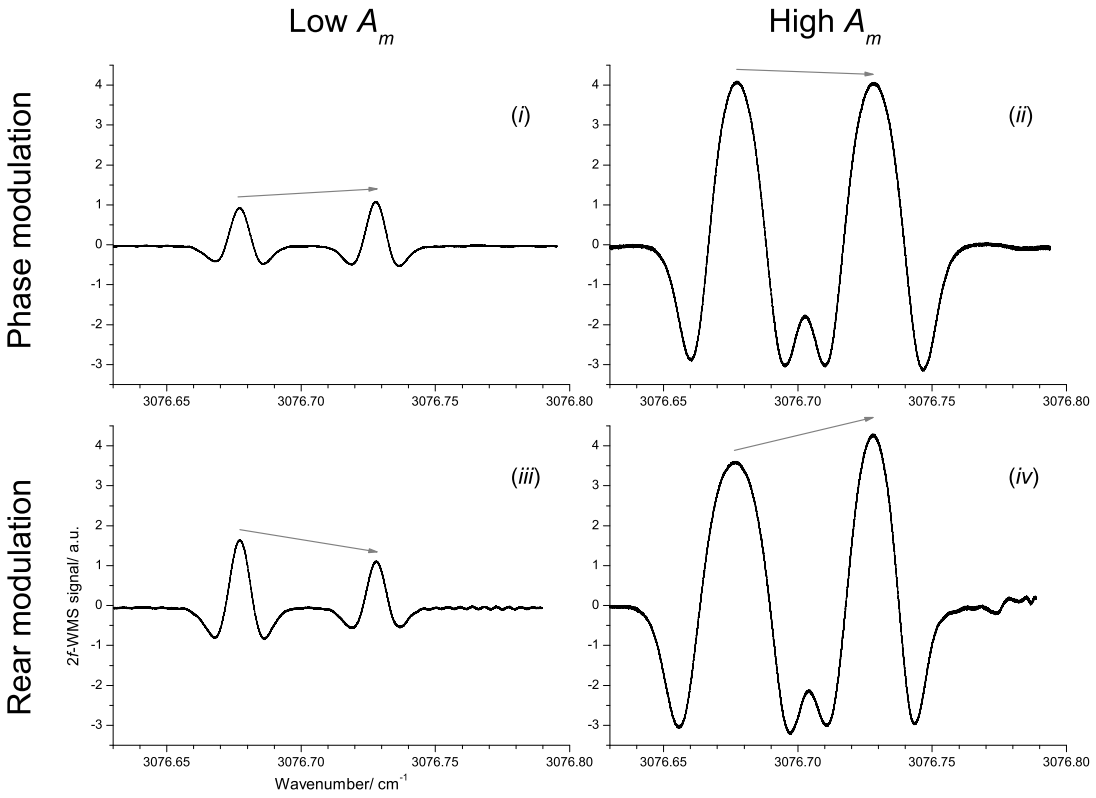

(a)

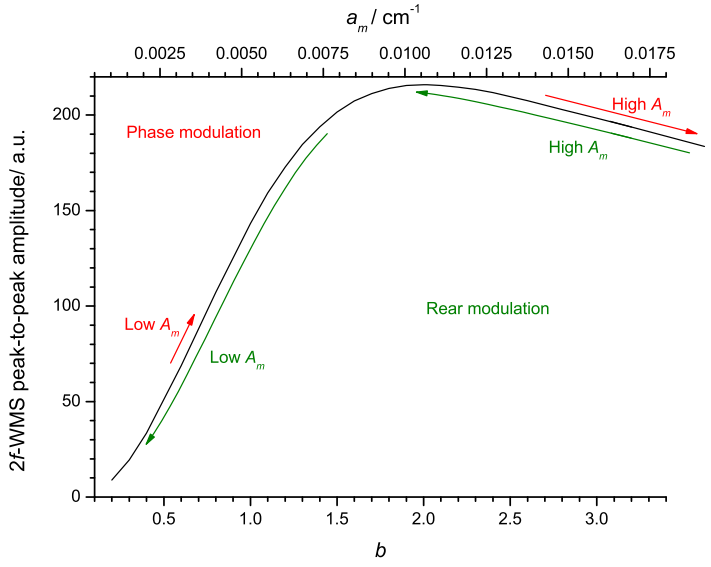

(b)

Figure 6.4: (a) $2f$-WMS spectra of the 3076.68 cm^{-1} (6 F_1 21 $\leftarrow$ 5 F_2 1) $R(5)$ and 3076.73 cm^{-1} (6 F_2 24 $\leftarrow$ 5 F_1 1) $R(5)$ CH_4 transitions of a 12 mTorr sample of CH_4 in 12.1 Torr of N_2, recorded when modulating the phase and rear injection currents of the DS-DBR at low and high lock-in amplifier modulation values, A_m. (b) Simulation of the $2f$-WMS peak-to-peak signal amplitude against modulation index, b. The arrows represent the range of b values accessed using the different A_m settings investigated. The direction of an arrow corresponds to the direction of increasing wavenumbers in the WMS spectrum, and the length corresponds to the range of b and a_m, in cm^{-1}, covered.

Modulation		Meas. pk-pk heights Ln 1/Ln 2	Gradient (a_m v $\tilde{\nu}_{rel}$)	a_m/ cm^{-1} at position Ln 1	Ln 2	Error	Pred. pk-pk heights Ln 1/Ln 2
None, *i.e.* direct		1.00					
Phase	Low A_m	1.11	0.0020	0.0034	0.0035	0.0001	1.05 ± 0.08
	High A_m	1.00	0.0149	0.0175	0.0182	0.0002	0.99 ± 0.01
Rear	Low A_m	0.67	-0.0157	0.0041	0.0034	0.0003	0.74 ± 0.18
	High A_m	1.08	-0.0754	0.0184	0.0148	0.0020	1.09 ± 0.09

Table 6.1: Table with ratios of the $2f$-WMS peak-to-peak heights for the WMS data (Meas. pk-pk heights) and those predicted using the simulation of Figure 6.4(b) (Pred. pk-pk heights). The two lines are two different $R(5)$ transitions in the fundamental ν_3 vibrational band: 'Ln 1' corresponds to the 3076.68 cm^{-1} (6 F_1 21 $\leftarrow$ 5 F_2 1) $R(5)$ transition, 'Ln 2' to the 3076.73 cm^{-1} (6 F_2 24 $\leftarrow$ 5 F_1 1) $R(5)$ transition. The gradient is the slope of the linear fit of the optical frequency modulation amplitude versus relative wavenumber (a_m v $\tilde{\nu}_{rel}$) calibration. This relationship was used to calculate the a_m at the positions of the two transitions of interest. For a given set of experimental modulation settings, the predicted peak-to-peak height can take a range of values due to the error in the determination of a_m at Ln 1 and Ln 2.

when it was subjected to the same scan and WMS modulation settings. The known FSR of the spectrum analyser allowed for calibration from the time to the relative frequency domain, and the widths of the spectrum analyser transmission features were then used to calculate a_m. Hence the variation of a_m with relative wavenumber, $\tilde{\nu}_{rel}$, as the DS-DBR was scanned was determined.

A simulation of the $2f$-WMS peak-to-peak signal amplitude against the modulation index b (Equation 1.35) was generated for a low pressure (Doppler-limited) system, and this is shown together with an overlay of the a_m regions scanned by the different A_m modulation settings experimentally applied in Figure 6.4(b). In this plot, the direction of the arrows correspond to the direction of increasing wavenumbers in the WMS spectra, and the lengths correspond to the range of a_m covered over the scan range. The effect that the change in modulation depth has on the observed trend in peak-to-peak heights across the WMS spectra is illustrated by the corresponding arrow in Figure 6.4(b) in terms of both the direction and amplitude of change, as seen in Table 6.1. An $\alpha_{\min}(BW)$ of 3.1×10^{-6} cm^{-1}Hz$^{-1/2}$ was calculated for the absorption feature at 3076.73 cm^{-1}.

This work demonstrated, once again, the need for care when using the DS-DBR laser for WMS, especially for quantitative studies such as calculating quantum state resolved populations. The laser can be frequency tuned by scanning i_r, i_p or both, and then WMS performed by applying a modulation to either i_r or i_p. Depending on the scanning and modulation settings chosen, the A_m-a_m relationship will be different, *i.e.* the position, direction and length of the corresponding arrow in Figure 6.4(b) will change. As such, a different A_m-a_m calibration would be required for every set of scan and modulation settings used.

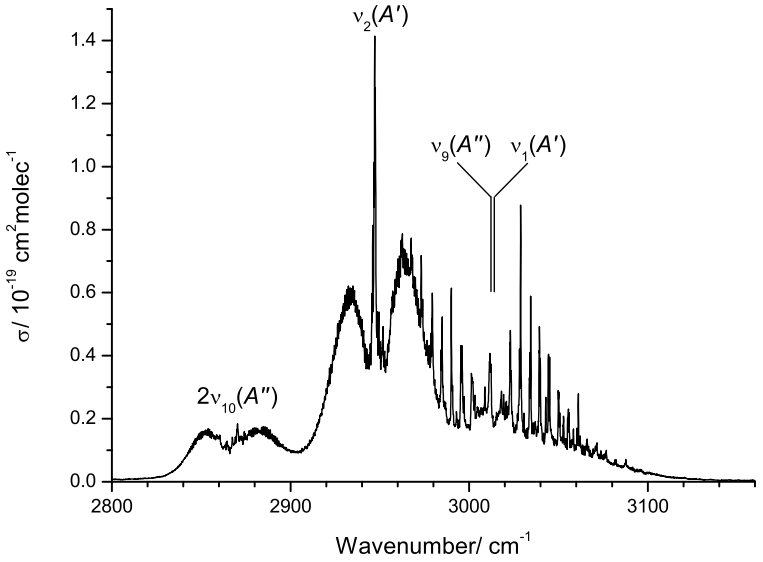

Figure 6.5: Absorption cross-section of CH_3SH at 3 µm, estimated from the 1 ppm-meter, 760 Torr, 296 K CH_3SH absorption spectrum reported in the PNNL database [403], together with assignments of the fundamental vibrational bands [447].

6.2.2 Methanethiol

As seen in Section 1.3.3, CH_3SH is a medically important molecule that absorbs at 3 µm [312]. It belongs to the class of organic sulphur-containing compounds known as mercaptans and its occurrence in human breath at elevated levels can be used as a biomarker for various diseases [90, 133, 440], particularly those concerning the liver and including maladies such as cirrhosis [441], hepatic encephalopathy [442, 443] and halitosis [444]. It is created by the incomplete metabolism of the sulphur-containing amino acid, methionine, in the transamination pathway controlled by gastrointestinal bacteria [445]. It has been discovered that CH_3SH hinders the synthesis of urea, resulting in higher circulating levels of ammonia and short-chain fatty acids in the blood, leading to an increased likelihood for hepatic disorders [446]; this explains the observed link between high concentrations of CH_3SH in exhaled breath and an impairment in liver function [441–443].

There are only a limited number of publications on the rotational and vibrational spectroscopy of CH_3SH [447, 448]. It has twelve IR active normal modes (eight of A' symmetry, four of A'') and, by approximating the molecule as a (nearly) symmetric top, the vibrational bands associated with these modes can be regarded as either parallel or perpendicular. Strong overlap between the vibrations associated with the methyl group result in a complicated ro-vibrational spectrum, part of which is illustrated in Figure 6.5 at 3 µm. A sharp Q branch at 2948 cm^{-1} of the symmetric C−H stretch, $\nu_2(A')$, which is assigned to the parallel band, is clearly discernible. This is a strong single feature because for parallel bands the selection rule for rotational transitions is $\Delta K = 0$, where K is the angular momentum quantum number for rotation about the symmetry axis and is limited to values

between $-J$ and $+J$, inclusive, with J defined as the total rotational angular momentum quantum number [3]. The absorbances within the $2975 - 3050$ cm^{-1} range have been attributed to the overlap between the perpendicular bands caused by the weak $\nu_1(A')$ and strong $\nu_9(A'')$ antisymmetric C−H stretches with band origins of 3015 cm^{-1} and 3012 cm^{-1}, respectively [447]. The intense, nearly equally spaced ($\sim$ 5.5 cm^{-1}) features within this region result from the $\Delta K = \pm 1$ selection rule associated with perpendicular transitions which cause the P, Q and R branches with different K values to spread out [3]. Though it is generally not possible to discern the P and R branches, the Q branches can often be distinguished. This is because each Q branch consists of such closely spaced transitions as to appear almost line-like, with a separation between adjacent Q branches of $2(A - B)$, where A and B are rotational constants. For CH_3SH, A and B have values of 3.4 cm^{-1} and 0.4 cm^{-1}, respectively, for the zero point energy level [448].

Initially, a survey spectrum of CH_3SH (*Fluka*, purum, 1164432 20105093) across the entire $3016 - 3096$ cm^{-1} range was recorded. The same process was used as that employed in Section 6.2.1: λ_p was set at 1064.288 nm and λ_s scanned by applying 40 different mode-hop free scan settings to the DS-DBR whilst changing T_{crys} to the corresponding optimum temperature appropriate for the wavelengths covered by each scan. The resultant radiation was passed through a 46.5 cm long aluminium box with CaF_2 windows filled with 3.2 Torr of CH_3SH. Each spectrum was averaged over five scans and the whole run took two hours, primarily due to the time taken to stabilise T_{crys}. From this survey spectrum, five regions of interest were identified for further, more detailed study.

As CH_3SH is a broadband absorber, it was necessary to record an I_0 baseline rather than simply determining I_0 by fitting a polynomial baseline to the I trace, which was the method previously used in Section 6.2.1. To accomplish this, the cell was flushed with N_2 for 30 mins between runs before it was evacuated and I_0 measured; 3.2 Torr of pure CH_3SH was then introduced and I recorded. However, this procedure did introduce potential errors, as the time delay between recording I_0 and I allowed the power and frequency of the mid-IR light to change due to drifts in T_{crys} and the laser frequencies. Also, the act of evacuating and filling the cell could have affected optical elements and so altered any baseline etalon.

The resultant CH_3SH direct absorption spectra of these five regions are shown in Figure 6.6, together with the absorbances predicted using the FTIR data from the PNNL database [403]. The dominant absorption features correspond to the intense Q branches of the perpendicular bands from the weak $\nu_1(A')$ and strong $\nu_9(A'')$ antisymmetric C−H stretching modes, with both bands giving rise to the same Q branches at approximately the same frequencies (though the transitions of the $\nu_9(A'')$ are stronger), and are labelled as ${}^{\Delta K}\Delta J_{K''}$, where the rotational quantum numbers for symmetric top entities, J and K, have been used and $''$ indicates the lower level. The experimental and PNNL data compare favourably in

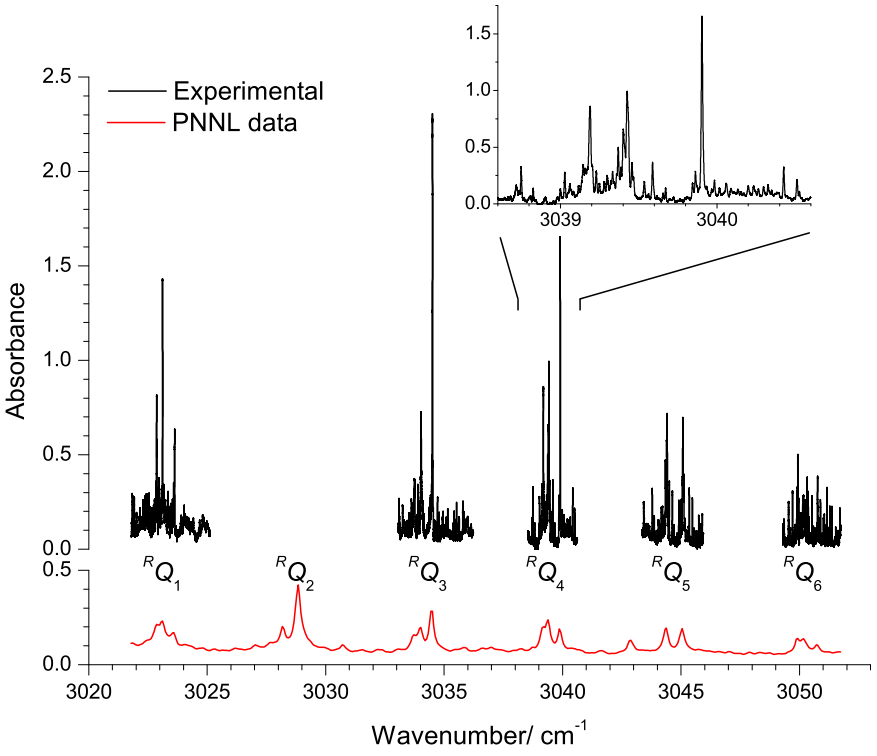

Figure 6.6: CH_3SH direct absorption spectra recorded at 3.2 Torr over a 46.5 cm path length and expected absorbance calculated using PNNL data [403] given these experimental conditions. The absorption features correspond to the strong Q branches of the perpendicular bands from the $\nu_1(A')$ and $\nu_9(A'')$ antisymmetric C−H stretching modes. Both bands have Q branch transitions occurring at approximately the same frequencies, though the transitions of the $\nu_9(A'')$ mode are stronger.

terms of both the positions and strengths of the major absorption features, as well as in the non-zero baseline absorbance visible across the region. However, the experimental data of this work was clearly recorded at a higher resolution than that reported in the PNNL database (10 MHz compared to 3360 MHz), which allows more structure of the CH_3SH absorption spectrum to be distinguished.

From Figure 6.6, the ${}^RQ_4$ absorption at 3040 cm^{-1} was identified as a potentially useful feature for monitoring the CH_3SH biomarker in exhaled breath at reduced pressures. This is because it was one of the stronger absorptions observed, with an estimated σ_{int} value of $4.66 \pm 0.15 \times 10^{-21}$ $cm^2cm^{-1}molec^{-1}$ found from these direct absorption measurements, and was least susceptible to interference from H_2O and CH_4 lines. To investigate this further, another spectrum of this feature was recorded using 1 Torr CH_3SH in 100 Torr N_2. This lineshape was then used to simulate the spectrum of a mixture of 1% H_2O, 1.78 ppm CH_4 and 10 ppb CH_3SH in air at 100 Torr total pressure. These are typical concentrations for these species in breath samples (Table 1.2 and references therein). The result is shown in Figure 6.7. At 100 Torr, the CH_3SH transition is seen to be relatively free from absorptions by H_2O and CH_4 which mean it could be used to find the amount of CH_3SH present in

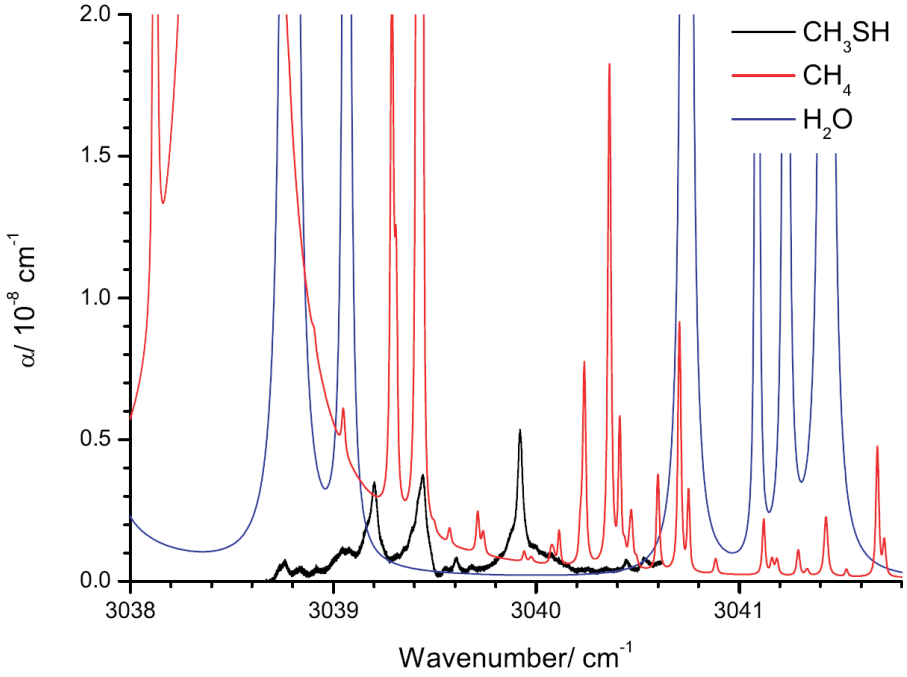

Figure 6.7: Simulation of the absorption for a sample of 1% H_2O, 1.78 ppm CH_4 and 10 ppb CH_3SH in air at 100 Torr in the 3038 – 3042 cm^{-1} region. This was generated using experimental CH_3SH data recorded at 1 Torr CH_3SH in 100 Torr N_2 to estimate the absorption for CH_3SH, and data from the HITRAN 2004 database [14] to calculate the expected absorbances from CH_4 and H_2O.

a breath sample; however, this selectivity was lost when the simulation was repeated at 760 Torr as the well-defined spectral features broadened and overlapped. So if this ${}^RQ_4$ 3040 cm^{-1} feature were to be used as an indicator for CH_3SH in breath, samples would need to be reduced in pressure before analysis. In addition, interference from absorptions by other VOCs, such as acetone and isoprene, would have to be considered, although these species are essentially uniform over the spectral range of interest encompassing the ${}^RQ_4$ CH_3SH absorption [403, 404, 449] and, furthermore, could be removed from the sample by selective chemical or molecular filters if required.

Figure 6.7 also indicated that the ${}^RQ_4$ absorption feature at 3040 cm^{-1}, measured under these conditions to imitate breath of 10 ppb CH_3SH in 100 Torr air, had an absorption of $\sim 5 \times 10^{-9}$ cm^{-1}. This is the level of sensitivity typically achieved by cavity-based methods; indeed, in Section 5.2.3, Allan variance studies revealed $\alpha_{\min}$ values of the order of 10^{-9} cm^{-1} were achievable with the DFG-based mid-IR CRD spectrometer created in Chapter 5.

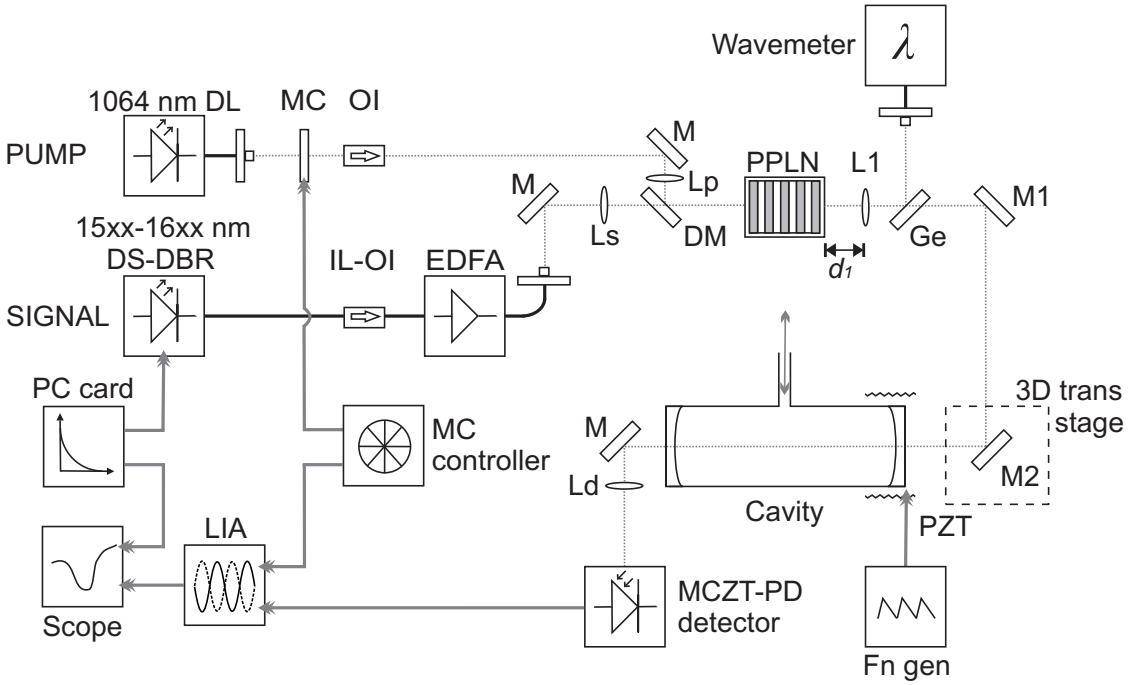

Figure 6.8: The experimental set-up for CEAS using the combined DS-DBR and QPM-DFG system as the mid-IR radiation source. Cavity properties were measured as $L = 77.0$ cm, $R \sim 0.999$. MC: mechanical chopper; M1, M2: turning mirrors; Fn gen: function generator; LIA: lock-in amplifier. M2 was mounted on a 3D translation stage to allow off-axis injection into the cavity.

6.3 Cavity-Based Mid-Infrared Spectroscopy Using the Combined DS-DBR Laser and QPM-DFG System

6.3.1 Experimental CEAS set-up

Given the noisy cavity modes observed with the DS-DBR in the near-IR (Section 3.3.2.1) and the anticipated translation of this behaviour to the mid-IR, together with the lower powers achievable in the mid-IR and the resultant reduction in cavity mode intensity this would entail, it was decided to use the DS-DBR sourced DFG system to perform CEAS, rather than CRDS, as an illustration of cavity-based mid-IR spectroscopy using the DS-DBR. The experimental set-up for these CEAS experiments is shown in Figure 6.8; once again, it is based on the QPM-DFG experimental set-up described in Section 4.3.1 and illustrated in Figure 4.11, still using the 1064 nm DL (*Lumics*, LU1064M150) as the pump source and the 2-stage thermoelectrically cooled MCZT-PD detector (*Vigo Systems*, PVI-2TE-4/VPDC-0.1l), but substituting the DS-DBR for the DL as the signal source.

In the work performed in this section, the DS-DBR was only varied between $1567-1574$ nm. As such, the 30.25 μm poling period of the PPLN crystal was employed and the crystal temperature set as appropriate according to the relationship between T_{opt} and λ_s found

in Section 6.1. In addition, the fact that only these low signal wavelengths were used allowed the C-band EDFA, rather than the L-band one, to be utilised. Both pump lasers of this EDFA were functioning correctly so could be employed, which meant that the signal power was amplified to 185 mW, generating 21 μW of mid-IR radiation. As the pump power incident on the crystal was 66 mW, this indicated a conversion efficiency of 0.043% $W^{-1}cm^{-1}$, similar to values reported earlier in this work (Sections 4.3.3, 5.2.1 and 5.4.1).

Suitable DS-DBR settings covering the wavelength ranges of interest were found based on the work conducted in Section 2.3, and the laser scanned over these settings at a frequency of 5 Hz using using the external ramping mode described in Section 2.2.2.2.

In order to increase transmission through the cavity, lower reflectivity mirrors than those previously used were employed. These 25.0 mm diameter, plano-concave mirrors (*Layertec GmbH*) were AR coated on the plane side and HR coated on the curved side with a quoted reflectivity of $R > 0.997$ over the range $3000 - 3500$ nm. As before, the first mirror was mounted on the PZT and the length of the cavity was 77 cm.

To achieve the congested mode structure required for CEAS, the second turning mirror (M2 in Figure 6.8) was placed on a 3D translation stage so that the laser light could be injected into the cavity off-axis [30, 71, 72, 92, 358, 393, 450]. Further disruption to the cavity modes was caused by applying a high frequency (267 Hz) sine wave modulation to the PZT in order to jitter the cavity length.

Due to the low power of the input mid-IR radiation, phase sensitive detection was also utilised to enhance the observed signal. This was accomplished using a mechanical chopper (*Bentham Instruments*, 218 optical chopper), which was situated directly in front of the pump laser and modulated the intensity of the light at 1.35 kHz, and a lock-in amplifier (*Stanford Research Systems*, SR830), which decoded the signal at this modulation frequency using a lock-in time constant of either 3 ms (for CH_4 measurements) or 1 ms (for CH_3SH measurements), sensitivity of 20 μV and a phase of $+141.44°$. The final results were recorded on an oscilloscope (*LeCroy*, Waverunner 6100A, 1 GHz, 10 GSa/s) and averaged over 80 scans of the up-ramp, giving a total acquisition time per spectrum of 8 s.

6.3.2 Spectroscopic measurements

6.3.2.1 Methane

CEAS studies of the (6 A_2 8 $\leftarrow$ 6 A_1 1) $Q(6)$ fundamental $\nu_3(F_2)$ transition of CH_4 at 3017.47 cm^{-1}, as investigated in Section 6.2.1.1, were performed. λ_p was set at 1064.269 nm and λ_s was scanned between $1567.710 - 1567.751$ nm, corresponding to a mid-IR wavelength range of $3313.94 - 3314.12$ nm ($3017.39 - 3017.56$ cm^{-1}). T_{crys} was set at 27.1°C.

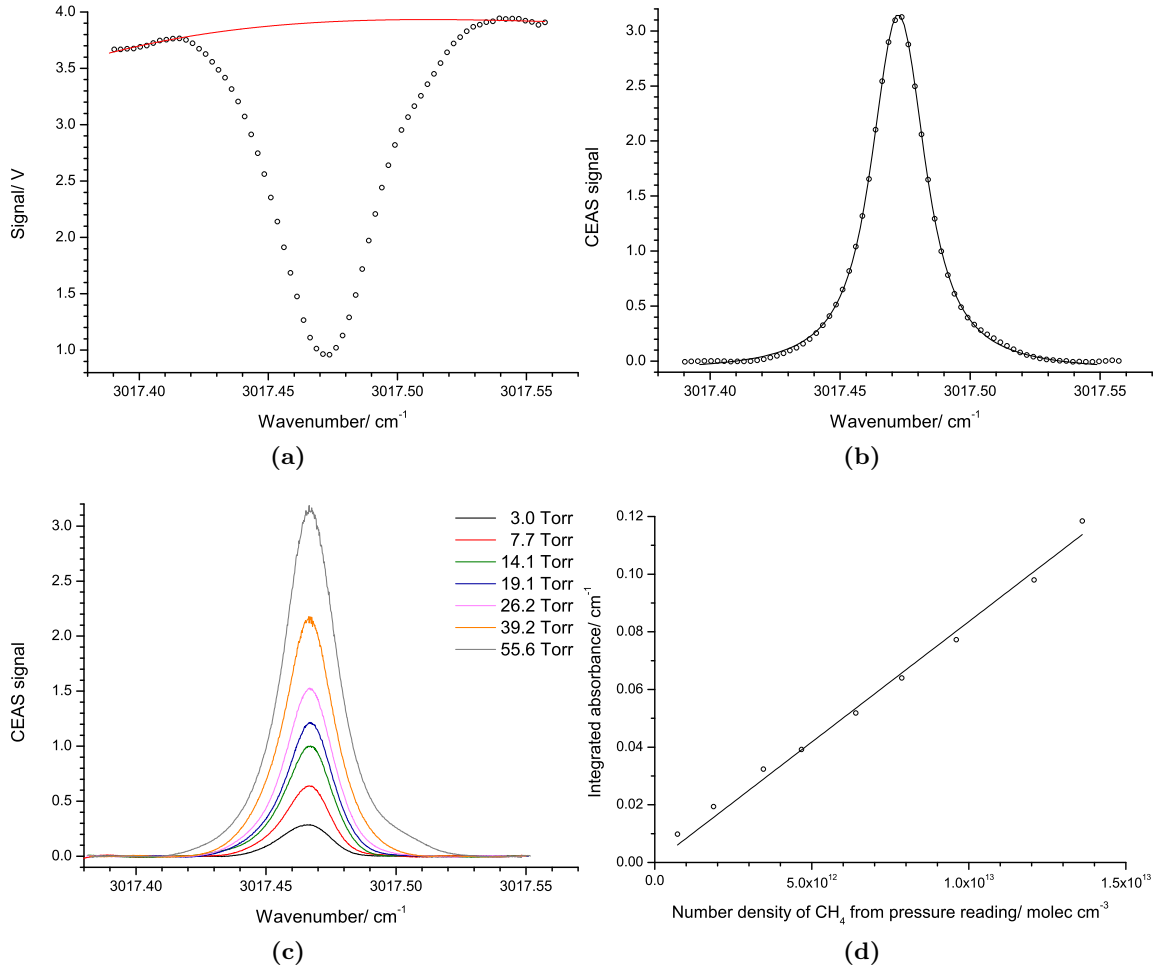

Figure 6.9: CEA spectra of the (6 A_2 8 $\leftarrow$ 6 A_1 1) $Q(6)$ transition of the fundamental $\nu_3(F_2)$ band of CH_4 at 3017.47 cm^{-1} for a calibrated 7.5 ppm mixture of CH_4 in air. (a) Initial signal data across the absorption feature (open circles) with a fitted low order polynomial I_0 baseline (solid line) recorded at 56 Torr. (b) The resultant CEA spectrum of the data in (a) (open circles) with a fitted Voigt profile (solid line). In both (a) and (b), the number of experimental points has been reduced for clarity. (c) CEA spectra for the CH_4 transition recorded at a range of pressures ($3 - 56$ Torr). Only a selected number of the spectra recorded have been included for clarity, and the plots have all been shifted to the line centre at 3017.47 cm^{-1}. (d) The linear relationship between the area of the fitted absorbance feature and the CH_4 concentration expected from the measured pressures. This line passes through the origin, and from its gradient the effective path length of the cavity at this wavelength was found to be 620 ± 10 m, indicating an average mirror reflectivity of $R = 0.9988$.

Initially, spectra were recorded of a calibrated 7.5 ppm mixture of CH_4 in air (*CK GAS*, Order Ref 15205) at various pressures ($3 - 56$ Torr), as shown in Figure 6.9. Voigt profiles were fitted to the absorption spectra by fixing the Gaussian width at the expected Doppler width of 280 MHz whilst allowing other parameters to float. It was noted that the widths of the absorption profiles returned by the fitting routine considerably exceeded that expected from normal Doppler and pressure broadening at these pressures. This phenomenon was

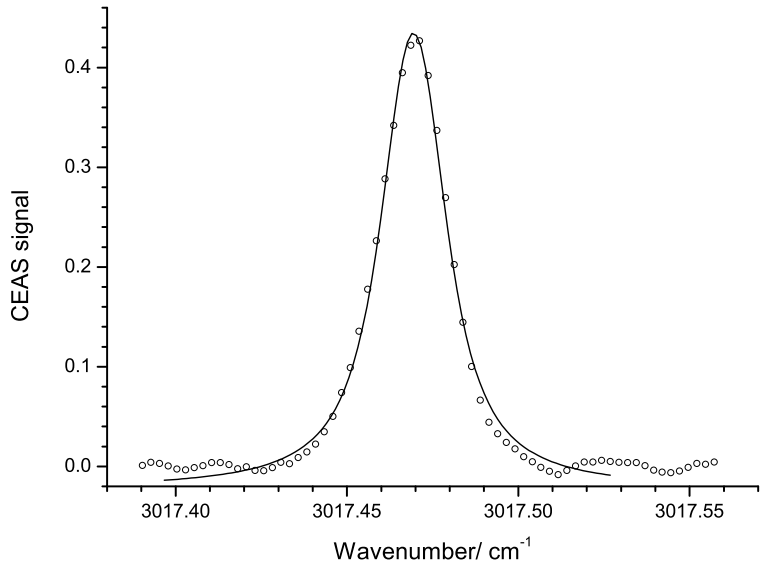

Figure 6.10: CEA spectrum of the (6 A_2 8 $\leftarrow$ 6 A_1 1) $Q(6)$ transition of the fundamental $\nu_3(F_2)$ band of CH_4 at 3017.47 cm^{-1} for 20.5 Torr of lab air. The data (open circles) have been fitted with a Voigt profile (solid line), and the number of experimental points reduced for clarity.

attributed to the instrumental broadening associated with the mismatch between the frequency of the applied modulation for lock-in detection and the chosen lock-in time constant, which was selected to optimise the SNR at the expense of a partially distorted spectral lineshape. This belief is corroborated by the fact that the returned Lorentzian widths for the fits were all much larger than anticipated ($500 - 670$ MHz compared to $14 - 280$ MHz predicted for the pressures studied) and demonstrated only a weak pressure dependence. Similar behaviour, where instrumental broadening dominates the retrieved lineshape at low pressures, has been observed in previous studies [333, 339, 451].

In such situations, though, the integrated signal should not be affected, and hence it was this area parameter that was utilised in quantitative analysis. A plot of the area of these Voigt fits against CH_4 concentration (Figure 6.9(d)) gave a straight line through the origin. As absorbance is given by $\sigma(\nu)Cl$, then the gradient of this line corresponds to $\sigma_{\text{int}}L_{\text{eff}}$, where L_{eff} is the effective path length of the cavity. Using the σ_{int} value for this transition of 1.348×10^{-19} $cm^2cm^{-1}molec^{-1}$ reported in HITRAN [14], an effective cavity path length of 620 ± 10 m, correlating to an average mirror reflectivity of $R = 0.9988$, was estimated at this wavelength.

Spectra of samples of lab air at ~ 20 Torr were then recorded, an example of which is given in Figure 6.10. The areas of the fitted Voigt profiles to the absorption spectra, combined with the σ_{int} value of this transition and the 620 m estimated effective path length found using the calibrated mixture studies, were used to calculate the concentration of CH_4 present in the lab air; the results of three such investigations are reported in Table 6.2. The

Take	p / Torr	CH_4 conc. / ppm	I_0 / V	ΔI_{min} / V	α_{min} / cm^{-1}
1	20.3	2.75	3.594	0.014	6.49×10^{-8}
2	20.3	2.92	3.458	0.013	5.95×10^{-8}
3	20.5	2.74	3.609	0.014	6.14×10^{-8}
		2.81 ± 0.10			$6.2 \pm 0.3 \times 10^{-8}$

Table 6.2: Results of the CEAS studies of the (6 A_2 8 $\leftarrow$ 6 A_1 1) $Q(6)$ fundamental $\nu_3(F_2)$ CH_4 transition at 3017.47 cm^{-1} in lab air. The CH_4 concentration (CH_4 conc./ ppm) was calculated using the area of the feature in the CEA absorbance plot, $\sigma_{int} = 1.348 \times 10^{-19}$ $cm^2cm^{-1}molec^{-1}$ [14] and the effective cavity path length of 620 m found at this wavelength using the calibrated mixture studies. α_{min} was estimated using Equation 1.60, where ΔI_{min} was taken as the RMSE of the fitted I_0 baseline.

average CH_4 concentration was found to be 2.81 ± 0.10 ppm; this concentration is typical of an indoor environment [96, 149], which is slightly higher than the well-known outdoor tropospheric CH_4 level of 1.7 ppm [452] due to the exhalation by people of endogenously produced CH_4. Using the error in the I_0 baseline fit and Equation 1.60, the sensitivity of the system was estimated as α_{min} of 6.2×10^{-8} cm^{-1} over an 8 s integration time, corresponding to an $\alpha_{min}(BW)$ of 1.8×10^{-7} $cm^{-1}Hz^{-1/2}$. This implies a detection limit of CH_4 at this wavelength of 9 ppb in 8 s at 20 Torr.

6.3.2.2 Methanethiol

In order to study the ${}^RQ_4$ CH_3SH absorption at 3040 cm^{-1} (identified in Section 6.2.2 as a potentially useful feature to monitor this biomarker in breath) with this CEA spectrometer, it was necessary to calibrate the mirror reflectivity at this wavelength. To achieve this, similar studies as performed in Section 6.3.2.1 of the nearby 3038.50 cm^{-1} (2 F_2 10 $\leftarrow$ 1 F_1 1) $R(1)$ fundamental $\nu_3(F_2)$ transition of CH_4 using the 7.5 ppm CH_4 calibrated mixture were conducted at various pressures ($3 - 55$ Torr). Settings of $\lambda_p = 1064.300$ nm, $\lambda_s = 1572.2961 - 1573.005$ nm and $T_{crys} = 44.3°C$ were implemented to monitor this transition. The gradient of a plot of the area of the Voigt fits of these spectra against CH_4 concentration (Figure 6.11(a)), together with the σ_{int} of this transition reported in HITRAN of 8.79×10^{-20} $cm^2cm^{-1}molec^{-1}$ [14], yielded an effective cavity path length of 715 ± 7 m, corresponding to an average mirror reflectivity of $R = 0.9989$, at this wavelength. Three spectra of this CH_4 transition in lab air at ~ 20 Torr were also recorded, an example of which is given in Figure 6.11(b). Using the calculated 715 m effective path length, the average CH_4 concentration of lab air from these spectra was determined as 2.84 ± 0.06 ppm, which agrees well with the value found in Section 6.3.2.1. The α_{min} for these spectra was

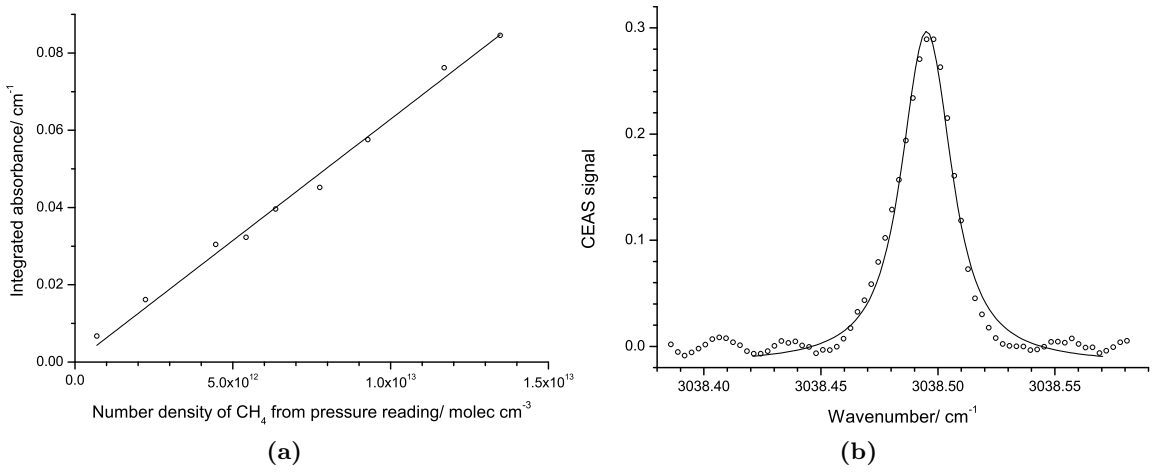

Figure 6.11: Results of CEAS studies of the (2 F_2 10 $\leftarrow$ 1 F_1 1) $R(1)$ transition of the fundamental $\nu_3(F_2)$ band of CH_4 at 3038.50 cm^{-1}. (a) CEA spectra of this transition of a calibrated 7.5 ppm CH_4 in air mixture were recorded at a range of pressures. The linear relationship between the area of the fitted absorption feature at 3038.50 cm^{-1} and the CH_4 concentration expected from the measured pressure, as shown here, allowed the effective path length of the cavity and the average mirror reflectivity at this wavelength to be determined; these were found to be 715 ± 7 m and 0.9989, respectively. (b) A CEA spectrum of the 3038.50 cm^{-1} CH_4 absorption of 18 Torr of lab air. The data (open circles) were fitted with a fitted Voigt profile (solid line), fixing the Gaussian width at the expected Doppler width of 280 MHz whilst allowing other parameters to float. The number of experimental points has been reduced for clarity.

7.1×10^{-8} cm^{-1} with an 8 s acquisition time, which, again, is similar to that ascertained previously.

Mixtures of CH_3SH in N_2 at various concentrations were prepared in the cavity by introducing small amounts ($\sim 1-2$ Torr) of pure CH_3SH (*Fluka*, purum, 1164432 20105093) to the cell and diluting these with N_2. This was accomplished by adding N_2 to the CH_3SH sample, pumping down the mixture, adding more N_2 and then re-evacuating the cavity to approximately 20 Torr, at which point the measurements were taken. The spectral region of interest was studied by setting $\lambda_p = 1064.294$ nm, $T_{\text{crys}} = 45.4°$C and scanning the DS-DBR over the range $1573.287 - 1573.346$ nm, generating mid-IR radiation covering $3289.45 - 3289.70$ nm ($3039.79 - 3040.02$ cm^{-1}). Because CH_3SH is a broadband absorber, it was necessary to record signal data across the required wavelength range for both a filled and evacuated cavity to obtain an I and I_0 spectrum, respectively. Figure 6.12 shows an example of the raw data recorded for one of the CH_3SH in N_2 mixtures, in which smaller transitions adjacent to the main absorption feature at lower wavenumbers are clearly visible; these neighbouring features had also been observed in the direct absorption experiments of this transition (inset in Figure 6.6). This data also emphasises the size of the noise observed in the baseline compared to that of the absorption feature to be studied. It is believed that the majority of this noise is intrinsic to the detector, and it is relatively large because the

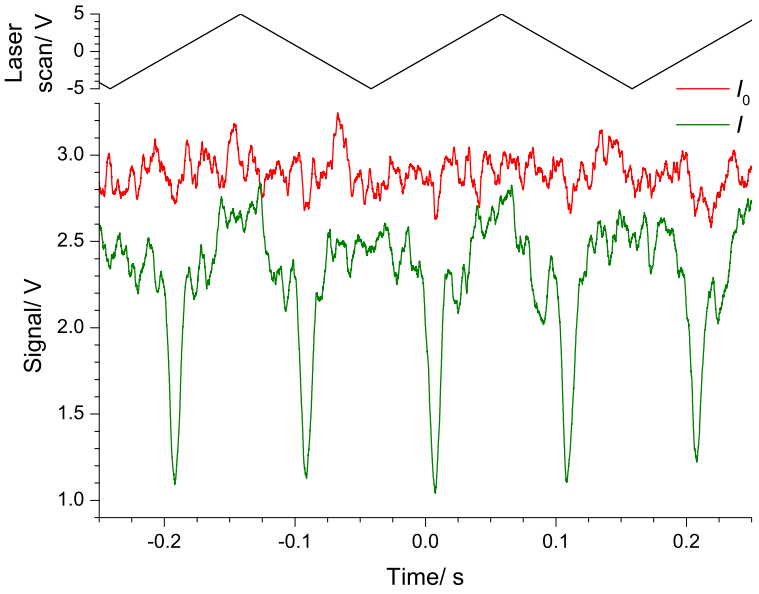

Figure 6.12: Raw data of the ${}^{R}Q_4$ CH_3SH absorption feature at 3039.9 cm^{-1} for the 233 ppm CH_3SH in N_2 sample at 19 Torr. The upper trace shows the laser scanning function in black, whereas the lower trace gives the I_0 and I signal data in red and green, respectively. The laser scanning function is applied to the DS-DBR signal laser, hence scanning the signal wavelength. An up-ramp of this modulation corresponds to a decrease in λ_s, and so to a decrease in $\tilde{\nu}_i$.

combination of low mid-IR powers and low transmission by the optical cavity means that only a small amount of radiation is incident on the detector, resulting in a small measured signal. This noisy background and poor SNR (the average baseline signal across one of the up-ramps in Figure 6.12 is 2.88 ± 0.08 V (1σ), giving a SNR of 35) will have repercussions in the sensitivity and detection limits of the system.

The results of repeating this process for a range of CH_3SH concentrations and creating absorption spectra, using the effective cavity path length estimated at this wavelength from the CH_4 studies of 715 ± 7 m, are given in Table 6.3 and Figure 6.13. Voigt profiles were fitted to the absorption feature of interest, utilising only data points which covered the main feature and not the two small side peaks observed at lower wavenumbers. These fits showed a general increase in the vertical offset of the Voigt fit as the concentration of CH_3SH increased, which is as expected due to the increase in the broadband absorption baseline. The reported line centres of the fits agree well with the line centre found in the direct absorption measurements, and their slight variation over the range $3039.90 - 3039.91$ cm^{-1} can be explained by a small drift in λ_p over the several hours in which the spectra were recorded. The Voigt width was approximately the same for all the spectra, as anticipated given that they were all recorded at roughly the same pressure and so should be subject to the same amount of pressure broadening. Again, it should be noted that the linewidths are dominated by the instrumental broadening associated with the lock-in amplifier, as discussed in Section 6.3.2.1, a fact which may also account for their uniformity.

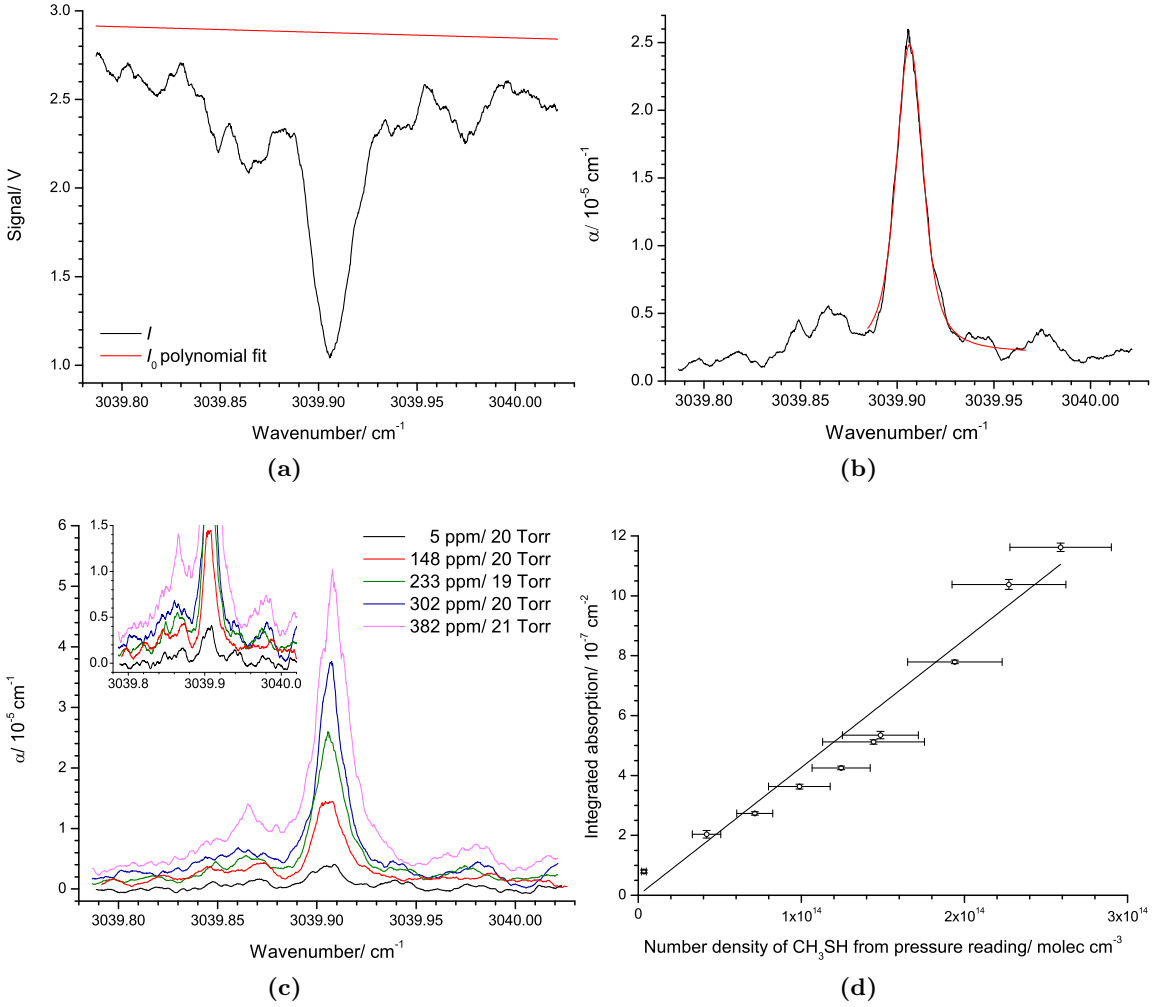

Figure 6.13: CEA spectra of the ${}^{R}Q_4$ CH_3SH absorption feature at 3039.9 cm^{-1} for diluted mixtures of CH_3SH in N_2, prepared *in situ* in the cavity. (a) and (b) illustrate the construction procedure of the absorption spectra, using as an example the data for the 233 ppm CH_3SH in N_2 sample at 19 Torr. (a) Signal data was recorded across the absorption feature for a filled (I, black) and evacuated cavity, and a low order polynomial fitted to the latter to yield the I_0 baseline (red). (b) The resultant CEA absorption spectrum of the data (black) was found using Equation 1.59 and the empirically determined effective cavity path length at this wavelength of 715 ± 7 m. A Voigt profile (red) was fitted utilising only data points which covered the main feature, and not the two small side peaks observed at lower wavenumbers. (c) CEA spectra for the CH_3SH feature recorded at a range of concentrations. The concentrations are reported as 'x ppm CH_3SH in N_2/ total pressure of sample'. Only a selection of the recorded spectra have been included for clarity, and the plots have been slightly shifted to account for the drift in λ_p over the spectra acquisition period and in order to overlay the main absorption. The inset shows a zoom in of the lower concentration spectra. (d) The linear relationship between the area of the fitted absorption feature and the CH_3SH concentration expected from the measured pressures and dilution procedure, with the y-error bars calculated from the error in the area of the Voigt fit and the x-error bars found by considering a 0.3 Torr uncertainty in each pressure reading. A weighted linear fit with the intercept fixed at the origin indicated an σ_{int} of $4.27 \pm 0.14 \times 10^{-21}$ $cm^2 cm^{-1} molec^{-1}$ for this absorption feature.

Take	CH_3SH conc. / molec cm^{-3}	CH_3SH conc. / ppm	p / Torr	Voigt fit parameters Offset / cm^{-1}	Line centre / cm^{-1}	Area / cm^{-2}	$\Delta\nu_V$ / MHz
1	$2.6 \pm 0.3 \times 10^{14}$	382	20.8	4.2×10^{-6}	3039.908	1.16×10^{-6}	543
2	$2.3 \pm 0.3 \times 10^{14}$	340	20.5	5.0×10^{-6}	3039.905	1.04×10^{-6}	522
3	$1.9 \pm 0.3 \times 10^{14}$	302	19.7	1.9×10^{-6}	3039.907	7.79×10^{-7}	424
4	$1.5 \pm 0.2 \times 10^{14}$	217	21.0	5.3×10^{-6}	3039.905	5.35×10^{-7}	518
5	$1.4 \pm 0.3 \times 10^{14}$	233	19.0	2.1×10^{-6}	3039.906	5.12×10^{-7}	499
6	$1.2 \pm 0.2 \times 10^{14}$	186	20.5	2.5×10^{-7}	3039.901	4.25×10^{-7}	434
7	$9.9 \pm 1.8 \times 10^{13}$	148	20.4	9.8×10^{-7}	3039.901	3.63×10^{-7}	487
8	$7.1 \pm 1.1 \times 10^{13}$	110	19.9	1.9×10^{-6}	3039.901	2.74×10^{-7}	560
9	$4.2 \pm 0.9 \times 10^{13}$	71	18.2	2.2×10^{-6}	3039.901	2.04×10^{-7}	499
10	$3.5 \pm 1.4 \times 10^{12}$	5	19.8	3.2×10^{-7}	3039.903	7.95×10^{-8}	512

Table 6.3: Results of the CEAS studies of the ${}^{R}Q_4$ CH_3SH absorption feature at 3039.9 cm^{-1} of the prepared CH_3SH in N_2 samples. The CH_3SH concentration (CH_3SH conc.) was estimated using the pressures noted in the dilution procedure, and the error approximated assuming a 0.3 Torr uncertainty in each baratron pressure measurement. The Voigt profiles were fit just over the main feature of interest, not the neighbouring side peaks, and the Voigt FWHM linewidth, $\Delta\nu_V$, found using Equation 1.18.

However, the most significant trait of these absorption Voigt fits is the change in area. A plot of the area of the Voigt fits against CH_3SH concentration is shown in Figure 6.13(d), and a straight line fitted with the intercept fixed at the origin. As $\alpha(\nu) = \sigma(\nu)C$, the gradient of this line is equal to the integrated absorption coefficient for this transition, and thus it was determined that $\sigma_{\text{int}} = 4.27 \pm 0.14 \times 10^{-21}$ $cm^2cm^{-1}molec^{-1}$ for this ${}^{R}Q_4$ CH_3SH absorption feature. This compares favourably with the approximate value of σ_{int} of $4.66 \pm 0.15 \times 10^{-21}$ $cm^2cm^{-1}molec^{-1}$ estimated from the direct absorption measurement of 3.2 Torr of pure CH_3SH performed in Section 6.2.2. Calculations using data from PNNL (Figure 6.5) [403] predicted a σ_{int} of 7.49×10^{-21} $cm^2cm^{-1}molec^{-1}$ for this ${}^{R}Q_4$ CH_3SH transition, but this involved fitting a line profile to a low resolution spectrum (the region of interest was covered by only 13 data points) in which the main absorption feature and the less intense neighbouring transitions identified in this work were broadened into one, amalgamated feature by virtue of this low resolution as well as by instrumental and pressure broadening.

An estimate of the sensitivity of the system was made utilising the data recorded for the experiment listed as Take 5 in Table 6.3, corresponding to the α plot in Figure 6.13(b). Using Equation 1.60 and the RMSE in the I_0 baseline fit of this data as ΔI_{min}, an α_{min} of 2.6×10^{-7} cm^{-1} over an 8 s integration time was found, indicating an $\alpha_{\text{min}}(BW)$ of 7.4×10^{-7} $cm^{-1}Hz^{-1/2}$. These values are worse than those obtained in the CH_4 studies because a smaller lock-in amplifier time constant was used here; this was done in order to fully examine the structure of the CH_3SH feature, but came at the cost of a noisier baseline. Given that in this 233 ppm CH_3SH in 19 Torr N_2 spectrum the height of the absorption

feature was 2.5×10^{-5} cm^{-1}, this $\alpha_{\min}$ value of 2.6×10^{-7} cm^{-1} implies that a CH_3SH detection limit of 2.4 ppm in 8 s at 19 Torr at this wavelength was achieved, corresponding to 460 ppb in 8 s at 100 Torr.

6.4 Conclusions

In this chapter, the potential of using widely tunable telecom lasers for QPM-DFG in the generation of mid-IR light has been demonstrated. Light from an L-band DS-DBR laser was combined with that from a 1064 nm diode laser in a bulk PPLN crystal, generating mid-IR radiation over the range $3130 - 3330$ nm with powers of up to 20 μW, depending on the EDFA used to amplify the signal radiation. Tunability across this range was enabled by changing the PPLN temperature and track accordingly. Due to the reliability and reproducibility of the DS-DBR, previous wavelength calibrations, carried out in the near-IR in either the internal or external ramping mode of operation, were used to provide an absolute frequency calibration in the mid-IR.

The use of this mid-IR radiation for applications in spectroscopy was illustrated by performing single-pass direct absorption experiments on CH_4 (a narrowband absorber) and CH_3SH (a broadband absorber) at low pressures. High resolution direct absorption spectra of 0.18 Torr of CH_4 in 6 Torr of air over $3016 - 3096$ cm^{-1}, covering the Q and R branches of the fundamental $\nu_3(F_2)$ transition, were acquired, and were found to be in good agreement with simulated spectra in terms of both the positions and intensities of the absorption features. In the CH_3SH spectrum, the ${}^RQ_4$ absorption at 3040 cm^{-1} was identified as a potentially useful feature for monitoring this biomarker in exhaled breath at reduced pressures (100 Torr). In addition, the possibility of using this DS-DBR DFG system for WMS was demonstrated by performing $2f$-WMS on CH_4 to study four $R(5)$ absorption lines in the ν_3 vibrational band at 3076.7 cm^{-1}; similar behaviour to that observed when conducting WMS with the DS-DBR in the near-IR was seen, which again highlighted the importance of the A_m-a_m calibration in both qualitative and quantitative studies.

The DS-DBR sourced, DFG-generated mid-IR radiation was then coupled into the mid-IR cavity to perform CEAS. Phase sensitive detection using a mechanical chopper and lock-in amplifier was also employed to enhance the observed signal. Spectroscopic studies of CH_4 transitions at 3017.47 cm^{-1} and 3038.50 cm^{-1} utilising a 7.5 ppm calibrated mixture allowed the system to be characterised and calibrated, yielding R values at the two wavelengths of 0.9988 and 0.9989, respectively. Experiments on ambient air were then conducted, in which the concentration of CH_4 was calculated as 2.8 ppm and $\alpha_{\min}$ estimated as 6.2×10^{-8} cm^{-1} over an 8 s acquisition time. Mixtures of CH_3SH in N_2 at different concentrations ($5 - 380$ ppm) were prepared in the cavity in order to investigate the ${}^RQ_4$ CH_3SH absorption

feature at 3039.9 cm^{-1} and yielded a σ_{int} of $4.27 \pm 0.14 \times 10^{-21}$ $cm^2cm^{-1}molec^{-1}$ for the main absorption feature. The lowest concentration of CH_3SH experimentally observed was 5 ppm in a 20 Torr sample, though the spectrometer was deemed sensitive enough to detect levels at half this value. The limiting factor in the sensitivity of the system was the low mid-IR powers. The average transmitted intensity by a CEA spectrometer is between $P_{in}(1-R)^2$ and $P_{in}(1-R)/(1+R)$, according to Equations 1.55 and 1.56 when no absorber is present in the cavity; in this case, using the mid-IR power measured for the CEAS set-up in Section 6.3.1 of 21 µW and an R of 0.9989 as found in Section 6.3.2.2 at 3038.50 cm^{-1}, this corresponds to powers of $0.03 - 11.5$ nW. The noise equivalent power, accounting for the detector bandwidth, for the PVI-2TE-4/VPDC-0.1l *Vigo Systems* detection module utilised in this work was 0.09 nW (Table 1.1); as NEP is the optical power which will yield a SNR of unity, this represents the limit of what can be detected. As the power of the cavity throughput of the CEAS system is comparable to the NEP of the detector, these low mid-IR signal intensities mean that CEAS cannot approach the same sensitivities as the CRDS system detailed in Chapter 5.

In summary, in this chapter the three major concepts identified for performing sensitive spectroscopy across a broad spectral range - namely the employment of a widely tunable laser source; the use of sensitive, cavity-based spectroscopic techniques; and the exploitation of the strong, fundamental transitions of the mid-IR - have been successfully combined to create a widely tunable, sensitive spectrometer in the mid-IR. Such a spectrometer has many possible future uses in the detection of multiple species or broadband absorbers for both medical and environmental applications, and has the potential to be further enhanced in terms of ease of use and sensitivity; some of these ideas for improvement are explored and discussed in Chapter 7.

Chapter 7

Conclusions and Outlook

7.1 Overall Conclusions

This thesis has described the development and application of laser absorption spectroscopic techniques in both the near- and mid-IR, focusing on the potential uses of such methods in breath analysis for medical diagnostics. In an ideal spectrometer, a wide tunability (which would permit monitoring of broadband absorbers or many, spectrally separated, absorption features from one or more species) would be combined with high sensitivities (to allow for the detection of weakly absorbing or dilute species) and selectivities (in order to measure compounds of interest in a complex background matrix) for the ultimate in trace gas sensing. These objectives can be achieved by implementing one or more of these three ideas: using a high fidelity laser source with a large spectral range, applying sensitivity enhancing techniques and utilising transitions in the mid-IR. In this thesis, each of these approaches has been investigated in turn, and the results of employing combinations of them explored.

In Chapter 2, a summary of near-IR laser sources was given and the novel, broadband DS-DBR laser introduced. This widely tunable ($1563-1613$ nm), single-mode laser source, with a Gaussian beam profile ($w_0 = 0.5$ mm), moderate output power (~ 20 mW) and narrow linewidth (~ 1 MHz), was characterised and its modes of operation, either by an internal or external voltage ramp, described. These operational methodologies meant that the laser wavelength could either be scanned or stepped across a region of interest, with the former approach resulting in mode-hops in the laser output of ~ 1.7 cm^{-1}, which were related to how the laser was tuned, and the latter allowing full coverage of the entire spectral range accessible with this laser. The first use of the DS-DBR as a useful spectroscopic laser source was illustrated by performing measurements on CO_2, highlighting its ability to both cover a large wavelength range and perform spectroscopy at a high spectral resolution. WMS

experiments were also carried out on CO_2 samples by applying fast current modulations to different sections of the device, and a variation in modulation amplitude across the spectral region observed due to the non-linear wavelength-current relationship of the laser unit. An Allan variance analysis carried out for the $2f$ detection scheme reported an optimal $\alpha_{\min}$ of 6.3×10^{-8} cm^{-1} measured over a 23 s acquisition time. Further investigations revealed that as well as presenting only small frequency drifts in the short term ($\sim$ 20 MHz), the DS-DBR also offered long term wavelength stability ($\pm$400 MHz between different days), exemplifying its reliability and reproducibility.

Work on the development of a near-IR CRD spectrometer, as well as examples of its spectroscopic use, were presented in Chapter 3. The software and hardware for the spectrometer were thoroughly detailed, including a description of the two key programs written in LabVIEW to record ring-downs either at a single, fixed wavelength or over many wavelengths. The CRDS set-up and programs were first tested by performing measurements with a traditional DFB diode laser source at 1577 nm, including studies of the $\nu(31112 \leftarrow 01101)$ $P(19)$ transition of CO_2 at 6340.13 cm^{-1} in a 20.3% mixture of CO_2 in air at various pressures. The system was then combined with the DS-DBR, and RDTs, varying between $19 - 26$ µs, were measured for an evacuated cavity across the whole $1563 - 1613$ nm DS-DBR wavelength range without the need for modifications to the cavity alignment. An Allan variance study of data acquired at 1605.476 nm indicated an optimal $\alpha_{\min}$ of 2.8×10^{-10} cm^{-1} over 20 s for this system when filtering and averaging 100 ring-downs per point. The use of the DS-DBR CRDS system for high resolution spectroscopy was demonstrated by several experiments conducted on variously sourced, low pressure samples of CO_2 at a selection of wavelengths: studies of the $\nu(30013 \leftarrow 00001)$ $R(14)$ transition at 6238.7 cm^{-1} were used to determine the concentration of CO_2 present in lab air (622 ± 13 ppm), and the $\nu(30013 \leftarrow 00001)$ $R(0)$ $^{12}CO_2$ and $\nu(30012 \leftarrow 00001)$ $R(4)$ $^{13}CO_2$ transitions were investigated in both calibrated CO_2 mixtures and breath samples with accuracies in the $r_{13/12}$ ratio of ~ 10‰, which is a promising value but not as low as the 1‰ gold standard required for medical diagnostic purposes. CEAS using the DS-DBR as the laser source was also performed to study these last two, medically relevant CO_2 transitions, though the determined accuracy was a factor of $2 - 3$ times poorer than that found in the CRDS measurements owing to CEAS being an intrinsically less sensitive technique.

Mid-IR radiation was generated using QPM-DFG, as described in Chapter 4. An experimental free-space QPM-DFG system was constructed, in which light from a 1560 nm DL, amplified by an EDFA, was mixed with 1064 nm radiation from another DL in a bulk PPLN crystal to create mid-IR light at 3.3 µm. In order to maximise the DFG conversion efficiency, and hence the amount of mid-IR radiation produced, temperature tuning experiments were conducted. For such an analysis performed using pump and signal wavelengths of 1064.295 nm and 1560.244 nm, respectively, an optimum crystal temperature

of T_{opt} = 83.1°C was found, with a temperature acceptance bandwidth of 7°C (FWHM). These conditions generated 20 μW of mid-IR light at 3348.247 nm, with an overall DFG conversion efficiency of 0.035% $W^{-1}cm^{-1}$, which is a typical performance for this type of configuration.

The radiation from this set-up was used to perform the mid-IR spectroscopy documented in Chapter 5. This chapter began with a review of the examples of coupling mid-IR radiation with cavity-based spectroscopic techniques currently reported in the literature, before the DFG-based CRD 3 μm spectrometer developed in this work was presented. The system, comprising a 77 cm long cavity with mirror reflectivities of 0.9996, gave τ_0 values of 6.07 ± 0.03 μs, which implied an α_{min} of 2.8×10^{-8} cm^{-1} over 6 s when filtering and averaging 100 ring-downs per point; Allan variance studies signified an optimal α_{min} of 2.9×10^{-9} cm^{-1} could be obtained by averaging 730 RDTs over 42 s. The use of the DFG CRDS system for spectroscopic purposes was illustrated by performing experiments on a variety of molecules. Studies of the (2 F_1 9 ← 3 F_2 1) $P(3)$ transition at 2988.933 cm^{-1} in the fundamental $\nu_3(F_2)$ band of CH_4 at low pressures (< 25 Torr) were conducted to ascertain the amount of CH_4 present in a 7.5 ppm calibrated mixture of CH_4 in air and breath samples from both methane and non-methane producers: the calculated concentrations of 7.59 ± 0.16 ppm, 29.4 ± 1.0 ppm and 2.26 ± 0.10 ppm, respectively, correlated well with those expected. Spectra of the $\nu(1 \leftarrow 0)$ $Q(2)$ transition of D_2 at 2987.29 cm^{-1} over a range of pressures (70 − 460 Torr) displayed the phenomenon of Dicke narrowing, with the experimental data best fitted by Galatry profiles which accounted for collisional narrowing: the fact that the spectrometer could detect these differences in lineshape indicated its capacity for high resolution studies. Values for the line centre and σ_{int} for this D_2 transition were calculated as 2987.279 ± 0.006 cm^{-1} and $2.29 \pm 0.03 \times 10^{-27}$ $cm^2cm^{-1}molec^{-1}$, respectively, which compare favourably with the estimates of these parameters found from theoretical calculations reported in the literature of 2987.2934 cm^{-1} and 2.378×10^{-27} $cm^2cm^{-1}molec^{-1}$, respectively. Measurements of acetone were also carried out in order to appraise the ability of the DFG CRDS set-up to detect broadband absorbers: the results of single wavelength studies at 2985.70 cm^{-1} of a 5 ppm calibrated mixture of acetone in N_2, performed by recording τ_0 and τ values of the cavity filled with ∼ 90 Torr of N_2 and the sample, respectively, estimated the concentration as 5.26 ± 0.08 ppm, in good agreement with the manufacturer's quoted value of 5.37 ± 0.27 ppm. Alterations were then implemented to improve the spectrometer: the pump radiation source was replaced with a more powerful Nd:YAG laser in order to increase the amount of mid-IR light generated, and a new detection system, comprising of a faster detector and a variable amplifier, was emplaced. This led to an enhanced α_{min} of 6.4×10^{-10} cm^{-1} over 151 s for an empty cavity.

In Chapter 6, the DL signal source in the QPM-DFG set-up was replaced with the DS-DBR, allowing mid-IR radiation between 3130 − 3330 nm to be produced. The poling period and

temperature of the PPLN crystal had to be altered in order to access the whole of this range, and powers between $3-21$ μW were generated depending on the EDFA utilised, which was dictated by the target wavelength range. This mid-IR light was used to study CH_4: direct absorption spectra of 0.18 Torr of CH_4 in 6 Torr of air over $3016-3096$ cm^{-1}, covering the Q and R branches of the fundamental $\nu_3(F_2)$ transition, were acquired and found to be in good agreement with simulated spectra in terms of both the positions and intensities of the absorption features; and $2f$-WMS was used to study four $R(5)$ absorption lines in the $\nu_3(F_2)$ vibrational band at 3076.7 cm^{-1}, with a similar non-linear wavelength-current relationship as observed in WMS studies in the near-IR. Direct absorption measurements of 3.2 Torr of CH_3SH between $3016-3096$ cm^{-1} revealed the ${}^{R}Q_4$ transition at 3040 cm^{-1} as a potentially useful feature for monitoring this biomarker in exhaled breath at reduced pressures. The DS-DBR sourced, DFG-generated mid-IR radiation was then coupled into a mid-IR cavity to perform CEAS combined with phase sensitive detection via a mechanical chopper and lock-in amplifier. Spectroscopic studies of the (6 A_2 8 $\leftarrow$ 6 A_1 1) $Q(6)$ and (2 F_2 10 $\leftarrow$ 1 F_1 1) $R(1)$ transitions of the fundamental $\nu_3(F_2)$ band of CH_4 at 3017.47 cm^{-1} and 3038.50 cm^{-1}, respectively, were conducted using a 7.5 ppm calibrated CH_4 mixture at various pressures in order to calibrate the system: effective path lengths at the two wavelengths of 620 ± 10 m and 715 ± 7 m, respectively, were determined. Experiments on ambient air were then performed, in which the concentration of CH_4 was calculated as 2.81 ± 0.10 ppm and α_{min} determined to be 6.2×10^{-8} cm^{-1} over an 8 s acquisition time. In addition, this set-up was also used to further examine the ${}^{R}Q_4$ CH_3SH absorption feature at 3039.9 cm^{-1} using mixtures of CH_3SH in N_2 at different concentrations ($5-380$ ppm) prepared in the cavity. A σ_{int} of $4.27 \pm 0.14 \times 10^{-21}$ cm^{2}cm^{-1}molec^{-1} for the main absorption feature at 3039.9 cm^{-1}, and a CH_3SH detection limit of 2.4 ppm at 19 Torr for this system at this wavelength, were established.

In summary, it has been shown that using a DS-DBR laser source to perform high resolution cavity-based spectroscopy, in both the near- and mid-IR, is a viable and useful technique for sensitive trace gas sensing. The three major concepts proposed for performing sensitive spectroscopy across a broad spectral range - namely the employment of a widely tunable laser source; the use of sensitive, cavity-based spectroscopic techniques; and the exploitation of the strong, fundamental transitions of the mid-IR - have each been investigated individually and in pairwise combinations with favourable results. Indeed, all three aspects have been successfully combined to create a widely tunable, sensitive spectrometer in the mid-IR. Such a spectrometer has many possible uses in the detection of multiple species or broadband absorbers, and there are many potential improvements that could be made to enhance the system; some of these ideas are explored in the following section.

7.2 Future Developments

There are various features of the spectrometers developed in this thesis that could be altered in order to improve their performance. One easy to implement change which would enable concentration determination over a reduced acquisition time would be to take measurements at just one, fixed wavelength corresponding to the top of an absorption feature, or at a few points which would cover the peak. The viability of such a procedure was ascertained in Section 3.3.3. The optimal number of scans or ring-downs to average, as found using Allan variance analyses, could then be used to yield the best possible minimum detectable absorption coefficient. The total acquisition time would thus be shorter than that associated with repeating measurements at several wavelengths to create a spectrum, which includes the dead time between spectral points as the laser is tuned. To achieve this, however, high wavelength and mechanical stability would be required. Furthermore, care would be needed to ensure that the correct spectral baseline was used, by taking regular measurements off-resonance or of an evacuated cavity. The former method could readily be implemented using the DS-DBR, and would involve recording I and I_0, or τ and τ_0, values at just two frequencies corresponding to the top and bottom of the absorption feature, respectively, by rapid switching of the DS-DBR between these well-defined frequency points, a feat made possible by the high reliability and wavelength reproducibility of this laser source; the latter methodology would be necessary if studying broadband absorbers. This approach of quickly and simply determining only the peak α values of the absorption features of interest in order to reduce data acquisition time could be adopted in both the near- and mid-IR. If specificity was a concern though, then taking data across the entire line profile, as done for most of the work in this thesis, would be preferable.

Another change which would enhance systems in both and the near- and mid-IR would be to link the LabVIEW programs developed with the reference calibration tables of the DS-DBR settings and output wavelength. Currently, the settings for the desired wavelength or wavelengths have to be imported manually into the LabVIEW program, having first been identified in the reference data by the user. It would be ideal if the user could simply input the single fixed wavelength, multiple fixed wavelengths or wavelength range of interest into the LabVIEW software, which then determined the appropriate settings. This automation would greatly help in the collection of data, especially when jumping between widely separated wavelengths.

With regards to work in the mid-IR, the frequency calibration could be improved by constantly monitoring the pump laser wavelength using a wavemeter or an etalon during the acquisition of spectra in order to account for any laser drift, or by locking the pump wavelength to a molecular transition.

Further enhancements could be made by increasing the amount of mid-IR power, which could be accomplished by boosting either the input pump power, the input signal power, the DFG conversion efficiency or a combination of these. One way the first approach could be achieved is by replacing the 1064 nm DL with a more powerful Nd:YAG laser, giving hundreds of mW of pump radiation. This strategy was investigated in Section 5.4, and led to a five-fold increase in mid-IR power and a clear improvement in the spectrometer sensitivity. The signal input power could be raised by using a higher power fibre amplifier: *Nuphoton Technologies* now offer high power C- and L-band EDFAs that output up to 10 W of amplified radiation [453]. In the case of the CRDS systems, an increase in signal power could also be realised by positioning the AOM before the EDFA so that the amount of signal radiation available for mid-IR generation is not reduced; this configuration could be possible by gain clamping the EDFA, either with an optical feedback loop or by adjusting the pump power [400]. Alternatively, the use of a waveguide PPLN module would result in an increased conversion efficiency and hence higher mid-IR powers, though this would come at the cost of a reduced spectral bandwidth. The poorer output beam profile often observed on using such a device would not prevent the application of techniques such as CEAS, though CRDS may be more problematic.

If it were desired to improve the mid-IR CRD spectrometer, the use of new and improved commercially available mid-IR technology, such as detectors and cavity mirrors, would be beneficial. *CRD Optics* [454] offer mirrors with R values of 0.9999 over the $3000-3400$ nm wavelength range; using the 77 cm long cavity employed in this thesis, such an increase in R would result in L_{eff} and τ_0 values of 7.7 km and 26 μs, respectively, but would also come with the penalty of lower powers incident on the detector. The use of improved detectors has already been explored in Section 5.4, in which a detection module combining a more sensitive photovoltaic detector chip with a higher bandwidth pre-amplifier was utilised; the higher bandwidth meant that the detection module had a faster response time allowing fast signals to be observed with smaller contributions from the electronics to the measured RDTs (Section 5.4.1), thereby reducing the error in the true RDT. Again, however, there is a trade off, as the increased temporal resolution unfortunately leads to a decrease in the overall sensitivity of the detector (Table 1.1).

If the mid-IR power could be increased sufficiently, the DS-DBR DFG system could be used for CRDS, rather than the CEAS performed in Section 6.3. Indeed, CRDS measurements with the current set-up were attempted, but the signal output from the cavity was too weak for triggering and detection owing to the noisy cavity modes of the DS-DBR, as seen in the near-IR in Section 3.3.2.1. The shorter coherence time for the DS-DBR compared to a DFB DL meant that the DS-DBR sourced, mid-IR cavity modes were broader and smaller in amplitude than expected, and of insufficient height to trigger the CRDS system to begin recording ring-downs. Previous studies with the DS-DBR in the near-IR had indicated that

noisy cavity modes could still be used to report accurate RDTs, so while the noise of the cavity modes was not in itself intractable, the combination of this effect with low mid-IR powers was. An increase in mid-IR power would overcome this difficulty, thus allowing CRDS to be implemented.

Concerning the ability to detect CH_3SH in breath, the ${}^RQ_4$ CH_3SH absorption feature at 3039.9 cm^{-1} was identified as a potential indicator for monitoring this biomarker because of its relative freedom from H_2O and CH_4 interference at low pressures. In order to observe this feature at 10 ppb in a 100 Torr total pressure sample without pre-concentration, it was established that a sensitivity of $\sim 5 \times 10^{-9}$ cm^{-1} was needed, a level which was achieved using the mid-IR CRD spectrometer in Chapter 5. As indicated above, such sensitivities were not attained when using the DS-DBR as the DFG signal source due to the current infeasibility of performing CRDS in the mid-IR with this laser; however, it is clear that if a DFB diode laser operating at the correct wavelength with a sufficiently long coherence time could be sourced, it could be combined with the DFG-based CRD spectrometer to produce a selective and sensitive CH_3SH detector at 3039.9 cm^{-1}. The improvements to the mid-IR power levels outlined above may enable the DS-DBR sourced, DFG-generated mid-IR radiation to be used with CRDS too, allowing detection at 3039.9 cm^{-1} at the required sensitivities using this widely tunable signal source. Having identified this small spectral region for use in the detection of CH_3SH in breath, an alternative, higher power laser source, such as a QCL or ICL, that can access this wavelength could be used as the radiation source for CRDS instead, which would overcome the difficulties of the low mid-IR powers encountered in this work. However, despite their recent technological advances, such devices may not yet be commercially available with the required continuous tunability across the necessary wavelength range. Furthermore, it is noteworthy that it was only through the wide tunability offered by the DS-DBR DFG system that the appropriate feature for monitoring this biomarker was determined; such extensive tunability combined with high spectral resolution at 3 μm is not possible with other mid-IR radiation sources. This rationale could be applied more generally to offer one potential future application of the widely tunable spectrometer developed in this work: the system could be used to record high resolution survey spectra of biomarkers of interest over the $3 - 3.3$ μm range in order to identify the optimal spectral regions for their detection, and, using this knowledge, tailor-made devices could then be created utilising different laser sources with the specific application of measuring a particular target molecule at a required sensitivity. However, the widely tunable mid-IR spectrometer of this thesis could also still offer the option of measuring multiple target species with a single instrument, if so wished.

An alternative approach to reaching the desired $\sim 5 \times 10^{-9}$ cm^{-1} sensitivity for monitoring the ${}^RQ_4$ CH_3SH absorption feature at 3039.9 cm^{-1} could be to conduct $2f$-WMS in combination with an astigmatic Herriott cell. The FWHM of the main ${}^RQ_4$ CH_3SH absorption

feature recorded at 3.2 Torr in Figure 6.6 was measured as 0.011 cm^{-1}. As the maximum sensitivity achievable with $2f$-WMS occurs when the modulation index, b, is approximately equal to two [28], this means that the optimal optical frequency modulation amplitude, a_m, to use would be 0.011 cm^{-1} (Equation 1.35). Such modulation amplitudes are readily realised; indeed, they have already been used, as demonstrated in Section 6.2.1.2 and Figure 6.4. Additional work in Section 6.2.1.2 also indicated an $\alpha_{\min}(BW)$ of 3.1×10^{-6} $cm^{-1}Hz^{-1/2}$, so in order to reach the required $\sim 5 \times 10^{-9}$ cm^{-1} sensitivity, a multi-pass cell with length of at least 6.2 m would be needed. Thus the typical path lengths attainable with Herriott cells of $50 - 250$ m [31] should easily reach the desired sensitivities. With such an approach, it is important to note that the cell volume may be large (several 100 cm^3), which could prove troublesome for conducting studies of single breath samples. Also, WMS is not an absolute quantification technique, hence reference, calibrated samples would be required. If necessary, pre-concentration of the breath samples could also be employed, either by solid phase extraction [455], Tenax trapping [456] or cryogenic trapping [457]; such a solution would not be ideal though as it would increase the complexity of the breath sampling procedure and may introduce problems of reproducibility. However, the work presented in this thesis, together with the ideas presented in the preceding discussion of possible improvements, should pave the way for the development of a CH_3SH sensor in order to measure this crucial biomarker in breath for medical diagnostics.

Appendix A

Beam Propagation and Ray Transfer Matrix Analysis

A plane wave can be characterised by an individual propagation direction given by a wavevector [10]. If the optical system has a symmetry axis, z, then the ray at a given cross-section (fixed value of z) can be described by the angle, θ, that the beam makes with this optical axis and its distance, y, from it. In the paraxial ray approximation, only those rays that are near and almost parallel to the z axis are considered, so that their angles to the optical axis are sufficiently small to permit the estimates $\sin\theta \approx \theta$ and $\tan\theta \approx \theta$ to be employed. This allows for the development of the concept of ray tracing, which reveals how light beams propagate through an optical system and interact with the various components within it. Before embarking upon this idea of ray tracing in earnest, it is important to clarify certain terms and sign conventions, as summarised in Equation A.1 and Figure A.1.

In ray tracing [2], we use linear algebra to calculate how the propagation direction of the beam changes on its interaction with an optical element. If the ray is initially moving in a direction specified by the coordinates (y_1, θ_1) and it subsequently interacts with an optical component that alters its trajectory, then the new beam propagation is now represented by the coordinates (y_2, θ_2):

$$\begin{pmatrix} y_2 \\ \theta_2 \end{pmatrix} = \begin{pmatrix} \mathrm{A} & \mathrm{B} \\ \mathrm{C} & \mathrm{D} \end{pmatrix} \begin{pmatrix} y_1 \\ \theta_1 \end{pmatrix} \tag{A.1}$$

where $\left(\begin{smallmatrix} \mathrm{A} & \mathrm{B} \\ \mathrm{C} & \mathrm{D} \end{smallmatrix}\right)$ is called an ABCD matrix and describes how the optical element interacts with and transforms the light ray. Different optical components have different effects on the light beam, so have different ABCD matrices. The main optical elements to consider are interfaces, lenses and mirrors, characterised by their refractive indices, n, focal lengths, f, and radii of curvature, r, respectively. Table A.1 gives several important ABCD matrices.

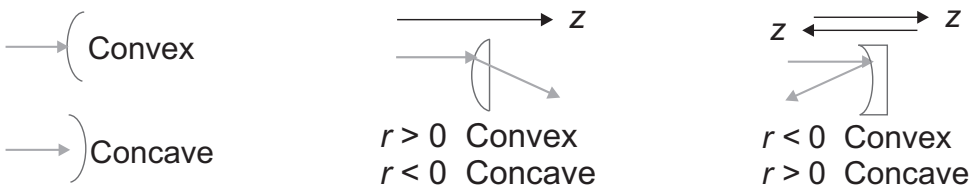

(a) Convex and concave **(b)** Refraction **(c)** Reflection

Figure A.1: Explanation of the sign conventions adopted in optical systems. z describes the general propagation direction of the light ray. (a) defines the terms convex and concave: as a ray of light travels towards it, a surface is said to be convex if the centre of curvature occurs after the interface (curve bulges outwards), whereas it is concave if the centre of curvature is before (curves inwards). When the direction of travel of the light beam is unaltered, as for refraction, propagation and transmission, the z axis remains in the same orientation; this is illustrated in (b) and sign convention 1 for the radii of curvature, r, is employed. When the direction of the light propagation is reversed, as for reflection, the positive z axis flips so the rays still travel positively; this is shown in (c) and sign convention 2 is used.

Optical systems are often made up of several different optical units put together, with the beam passing through each part in turn. If the ray passes through or interacts with m optical elements in the order $1, 2, 3, ..., m$, the overall transformation of the beam from its initial propagation trajectory, given by (y_1, θ_1), to its final one, (y_2, θ_2), can be summarised as:

$$\begin{pmatrix} y_2 \\ \theta_2 \end{pmatrix} = \mathbf{M}_m \cdot \ldots \cdot \mathbf{M}_3 \cdot \mathbf{M}_2 \cdot \mathbf{M}_1 \cdot \begin{pmatrix} y_1 \\ \theta_1 \end{pmatrix} \tag{A.2}$$

$$= \mathbf{M} \cdot \begin{pmatrix} y_1 \\ \theta_1 \end{pmatrix} \tag{A.3}$$

So the ABCD matrix for the whole system, $\mathbf{M}$, is simply the result of the matrix multiplication of the ABCD matrices of the individual components in the order in which they interact with the light ray, $\mathbf{M}_m \cdot \ldots \cdot \mathbf{M}_3 \cdot \mathbf{M}_2 \cdot \mathbf{M}_1$.

Laser light often has a Gaussian shaped beam profile, as illustrated in Figure A.2. A Gaussian laser beam of any order can be described by the complex beam parameter, $q(z)$, which varies as the beam travels along the z axis according to $q(z) = q_0 + z$ [10], with q_0 given by:

$$q_0 = \frac{\mathrm{i}\pi w_0^2}{\lambda} \tag{A.4}$$

where w_0 is the beam waist and λ is the wavelength of the light. $q(z)$ can also be expressed as [10]:

$$\frac{1}{q(z)} = \frac{1}{r(z)} - \frac{\mathrm{i}\lambda}{\pi w_0^2} \tag{A.5}$$

where $r(z)$ is the radius of curvature of the spherical phase front of the beam at the point

Transformation description	Sign convention	Figure	Matrix	Notes
Propagation in homogeneous medium	1	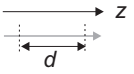	$\begin{pmatrix} 1 & d \\ 0 & 1 \end{pmatrix}$	d = distance
Refraction at planar interface	1	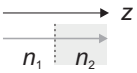	$\begin{pmatrix} 1 & 0 \\ 0 & \frac{n_1}{n_2} \end{pmatrix}$	n = refractive index n_1 = initial n n_2 = final n
Refraction at curved surface	1	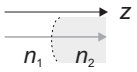	$\begin{pmatrix} 1 & 0 \\ \frac{n_1-n_2}{rn_2} & \frac{n_1}{n_2} \end{pmatrix}$	r = radius of curvature $r > 0$ convex $r < 0$ concave
Refraction of thin lens	1	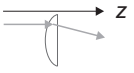	$\begin{pmatrix} 1 & 0 \\ -\frac{1}{f} & 1 \end{pmatrix}$	f = focal length of lens $f > 0$ converging/convex $f < 0$ diverging/concave
Refraction of plano-curved mirror	1	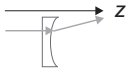	$\begin{pmatrix} 1 & 0 \\ \frac{n_m-1}{r} & 1 \end{pmatrix}$	$n_m = n$ of mirror $r > 0$ convex $r < 0$ concave
Reflection at curved mirror	2	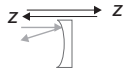	$\begin{pmatrix} 1 & 0 \\ -\frac{2}{r} & 1 \end{pmatrix}$	$r > 0$ concave $r < 0$ convex

Table A.1: Summary of the ray transfer ABCD matrices for selected interfaces and components. The ray matrix for refraction of a plano-curved mirror, with the order of the interactions of the incoming light beam with the plane and curved surfaces of the mirror as indicated in the diagram, was found by considering the mirror as a thin lens and the lens makers' equation for a thin lens of $1/f = (n_2-n_1)/n_1\,(1/r_1 - 1/r_2)$, where n_1 and n_2 are the refractive indices of the initial medium and mirror material, respectively, and r_1 and r_2 refer to the first and second radius of curvature of the optical element, respectively. In this case, $r_1 = \infty$ as the first surface is planar and r_2 is equal to the radius of curvature of the mirror, r, with its sign dependent on whether the surface is convex or concave to the incoming light ray, as defined in Figure A.1(a), and using sign convention 1. Assuming the initial medium is air, so $n_1 = 1$, and labelling the refractive index of the mirror as n_m, this formula reduces to $1/f = -(n_m-1)/r$. This can then be substituted into the ray matrix for refraction of a thin lens to generate the appropriate ABCD matrix. It is noteworthy that this means a plano-concave mirror, with the light propagating through it as drawn, acts as a diverging lens.

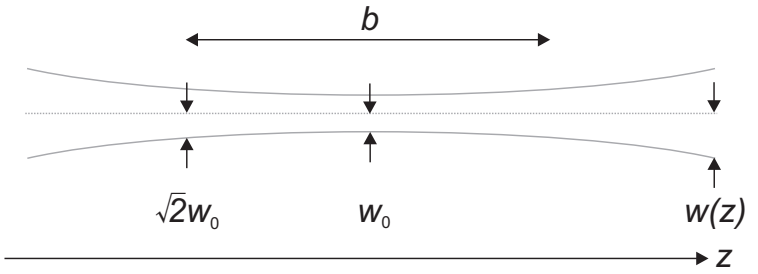

Figure A.2: A focused Gaussian beam. The confocal parameter, b, is twice the distance over which the beam waist, w_0, is increased by a factor of $\sqrt{2}$.

z along the axis:

$$r(z) = z\left[1 + \left(\frac{\pi w_0^2}{\lambda z}\right)^2\right] \tag{A.6}$$

It can be shown that ray transfer matrix analysis and the ABCD matrices outlined above can also be used to describe Gaussian beam propagation [2, 458, 459], allowing the parameters of a Gaussian beam exiting an optical system to be predicted, given the parameters of the input Gaussian beam. If $q_1(z)$ and $q_2(z)$ are the complex beam parameters of the Gaussian beam before and after the optical system, respectively, then [10, 458, 459]:

$$q_2(z) = \frac{\mathrm{A}q_1(z) + \mathrm{B}}{\mathrm{C}q_1(z) + \mathrm{D}} \tag{A.7}$$

where $\left(\begin{smallmatrix}\mathrm{A} & \mathrm{B}\\ \mathrm{C} & \mathrm{D}\end{smallmatrix}\right)$ is the transfer matrix found for paraxial rays for the overall optical system. This approach can be exploited in order to accomplish mode-matching of a laser beam into a cavity.

Mode-matching is required to convert the properties of the incident laser beam into those best supported by the cavity in order to maximise the coupling of the light into the resonator [57]. It is achieved by the use of mode-matching optics placed before the cavity. The simplest arrangement is shown in Figure A.3 where one lens of focal length f is placed a distance d in front of the cavity to focus a collimated laser beam into the cavity.

For a collimated or focused beam, $r = \infty$. As the beam is collimated before the mode-matching lens, with a spot size of w_{far}, and focused at the cavity centre, with a spot size equal to the beam waist of w_0, then the complex beam parameters at these two positions, q_{far} and q_0, are equal to:

$$q_{\mathrm{far}} = \frac{\mathrm{i}\pi w_{\mathrm{far}}^2}{\lambda} \tag{A.8}$$

$$q_0 = \frac{\mathrm{i}\pi w_0^2}{\lambda} \tag{A.9}$$

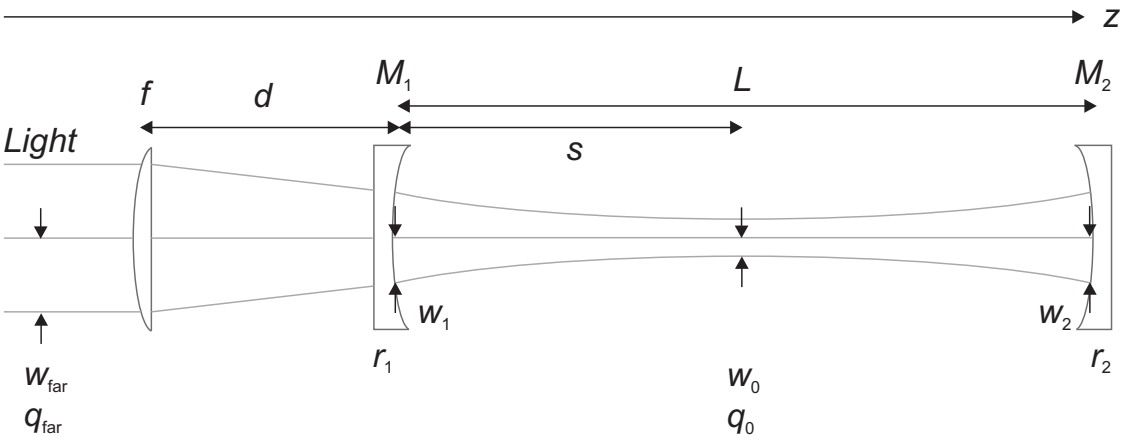

Figure A.3: A simple mode-matching arrangement with a single lens of focal length f placed a distance d before the cavity formed of mirrors with radii of curvature $r_{1,2}$ separated by a distance L. The beam waist inside the cavity occurs a distance s after the first mirror and has a complex beam parameter q_0 with radius w_0; if $r_1 = r_2$, this occurs in the middle of the cavity so that $s = L/2$. The incoming Gaussian beam is assumed to be collimated and described by q_{far} with spot size w_{far}.

From the input position, the path of the beam can be followed and the optical elements it encounters noted. These are, in order:

1. Focusing by the mode-matching lens: $\begin{pmatrix} 1 & 0 \\ -\frac{1}{f} & 1 \end{pmatrix}$
2. Free space propagation from the lens to the cavity mirror M_1: $\begin{pmatrix} 1 & d \\ 0 & 1 \end{pmatrix}$
3. Refraction at M_1: $\begin{pmatrix} 1 & 0 \\ \frac{n_m - 1}{r_1} & 1 \end{pmatrix}$
4. Free space propagation from M_1 to the cavity waist: $\begin{pmatrix} 1 & s \\ 0 & 1 \end{pmatrix}$

It is worthy of note that the curved surface of the cavity mirror M_1 is convex relative to the incoming light ray (as defined in Figure A.1(a)) and sign convention 1 must be employed as the beam is being refracted by the mirror, hence $r > 0$. In this thesis, the work conducted in the near-IR used cavity mirrors composed of fused silica, with $n_m = 1.44384$ and 1.44324 at 1565 nm and 1615 nm, respectively; in the mid-IR, ZnSe mirrors were utilised with $n_m = 2.43586$ at 3345.676 nm [460].

These matrices can then be multiplied together as according to the relationship $\mathbf{M} = \mathbf{M}_m \cdot \ldots \cdot \mathbf{M}_3 \cdot \mathbf{M}_2 \cdot \mathbf{M}_1$ outlined in Equations A.2 and A.3, and the overall ABCD matrix then used in Equation A.7:

$$q_0 = \frac{\mathrm{A}q_{\text{far}} + \mathrm{B}}{\mathrm{C}q_{\text{far}} + \mathrm{D}} \tag{A.10}$$

By setting w_0 as the beam waist of the optical cavity as given by Equation 1.45 and w_{far} as the experimentally measured spot size of the input collimated beam, this equation can be solved to give a single solution for f and d for perfect mode-matching if $w_{\text{far}} > w_0$. However, restrictions imposed by the defined focal lengths of commercially available lenses and practical considerations of the spatial configuration of the experimental set-up often means that this ideal solution cannot be implemented, so instead compromise values for f and d are used. Alternatively, two mode matching lenses can be used to give more flexibility; this requires further ABCD matrices to be included in the ray transfer matrix analysis and introduces two new parameters (another focal length and distance) which can be varied to optimise the mode-matching.

Bibliography

[1] E. Hecht, *Optics*, Addison-Wesley Publishing Company, Inc., Reading, MA, USA, ISBN 0201116111, 1987.

[2] J. Peatross and M. Ware, *Physics of Light and Optics*, Brigham Young University, Provo, UT, USA, URL http://optics.byu.edu/textbook.aspx, 2012.

[3] J. M. Hollas, *Modern Spectroscopy*, John Wiley & Sons, Inc., Chichester, UK, ISBN 0470844167, 2004.

[4] P. W. Atkins, *Physical Chemistry*, Oxford University Press, Oxford, UK, ISBN 0198557302, 1994.

[5] P. W. Atkins and R. Friedman, *Molecular Quantum Mechanics*, Oxford University Press, Oxford, UK, ISBN 0199274983, 2005.

[6] D. H. Whiffen, *Spectroscopy*, Logmans Green and Co Ltd, London, UK, ISBN 0582446562, 1972.

[7] W. Demtroder, *Laser Spectroscopy: Basic Concepts and Instrumentation*, Springer-Verlag Berlin and Heidelberg GmbH & Co., Berlin, Germany, ISBN 3540652256, 2003.

[8] R. C. Hilborn, 'Einstein coefficients, cross sections, f values, dipole moments, and all that', *American Journal of Physics*, **50**, 982–986, doi:10.1119/1.12937, 1982.

[9] D. F. Swinehart, 'The Beer-Lambert law', *Journal of Chemical Education*, **39**, 333–335, doi:10.1021/ed039p333, 1962.

[10] C. C. Davis, *Lasers and Electro-Optics: Fundamentals and Engineering*, Cambridge University Press, Cambridge, UK, ISBN 0521484030, 1996.

[11] V. Ebert and J. Wolfrum, 'Absorption', in *Optical Measurements - Techniques and Applications*, edited by F. Mayinger and O. Feldmann, chap. 13, pp. 231–266, Springer-Verlag Berlin and Heidelberg GmbH & Co., Berlin, Germany, ISBN 3540666907, 2001.

[12] P. Ortwein, W. Woiwode, S. Wagner, M. Gisi and V. Ebert, 'Laser-based measurements of line strength, self- and pressure-broadening coefficients of the $H^{35}Cl$ $R(3)$ absorption line in the first overtone region for pressures up to 1 MPa', *Applied Physics B: Lasers and Optics*, **100**, 341–347, doi:10.1007/s00340-009-3862-8, 2010.

[13] L. S. Rothman, A. Barbe, D. Chris Benner, L. R. Brown, C. Camy-Peyret, M. R. Carleer, K. Chance, C. Clerbaux, V. Dana, V. M. Devi, A. Fayt, J.-M. Flaud, R. R. Gamache, A. Goldman, D. Jacquemart, K. W. Jucks, W. J. Lafferty, J.-Y. Mandin, S. T. Massie, V. Nemtchinov, D. A. Newnham, A. Perrin, C. P. Rinsland, J. Schroeder, K. M. Smith, M. A. Smith, K. Tang, R. A. Toth, J. Vander Auwera, P. Varanasi and K. Yoshino, 'The HITRAN molecular spectroscopic database: edition of 2000 including updates through 2001', *Journal of Quantitative Spectroscopy and Radiative Transfer*, **82**, 5–44, doi:10.1016/S0022-4073(03)00146-8, 2003.

[14] L. S. Rothman, D. Jacquemart, A. Barbe, D. Chris Benner, M. Birk, L. R. Brown, M. R. Carleer, C. Chackerian Jr, K. Chance, L. H. Coudert, V. Dana, V. M. Devi, J.-M. Flaud, R. R. Gamache, A. Goldman, J.-M. Hartmann, K. W. Jucks, A. G. Maki, J.-Y. Mandin, S. T. Massie, J. Orphal, A. Perrin, C. P. Rinsland, A. M. H. Smith, J. Tennyson, R. N. Tolchenov, R. A. Toth, J. Vander Auwera, P. Varanasi and G. Wagner, 'The HITRAN 2004 molecular spectroscopic database', *Journal of Quantitative Spectroscopy and Radiative Transfer*, **96**, 139–204, doi:10.1016/j.jqsrt.2004.10.008, 2005.

[15] L. S. Rothman, I. E. Gordon, A. Barbe, D. Chris Benner, P. F. Bernath, M. Birk, V. Boudon, L. R. Brown, A. Campargue, J.-P. Champion, K. Chance, L. H. Coudert, V. Dana, V. M. Devi, S. Fally, J.-M. Flaud, R. R. Gamache, A. Goldman, D. Jacquemart, I. Kleiner, N. Lacome, W. J. Lafferty, J.-Y. Mandin, S. T. Massie, S. N. Mikhailenko, C. E. Miller, N. Moazzen-Ahmadi, O. V. Naumenko, A. V. Nikitin, J. Orphal, V. I. Perevalov, A. Perrin, A. Predoi-Cross, C. P. Rinsland, M. Rotger, M. Simeckova, A. M. H. Smith, K. Sung, S. A. Tashkun, J. Tennyson, R. N. Tolchenov, R. A. Toth, A. C. Vandaele and J. Vander Auwera, 'The HITRAN 2008 molecular spectroscopic database', *Journal of Quantitative Spectroscopy and Radiative Transfer*, **110**, 533–572, doi:10.1016/j.jqsrt.2009.02.013, 2009.

[16] M. Abramowitz and I. A. Stegun (editors), *Handbook of Mathematical Functions: with Formulas, Graphs and Mathematical Tables*, Dover Publications, Inc., New York, NY, USA, ISBN 0486612724, 1965.

[17] J. Humlicek, 'Optimized computation of the Voigt and complex probability functions', *Journal of Quantitative Spectroscopy and Radiative Transfer*, **27**, 437–444, doi:10.1016/0022-4073(82)90078-4, 1982.

[18] J. J. Olivero and R. L. Longbothum, 'Empirical fits to the Voigt line width: a brief review', *Journal of Quantitative Spectroscopy and Radiative Transfer*, **17**, 233–236, doi:10.1016/0022-4073(77)90161-3, 1977.

[19] D. Rehle, D. Leleux, M. Erdelyi, F. Tittel, M. Fraser and S. Friedfeld, 'Ambient formaldehyde detection with a laser spectrometer based on difference-frequency generation in PPLN', *Applied Physics B: Lasers and Optics*, **72**, 947–952, doi:10.1007/s003400100549, 2001.

[20] L. Galatry, 'Simultaneous effect of Doppler and foreign gas broadening on spectral lines', *Physical Review*, **122**, 1218–1223, doi:10.1103/PhysRev.122.1218, 1961.

[21] P. L. Varghese and R. K. Hanson, 'Collisional narrowing effects on spectral line shapes measured at high resolution', *Applied Optics*, **23**, 2376–2385, doi:10.1364/AO.23.002376, 1984.

[22] R. H. Dicke, 'The effect of collisions upon the Doppler width of spectral lines', *Physical Review*, **89**, 472–473, doi:10.1103/PhysRev.89.472, 1953.

[23] J.-M. Hartmann, C. Boulet and D. Robert, *Collisional Effects on Molecular Spectra: Laboratory Experiments and Models, Consequences for applications*, Elsevier B.V., Amsterdam, The Netherlands, ISBN 9780444520173, 2008.

[24] F. K. Tittel, D. Richter and A. Fried, 'Mid-Infrared Laser Applications in Spectroscopy', in *Topics in Applied Physics, Vol. 89: Solid-State Mid-Infrared Laser Sources*, edited by I. T. Sorokina and K. L. Vodopyanov, chap. 11, pp. 445–510, Springer-Verlag Berlin and Heidelberg GmbH & Co., Berlin, Germany, ISBN 3540006214, 2003.

[25] J. J. Scherer, J. B. Paul, H. J. Jost and M. L. Fischer, 'Mid-IR difference frequency laser-based sensors for ambient CH_4, CO, and N_2O monitoring', *Applied Physics B: Lasers and Optics*, **110**, 271–277, doi:10.1007/s00340-012-5244-x, 2013.

[26] A. Fried and D. Richter, 'Infrared Absorption Spectroscopy', in *Analytical Techniques for Atmospheric Measurement*, edited by D. E. Heard, chap. 2, pp. 72–146, Blackwell, ISBN 1405123575, 2006.

[27] S. Welzel, F. Hempel, M. Hübner, N. Lang, P. B. Davies and J. Röpcke, 'Quantum cascade laser absorption spectroscopy as a plasma diagnostic tool: an overview', *Sensors*, **10**, 6861–6900, doi:10.3390/s100706861, 2010.

[28] J. A. Silver, 'Frequency-modulation spectroscopy for trace species detection: theory and comparison among experimental methods', *Applied Optics*, **31**, 707–717, doi:10.1364/AO.31.004927, 1992.

[29] G. E. Hall and S. W. North, 'Transient laser frequency modulation spectroscopy', *Annual Review of Physical Chemistry*, **51**, 243–274, doi:10.1146/annurev.physchem.51.1.243, 2000.

[30] B. A. Paldus and A. A. Kachanov, 'An historical overview of cavity-enhanced methods', *Canadian Journal of Physics*, **83**, 975–999, doi:10.1139/P05-054, 2005.

[31] D. Herriott, H. Kogelnik and R. Kompfner, 'Off-axis paths in spherical mirror interferometers', *Applied Optics*, **3**, 523–526, doi:10.1364/AO.3.000523, 1964.

[32] S. S. Brown, 'Absorption spectroscopy in high-finesse cavities for atmospheric studies', *Chemical Reviews*, **103**, 5219–5238, doi:10.1021/cr020645c, 2003.

[33] M. Mazurenka, A. J. Orr-Ewing, R. Peverall and G. A. D. Ritchie, 'Cavity ring-down and cavity enhanced spectroscopy using diode lasers', *Annual Reports on the Progress of Chemistry, Section C (Physical Chemistry)*, **101**, 100–142, doi:10.1039/b408909j, 2005.

[34] A. O'Keefe, 'Integrated cavity output analysis of ultra-weak absorption', *Chemical Physics Letters*, **293**, 331–336, doi:10.1016/S0009-2614(98)00785-4, 1998.

[35] R. Engeln, G. Berden, R. Peeters and G. Meijer, 'Cavity enhanced absorption and cavity enhanced magnetic rotation spectroscopy', *Review of Scientific Instruments*, **69**, 3763–3769, doi:10.1063/1.1149176, 1998.

[36] J. Morville, S. Kassi, M. Chenevier and D. Romanini, 'Fast, low-noise, mode-by-mode, cavity-enhanced absorption spectroscopy by diode-laser self-locking', *Applied Physics B: Lasers and Optics*, **80**, 1027–1038, doi:10.1007/s00340-005-1828-z, 2005.

[37] A. O'Keefe and D. A. G. Deacon, 'Cavity ring-down optical spectrometer for absorption measurements using pulsed laser sources', *Review of Scientific Instruments*, **59**, 2544–2551, doi:10.1063/1.1139895, 1988.

[38] G. Berden and R. Engeln (editors), *Cavity Ring-Down Spectroscopy: Techniques and Applications*, John Wiley & Sons, Inc., Chichester, UK, ISBN 1405176881, 2009.

[39] J. M. Herbelin, J. A. McKay, M. A. Kwok, R. H. Ueunten, D. S. Urevig, D. J. Spencer and D. J. Benard, 'Sensitive measurement of photon lifetime and true reflectances in an optical cavity by a phase-shift method', *Applied Optics*, **19**, 144–147, doi:10.1364/AO.19.000144, 1980.

[40] G. Giusfredi, S. Bartalini, S. Borri, P. Cancio, I. Galli, D. Mazzotti and P. de Natale, 'Saturated-absorption cavity ring-down spectroscopy', *Physical Review Letters*, **104**, 110801, doi:10.1103/PhysRevLett.104.110801, 2010.

[41] J. Ye, L.-S. Ma and J. L. Hall, 'Ultrasensitive detections in atomic and molecular physics: demonstration in molecular overtone spectroscopy', *Journal of the Optical Society of America B: Optical Physics*, **15**, 6–15, doi:10.1364/JOSAB.15.000006, 1998.

[42] H. I. Schiff, G. I. Mackay and J. Bechara, 'The Use of Tunable Diode Laser Absorption Spectroscopy for Atmospheric Measurements', in *Chemical Analysis, Vol 127: Air Monitoring by Spectroscopic Techniques*, edited by M. W. Sigrist, chap. 5, pp. 239–334, John Wiley & Sons, Inc., New York, NY, USA, ISBN 0471558753, 1994.

[43] A. Yariv and P. Yeh, *Photonics: Optical Electronics in Modern Communication*, Oxford University Press, Oxford, UK, ISBN 0195179463, 2006.

[44] C. Downs and T. E. Vandervelde, 'Progress in infrared photodetectors since 2000', *Sensors*, **13**, 5054–5098, doi:10.3390/s130405054, 2013.

[45] Thorlabs Ltd, 'Thorlabs', URL http://www.thorlabs.co.uk/.

[46] VIGO Systems S.A., 'Vigo', URL http://www.vigo.com.pl/en.

[47] J. Reid, J. Shewchun, B. K. Garside and E. A. Ballik, 'High sensitivity pollution detection employing tunable diode lasers', *Applied Optics*, **17**, 300–307, doi:10.1364/AO.17.000300, 1978.

[48] P. Werle, 'A review of recent advances in semiconductor laser based gas monitors', *Spectrochimica Acta Part A: Molecular and Biomolecular Spectroscopy*, **54**, 197–236, doi:10.1016/S1386-1425(97)00227-8, 1998.

[49] J. M. Supplee, E. A. Whittaker and W. Lenth, 'Theoretical description of frequency modulation and wavelength modulation spectroscopy', *Applied Optics*, **33**, 6294–6302, doi:10.1364/AO.33.006294, 1994.

[50] J. Henningsen and H. Simonsen, 'Quantitative wavelength-modulation spectroscopy without certified gas mixtures', *Applied Physics B: Lasers and Optics*, **70**, 627–633, doi:10.1007/s003400050871, 2000.

[51] L. Xiao, C. Li, Q. Li, S. Jia and G. Zhou, 'Low-frequency wavelength modulation spectroscopy with D_2 transition of atomic cesium by use of an external-cavity diode laser', *Applied Optics*, **39**, 1049–1052, doi:10.1364/AO.39.001049, 2000.

[52] K. Duffin, A. J. McGettrick, W. Johnstone, G. Stewart and D. G. Moodie, 'Tunable diode-laser spectroscopy with wavelength modulation: a calibration-free approach to the recovery of absolute gas absorption line shapes', *Journal of Lightwave Technology*, **25**, 3114–3125, doi:10.1109/JLT.2007.904937, 2007.

[53] A. J. McGettrick, W. Johnstone, R. Cunningham and J. D. Black, 'Tunable diode laser spectroscopy with wavelength modulation: calibration-free measurement of gas compositions at elevated temperatures and varying pressure', *Journal of Lightwave Technology*, **27**, 3150–3161, doi:10.1109/JLT.2008.2008729, 2009.

[54] C. Fabry and A. Perot, 'Theorie et applications d'une nouvelle methode de spectroscopie interferentielle', *Annales de Chimie et de Physique*, **16**, 115–144, 1899.

[55] H. Kogelnik and T. Li, 'Laser beams and resonators', *Applied Optics*, **5**, 1550–1567, doi:10.1364/AO.5.001550, 1966.

[56] A. E. Siegman, *Lasers*, University Science Books, Mill Valley, CA, USA, ISBN 0935702113, 1986.

[57] J.-P. H. van Helden, R. Peverall and G. A. D. Ritchie, 'Cavity Enhanced Techniques Using Continuous Wave Lasers', in *Cavity Ring-Down Spectroscopy*, edited by G. Berden and R. Engeln, chap. 2, pp. 27–56, John Wiley & Sons, Inc., Chichester, UK, ISBN 1405176881, 2009.

[58] P. Zalicki and R. N. Zare, 'Cavity ring-down spectroscopy for quantitative absorption measurements', *The Journal of Chemical Physics*, **102**, 2708–2717, doi:10.1063/1.468647, 1995.

[59] M. D. Wheeler, S. M. Newman, A. J. Orr-Ewing and M. N. R. Ashfold, 'Cavity ring-down spectroscopy', *Journal of the Chemical Society, Faraday Transactions*, **94**, 337–351, doi:10.1039/a707686j, 1998.

[60] K. W. Busch and M. A. Busch (editors), *Cavity-Ringdown Spectroscopy: An Ultratrace-Absorption Measurement Technique*, American Chemical Society, Washington, DC, USA, ISBN 0841236003, 1999.

[61] G. Berden, R. Peeters and G. Meijer, 'Cavity ring-down spectroscopy: experimental schemes and applications', *International Reviews in Physical Chemistry*, **19**, 565–607, doi:10.1080/014423500750040627, 2000.

[62] C. Vallance, 'Innovations in cavity ringdown spectroscopy', *New Journal of Chemistry*, **29**, 867–874, doi:10.1002/chin.200543291, 2005.

[63] K. K. Lehmann, G. Berden and R. Engeln, 'An Introduction to Cavity Ring-Down Spectroscopy', in *Cavity Ring-Down Spectroscopy*, edited by G. Berden and R. Engeln, chap. 1, pp. 1–26, John Wiley & Sons, Inc., ISBN 1405176881, 2009.

[64] A. O'Keefe, J. J. Scherer and J. B. Paul, 'cw Integrated cavity output spectroscopy', *Chemical Physics Letters*, **307**, 343–349, doi:10.1016/S0009-2614(99)00547-3, 1999.

[65] D. Romanini and K. K. Lehmann, 'Ring-down cavity absorption spectroscopy of the very weak HCN overtone bands with six, seven, and eight stretching quanta', *The Journal of Chemical Physics*, **99**, 6287–6301, doi:10.1063/1.465866, 1993.

[66] D.-H. Lee, Y. Yoon, B. Kim, J. Lee, Y. Yoo and J. Hahn, 'Optimization of the mode matching in pulsed cavity ringdown spectroscopy by monitoring non-degenerate transverse mode beating', *Applied Physics B: Lasers and Optics*, **74**, 435–440, doi:10.1007/s003400200802, 2002.

[67] D. Romanini, A. A. Kachanov and F. Stoeckel, 'Diode laser cavity ring down spectroscopy', *Chemical Physics Letters*, **270**, 538–545, doi:10.1016/S0009-2614(97)00406-5, 1997.

[68] D. Romanini, A. A. Kachanov, N. Sadeghi and F. Stoeckel, 'CW cavity ring down spectroscopy', *Chemical Physics Letters*, **264**, 316–322, doi:10.1016/S0009-2614(96)01351-6, 1997.

[69] J. W. Hahn, Y. S. Yoo, J. Y. Lee, J. W. Kim and H. W. Lee, 'Cavity ringdown spectroscopy with a continuous-wave laser: calculation of coupling efficiency and a new spectrometer design', *Applied Optics*, **38**, 1859–1866, doi:10.1364/AO.38.001859, 1999.

[70] B. Bakowski, L. Corner, G. Hancock, R. Kotchie, R. Peverall and G. A. D. Ritchie, 'Cavity-enhanced absorption spectroscopy with a rapidly swept diode laser', *Applied Physics B: Lasers and Optics*, **75**, 745–750, doi:10.1007/s00340-002-1026-1, 2002.

[71] J. B. Paul, L. Lapson and J. G. Anderson, 'Ultrasensitive absorption spectroscopy with a high-finesse optical cavity and off-axis alignment', *Applied Optics*, **40**, 4904–4910, doi:10.1364/AO.40.004904, 2001.

[72] D. Baer, J. Paul, M. Gupta and A. O'Keefe, 'Sensitive absorption measurements in the near-infrared region using off-axis integrated-cavity-output spectroscopy', *Applied Physics B: Lasers and Optics*, **75**, 261–265, doi:10.1007/s00340-002-0971-z, 2002.

[73] V. L. Kasyutich, P. A. Martin and R. J. Holdsworth, 'An off-axis cavity-enhanced absorption spectrometer at 1605 nm for the $^{12}CO_2/^{13}CO_2$ measurement', *Applied Physics B: Lasers and Optics*, **85**, 413–420, doi:10.1007/s00340-006-2312-0, 2006.

[74] D. D. Arslanov, K. Swinkels, S. M. Cristescu and F. J. M. Harren, 'Real-time, subsecond, multicomponent breath analysis by optical parametric oscillator based off-axis integrated cavity output spectroscopy', *Optics Express*, **19**, 24078–24089, doi:10.1364/OE.19.024078, 2011.

[75] M. W. Sigrist (editor), *Chemical Analysis, Vol. 127: Air Monitoring by Spectroscopic Techniques*, John Wiley & Sons, Inc., New York, NY, USA, ISBN 0471558753, 1994.

[76] A. A. Kosterev and F. K. Tittel, 'Chemical sensors based on quantum cascade lasers', *IEEE Journal of Quantum Electronics*, **38**, 582–591, doi:10.1109/JQE.2002.1005408, 2002.

[77] P. A. Martin, 'Near-infrared diode laser spectroscopy in chemical process and environmental air monitoring', *Chemical Society Reviews*, **31**, 201–210, doi:10.1039/b003936p, 2002.

[78] P. Werle, F. Slemr, K. Maurer, R. Kormann, R. Mucke and B. Janker, 'Near- and mid-infrared laser-optical sensors for gas analysis', *Optics and Lasers in Engineering*, **37**, 101–114, doi:10.1016/S0143-8166(01)00092-6, 2002.

[79] D. B. Atkinson, 'Solving chemical problems of environmental importance using cavity ring-down spectroscopy', *The Analyst*, **128**, 117–125, doi:10.1039/b206699h, 2003.

[80] K. Song and E. C. Jung, 'Recent developments in modulation spectroscopy for trace gas detection using tunable diode lasers', *Applied Spectroscopy Reviews*, **38**, 395–432, doi:10.1081/ASR-120026329, 2003.

[81] G. Duxbury, N. Langford, M. T. McCulloch and S. Wright, 'Quantum cascade semiconductor infrared and far-infrared lasers: from trace gas sensing to non-linear optics', *Chemical Society Reviews*, **34**, 921–934, doi:10.1039/b400914m, 2005.

[82] T. Risby and S. Solga, 'Current status of clinical breath analysis', *Applied Physics B: Lasers and Optics*, **85**, 421–426, doi:10.1007/s00340-006-2280-4, 2006.

[83] M. Sigrist, R. Bartlome, D. Marinov, J. Rey, D. Vogler and H. Wachter, 'Trace gas monitoring with infrared laser-based detection schemes', *Applied Physics B: Lasers and Optics*, **90**, 289–300, doi:10.1007/s00340-007-2875-4, 2007.

[84] A. Fried, G. Diskin, P. Weibring, D. Richter, J. G. Walega, G. Sachse, T. Slate, M. Rana and J. Podolske, 'Tunable infrared laser instruments for airborne atmospheric studies', *Applied Physics B: Lasers and Optics*, **92**, 409–417, doi:10.1007/s00340-008-3136-x, 2008.

[85] A. Kosterev, G. Wysocki, Y. Bakhirkin, S. So, R. Lewicki, M. Fraser, F. Tittel and R. F. Curl, 'Application of quantum cascade lasers to trace gas analysis', *Applied Physics B: Lasers and Optics*, **90**, 165–176, doi:10.1007/s00340-007-2846-9, 2008.

[86] M. N. Fiddler, I. Begashaw, M. A. Mickens, M. S. Collingwood, Z. Assefa and S. Bililign, 'Laser spectroscopy for atmospheric and environmental sensing', *Sensors*, **9**, 10447–10512, doi:10.3390/s91210447, 2009.

[87] G. Hancock and A. J. Orr-Ewing, 'Applications of Cavity Ring-Down Spectroscopy in Atmospheric Chemistry', in *Cavity Ring-Down Spectroscopy*, edited by G. Berden and R. Engeln, chap. 7, pp. 181–212, John Wiley & Sons, Inc., Chichester, UK, ISBN 1405176881, 2009.

[88] C. Wang and P. Sahay, 'Breath analysis using laser spectroscopic techniques: breath biomarkers, spectral fingerprints, and detection limits', *Sensors*, **9**, 8230–8262, doi:10.3390/s91008230, 2009.

[89] T. H. Risby and F. K. Tittel, 'Current status of midinfrared quantum and interband cascade lasers for clinical breath analysis', *Optical Engineering*, **49**, 111123, doi:10.1117/1.3498768, 2010.

[90] L. Ciaffoni, R. Peverall and G. A. D. Ritchie, 'Laser spectroscopy on volatile sulfur compounds: possibilities for breath analysis', *Journal of Breath Research*, **5**, 024002, doi:10.1088/1752-7155/5/2/024002, 2011.

[91] H. Nasim and Y. Jamil, 'Recent advancements in spectroscopy using tunable diode lasers', *Laser Physics Letters*, **10**, 043001, doi:10.1088/1612-2011/10/4/043001, 2013.

[92] J. Hodgkinson and R. P. Tatam, 'Optical gas sensing: a review', *Measurement Science and Technology*, **24**, 012004, doi:10.1088/0957-0233/24/1/012004, 2013.

[93] P. Malara, P. Maddaloni, G. Gagliardi and P. de Natale, 'Combining a difference-frequency source with an off-axis high-finesse cavity for trace-gas monitoring around 3 μm', *Optics Express*, **14**, 1304–1313, doi:10.1364/OE.14.001304, 2006.

[94] S. Stry, P. Hering and M. Mürtz, 'Portable difference-frequency laser-based cavity leak-out spectrometer for trace-gas analysis', *Applied Physics B: Lasers and Optics*, **75**, 297–303, doi:10.1007/s00340-002-0966-9, 2002.

[95] S. Welzel, G. Lombardi, P. B. Davies, R. Engeln, D. C. Schram and J. Ropcke, 'Trace gas measurements using optically resonant cavities and quantum cascade lasers operating at room temperature', *Journal of Applied Physics*, **104**, 093115, doi:10.1063/1.3008014, 2008.

[96] U. Gustafsson, J. Sandsten and S. Svanberg, 'Simultaneous detection of methane, oxygen and water vapour utilising near-infrared diode lasers in conjunction with difference-frequency generation', *Applied Physics B: Lasers and Optics*, **71**, 853–857, doi:10.1007/s003400000431, 2000.

[97] C. Wang, N. Srivastava, B. A. Jones and R. B. Reese, 'A novel multiple species ring-down spectrometer for in situ measurements of methane, carbon dioxide, and carbon

isotope', *Applied Physics B: Lasers and Optics*, **92**, 259–270, doi:10.1007/s00340-008-3077-4, 2008.

[98] D. G. Lancaster, D. Richter, R. F. Curl and F. K. Tittel, 'Real-time measurements of trace gases using a compact difference-frequency-based sensor operating at 3.5 μm', *Applied Physics B: Lasers and Optics*, **67**, 339–345, doi:10.1007/s003400050513, 1998.

[99] H. Dahnke, G. von Basum, K. Kleinermanns, P. Hering and M. Mürtz, 'Rapid formaldehyde monitoring in ambient air by means of mid-infrared cavity leak-out spectroscopy', *Applied Physics B: Lasers and Optics*, **75**, 311–316, doi:10.1007/s00340-002-0986-5, 2002.

[100] D. Richter, M. Erdelyi, R. F. Curl, F. K. Tittel, C. Oppenheimer, H. J. Duffell and M. Burton, 'Field measurements of volcanic gases using tunable diode laser based mid-infrared and Fourier transform infrared spectrometers', *Optics and Lasers in Engineering*, **37**, 171–186, doi:10.1016/S0143-8166(01)00094-X, 2002.

[101] I. Galli, S. Bartalini, S. Borri, P. Cancio, D. Mazzotti, P. de Natale and G. Giusfredi, 'Molecular gas sensing below parts per trillion: radiocarbon-dioxide optical detection', *Physical Review Letters*, **107**, 270802, doi:10.1103/PhysRevLett.107.270802, 2011.

[102] S. Vance, L. E. Christensen, C. R. Webster and K. Sung, 'Volatile organic sulfur compounds as biomarkers complementary to methane: infrared absorption spectroscopy of CH_3SH enables in situ measurements on Earth and Mars', *Planetary and Space Science*, **59**, 299–303, doi:10.1016/j.pss.2010.08.023, 2011.

[103] B. L. Fawcett, A. M. Parkes, D. E. Shallcross and A. J. Orr-Ewing, 'Trace detection of methane using continuous wave cavity ring-down spectroscopy at 1.65 μm', *Physical Chemistry Chemical Physics*, **4**, 5960–5965, doi:10.1039/b208486b, 2002.

[104] D. J. Hamilton and A. J. Orr-Ewing, 'A quantum cascade laser-based optical feedback cavity-enhanced absorption spectrometer for the simultaneous measurement of CH_4 and N_2O in air', *Applied Physics B: Lasers and Optics*, **102**, 879–890, doi:10.1007/s00340-010-4259-4, 2011.

[105] D. Kleine, M. Mürtz, J. Lauterbach, H. Dahnke, W. Urban, P. Hering and K. Kleinermanns, 'Atmospheric trace gas analysis with cavity ring-down spectroscopy', *Israel Journal of Chemistry*, **41**, 111–116, doi:10.1560/R4DB-AD8N-687H-105G, 2001.

[106] A. M. Parkes, B. L. Fawcett, R. E. Austin, S. Nakamichi, D. E. Shallcross and A. J. Orr-Ewing, 'Trace detection of volatile organic compounds by diode laser cavity ring-down spectroscopy', *The Analyst*, **128**, 960–965, doi:10.1039/b303834c, 2003.

[107] M. Bitter, S. M. Ball, I. M. Povey and R. L. Jones, 'A broadband cavity ringdown spectrometer for in-situ measurements of atmospheric trace gases', *Atmospheric Chemistry and Physics Discussions*, **5**, 2547–2560, doi:10.5194/acpd-5-3491-2005, 2005.

[108] C. J. Smith, S. So, L. Xia, S. Pitz, K. Szlavecz, D. Carlson, A. Terzis and G. Wysocki, 'Wireless laser spectroscopic sensor node for atmospheric CO_2 monitoring - laboratory and field test', *Applied Physics B: Lasers and Optics*, **110**, 241–248, doi:10.1007/s00340-012-5157-8, 2013.

[109] E. Richard, K. Kelly, R. Winkler, R. Wilson, T. Thompson, R. McLaughlin, A. Schmeltekopf and A. Tuck, 'A fast-response near-infrared tunable diode laser absorption spectrometer for in situ measurements of CH_4 in the upper troposphere and lower stratosphere', *Applied Physics B: Lasers and Optics*, **75**, 183–194, doi:10.1007/s00340-002-0935-3, 2002.

[110] C. R. Webster and R. D. May, 'In situ stratospheric measurements of CH_4, $^{13}CH_4$, N_2O, and $OC^{18}O$ using the BLISS tunable diode laser spectrometer', *Geophysical Research Letters*, **19**, 45–48, doi:10.1029/91GL02782, 1992.

[111] L. E. Christensen, C. R. Webster and R. Q. Yang, 'Aircraft and balloon in situ measurements of methane and hydrochloric acid using interband cascade lasers', *Applied Optics*, **46**, 1132–1138, doi:10.1364/AO.46.001132, 2007.

[112] G. P. Brasseur, J. J. Orlando and G. S. Tyndall, *Atmospheric Chemistry and Global Change*, Oxford University Press, Oxford, UK, ISBN 0195105214, 1999.

[113] L. T. Molina and M. J. Molina, 'Production of Cl_2O_2 from the self-reaction of theClO radical', *The Journal of Physical Chemistry*, **91**, 433–436, doi:10.1021/j100286a035, 1987.

[114] A. J. G. Anderson, D. W. Toohey and W. H. Brune, 'Free radicals within the Antarctic vortex: the role of CFCs in Antarctic ozone loss', *Science*, **251**, 39–46, doi:10.1126/science.251.4989.39, 1991.

[115] S. Solomon, 'Stratospheric ozone depletion: a review of concepts and history', *Reviews of Geophysics*, **37**, 275–316, doi:10.1029/1999RG900008, 1999.

[116] F. D. Pope, J. C. Hansen, K. D. Bayes, R. R. Friedl and S. P. Sander, 'Ultraviolet absorption spectrum of chlorine peroxide, ClOOCl', *The Journal of Physical Chemistry A*, **111**, 4322–4332, doi:10.1021/jp067660w, 2007.

[117] M. Schupp, P. Bergamaschi, G. W. Harris and P. J. Crutzen, 'Development of a tunable diode laser absorption spectrometer for measurements of the $^{13}C/^{12}C$ ratio in methane', *Chemosphere*, **26**, 13–22, doi:10.1016/0045-6535(93)90409-X, 1993.

[118] P. Bergamaschi, M. Schupp and G. W. Harris, 'High-precision direct measurements of $^{13}CH_4/^{12}CH_4$ and $^{12}CH_3D/^{12}CH_4$ ratios in atmospheric methane sources by means of a long-path tunable diode laser absorption spectrometer', *Applied Optics*, **33**, 7704–7716, doi:10.1364/AO.33.007704, 1994.

[119] D. Kleine, H. Dahnke, W. Urban, P. Hering and M. Mürtz, 'Real-time detection of $^{13}CH_4$ in ambient air by use of mid-infrared cavity leak-out spectroscopy', *Optics Letters*, **25**, 1606–1608, doi:10.1364/OL.25.001606, 2000.

[120] H. Dahnke, D. Kleine, W. Urban, P. Hering and M. Mürtz, 'Isotopic ratio measurement of methane in ambient air using mid-infrared cavity leak-out spectroscopy', *Applied Physics B: Lasers and Optics*, **72**, 121–125, doi:10.1007/s003400000509, 2001.

[121] M. Todd, R. Provencal, T. Owano, B. Paldus, A. Kachanov, K. Vodopyanov, M. Hunter, S. Coy, J. Steinfeld and J. Arnold, 'Application of mid-infrared cavity-ringdown spectroscopy to trace explosives vapor detection using a broadly tunable $(6-8\ \mu m)$ optical parametric oscillator', *Applied Physics B: Lasers and Optics*, **75**, 367–376, doi:10.1007/s00340-002-0991-8, 2002.

[122] K. L. McNesby, R. T. Wainner, R. G. Daniel, A. W. Miziolek, W. M. Jackson and I. A. McLaren, 'High-sensitivity laser absorption measurements of broadband absorbers in the near-infrared spectral region', *Applied Optics*, **39**, 5006–5011, doi:10.1364/AO.39.005006, 2000.

[123] V. L. Kasyutich, D. Poulidi, M. Jalil, I. S. Metcalfe and P. A. Martin, 'Application of a cw quantum cascade laser CO_2 analyser to catalytic oxidation reaction monitoring', *Applied Physics B: Lasers and Optics*, **110**, 263–269, doi:10.1007/s00340-012-5154-y, 2013.

[124] T. Aizawa, 'Diode-laser wavelength-modulation absorption spectroscopy for quantitative in situ measurements of temperature and OH radical concentration in combustion gases', *Applied Optics*, **40**, 4894–4903, doi:10.1364/AO.40.004894, 2001.

[125] A. D. Griffiths, *Development and Demonstration of a Diode Laser Sensor for a Scramjet Combustor*, Ph.D thesis, Australian National University, 2005.

[126] R. Barron-Jimenez, J. Caton, T. Anderson, R. Lucht, T. Walther, S. Roy, M. Brown and J. Gord, 'Application of a difference-frequency-mixing based diode-laser sensor for carbon monoxide detection in the $4.4-4.8\ \mu m$ spectral region', *Applied Physics B: Lasers and Optics*, **85**, 185–197, doi:10.1007/s00340-006-2281-3, 2006.

[127] V. L. Kasyutich, R. J. Holdsworth and P. A. Martin, 'Mid-infrared laser absorption spectrometers based upon all-diode laser difference frequency generation and a room

temperature quantum cascade laser for the detection of CO, N_2O and NO', *Applied Physics B: Lasers and Optics*, **92**, 271–279, doi:10.1007/s00340-008-3097-0, 2008.

[128] M. E. Webber, D. S. Baer and R. K. Hanson, 'Ammonia monitoring near 1.5 µm with diode-laser absorption sensors', *Optical Society of America*, **40**, 2031–2042, doi:10.1364/AO.40.002031, 2001.

[129] M. E. Webber, *Diode Laser Measurements of NH_3 and CO_2 for Combustion and Bioreactor Applications*, Ph.D thesis, Stanford University, 2001.

[130] L. Pauling, A. B. Robinson, R. Teranishi and P. Cary, 'Quantitative analysis of urine vapor and breath by gas-liquid partition chromatography', *Proceedings of the National Academy of Sciences of the United States of America*, **68**, 2374–2376, doi:10.1073/pnas.68.10.2374, 1971.

[131] S. M. Gordon, J. P. Szldon, B. K. Krotoszynski, R. D. Gibbons and J. O'Neill, 'Volatile organic compounds in exhaled air from patients with lung cancer', *Clinical Chemistry*, **31**, 1278–1282, 1985.

[132] A. Manolis, 'The diagnostic potential of breath analysis', *Clinical Chemistry*, **29**, 5–15, 1983.

[133] B. Buszewski, M. Kesy, T. Ligor and A. Amann, 'Human exhaled air analytics: biomarkers of diseases', *Biomedical Chromatography*, **21**, 553–566, doi:10.1002/bmc.835, 2007.

[134] W. Miekisch, J. K. Schubert and G. F. E. Noeldge-Schomburg, 'Diagnostic potential of breath analysis - focus on volatile organic compounds', *Clinica Chimica Acta*, **347**, 25–39, doi:10.1016/j.cccn.2004.04.023, 2004.

[135] D. E. Cooper, R. U. Martinelli, C. B. Carlisle, H. Riris, D. B. Bour and R. J. Menna, 'Measurement of $^{12}CO_2$:$^{13}CO_2$ ratios for medical diagnostics with 1.6-µm distributed-feedback semiconductor diode lasers', *Applied Optics*, **32**, 6727–6731, doi:10.1364/AO.32.006727, 1993.

[136] S. N. Andreev, E. S. Mironchuk, I. V. Nikolaev, V. N. Ochkin, M. V. Spiridonov and S. N. Tskhai, 'High precision measurements of the $^{13}CO_2/^{12}CO_2$ isotope ratio at atmospheric pressure in human breath using a 2 µm diode laser', *Applied Physics B: Lasers and Optics*, **104**, 73–79, doi:10.1007/s00340-011-4602-4, 2011.

[137] V. L. Kasyutich and P. A. Martin, '$^{13}CO_2/^{12}CO_2$ isotopic ratio measurements with a continuous-wave quantum cascade laser in exhaled breath', *Infrared Physics & Technology*, **55**, 60–66, doi:10.1016/j.infrared.2011.09.003, 2012.

[138] D. E. Butz, M. E. Cook, H. R. Eghbalnia, F. Assadi-Porter and W. P. Porter, 'Changes in the natural abundance of $^{13}CO_2/^{12}CO_2$ in breath due to lipopolysacchride-induced acute phase response', *Rapid Communications in Mass Spectrometry*, **23**, 3729–3735, doi:10.1002/rcm.4310, 2009.

[139] V. Savarino, S. Vigneri and G. Celle, 'The ^{13}C urea breath test in the diagnosis of *Helicobacter pylori* infection', *Gut*, **45**, I18–I22, doi:10.1136/gut.45.2008.i18, 1999.

[140] R. J. Saad and W. D. Chey, 'Breath tests for gastrointestinal disease: the real deal or just a lot of hot air?', *Gastroenterology*, **133**, 1763–1766, doi:10.1053/j.gastro.2007.10.059, 2007.

[141] M. M. Walker, L. Teare and C. McNulty, 'Gastric cancer and *Helicobacter pylori*: the bug, the host or the environment?', *Postgraduate Medical Journal*, **84**, 169–170, doi:10.1136/pgmj.2008.068346, 2008.

[142] E. R. Crosson, K. N. Ricci, B. A. Richman, F. C. Chilese, T. G. Owano, R. A. Provencal, M. W. Todd, J. Glasser, A. A. Kachanov, B. A. Paldus, T. G. Spence and R. N. Zare, 'Stable isotope ratios using cavity ring-down spectroscopy: determination of $^{13}C/^{12}C$ for carbon dioxide in human breath', *Analytical Chemistry*, **74**, 2003–2007, doi:10.1021/ac025511d, 2002.

[143] T. Rubin, T. von Haimberger, A. Helmke and K. Heine, 'Quantitative determination of metabolization dynamics by a real-time $^{13}CO_2$ breath test', *Journal of Breath Research*, **5**, 027102, doi:10.1088/1752-7155/5/2/027102, 2011.

[144] K. L. Moskalenko, A. I. Nadezhdinskii and I. A. Adamovskaya, 'Human breath trace gas content study by tunable diode laser spectroscopy technique', *Infrared Physics and Technology*, **37**, 181–192, doi:10.1016/1350-4495(95)00097-6, 1996.

[145] I. Ventrillard-Courtillot, T. Gonthiez, C. Clerici and D. Romanini, 'Multispecies breath analysis faster than a single respiratory cycle by optical-feedback cavity-enhanced absorption spectroscopy', *Journal of Biomedical Optics*, **14**, 064026, doi:10.1117/1.3269677, 2009.

[146] H. Dahnke, D. Kleine, P. Hering and M. Mürtz, 'Real-time monitoring of ethane in human breath using mid-infrared cavity leak-out spectroscopy', *Applied Physics B: Lasers and Optics*, **72**, 971–975, doi:10.1007/s003400100609, 2001.

[147] G. von Basum, H. Dahnke, D. Halmer, P. Hering and M. Mürtz, 'Online recording of ethane traces in human breath via infrared laser spectroscopy', *Journal of Applied Physiology*, **95**, 2583–2590, doi:10.1152/japplphysiol.00542.2003, 2003.

[148] D. Halmer, S. Thelen, P. Hering and M. Mürtz, 'Online monitoring of ethane traces in exhaled breath with a difference frequency generation spectrometer', *Applied Physics B: Lasers and Optics*, **85**, 437–443, doi:10.1007/s00340-006-2288-9, 2006.

[149] K. Dryahina, D. Smith and P. Spanel, 'Quantification of methane in humid air and exhaled breath using selected ion flow tube mass spectrometry', *Rapid Communications in Mass Spectrometry*, **24**, 1296–1304, doi:10.1002/rcm.4513, 2010.

[150] L. le Marchand, L. R. Wilkens, P. Harwood and R. V. Cooney, 'Use of breath hydrogen and methane of colonic fermentation in epidemiologic studies: circadian patterns of excretion', *Environmental Health Perspectives*, **98**, 199–202, 1992.

[151] J. Fernandes, T. M. S. Wolever and A. V. Rao, 'Interrelationships between age, total dietary fiber intake and breath methane in humans', *Nutrition Research*, **20**, 929–940, doi:10.1016/S0271-5317(00)00184-6, 2000.

[152] M. Pimentel, A. G. Mayer, S. Park, E. J. Chow, A. Hasan and Y. Kong, 'Methane production during lactulose breath test is associated with gastrointestinal disease presentation', *Digestive Diseases and Sciences*, **48**, 86–92, doi:10.1023/A:1021738515885, 2003.

[153] L. Hwang, K. Low, R. Khoshini, G. Melmed, A. Sahakian, M. Makhani, V. Pokkunuri and M. Pimentel, 'Evaluating breath methane as a diagnostic test for constipation-predominant IBS', *Digestive Diseases and Sciences*, **55**, 398–403, doi:10.1007/s10620-009-0778-4, 2010.

[154] R. D. Stewart, E. A. Boettner and B. T. Stubbs, 'Rapid infra-red determination of acetone in the blood and the exhaled air of diabetic patients', *Nature*, **191**, 1008, doi:10.1038/1911008a0, 1961.

[155] V. L. Brechner and R. W. Bethune, 'Determination of acetone concentration in arterial blood by vapor phase chromatography of alveolar gas', *Diabetes*, **14**, 663–665, doi:10.2337/diab.14.10.663, 1965.

[156] M. Kupari, J. Lommi, M. Ventila and U. Karjalainen, 'Breath acetone in congestive heart failure', *The American Journal of Cardiology*, **76**, 1076–1078, doi:10.1016/S0002-9149(99)80304-X, 1995.

[157] M. Kinoyama, H. Nitta, A. Watanabe and H. Ueda, 'Acetone and isoprene concentrations in exhaled breath in healthy subjects', *Journal of Health Science*, **54**, 471–477, doi:10.1248/jhs.54.471, 2008.

[158] C. Wang and A. B. Surampudi, 'An acetone breath analyzer using cavity ringdown spectroscopy: an initial test with human subjects under various situations', *Measurement Science and Technology*, **19**, 105604, doi:10.1088/0957-0233/19/10/105604, 2008.

[159] W. Denzer, G. Hancock, M. Islam, C. E. Langley, R. Peverall, G. A. D. Ritchie and D. Taylor, 'Trace species detection in the near infrared using Fourier transform broadband cavity enhanced absorption spectroscopy: initial studies on potential breath analytes', *The Analyst*, **136**, 801–806, doi:10.1039/c0an00462f, 2011.

[160] L. Ciaffoni, G. Hancock, J. J. Harrison, J.-P. H. van Helden, C. E. Langley, R. Peverall, G. A. D. Ritchie and S. Wood, 'Demonstration of a mid-infrared cavity enhanced absorption spectrometer for breath acetone detection', *Analytical Chemistry*, **85**, 846–850, doi:10.1021/ac3031465, 2013.

[161] M. J. Thorpe, D. Balslev-Clausen, M. S. Kirchner and J. Ye, 'Cavity-enhanced optical frequency comb spectroscopy: application to human breath analysis', *Optics Express*, **16**, 2387–2397, doi:10.1364/OE.16.002387, 2008.

[162] K. Namjou, C. B. Roller and G. McMillen, 'Breath-analysis using mid-infrared tunable laser spectroscopy', in *2007 IEEE Sensors*, Dublin, Ireland, doi:10.1109/ICSENS.2007.4388658, 2007.

[163] L. R. Narasimhan, W. Goodman and C. K. Patel, 'Correlation of breath ammonia with blood urea nitrogen and creatinine during hemodialysis', *Proceedings of the National Academy of Sciences of the United States of America*, **98**, 4617–4621, doi:10.1073/pnas.071057598, 2001.

[164] C. Roller, K. Namjou, J. D. Jeffers, M. Camp, A. Mock, P. J. McCann and J. Grego, 'Nitric oxide breath testing by tunable-diode laser absorption spectroscopy: application in monitoring respiratory inflammation', *Applied Optics*, **41**, 6018–6029, doi:10.1364/AO.41.006018, 2002.

[165] D. H. Yates, 'Role of exhaled nitric oxide in asthma', *Immunology and Cell Biology*, **79**, 178–190, doi:10.1046/j.1440-1711.2001.00990.x, 2001.

[166] O. Svelto, *Principles of Lasers*, Plenum Press, New York, NY, USA, ISBN 0306457482, 1998.

[167] V. Shidlovski, 'Superluminescent diodes: short overview of device operation principles and performance parameters', *Tech. rep.*, SuperlumDiodes Ltd., URL `http://www.superlumdiodes.com/pdf/sld_overview.pdf`, 2004.

[168] G. Alphonse, D. Gilbert, M. Harvey and M. Ettenberg, 'High-power superluminescent diodes', *IEEE Journal of Quantum Electronics*, **24**, 2454–2457, doi:10.1109/3.14376, 1988.

[169] W. Denzer, M. L. Hamilton, G. Hancock, M. Islam, C. E. Langley, R. Peverall and G. A. D. Ritchie, 'Near-infrared broad-band cavity enhanced absorption spectroscopy using a superluminescent light emitting diode', *The Analyst*, **134**, 2220–2223, doi:10.1039/b916807a, 2009.

[170] J. M. Dudley, G. Genty and S. Coen, 'Supercontinuum generation in photonic crystal fiber', *Reviews of Modern Physics*, **78**, 1135–1184, doi:10.1103/RevModPhys.78.1135, 2006.

[171] R. R. Alfano (editor), *The Supercontinuum Laser Source: Fundamentals with Updated References*, Springer, New York, NY, USA, ISBN 0387245049, 2006.

[172] R. R. Alfano and S. L. Shapiro, 'Observation of self-phase modulation and small-scale filaments in crystals and glasses', *Physical Review Letters*, **24**, 592–594, doi:10.1103/PhysRevLett.24.592, 1970.

[173] G. New, *Introduction to Nonlinear Optics*, Cambridge University Press, Cambridge, UK, ISBN 0521877016, 2011.

[174] R. W. Boyd, *Nonlinear Optics*, Academic Press, San Diego, CA, USA, ISBN 0121216829, 2003.

[175] J. M. Langridge, T. Laurila, R. S. Watt, R. L. Jones, C. F. Kaminski and J. Hult, 'Cavity enhanced absorption spectroscopy of multiple trace gas species using a supercontinuum radiation source', *Optics Express*, **16**, 10178–10188, doi:10.1364/OE.16.010178, 2008.

[176] M. Islam, L. Ciaffoni, G. Hancock and G. A. D. Ritchie, 'Demonstration of a novel laser-driven light source for broadband spectroscopy between 170 nm and 2.1 μm', *The Analyst*, **138**, 4741–4745, doi:10.1039/c3an01020a, 2013.

[177] C. Xia, Z. Xu, M. N. Islam, F. L. Terry, M. J. Freeman, A. Zakel and J. Mauricio, '10.5 W time-averaged power mid-IR supercontinuum generation extending beyond 4 μm with direct pulse pattern modulation', *IEEE Journal of Selected Topics in Quantum Electronics*, **15**, 422–434, doi:10.1109/JSTQE.2008.2010233, 2009.

[178] Energetiq Technology Inc., 'Energetiq', URL `http://www.energetiq.com`.

[179] C. Kaminski, R. Watt, A. Elder, J. Frank and J. Hult, 'Supercontinuum radiation for applications in chemical sensing and microscopy', *Applied Physics B: Lasers and Optics*, **92**, 367–378, doi:10.1007/s00340-008-3132-1, 2008.

[180] T. L. Koch and U. Koren, 'Semiconductor lasers for coherent optical fiber communications', *Journal of Lightwave Technology*, **8**, 274–293, doi:10.1109/50.50725, 1990.

[181] J. Buus and E. J. Murphy, 'Tunable lasers in optical networks', *Journal of Lightwave Technology*, **24**, 5–11, doi:10.1109/JLT.2005.859839, 2006.

[182] A. Q. Liu and X. M. Zhang, 'A review of MEMS external-cavity tunable lasers', *Journal of Micromechanics and Microengineering*, **17**, R1–R13, doi:10.1088/0960-1317/17/1/R01, 2007.

[183] M. Lackner, M. Schwarzott, F. Winter, B. Kögel, S. Jatta, H. Halbritter and P. Meissner, 'CO and CO_2 spectroscopy using a 60 nm broadband tunable MEMS-VCSEL at $\sim$ 1.55 µm', *Optics Letters*, **31**, 3170–3172, doi:10.1364/OL.31.003170, 2006.

[184] L. A. Coldren, 'Monolithic tunable diode lasers', *IEEE Journal of Selected Topics in Quantum Electronics*, **6**, 988–999, doi:10.1109/2944.902147, 2000.

[185] V. Weldon, D. McInerney, R. Phelan, M. Lynch and J. Donegan, 'Characteristics of several NIR tuneable diode lasers for spectroscopic based gas sensing: a comparison', *Spectrochimica Acta Part A: Molecular and Biomolecular Spectroscopy*, **63**, 1013–1020, doi:10.1016/j.saa.2005.10.051, 2006.

[186] R. Phelan, M. Lynch, J. F. Donegan and V. Weldon, 'Simultaneous multispecies gas sensing by use of a sampled grating distributed Bragg reflector and modulated grating Y laser diode', *Applied Optics*, **44**, 5824–5831, doi:10.1364/AO.44.005824, 2005.

[187] M. Chacinski, M. Isaksson and R. Schatz, 'High-speed direct modulation of widely tunable MG-Y laser', *IEEE Photonics Technology Letters*, **17**, 1157–1159, doi:10.1109/LPT.2005.846489, 2005.

[188] M. Lewander, A. Fried, P. Weibring, D. Richter, S. Spuler and L. Rippe, 'Fast and sensitive time-multiplexed gas sensing of multiple lines using a miniature telecom diode laser between 1529 nm and 1565 nm', *Applied Physics B: Lasers and Optics*, **104**, 715–723, doi:10.1007/s00340-011-4587-z, 2011.

[189] V. Jayaraman, Z.-M. Chuang and L. A. Coldren, 'Theory, design, and performance of extended tuning range semiconductor lasers with sampled gratings', *IEEE Journal of Quantum Electronics*, **29**, 1824–1834, doi:10.1109/3.234440, 1993.

[190] D. Reid, D. Robbins, A. Ward, N. Whitbread, P. Williams, G. Busico, A. Carter, A. Wood, N. Carr, J. Asplin, M. Kearley, W. Hunt, D. Brambley and J. Rawsthorne, 'A novel broadband DBR laser for DWDM networks with simplified quasi-digital wavelength selection', in *2002 Optical Fiber Communication Conference (OFC 2002)*, Anaheim, CA, USA, doi:10.1109/OFC.2002.1036543, 2002.

[191] A. J. Ward, D. J. Robbins, G. Busico, E. Barton, L. Ponnampalam, J. P. Duck, N. D. Whitbread, P. J. Williams, D. C. J. Reid, A. C. Carter and M. J. Wale, 'Widely tunable DS-DBR laser with monolithically integrated SOA: design and performance', *IEEE Journal of Selected Topics in Quantum Electronics*, **11**, 149–156, doi:10.1109/JSTQE.2004.841698, 2005.

[192] L. Ponnampalam, A. J. Ward and D. J. Robbins, 'Monolithic digital supermode distributed Bragg reflector laser with record tuned ex-facet power in excess of 20 dBm over C-band', *Electronics Letters*, **43**, 872–873, doi:10.1049/el:20071370, 2007.

[193] L. Ponnampalam, D. J. Robbins, A. J. Ward, N. D. Whitbread, J. P. Duck, G. Busico and D. J. Bazley, 'Equivalent performance in C- and L-bands of digital supermode distributed Bragg reflector lasers', *IEEE Journal of Quantum Electronics*, **43**, 798–803, doi:10.1109/JQE.2007.902380, 2007.

[194] A. J. Ward, G. Busico, N. D. Whitbread, L. Ponnampalam, J. P. Duck and D. J. Robbins, 'Linewidth in widely tunable digital supermode distributed Bragg reflector lasers: comparison between theory and measurement', *IEEE Journal of Quantum Electronics*, **42**, 1122–1127, doi:10.1109/JQE.2006.882559, 2006.

[195] G. Busico, N. D. Whitbread, P. J. Williams, D. J. Robbins, A. J. Ward and D. C. J. Reid, 'A widely tunable Digital Supermode DBR laser with high SMSR', in *The 28th European Conference on Optical Communication (ECOC 2002)*, Copenhagen, Denmark, 2002.

[196] D. J. Robbins, G. Busico, L. Ponnampalam, J. P. Duck, P. J. Williams, R. Griffin, A. J. Ward, D. C. J. Reid, N. D. Whitbread, E. Barton, B. Reid and K. Kasunic, 'A high power, broadband tuneable laser module based on a DS-DBR laser with integrated SOA', in *2004 Optical Fiber Communication Conference (OFC 2004)*, Los Angeles, CA, USA, 2004.

[197] N. Whitbread, 'Widely tunable lasers: the digital supermode DBR', in *The 16th Annual Meeting of the IEEE Lasers and Electro-Optics Society*, Tuscon, AZ, USA, doi:10.1109/LEOS.2003.1252960, 2003.

[198] A. J. Ward, D. J. Robbins, G. Busico, N. D. Whitbread, P. J. Williams, D. C. J. Reid and J. R. Rawsthorne, 'Modelling of phase-grating based wideband tuneable lasers with simplified quasi-digital wavelength selection', *IEE Proceedings - Optoelectronics*, **150**, 199–204, doi:10.1049/ip-opt:20030315, 2003.

[199] G. Sarlet, G. Morthier, R. Baets, D. J. Robbins and D. C. J. Reid, 'Optimization of multiple exposure gratings for widely tunable lasers', *IEEE Photonics Technology Letters*, **11**, 21–23, doi:10.1109/68.736377, 1999.

[200] A. J. Ward, D. J. Robbins, D. C. J. Reid, N. D. Whitbread, G. Busico, P. J. Williams, J. P. Duck, D. Childs and A. C. Carter, 'Realization of phase grating comb reflectors and their application to widely tunable DBR lasers', *IEEE Photonics Technology Letters*, **16**, 2427–2429, doi:10.1109/LPT.2004.834887, 2004.

[201] A. J. Ward, N. D. Whitbread, P. J. Williams, A. K. Wood and M. J. Wale, 'Extending the tuning range of DS-DBR lasers', in *The IEEE 21st International Semiconductor Laser Conference*, Sorrento, Italy, doi:10.1109/ISLC.2008.4636052, 2008.

[202] L. Ciaffoni, G. Hancock, P. L. Hurst, M. Kingston, C. E. Langley, R. Peverall, G. A. D. Ritchie and K. E. Whittaker, 'Demonstration of a widely tunable digital supermode distributed Bragg reflector laser as a versatile source for near-infrared spectroscopy', *Applied Physics B: Lasers and Optics*, **110**, 139–145, doi:10.1007/s00340-011-4869-5, 2013.

[203] C. E. Langley, *Development of New Technologies for Highly Sensitive Trace Gas Detection*, D.Phil thesis, University of Oxford, 2012.

[204] M. Kingston, *Characterisation and Applications of a Digital Supermode Laser*, Pt II thesis, University of Oxford, 2011.

[205] K. E. Whittaker, L. Ciaffoni, G. Hancock, M. Islam, R. Peverall and G. A. D. Ritchie, 'Combining a DS-DBR laser with QPM-DFG for mid-infrared spectroscopy', *Applied Physics B: Lasers and Optics*, **109**, 423–432, doi:10.1007/s00340-012-5071-0, 2012.

[206] K. E. Whittaker, L. Ciaffoni, G. Hancock, P. L. Hurst, R. Peverall and G. A. D. Ritchie, 'Using a DS-DBR laser for widely tunable near-infrared cavity ring-down spectroscopy', *Applied Physics B: Lasers and Optics*, **116**, 157–168, doi:10.1007/s00340-013-5667-z, 2014.

[207] B. Puttnam, M. Dueser, B. Thomsen, P. Bayvel, A. Bianciotto, R. Gaudino, G. Busico, L. Ponnampalam, D. Robbins and N. Whitbread, 'Burst mode operation of a DS-DBR widely tunable laser for wavelength agile system applications', in *2006 Optical Fiber Communication Conference and the National Fiber Optic Engineers Conference*, Anaheim, CA, USA, 2006.

[208] L. Ponnampalam, N. D. Whitbread, R. Barlow, G. Busico, A. J. Ward, J. P. Duck and D. J. Robbins, 'Dynamically controlled channel-to-channel switching in a full-band DS-DBR laser', *IEEE Journal of Quantum Electronics*, **42**, 223–230, doi:10.1109/JQE.2005.863700, 2006.

[209] L. S. Rothman and L. D. G. Young, 'Infrared energy levels and intensities of carbon dioxide - II', *Journal of Quantitative Spectroscopy and Radiative Transfer*, **25**, 505–524, doi:10.1016/0022-4073(81)90026-1, 1981.

[210] N. P. Caponio, M. Goano, I. Maio, M. Meliga, G. P. Bava, G. Destefanis and I. Montrosset, 'Analysis and design criteria of three-section DBR tunable lasers', *IEEE Journal on Selected Areas in Communications*, **8**, 1203–1213, doi:10.1109/49.57827, 1990.

[211] National Instruments, 'LabVIEW', URL http://www.ni.com/labview/.

[212] D. Halmer, G. von Basum, P. Hering and M. Mürtz, 'Fast exponential fitting algorithm for real-time instrumental use', *Review of Scientific Instruments*, **75**, 2187–2191, doi:10.1063/1.1711189, 2004.

[213] D. R. Skinner and R. E. Whitcher, 'Measurement of the radius of a high-power laser beam near the focus of a lens', *Journal of Physics E: Scientific Instruments*, **5**, 237–238, doi:10.1088/0022-3735/5/3/015, 1972.

[214] K. J. Schulz and W. R. Simpson, 'Frequency-matched cavity ring-down spectroscopy', *Chemical Physics Letters*, **297**, 523–529, doi:10.1016/S0009-2614(98)01173-7, 1998.

[215] G. Rempe, R. J. Thompson, H. J. Kimble and R. Lalezari, 'Measurement of ultralow losses in an optical interferometer', *Optics Letters*, **17**, 363–365, doi:10.1364/OL.17.000363, 1992.

[216] Sintec Optronics Technology Pte Ltd, 'Acousto-optic Modulators (AOMs)', URL http://www.sintecoptronics.com/aom.asp.

[217] M. A. Everest and D. B. Atkinson, 'Discrete sums for the rapid determination of exponential decay constants', *Review of Scientific Instruments*, **79**, 023108, doi:10.1063/1.2839918, 2008.

[218] National Instruments Community, 'Rapid Determination of Exponential Decay Constants', URL http://decibel.ni.com/content/docs/DOC-6237.

[219] T. H. Lee, *The Design of CMOS Radio-Frequency Integrated Circuits*, Cambridge University Press, Cambridge, UK, ISBN 0521835399, 2004.

[220] OriginLab Corporation, 'Origin', URL http://www.originlab.com/.

[221] J. P. M. Hoefnagels, *Cavity Ringdown Study of the Densities and Kinetics of SiH_x radicals in a Remote SiH_4 Plasma*, Masters thesis, Eindhoven University of Technology, 2000.

[222] G. F. Marshall and G. E. Stutz (editors), *Handbook of Optical and Laser Scanning*, CRC Press, Taylor & Francis Group, London, UK, ISBN 1439808791, 2012.

[223] G. P. Agrawal, *Nonlinear Fiber Optics*, Academic Press, London, UK, ISBN 0123695163, 2006.

[224] J. Morville, D. Romanini, M. Chenevier and A. Kachanov, 'Effects of laser phase noise on the injection of a high-finesse cavity', *Applied Optics*, **41**, 6980–6990, doi:10.1364/AO.41.006980, 2002.

[225] P. Werle, R. Mucke and F. Slemr, 'The limits of signal averaging in atmospheric trace-gas monitoring by tunable diode-laser absorption spectroscopy (TDLAS)', *Applied Physics B: Photo-physics and Laser Chemistry*, **57**, 131–139, doi:10.1007/BF00425997, 1993.

[226] N. Kaiser and H. K. Pulker (editors), *Optical Interference Coatings*, Springer-Verlag Berlin and Heidelberg GmbH & Co., Berlin, Germany, ISBN 3540003649, 2003.

[227] O. A. Seppanen, W. J. Fisk and M. J. Mendell, 'Association of ventilation rates and CO_2 concentrations with health and other responses in commercial and institutional buildings', *Indoor Air*, **9**, 226–252, doi:10.1111/j.1600-0668.1999.00003.x, 1999.

[228] S. E. Crowe, '*Helicobacter* infection, chronic inflammation, and the development of malignancy', *Current Opinion in Gastroenterology*, **21**, 32–38, 2005.

[229] P. Malfertheiner, J. E. Dominguez-Munoz, H. Heckenmuller, M. Neubrand, F. H-P and T. Sauerbruch, 'Modified rapid urease test for detection of *Helicobacter pylori* infection', *European Journal of Gastroenterology & Hepatology*, **8**, 53–56, doi:10.1097/00042737-199601000-00010, 1996.

[230] B. E. Dunn, H. Cohen and M. J. Blaser, '*Helicobacter pylori*', *Clinical Microbiology Reviews*, **10**, 720–741, 1997.

[231] A. F. Goddard and R. P. Logan, 'Review article: urea breath tests for detecting *Helicobacter pylori*', *Alimentary Pharmacology & Therapeutics*, **11**, 641–649, doi:10.1046/j.1365-2036.1997.00206.x, 1997.

[232] P. D. Klein, '^{13}C breath tests: visions and realities', *The Journal of Nutrition*, **131**, 1637S–1642S, 2001.

[233] J. P. Gisbert and J. M. Pajares, 'Review article: ^{13}C-urea breath test in the diagnosis of *Helicobacter pylori* infection - a critical review', *Alimentary Pharmacology & Therapeutics*, **20**, 1001–1017, doi:10.1111/j.1365-2036.2004.02203.x, 2004.

[234] K. J. Goodman and J. T. Brenna, 'High sensitivity tracer detection using high-precision gas chromatography-combustion isotope ratio mass spectrometry and highly enriched [U-^{13}C]-labeled precursors', *Analytical Chemistry*, **64**, 1088–1095, doi:10.1021/ac00034a004, 1992.

[235] B. S. Sheu, S. C. Lee, H. B. Yang, H. W. Wu, C. S. Wu, X. Z. Lin and J. J. Wu, 'Lower-dose ^{13}C-urea breath test to detect *Helicobacter pylori* infection - comparison between infrared spectrometer and mass spectrometry analysis', *Alimentary Pharmacology & Therapeutics*, **14**, 1359–1363, doi:10.1046/j.1365-2036.2000.00848.x, 2000.

[236] M. B. Esler, D. W. Griffith, S. R. Wilson and L. P. Steele, 'Precision trace gas analysis by FT-IR spectroscopy. 2. The ^{13}C/^{12}C isotope ratio of CO_2', *Analytical Chemistry*, **72**, 216–221, doi:10.1021/ac990563x, 2000.

[237] F. Jäger, G. Wagner, H. A. J. Meijer and E. R. T. Kerstel, 'Measuring δ^{13}C of atmospheric air with non-dispersive infrared spectroscopy', *Isotopes in Environmental and Health Studies*, **41**, 373–378, doi:10.1080/10256010500384275, 2005.

[238] D. E. Murnick and B. J. Peer, 'Laser-based analysis of carbon isotope ratios', *Science*, **263**, 945–947, doi:10.1126/science.8310291, 1994.

[239] M. Wolff, M. Germer, H. G. Groninga and H. Harde, 'Photoacoustic CO_2 sensor based on a DFB diode laser at 2.7 µm', *The European Physical Journal Special Topics*, **153**, 409–413, doi:10.1140/epjst/e2008-00473-9, 2008.

[240] D. Weidmann, G. Wysocki, C. Oppenheimer and F. Tittel, 'Development of a compact quantum cascade laser spectrometer for field measurements of CO_2 isotopes', *Applied Physics B: Lasers and Optics*, **80**, 255–260, doi:10.1007/s00340-004-1639-7, 2005.

[241] L. G. Sandstrom, S. H. Lundqvist, A. B. Petterson and M. S. Shumate, 'Tunable diode laser spectroscopy at 1.6 and 2 µm for detection of *Helicobacter Pylori* infection using ^{13}C-urea breath test', *IEEE Journal of Selected Topics in Quantum Electronics*, **5**, 1040–1048, doi:10.1109/2944.796328, 1999.

[242] P. de Bievre, M. Gallet, N. E. Holden and I. L. Barnes, 'Isotopic abundances and atomic weights of the elements', *Journal of Physical and Chemical Reference Data*, **13**, 809–891, doi:10.1063/1.555720, 1984.

[243] Systat Software Inc, 'PeakFit', URL `http://www.sigmaplot.com/products/peakfit/peakfit.php`.

[244] W. Chen, J. Cousin, E. Poullet, J. Burie, D. Boucher, X. Gao, M. Sigrist and F. Tittel, 'Continuous-wave mid-infrared laser sources based on difference frequency generation', *Comptes Rendus Physique*, **8**, 1129–1150, doi:10.1016/j.crhy.2007.09.011, 2007.

[245] A. Godard, 'Infrared (2-12 µm) solid-state laser sources: a review', *Comptes Rendus Physique*, **8**, 1100–1128, doi:10.1016/j.crhy.2007.09.010, 2007.

[246] I. T. Sorokina and K. L. Vodopyanov (editors), *Topics in Applied Physics, Vol 89: Solid-State Mid-Infrared Laser Sources*, Springer-Verlag Berlin and Heidelberg GmbH & Co., Berlin, Germany, ISBN 3540006214, 2003.

[247] G. Phillipps, P. Hinske, W. Demtroder, K. Mollmann and R. Beigang, 'NaCl Color center laser with birefringent tuning', *Applied Physics B: Photo-physics and Laser Chemistry*, **47**, 127–133, doi:10.1007/BF00684079, 1988.

[248] S.-C. Hsu, R. H. Schwendeman and M. Gottfried, 'Infrared microwave sideband laser spectroscopy in the CO laser region', *IEEE Journal of Quantum Electronics*, **24**, 2294–2301, doi:10.1109/3.8573, 1988.

[249] G. Magerl, W. Schupita and E. Bonek, 'Tunable CO_2 laser sideband spectrometer', *IEEE Journal of Quantum Electronics*, **18**, 1214–1220, doi:10.1109/JQE.1982.1071701, 1982.

[250] J. Faist, F. Capasso, D. L. Sivco, C. Sirtori, A. L. Hutchinson and A. Y. Cho, 'Quantum cascade laser', *Science*, **264**, 553–556, doi:10.1126/science.264.5158.553, 1994.

[251] F. Capasso, A. Tredicucci, C. Gmachl, D. Sivco, A. Hutchinson, A. Cho and G. Scamarcio, 'High-performance superlattice quantum cascade lasers', *IEEE Journal of Selected Topics in Quantum Electronics*, **5**, 792–807, doi:10.1109/2944.788453, 1999.

[252] C. Gmachl, F. Capasso, D. L. Sivco and A. Y. Cho, 'Recent progress in quantum cascade lasers and applications', *Reports on Progress in Physics*, **64**, 1533–1601, doi:10.1088/0034-4885/64/11/204, 2001.

[253] R. F. Curl, F. Capasso, C. Gmachl, A. A. Kosterev, B. McManus, R. Lewicki, M. Pusharsky, G. Wysocki and F. K. Tittel, 'Quantum cascade lasers in chemical physics', *Chemical Physics Letters*, **487**, 1–18, doi:10.1016/j.cplett.2009.12.073, 2010.

[254] K. Namjou, S. Cai, E. A. Whittaker, J. Faist, C. Gmachl, F. Capasso, D. L. Sivco and A. Y. Cho, 'Sensitive absorption spectroscopy with a room-temperature distributed-feedback quantum-cascade laser', *Optics Letters*, **23**, 219–221, doi:10.1364/OL.23.000219, 1998.

[255] J.-P. H. van Helden, R. Peverall, G. A. D. Ritchie and R. J. Walker, 'Rapid passage effects in nitrous oxide induced by a chirped external cavity quantum cascade laser', *Applied Physics Letters*, **94**, 051116, doi:10.1063/1.3079420, 2009.

[256] A. Evans, J. S. Yu, S. Slivken and M. Razeghi, 'Continuous-wave operation of $\lambda \sim 4.8$ μm quantum-cascade lasers at room temperature', *Applied Physics Letters*, **85**, 2166–2168, doi:10.1063/1.1793340, 2004.

[257] Daylight Solutions Inc, 'Daylight Solutions', URL http://www.daylightsolutions.com/.

[258] Alpes Lasers AS, 'Alpes Lasers', URL http://www.alpeslasers.ch/.

[259] J. S. Yu, S. Slivken, S. R. Darvish, A. Evans, B. Gokden and M. Razeghi, 'High-power, room-temperature, and continuous-wave operation of distributed-feedback quantum-cascade lasers at $\lambda \sim 4.8$ μm', *Applied Physics Letters*, **87**, 041104, doi:10.1063/1.2000343, 2005.

[260] A. Evans, J. Nguyen, S. Slivken, J. S. Yu, S. R. Darvish and M. Razeghi, 'Quantum-cascade lasers operating in continuous-wave mode above 90°C at $\lambda \sim 5.25$ μm', *Applied Physics Letters*, **88**, 051105, doi:10.1063/1.2171476, 2006.

[261] A. Hugi, R. Terazzi, Y. Bonetti, A. Wittmann, M. Fischer, M. Beck, J. Faist and E. Gini, 'External cavity quantum cascade laser tunable from 7.6 to 11.4 μm', *Applied Physics Letters*, **95**, 061103, doi:10.1063/1.3193539, 2009.

[262] G. Wysocki, R. Lewicki, R. F. Curl, F. K. Tittel, L. Diehl, F. Capasso, M. Troccoli, G. Hofler, D. Bour, S. Corzine, R. Maulini, M. Giovannini and J. Faist, 'Widely tunable mode-hop free external cavity quantum cascade lasers for high resolution spectroscopy and chemical sensing', *Applied Physics B: Lasers and Optics*, **92**, 305–311, doi:10.1007/s00340-008-3047-x, 2008.

[263] C. Gmachl, D. L. Sivco, J. N. Baillargeon, A. L. Hutchinson, F. Capasso and A. Y. Cho, 'Quantum cascade lasers with a heterogeneous cascade: two-wavelength operation', *Applied Physics Letters*, **79**, 572–574, doi:10.1063/1.1383806, 2001.

[264] B. G. Lee, M. A. Belkin, C. Pflügl, L. Diehl, H. A. Zhang, R. M. Audet, J. Macarthur, D. P. Bour, S. W. Corzine, G. E. Höfler and F. Capasso, 'DFB quantum cascade laser arrays', *IEEE Journal of Quantum Electronics*, **45**, 554–565, doi:10.1109/JQE.2009.2013175, 2009.

[265] F. Capasso, 'High-performance midinfrared quantum cascade lasers', *Optical Engineering*, **49**, 111102, doi:10.1117/1.3505844, 2010.

[266] J. Röpcke, S. Welzel, N. Lang, F. Hempel, L. Gatilova, O. Guaitella, A. Rousseau and P. Davies, 'Diagnostic studies of molecular plasmas using mid-infrared semiconductor lasers', *Applied Physics B: Lasers and Optics*, **92**, 335–341, doi:10.1007/s00340-008-3094-3, 2008.

[267] J. Y.-T. Huang, D. P. Xu, L. J. Mawst, T. F. Kuech, I. Vurgaftman and J. R. Meyer, 'GaAsSbN-GaAsSb-InP type-II 'W' quantum wells for mid-IR emission', *IEEE Journal of Selected Topics in Quantum Electronics*, **13**, 1065–1073, doi:10.1109/JSTQE.2007.902831, 2007.

[268] R. Q. Yang, 'Infrared laser based on intersubband transitions in quantum wells', *Superlattices and Microstructures*, **17**, 77–83, doi:10.1006/spmi.1995.1017, 1995.

[269] K. Mansour, Y. Qiu, C. J. Hill, A. Soibel and R. Q. Yang, 'Mid-infrared interband cascade lasers at thermoelectric cooler temperatures', *Electronics Letters*, **42**, 1034–1036, doi:10.1049/el:20062442, 2006.

[270] M. Kim, C. L. Canedy, W. W. Bewley, C. S. Kim, J. R. Lindle, J. Abell, I. Vurgaftman and J. R. Meyer, 'Interband cascade laser emitting at $\lambda = 3.75$ µm in continuous wave above room temperature', *Applied Physics Letters*, **92**, 191110, doi:10.1063/1.2930685, 2008.

[271] I. Vurgaftman, C. L. Canedy, C. S. Kim, M. Kim, W. W. Bewley, J. R. Lindle, J. Abell and J. R. Meyer, 'Mid-infrared interband cascade lasers operating at ambient temperatures', *New Journal of Physics*, **11**, 125015, doi:10.1088/1367-2630/11/12/125015, 2009.

[272] I. Vurgaftman, W. W. Bewley, C. L. Canedy, C. S. Kim, M. Kim, J. R. Lindle, C. D. Merritt, J. Abell and J. R. Meyer, 'Mid-IR type-II interband cascade lasers', *IEEE Journal of Selected Topics in Quantum Electronics*, **17**, 1435–1444, doi:10.1109/JSTQE.2011.2114331, 2011.

[273] C. L. Canedy, W. W. Bewley, J. R. Lindle, C. S. Kim, M. Kim, I. Vurgaftman and J. R. Meyer, 'Investigation of mid-infrared type-II W diode lasers', *Journal of Electronic Materials*, **35**, 453–461, doi:10.1007/BF02690532, 2006.

[274] A. Bauer, M. Dallner, M. Kamp, S. Hofling, L. Worschech and A. Forchel, 'Shortened injector interband cascade lasers for 3.3− to 3.6−µm emission', *Optical Engineering*, **49**, 111117, doi:10.1117/1.3505831, 2010.

[275] R. Q. Yang, C. J. Hill, B. Yang and J. K. Liu, 'Room-temperature type-II interband cascade lasers near 4.1 µm', *Applied Physics Letters*, **83**, 2109–2111, doi:10.1063/1.1611260, 2003.

[276] R. Q. Yang, C. J. Hill and B. H. Yang, 'High-temperature and low-threshold midinfrared interband cascade lasers', *Applied Physics Letters*, **87**, 151109, doi:10.1063/1.2103387, 2005.

[277] B. A. Ikyo, I. P. Marko, A. R. Adams, S. J. Sweeney, C. L. Canedy, I. Vurgaftman, C. S. Kim, M. Kim, W. W. Bewley and J. R. Meyer, 'Temperature dependence of 4.1 µm mid-infrared type II 'W' interband cascade lasers', *Applied Physics Letters*, **99**, 021102, doi:10.1063/1.3606533, 2011.

[278] D. Caffey, T. Day, C. S. Kim, M. Kim, I. Vurgaftman, W. W. Bewley, J. R. Lindle, C. L. Canedy, J. Abell and J. R. Meyer, 'Performance characteristics of a continuous-wave compact widely tunable external cavity interband cascade lasers', *Optics Express*, **18**, 15691–15696, doi:10.1364/OE.18.015691, 2010.

[279] D. M. Sonnenfroh, R. T. Wainner and M. G. Allen, 'Interband cascade laser-based sensor for ambient CH_4', *Optical Engineering*, **49**, 111118, doi:10.1117/1.3498769, 2010.

[280] T. Lehnhardt, M. Hummer, K. Rossner, M. Muller, S. Hofling and A. Forchel, 'Continuous wave single mode operation of GaInAsSb/GaSb quantum well lasers emitting beyond 3 µm', *Applied Physics Letters*, **92**, 183508, doi:10.1063/1.2926657, 2008.

[281] M. Hummer, K. Rossner, T. Lehnhardt, M. Muller, A. Forchel, R. Werner, M. Fischer and J. Koeth, 'Long wavelength GaInAsSb-AlGaAsSb distributed-feedback lasers emitting at 2.84 µm', *Electronics Letters*, **42**, 583–584, doi:10.1049/el:20060528, 2006.

[282] M. Grau, C. Lin, O. Dier, C. Lauer and M.-C. Amann, 'Room-temperature operation of 3.26 µm GaSb-based type-I lasers with quinternary AlGaInAsSb barriers', *Applied Physics Letters*, **87**, 241104, doi:10.1063/1.2140875, 2005.

[283] S. Belahsene, L. Naehle, M. Fischer, J. Koeth, G. Boissier, P. Grech, G. Narcy, A. Vicet and Y. Rouillard, 'Laser diodes for gas sensing emitting at 3.06 µm at room temperature', *IEEE Photonics Technology Letters*, **22**, 1084–1086, doi:10.1109/LPT.2010.2049989, 2010.

[284] L. Naehle, S. Belahsene, M. von Edlinger, M. Fischer, G. Boissier, P. Grech, G. Narcy, A. Vicet, Y. Rouillard, J. Koeth and L. Worschech, 'Continuous-wave operation of type-I quantum well DFB laser diodes emitting in 3.4 µm wavelength range around room temperature', *Electronics Letters*, **47**, 46–47, doi:10.1049/el.2010.2733, 2011.

[285] M. H. Dunn and M. Ebrahimzadeh, 'Parametric generation of tunable light from continuous-wave to femtosecond pulses', *Science*, **286**, 1513–1517, doi:10.1126/science.286.5444.1513, 1999.

[286] G. A. Turnbull, D. McGloin, I. D. Lindsay, M. Ebrahimzadeh and M. H. Dunn, 'Extended mode-hop-free tuning by use of a dual-cavity, pump-enhanced optical parametric oscillator', *Optics Letters*, **25**, 341–343, doi:10.1364/OL.25.000341, 2000.

[287] M. Ebrahimzadeh, 'Mid-Infrared Ultrafast and Continuous-Wave Optical Paramertric Oscillators', in *Topics in Applied Physics, Vol. 89: Solid-State Mid-Infrared Laser Sources*, edited by I. Sorokina and K. Vodopyanov, chap. 5, pp. 179–213, Springer-Verlag Berlin and Heidelberg GmbH & Co., Berlin, Germany, ISBN 3540006214, 2003.

[288] A. S. Pine, 'Doppler-limited molecular spectroscopy by difference-frequency mixing', *Journal of the Optical Society of America*, **64**, 1683–1690, doi:10.1364/JOSA.64.001683, 1974.

[289] P. Canarelli, Z. Benko, R. Curl and F. K. Tittel, 'Continuous-wave infrared laser spectrometer based on difference frequency generation in $AgGaS_2$ for high-resolution spectroscopy', *Journal of the Optical Society of America B: Optical Physics*, **9**, 197–202, doi:10.1364/JOSAB.9.000197, 1992.

[290] A. H. Hielscher, C. E. Miller, D. C. Bayard, U. Simon, K. P. Smolka, R. F. Curl and F. K. Tittel, 'Optimization of a midinfrared high-resolution difference-frequency laser spectrometer', *Journal of the Optical Society of America B: Optical Physics*, **9**, 1962–1967, doi:10.1364/JOSAB.9.001962, 1992.

[291] P. N. Butcher and D. Cotter, *The Elements of Nonlinear Optics*, Cambridge University Press, Cambridge, UK, ISBN 0521341833, 1990.

[292] P. Mandel, *Nonlinear Optics*, Wiley-VCH Verlag GmbH & Co., Weinheim, Germany, ISBN 3527409238, 2010.

[293] P. E. Powers, *Fundamentals of Nonlinear Optics*, CRC Press, Taylor & Francis Group, Boca Raton, FL, USA, ISBN 1420093517, 2011.

[294] R. L. Byer and R. L. Herbst, 'Parametric Oscillation and Mixing', in *Topics in Applied Physics, Vol. 16: Nonlinear Infrared Generation*, edited by Y. R. Shen, chap. 3, pp. 81–137, Springer-Verlag Berlin and Heidelberg GmbH & Co., Berlin, Germany, ISBN 0387079459, 1977.

[295] R. C. Miller, 'Dependence of second-harmonic-generation coefficients of $LiNbO_3$ on melt composition', *Journal of Applied Physics*, **42**, 4145–4147, doi:10.1063/1.1659746, 1971.

[296] D. Xue and K. Betzler, 'Influence of optical-damage-resistant dopants on the nonlinear optical properties of lithium niobate', *Applied Physics B: Lasers and Optics*, **72**, 641–645, doi:10.1007/s003400100547, 2001.

[297] C. Fischer and M. Sigrist, 'Mid-IR Difference Frequency Generation', in *Topics in Applied Physics, Vol. 89: Solid-State Mid-Infrared Laser Sources*, edited by I. Sorokina and K. Vodopyanov, chap. 3, pp. 97–140, Springer-Verlag Berlin and Heidelberg GmbH & Co., Berlin, Germany, ISBN 3540006214, 2003.

[298] D. Hum and M. Fejer, 'Quasi-phasematching', *Comptes Rendus Physique*, **8**, 180–198, doi:10.1016/j.crhy.2006.10.022, 2007.

[299] D. Richter, A. Fried and P. Weibring, 'Difference frequency generation laser based spectrometers', *Laser & Photonics Review*, **3**, 343–354, doi:10.1002/lpor.200810048, 2009.

[300] G. J. Edwards and M. Lawrence, 'A temperature-dependent dispersion equation for congruently grown lithium niobate', *Optical and Quantum Electronics*, **16**, 373–375, doi:10.1007/BF00620081, 1984.

[301] J. Q. Yao and T. S. Fahlen, 'Calculations of optimum phase match parameters for the biaxial crystal $KTiOPO_4$', *Journal of Applied Physics*, **55**, 65–68, doi:10.1063/1.332850, 1984.

[302] D. H. Jundt, 'Temperature-dependent Sellmeier equation for the index of refraction, n_e, in congruent lithium niobate', *Optics Letters*, **22**, 1553–1555, doi:10.1364/OL.22.001553, 1997.

[303] R. Bartlome, J. M. Rey and M. W. Sigrist, 'Vapor-phase infrared laser spectroscopy: from gas sensing to forensic urinalysis', *Analytical Chemistry*, **80**, 5334–5341, doi:10.1021/ac8001897, 2008.

[304] M. Seiter, D. Keller and M. Sigrist, 'Broadly tunable difference-frequency spectrometer for trace gas detection with noncollinear critical phase-matching in $LiNbO_3$', *Applied Physics B: Lasers and Optics*, **67**, 351–356, doi:10.1007/s003400050515, 1998.

[305] J. A. Armstrong, N. Bloembergen, J. Ducuing and P. S. Pershan, 'Interactions between light waves in a nonlinear dielectric', *Physical Review*, **127**, 1918–1939, doi:10.1103/PhysRev.127.1918, 1962.

[306] P. A. Franken and J. F. Ward, 'Optical harmonics and nonlinear phenomena', *Reviews of Modern Physics*, **35**, 23–39, doi:10.1103/RevModPhys.35.23, 1963.

[307] M. M. Fejer, G. A. Magel, D. H. Jundt and R. L. Byer, 'Quasi-phase-matched second harmonic generation: tuning and tolerances', *IEEE Journal of Quantum Electronics*, **28**, 2631–2654, doi:10.1109/3.161322, 1992.

[308] S.-N. Zhu, Y.-Y. Zhu, H.-F. Wang, Z.-Y. Zhang, N.-B. Ming, W.-Z. Shen, Y. Chang and X.-C. Shen, 'Second-order quasi-phase-matched blue light generation in a bulk periodically poled $LiTaO_3$', *Journal of Physics D: Applied Physics*, **28**, 2389–2391, doi:10.1088/0022-3727/28/11/025, 1995.

[309] M. Okada, K. Takizawa and S. Ieiri, 'Second harmonic generation by periodic laminar structure of nonlinear optical crystal', *Optics Communications*, **18**, 331–334, doi:10.1016/0030-4018(76)90144-9, 1976.

[310] H. Ishizuki, I. Shoji and T. Taira, 'Periodical poling characteristics of congruent MgO:$LiNbO_3$ crystals at elevated temperature', *Applied Physics Letters*, **82**, 4062–4064, doi:10.1063/1.1582371, 2003.

[311] P. Maddaloni, G. Gagliardi, P. Malara and P. de Natale, 'A 3.5-mW continuous-wave difference-frequency source around 3 µm for sub-Doppler molecular spectroscopy', *Applied Physics B: Lasers and Optics*, **80**, 141–145, doi:10.1007/s00340-004-1714-0, 2005.

[312] W. Denzer, G. Hancock, A. Hutchinson, M. Munday, R. Peverall and G. A. D. Ritchie, 'Mid-infrared generation and spectroscopy with a PPLN ridge waveguide', *Applied Physics B: Lasers and Optics*, **86**, 437–441, doi:10.1007/s00340-006-2570-x, 2007.

[313] J. Liao, J.-L. He, H. Liu, H.-T. Wang, S. N. Zhu, Y. Y. Zhu and N. B. Ming, 'Simultaneous generation of red, green, and blue quasi-continuous-wave coherent radiation based on multiple quasi-phase-matched interactions from a single, aperiodically-poled $LiTaO_3$', *Applied Physics Letters*, **82**, 3159–3161, doi:10.1063/1.1570941, 2003.

[314] K. Fradkin, A. Arie, A. Skliar and G. Rosenman, 'Tunable midinfrared source by difference frequency generation in bulk periodically poled $KTiOPO_4$', *Applied Physics Letters*, **74**, 914–916, doi:10.1063/1.123408, 1999.

[315] K. Fradkin-Kashi, A. Arie, P. Urenski and G. Rosenman, 'Mid-infrared difference-frequency generation in periodically poled $KTiOAsO_4$ and application to gas sensing', *Optics Letters*, **25**, 743–745, doi:10.1364/OL.25.000743, 2000.

[316] P. A. Budni, L. A. Pomeranz, M. L. Lemons, C. A. Miller, J. R. Mosto and E. P. Chicklis, 'Efficient mid-infrared laser using 1.9-µm-pumped Ho:YAG and $ZnGeP_2$ optical parametric oscillators', *Journal of the Optical Society of America B: Optical Physics*, **17**, 723–728, doi:10.1364/JOSAB.17.000723, 2000.

[317] S. Haidar, K. Miyamoto and H. Ito, 'Generation of tunable mid-IR ($5.5 - 9.3$ µm) from a 2-µm pumped $ZnGeP_2$ optical parametric oscillator', *Optics Communications*, **241**, 173–178, doi:10.1016/j.optcom.2004.06.065, 2004.

[318] T. H. Allik, S. Chandra, D. M. Rines, P. G. Schunemann, J. A. Hutchinson and R. Utano, 'Tunable $7 - 12$ µm optical parametric oscillator using a Cr,Er:YSGG laser to pump CdSe and $ZnGeP_2$ crystals', *Optics Letters*, **22**, 597–599, doi:10.1364/OL.22.000597, 1997.

[319] B. Sumpf, D. Rehle, T. Kelz and H.-D. Kronfeldt, 'A tunable diode-laser spectrometer for the MIR region near 7.2 µm applying difference-frequency generation in $AgGaSe_2$', *Applied Physics B: Lasers and Optics*, **67**, 369–373, doi:10.1007/s003400050518, 1998.

[320] D. Lee, T. Kaing and J. Zondy, 'An all-diode-laser-based, dual-cavity $AgGaS_2$ cw difference-frequency source for the $9-11$ μm range', *Applied Physics B: Lasers and Optics*, **367**, 363–367, doi:10.1007/s003400050517, 1998.

[321] K. L. Vodopyanov, O. Levi, P. S. Kuo, T. J. Pinguet, J. S. Harris, M. M. Fejer, B. Gerard, L. Becouarn and E. Lallier, 'Optical parametric oscillation in quasi-phase-matched GaAs', *Optics Letters*, **29**, 1912–1914, doi:10.1364/OL.29.001912, 2004.

[322] S. Bisson, T. Kulp, O. Levi, J. Harris and M. Fejer, 'Long-wave IR chemical sensing based on difference frequency generation in orientation-patterned GaAs', *Applied Physics B: Lasers and Optics*, **85**, 199–206, doi:10.1007/s00340-006-2311-1, 2006.

[323] W. C. Eckhoff, R. S. Putnam, S. Wang, R. F. Curl and F. K. Tittel, 'A continuously tunable long-wavelength cw IR source for high-resolution spectroscopy and trace-gas detection', *Applied Physics B: Lasers and Optics*, **63**, 437–441, doi:10.1007/s003400050106, 1996.

[324] R. S. Putnam and D. G. Lancaster, 'Continuous-wave laser spectrometer automatically aligned and continuously tuned from 11.8 to 16.1 μm by use of diode-laser-pumped difference-frequency generation in GaSe', *Applied Optics*, **38**, 1513–1522, doi:10.1364/AO.38.001513, 1999.

[325] K. L. Vodopyanov, 'Mid-infrared optical parametric generator with extra-wide ($3-19$-μm) tunability: applications for spectroscopy of two-dimensional electrons in quantum wells', *Journal of the Optical Society of America B: Optical Physics*, **16**, 1579–1586, doi:10.1364/JOSAB.16.001579, 1999.

[326] D. A. Bryan, R. Gerson and H. E. Tomaschke, 'Increased optical damage resistance in lithium niobate', *Applied Physics Letters*, **44**, 847–849, doi:10.1063/1.94946, 1984.

[327] D. Lu, L. Qian, Y. Li, H. Yang, H. Zhu and D. Fan, 'Phase velocity nonuniformity-resulted beam patterns in difference frequency generation', *Optics Express*, **15**, 5050–5058, doi:10.1364/OE.15.005050, 2007.

[328] S. Guha, 'Focusing dependence of the efficiency of a singly resonant optical parametric oscillator', *Applied Physics B: Lasers and Optics*, **66**, 663–675, doi:10.1007/s003400050453, 1998.

[329] G. D. Boyd and D. A. Kleinman, 'Parametric interaction of focused gaussian light beams', *Journal of Applied Physics*, **39**, 3597–3639, doi:10.1063/1.1656831, 1968.

[330] P. Malara, P. Maddaloni, G. Mincuzzi, S. de Nicola and P. de Natale, 'Non-collinear quasi phase matching and annular profiles in difference frequency generation with

focused Gaussian beams', *Optics Express*, **16**, 8056–8066, doi:10.1364/OE.16.008056, 2008.

[331] S. Borri, P. Cancio, P. de Natale, G. Giusfredi, D. Mazzotti and F. Tamassia, 'Power-boosted difference-frequency source for high-resolution infrared spectroscopy', *Applied Physics B: Lasers and Optics*, **76**, 473–477, doi:10.1007/s00340-003-1133-7, 2003.

[332] T. B. Chu and M. Broyer, 'Intracavity cw difference frequency generation by mixing three photons and using gaussian laser beams', *Journal de Physique*, **46**, 523–533, doi:10.1051/jphys:01985004604052300, 1985.

[333] L. Ciaffoni, *Laser Spectroscopy for the Detection of Volatile Sulfur-containing Compounds in Breath*, D.Phil thesis, University of Oxford, 2010.

[334] Y. S. Kim and R. T. Smith, 'Thermal expansion of lithium tantalate and lithium niobate single crystals', *Journal of Applied Physics*, **40**, 4637–4641, doi:10.1063/1.1657244, 1969.

[335] G. D. Boyd and A. Ashkin, 'Theory of parametric oscillator threshold with single-mode optical masers and observation of amplification in $LiNbO_3$', *Physical Review*, **146**, 187–198, doi:10.1103/PhysRev.146.187, 1966.

[336] M. Seiter and M. W. Sigrist, 'Trace-gas sensor based on mid-IR difference-frequency generation in PPLN with saturated output power', *Infrared Physics & Technology*, **41**, 259–269, doi:10.1016/S1350-4495(00)00043-8, 2000.

[337] P. Weibring, D. Richter, J. G. Walega and A. Fried, 'First demonstration of a high performance difference frequency spectrometer on airborne platforms', *Optics Express*, **15**, 13476–13495, doi:10.1007/BF00425997, 2007.

[338] D. Marinov, J. Rey and M. W. Sigrist, 'Mid-infrared spectroscopic investigation of methylamines by a continuous-wave difference-frequency-generation-based system', *Applied Optics*, **47**, 1956–1962, doi:10.1364/AO.47.001956, 2008.

[339] R. Grilli, L. Ciaffoni, G. Hancock, R. Peverall, G. A. D. Ritchie and A. J. Orr-Ewing, 'Mid-infrared ethene detection using difference frequency generation in a quasi-phase-matched $LiNbO_3$ waveguide', *Applied Optics*, **48**, 5696–5703, doi:10.1364/AO.48.005696, 2009.

[340] L. Ciaffoni, R. Grilli, G. Hancock, A. J. Orr-Ewing, R. Peverall and G. A. D. Ritchie, '3.5-μm high-resolution gas sensing employing a $LiNbO_3$ QPM-DFG waveguide module', *Applied Physics B: Lasers and Optics*, **94**, 517–525, doi:10.1007/s00340-008-3291-0, 2009.

[341] D. Richter, P. Weibring, A. Fried, O. Tadanaga, Y. Nishida, M. Asobe and H. Suzuki, 'High-power, tunable difference frequency generation source for absorption spectroscopy based on a ridge waveguide periodically poled lithium niobate crystal', *Optics Express*, **15**, 564–571, doi:10.1364/OE.15.000564, 2007.

[342] O. Tadanaga, T. Yanagawa, Y. Nishida, H. Miyazawa, K. Magari, M. Asobe and H. Suzuki, 'Efficient 3-μm difference frequency generation using direct-bonded quasi-phase-matched $LiNbO_3$ ridge waveguides', *Applied Physics Letters*, **88**, 061101, doi:10.1063/1.2172400, 2006.

[343] S. Kuma, Y. Miyamoto, K. Tsutsumi, N. Sasao and S. Uetake, '4.8 μm difference-frequency generation using a waveguide-PPLN crystal and its application to mid-infrared Lamb-dip spectroscopy', *Optics Letters*, **38**, 2825–2828, doi:10.1364/OL.38.002825, 2013.

[344] L. G. Deng, K. He, T. Zhou and C. Li, 'Formation and evolution of far-field diffraction patterns of divergent and convergent Gaussian beams passing through self-focusing and self-defocusing media', *Journal of Optics A: Pure and Applied Optics*, **7**, 409–415, doi:10.1088/1464-4258/7/8/011, 2005.

[345] T. Theeg, H. Sayinc, J. Neumann and D. Kracht, 'All-fiber counter-propagation pumped single frequency amplifier stage with 300 W output power', *IEEE Photonics Technology Letters*, **24**, 1864–1867, doi:10.1109/LPT.2012.2217487, 2012.

[346] K. Rottwitt, A. Bjarklev, J. H. Povlsen, O. Lumholt and T. P. Rasmussen, 'Fundamental design of a distributed erbium-doped fiber amplifier for long-distance transmission', *Journal of Lightwave Technology*, **10**, 1544–1552, doi:10.1109/50.184892, 1992.

[347] J. M. Ezquerro, G. Hernández, M. Nombela, O. G. Calderón and S. Melle, 'Fast light enhancement by bidirectional pumping in erbium-doped fibers', *Journal of Nonlinear Optical Physics & Materials*, **19**, 153–165, doi:10.1142/S021886351000498X, 2010.

[348] V. Sinivasagam, M. A. G. Abushagur, K. Dimyati and F. Tumiran, 'New pumping scheme for high gain and low noise figure in an erbium-doped fiber amplifier', *IEICE Electronics Express*, **2**, 154–158, doi:10.1587/elex.2.154, 2005.

[349] A. Cokrak and A. Altuncu, 'Gain and noise figure performance of erbium doped fiber amplifiers (EDFAs)', *Journal of Electrical & Electronics Engineering*, **4**, 1111–1122, doi:10.1016/j.ijleo.2010.02.028, 2004.

[350] D. A. Roberts, 'Simplified characterization of uniaxial and biaxial nonlinear optical crystals: a plea for standardization of nomenclature and conventions', *IEEE Journal of Quantum Electronics*, **28**, 2057–2074, doi:10.1109/3.159516, 1992.

[351] L. E. Myers, R. C. Eckardt, M. M. Fejer, R. L. Byer, W. R. Bosenberg and J. W. Pierce, 'Quasi-phase-matched optical parametric oscillators in bulk periodically poled $LiNbO_3$', *Journal of the Optical Society of America B: Optical Physics*, **12**, 2102–2116, doi:10.1364/JOSAB.12.002102, 1995.

[352] D. Richter, D. G. Lancaster and F. K. Tittel, 'Development of an automated diode-laser-based multicomponent gas sensor', *Applied Optics*, **39**, 4444–4450, doi:10.1364/AO.39.004444, 2000.

[353] D. G. Lancaster, A. Fried, B. Wert, B. Henry and F. K. Tittel, 'Difference-frequency-based tunable absorption spectrometer for detection of atmospheric formaldehyde', *Applied Optics*, **39**, 4436–4443, doi:10.1364/AO.39.004436, 2000.

[354] H. Y. Clark, L. Corner, W. Denzer, G. Hancock, A. Hutchinson, M. Islam, R. Peverall and G. A. D. Ritchie, 'Difference frequency generation in periodically poled lithium niobate and its use in the detection of atmospheric methane', *Chemical Physics Letters*, **399**, 102–108, doi:10.1016/j.cplett.2004.09.146, 2004.

[355] L. Deng, L. Han, W. Liang, Z. Cao, C. Xu, W. Zhang, Z. Gong and X. Gao, 'A mid-infrared spectrometer based on difference frequency generation', *Optics and Lasers in Engineering*, **45**, 1055–1058, doi:10.1016/j.optlaseng.2007.05.002, 2007.

[356] A. A. Kosterev, A. L. Malinovsky, F. K. Tittel, C. Gmachl, F. Capasso, D. L. Sivco, J. N. Baillargeon, A. L. Hutchinson and A. Y. Cho, 'Cavity ringdown spectroscopic detection of nitric oxide with a continuous-wave quantum-cascade laser', *Applied Optics*, **40**, 5522–5529, doi:10.1364/AO.40.005522, 2001.

[357] L. Menzel, A. A. Kosterev, R. F. Curl, F. K. Tittel, C. Gmachl, F. Capasso, D. L. Sivco, J. N. Baillargeon, A. L. Hutchinson, A. Y. Cho and W. Urban, 'Spectroscopic detection of biological NO with a quantum cascade laser', *Applied Physics B: Lasers and Optics*, **72**, 859–863, doi:10.1007/s003400100562, 2001.

[358] Y. A. Bakhirkin, A. A. Kosterev, C. Roller, R. F. Curl and F. K. Tittel, 'Mid-infrared quantum cascade laser based off-axis integrated cavity output spectroscopy for biogenic nitric oxide detection', *Applied Optics*, **43**, 2257–2266, doi:10.1364/AO.43.002257, 2004.

[359] M. R. McCurdy, Y. Bakhirkin, G. Wysocki and F. K. Tittel, 'Performance of an exhaled nitric oxide and carbon dioxide sensor using quantum cascade laser-based integrated cavity output spectroscopy', *Journal of Biomedical Optics*, **12**, 034034, doi:10.1117/1.2747608, 2007.

[360] Y. Bakhirkin, A. Kosterev, R. Curl, F. Tittel, D. Yarekha, L. Hvozdara, M. Giovannini and J. Faist, 'Sub-ppbv nitric oxide concentration measurements using cw

thermoelectrically cooled quantum cascade laser-based integrated cavity output spectroscopy', *Applied Physics B: Lasers and Optics*, **82**, 149–154, doi:10.1007/s00340-005-2058-0, 2006.

[361] M. McCurdy, Y. Bakhirkin and F. Tittel, 'Quantum cascade laser-based integrated cavity output spectroscopy of exhaled nitric oxide', *Applied Physics B: Lasers and Optics*, **85**, 445–452, doi:10.1007/s00340-006-2365-0, 2006.

[362] J. Miller, Y. Bakhirkin, T. Ajtai, F. Tittel, C. Hill and R. Yang, 'Detection of formaldehyde using off-axis integrated cavity output spectroscopy with an interband cascade laser', *Applied Physics B: Lasers and Optics*, **85**, 391–396, doi:10.1007/s00340-006-2310-2, 2006.

[363] D. D. Arslanov, S. M. Cristescu and F. J. M. Harren, 'Optical parametric oscillator based off-axis integrated cavity output spectroscopy for rapid chemical sensing', *Optics Letters*, **35**, 3300–3302, doi:10.1364/OL.35.003300, 2010.

[364] R. Grilli, L. Ciaffoni and A. J. Orr-Ewing, 'Phase-shift cavity ring-down spectroscopy using mid-IR light from a difference frequency generation PPLN waveguide', *Optics Letters*, **35**, 1383–1385, doi:10.1364/OL.35.001383, 2010.

[365] D. Halmer, G. von Basum, P. Hering and M. Mürtz, 'Mid-infrared cavity leak-out spectroscopy for ultrasensitive detection of carbonyl sulfide', *Optics Letters*, **30**, 2314–2316, doi:10.1364/OL.30.002314, 2005.

[366] K. Heinrich, T. Fritsch, P. Hering and M. Mürtz, 'Infrared laser-spectroscopic analysis of ^{14}NO and ^{15}NO in human breath', *Applied Physics B: Lasers and Optics*, **95**, 281–286, doi:10.1007/s00340-009-3423-1, 2009.

[367] M. Sowa, M. Mürtz and P. Hering, 'Mid-infrared laser spectroscopy for online analysis of exhaled CO', *Journal of Breath Research*, **4**, 047101, doi:10.1088/1752-7155/4/4/047101, 2010.

[368] B. A. Paldus, C. C. Harb, T. G. Spence, R. N. Zare, C. Gmachl, F. Capasso, D. L. Sivco, J. N. Baillargeon, A. L. Hutchinson and A. Y. Cho, 'Cavity ringdown spectroscopy using mid-infrared quantum-cascade lasers', *Optics Letters*, **25**, 666–668, doi:10.1364/OL.25.000666, 2000.

[369] A. Popp, F. Müller, F. Kühnemann, S. Schiller, G. von Basum, H. Dahnke, P. Hering and M. Mürtz, 'Ultra-sensitive mid-infrared cavity leak-out spectroscopy using a cw optical parametric oscillator', *Applied Physics B: Lasers and Optics*, **75**, 751–754, doi:10.1007/s00340-002-1047-9, 2002.

[370] J. Morville, D. Romanini, A. A. Kachanov and M. Chenevier, 'Two schemes for trace detection using cavity ringdown spectroscopy', *Applied Physics B: Lasers and Optics*, **78**, 465–476, doi:10.1007/s00340-003-1363-8, 2004.

[371] G. Maisons, P. Gorrotxategi-Carbajo, M. Carras and D. Romanini, 'Optical-feedback cavity-enhanced absorption spectroscopy with a quantum cascade laser', *Optics Letters*, **35**, 3607–3609, doi:10.1364/OL.35.00360, 2010.

[372] P. Gorrotxategi-Carbajo, E. Fasci, I. Ventrillard, M. Carras, G. Maisons and D. Romanini, 'Optical-feedback cavity-enhanced absorption spectroscopy with a quantum-cascade laser yields the lowest formaldehyde detection limit', *Applied Physics B: Lasers and Optics*, **110**, 309–314, doi:10.1007/s00340-013-5340-6, 2013.

[373] A. G. V. Bergin, G. Hancock, G. A. D. Ritchie and D. Weidmann, 'Linear cavity optical-feedback cavity-enhanced absorption spectroscopy with a quantum cascade laser', *Optics Letters*, **38**, 2475–2477, doi:10.1364/OL.38.002475, 2013.

[374] M. S. Taubman, T. L. Myers, B. D. Cannon and R. M. Williams, 'Stabilization, injection and control of quantum cascade lasers, and their application to chemical sensing in the infrared', *Spectrochimica Acta Part A: Molecular and Biomolecular Spectroscopy*, **60**, 3457–3468, doi:10.1016/j.saa.2003.12.057, 2004.

[375] M. W. Porambo, B. M. Siller, J. M. Pearson and B. J. McCall, 'Broadly tunable mid-infrared noise-immune cavity-enhanced optical heterodyne molecular spectrometer', *Optics Letters*, **37**, 4422–4424, doi:10.1364/OL.37.004422, 2012.

[376] A. Foltynowicz, P. Mas, T. Ban, F. Adler, K. C. Cossel, T. C. Briles and J. Ye, 'Optical frequency comb spectroscopy', *Faraday Discussions*, **150**, 23–31, doi:10.1039/c1fd00005e, 2011.

[377] A. Foltynowicz, P. Masowski, A. Fleisher, B. Bjork and J. Ye, 'Cavity-enhanced optical frequency comb spectroscopy in the mid-infrared application to trace detection of hydrogen peroxide', *Applied Physics B: Lasers and Optics*, **110**, 163–175, doi:10.1007/s00340-012-5024-7, 2013.

[378] D. Mazzotti, P. Cancio, G. Giusfredi, P. de Natale and M. Prevedelli, 'Frequency-comb-based absolute frequency measurements in the mid-infrared with a difference-frequency spectrometer', *Optics Letters*, **30**, 997–999, doi:10.1364/OL.30.000997, 2005.

[379] D. Mazzotti, P. Cancio, A. Castrillo, I. Galli, G. Giusfredi and P. de Natale, 'A comb-referenced difference-frequency spectrometer for cavity ring-down spectroscopy in the 4.5 μm region', *Journal of Optics A: Pure and Applied Optics*, **8**, S490–S493, doi:10.1088/1464-4258/8/7/S28, 2006.

[380] I. Galli, S. Bartalini, P. Cancio, G. Giusfredi, D. Mazzotti and P. de Natale, 'Ultra-stable, widely tunable and absolutely linked mid-IR coherent source', *Optics Express*, **17**, 9582–9587, doi:10.1364/OE.17.009582, 2009.

[381] I. Galli, S. Bartalini, S. Borri, P. Cancio, G. Giusfredi, D. Mazzotti and P. de Natale, 'Ti:sapphire laser intracavity difference-frequency generation of 30 mW cw radiation around 4.5 μm', *Optics Letters*, **35**, 3616–3618, doi:10.1364/OL.35.003616, 2010.

[382] I. Galli, P. C. Pastor, G. di Lonardo, L. Fusina, D. Mazzotti, F. Tamassia and P. de Natale, 'The ν_3 band of $^{14}C^{16}O_2$ molecule measured by optical-frequency-comb-assisted cavity ring-down spectroscopy', *Molecular Physics*, **109**, 2267–2272, doi:10.1080/00268976.2011.614284, 2011.

[383] P. Cancio, S. Bartalini, S. Borri, I. Galli, G. Gagliardi, G. Giusfredi, P. Maddaloni, P. Malara, D. Mazzotti and P. de Natale, 'Frequency-comb-referenced mid-IR sources for next-generation environmental sensors', *Applied Physics B: Lasers and Optics*, **102**, 255–269, doi:10.1007/s00340-010-4216-2, 2011.

[384] K. E. Whittaker, L. Ciaffoni, G. Hancock, R. Peverall and G. A. D. Ritchie, 'A DFG-based cavity ring-down spectrometer for trace gas sensing in the mid-infrared', *Applied Physics B: Lasers and Optics*, **109**, 333–343, doi:10.1007/s00340-012-5150-2, 2012.

[385] D. S. Sayres, E. J. Moyer, T. F. Hanisco, J. M. St Clair, F. N. Keutsch, A. O'Brien, N. T. Allen, L. Lapson, J. N. Demusz, M. Rivero, T. Martin, M. Greenberg, C. Tuozzolo, G. S. Engel, J. H. Kroll, J. B. Paul and J. G. Anderson, 'A new cavity based absorption instrument for detection of water isotopologues in the upper troposphere and lower stratosphere', *Review of Scientific Instruments*, **80**, 044102, doi:10.1063/1.3117349, 2009.

[386] K. W. Aniolek, P. E. Powers and T. J. Kulp, 'Cavity ringdown laser absorption spectroscopy with a 1 kHz mid-infrared periodically poled lithium niobate optical parametric generator/ optical parametric amplifier', *Chemical Physics Letters*, **302**, 555–562, doi:10.1016/S0009-2614(99)00139-6, 1999.

[387] B. A. Richman, K. W. Aniolek, T. J. Kulp and S. E. Bisson, 'Continuously tunable, single-longitudinal-mode, pulsed mid-infrared optical parametric oscillator based on periodically poled lithium niobate', *Journal of the Optical Society of America B: Optical Physics*, **17**, 1233–1239, doi:10.1364/JOSAB.17.001233, 2000.

[388] J. Wojtas, J. Mikolajczyk, M. Nowakowski, B. Rutecka, R. Medrzycki and Z. Bielecki, 'Applying CEAS method to UV, VIS, and IR spectroscopy sensors', *Bulletin of the*

Polish Acadamey of Sciences: Technical Sciences, **59**, 415–418, doi:10.2478/v10175-011-0050-x, 2011.

[389] T. Stacewicz, J. Wojtas, Z. Bielecki, M. Nowakowski and J. Mikoajczyk, 'Cavity ring down spectroscopy: detection of trace amounts of substance', *Opto-Electronics Review*, **20**, 53–60, doi:10.2478/s11772, 2012.

[390] J. Scherer, D. Voelkel and D. Rakestraw, 'Infrared cavity ringdown laser absorption spectroscopy (IR-CRLAS) in low pressure flames', *Applied Physics B: Lasers and Optics*, **64**, 699–705, doi:10.1007/s003400050236, 1997.

[391] H. Sumizawa, H. Yamada and K. Tonokura, 'Real-time monitoring of nitric oxide in diesel exhaust gas by mid-infrared cavity ring-down spectroscopy', *Applied Physics B: Lasers and Optics*, **100**, 925–931, doi:10.1007/s00340-010-4138-z, 2010.

[392] Y. Yamamoto, H. Sumizawa, H. Yamada and K. Tonokura, 'Real-time measurement of nitrogen dioxide in vehicle exhaust gas by mid-infrared cavity ring-down spectroscopy', *Applied Physics B: Lasers and Optics*, **105**, 923–931, doi:10.1007/s00340-011-4647-4, 2011.

[393] K. R. Parameswaran, D. I. Rosen, M. G. Allen, A. M. Ganz and T. H. Risby, 'Off-axis integrated cavity output spectroscopy with a mid-infrared interband cascade laser for real-time breath ethane measurements', *Applied Optics*, **48**, B73–B79, doi:10.1364/AO.48.000B73, 2009.

[394] J. Peltola, M. Vainio, V. Ulvila, M. Siltanen, M. Metsälä and L. Halonen, 'Off-axis re-entrant cavity ring-down spectroscopy with a mid-infrared continuous-wave optical parametric oscillator', *Applied Physics B: Lasers and Optics*, **107**, 839–847, doi:10.1007/s00340-012-5074-x, 2012.

[395] P. Maddaloni, P. Malara, E. de Tommasi, M. de Rosa, I. Ricciardi, G. Gagliardi, F. Tamassia, G. di Lonardo and P. de Natale, 'Absolute measurement of the S(0) and S(1) lines in the electric quadrupole fundamental band of D_2 around 3 μm', *The Journal of Chemical Physics*, **133**, 154317, doi:10.1063/1.3493393, 2010.

[396] C. R. Bucher, K. K. Lehmann, D. F. Plusquellic and G. T. Fraser, 'Doppler-free nonlinear absorption in ethylene by use of continuous-wave cavity ringdown spectroscopy', *Applied Optics*, **39**, 3154–3164, doi:10.1364/AO.39.003154, 2000.

[397] J. B. Paul, R. A. Provencal and R. J. Saykally, 'Characterization of the $(D_2O)_2$ hydrogen-bond-acceptor antisymmetric stretch by IR cavity ringdown laser absorption spectroscopy', *The Journal of Physical Chemistry A*, **102**, 3279–3283, doi:10.1021/jp980763x, 1998.

[398] D. Zhao, J. Guss, A. J. Walsh and H. Linnartz, 'Mid-infrared continuous wave cavity ring-down spectroscopy of a pulsed hydrocarbon plasma', *Chemical Physics Letters*, **565**, 132–137, doi:10.1016/j.cplett.2013.02.025, 2013.

[399] G. A. Marcus and H. A. Schwettman, 'Cavity ringdown spectroscopy of thin films in the mid-infrared', *Applied Optics*, **41**, 5167–5171, doi:10.1364/AO.41.005167, 2002.

[400] H. Feng, E. Patzak and J. Sanitar, 'Methods for stabilizing the gain of EDFAs in burst switching optical networks', *Photonic Network Communications*, **4**, 151–166, doi:10.1023/A:1015339328411, 2002.

[401] L. G. Kazovsky, S.-W. Wong, V. Gudla, P. T. Afshar, S.-H. Yen, S. Yamashita and Y. Yan, 'Challenges in next-generation optical access networks: addressing reach extension and security weaknesses', *IET Optoelectronics*, **5**, 133–143, doi:10.1049/iet-opt.2011.0027, 2011.

[402] S. Kassi, A. Campargue, K. Pachucki and J. Komasa, 'The absorption spectrum of D_2: ultrasensitive cavity ring down spectroscopy of the (2-0) band near 1.7 μm and accurate *ab initio* line list up to 24 000 cm^{-1}', *The Journal of Chemical Physics*, **136**, 184309, doi:10.1063/1.4707708, 2012.

[403] Pacific Northwest National Laboratory, 'Vapor Phase Infrared Spectral Library', URL http://nwir.pnl.gov.

[404] J. J. Harrison, N. D. Allen and P. F. Bernath, 'Infrared absorption cross sections for acetone (propanone) in the 3 μm region', *Journal of Quantitative Spectroscopy and Radiative Transfer*, **112**, 53–58, doi:10.1016/j.jqsrt.2010.08.011, 2011.

[405] National Institute of Standards and Technology, 'NIST Chemistry WebBook', URL http://webbook.nist.gov/chemistry/.

[406] P. J. Crutzen, 'Methane's sinks and sources', *Nature*, **350**, 380–381, doi:10.1038/350380a0, 1991.

[407] S. Tylor, '$^{13}C/^{12}C$ Ratios in Atmospheric Methane and Some of Its Sources', in *Stable Isotopes in Ecological Research*, edited by P. Rundel, J. Ehleringer and K.A. Nagy, chap. 22, pp. 395–409, Springer-Verlag Berlin and Heidelberg GmbH & Co., New York, NY, USA, ISBN 0387967125, 1988.

[408] C. M. Stevens and A. Engelkemeir, 'Stable carbon isotopic composition of methane from some natural and anthropogenic sources', *Journal of Geophysical Research*, **93**, 725–733, doi:10.1029/JD093iD01p00725, 1988.

[409] E. J. Mroz, 'Deuteromethanes: potential fingerprints of the sources of atmospheric methane', *Chemosphere*, **26**, 45–53, doi:10.1016/0045-6535(93)90411-W, 1993.

[410] J. W. Forsman, P. M. Sinclair, A. D. May, P. Duggan and J. R. Drummond, 'Departures from the soft collision model for Dicke narrowing: Raman measurements in the Q branch of D_2', *The Journal of Chemical Physics*, **97**, 5355–5362, doi:10.1063/1.463795, 1992.

[411] K. C. Smyth, G. J. Rosasco and W. S. Hurst, 'Measurement and rate law analysis of D_2 Q-branch line broadening coefficients for collisions with D_2, He, Ar, H_2, and CH_4', *The Journal of Chemical Physics*, **87**, 1001–1011, doi:10.1063/1.453333, 1987.

[412] R. Blackmore, S. Green and L. Monchick, 'Dicke narrowing of the polarized Stokes-Raman Q branch of the $\nu = 0 \rightarrow 1$ transition of D_2 in He', *The Journal of Chemical Physics*, **91**, 3846–3853, doi:10.1063/1.457640, 1989.

[413] K. Musa-Veloso, S. S. Likhodii and S. C. Cunnane, 'Breath acetone is a reliable indicator of ketosis in adults consuming ketogenic meals', *The American Journal of Clinical Nutrition*, **76**, 65–70, 2002.

[414] K. Musa-Veloso, S. S. Likhodii, E. Rarama, S. Benoit, Y.-M. C. Liu, D. Chartrand, R. Curtis, L. Carmant, A. Lortie, F. J. E. Comeau and S. C. Cunnane, 'Breath acetone predicts plasma ketone bodies in children with epilepsy on a ketogenic diet', *Nutrition*, **22**, 1–8, doi:10.1016/j.nut.2005.04.008, 2006.

[415] C. Tassopoulos, D. Barnett and T. R. Fraser, 'Breath-acetone and blood-sugar measurements in diabetes', *The Lancet*, **293**, 1282–1286, doi:10.1016/S0140-6736(69)92222-3, 1969.

[416] P. R. Galassetti, B. Novak, D. Nemet, C. Rose-Gottron, D. M. Cooper, S. Meinardi, R. Newcomb, F. Zaldivar and D. R. Blake, 'Breath ethanol and acetone as indicators of serum glucose levels: an initial report', *Diabetes Technology & Therapeutics*, **7**, 115–123, doi:10.1089/dia.2005.7.115, 2005.

[417] T. D. C. Minh, D. R. Blake and P. R. Galassetti, 'The clinical potential of exhaled breath analysis for diabetes mellitus', *Diabetes Research and Clinical Practice*, **97**, 195–205, doi:10.1016/j.diabres.2012.02.006, 2012.

[418] G. Herzberg, *Molecular Spectra And Molecular Structure. Volume II: Infrared And Raman Spectra Of Polyatomic Molecules*, Van Nostrand Reinhold Company, London, UK, ISBN 0442033869, 1945.

[419] T. Shimanouchi, *Tables of Molecular Vibrational Frequencies: Consolidated Volume 1*, National Standard Reference Data System (NSRDS), Washington, DC, USA, 1972.

[420] A. S. Pine, 'High-resolution methane ν_3-band spectra using a stabilized tunable difference-frequency laser system', *Journal of the Optical Society of America*, **66**, 97–108, doi:10.1364/JOSA.66.000097, 1976.

[421] L. R. Brown, D. C. Benner, J. P. Champion, V. M. Devi, L. Fejard, R. R. Gamache, T. Gabard, J. C. Hilico, B. Lavorel, M. Loete, G. C. Mellau, A. Nikitin, A. S. Pine, A. Predoi-Cross, C. P. Rinsland, O. Robert, R. L. Sams, M. A. H. Smith, S. A. Tashkun and V. G. Tyuterev, 'Methane line parameters in HITRAN', *Journal of Quantitative Spectroscopy and Radiative Transfer*, **82**, 219–238, doi:10.1016/S0022-4073(03)00155-9, 2003.

[422] P. J. Brannon, C. H. Church and C. W. Peters, 'Electric field induced spectra of molecular hydrogen, deuterium and deuterium hydride', *Journal of Molecular Spectroscopy*, **27**, 44–54, doi:10.1016/0022-2852(68)90018-0, 1968.

[423] D. E. Jennings, A. Weber and J. W. Brault, 'Raman spectroscopy of gases with a Fourier transform spectrometer: the spectrum of D_2', *Applied Optics*, **25**, 284–290, doi:10.1364/AO.25.000284, 1986.

[424] G. J. Rosasco, W. J. Bowers, W. S. Hurst, J. P. Looney, K. C. Smyth and A. D. May, 'Simultaneous forwardbackward Raman scattering studies of D_2 broadened by D_2, He, and Ar', *The Journal of Chemical Physics*, **94**, 7625–7633, doi:10.1063/1.460149, 1991.

[425] S. Fakhr-Eslam, G. Sheldon, P. Sinclair, J. Drummond and A. May, 'Anomalous broadening and shifting in D_2 and D_2−He mixtures', *Journal of Quantitative Spectroscopy and Radiative Transfer*, **68**, 377–399, doi:10.1016/S0022-4073(00)00031-5, 2001.

[426] A. R. W. McKellar and T. Oka, 'A study of the electric quadrupole fundamental band of D_2 using an infrared difference frequency laser system', *Canadian Journal of Physics*, **56**, 1315–1320, doi:10.1139/p78-172, 1978.

[427] M. Gupta, T. Owano, D. S. Baer and A. O'Keefe, 'Quantitative determination of the (2,0) band of deuterium in the near infrared via off-axis ICOS', *Chemical Physics Letters*, **441**, 204–208, doi:10.1016/j.cplett.2007.05.031, 2007.

[428] J. Komasa, K. Piszczatowski, G. Lach, M. Przybytek, B. Jeziorski and K. Pachucki, 'Quantum electrodynamics effects in rovibrational spectra of molecular hydrogen', *Journal of Chemical Theory and Computation*, **7**, 3105–3115, doi:10.1021/ct200438t, 2011.

[429] P. Maddaloni, P. Malara and P. de Natale, 'Simulation of Dicke-narrowed molecular spectra recorded by off-axis high-finesse optical cavities', *Molecular Physics*, **108**, 749–755, doi:10.1080/00268971003601571, 2010.

[430] C. D. Rodgers, 'Collisional narrowing: its effect on the equivalent widths of spectral lines', *Applied Optics*, **15**, 714–716, doi:10.1364/AO.15.000714, 1976.

[431] D. H. Rank and T. A. Wiggins, 'Collision narrowing of spectral lines. H_2 quadrupole spectrum', *The Journal of Chemical Physics*, **39**, 1348–1349, doi:10.1063/1.1734441, 1963.

[432] F. Herbert, 'Spectrum line profiles: a generalized Voigt function including collisional narrowing', *Journal of Quantitative Spectroscopy and Radiative Transfer*, **14**, 943–951, doi:10.1016/0022-4073(74)90021-1, 1974.

[433] J. O. Hirschfelder, C. F. Curtiss and R. B. Bird, *The Molecular Theory of Gases and Liquids*, John Wiley & Sons, Inc., New York, NY, USA, ISBN 0471400653, 1964.

[434] D. Long, D. Havey, M. Okumura, H. Pickett, C. Miller and J. Hodges, 'Laboratory measurements and theoretical calculations of O_2 A band electric quadrupole transitions', *Physical Review A*, **80**, 042513, doi:10.1103/PhysRevA.80.042513, 2009.

[435] S. Kassi and A. Campargue, 'Cavity ring down spectroscopy with 5×10^{-13} cm^{-1} sensitivity', *The Journal of Chemical Physics*, **137**, 234201, doi:10.1063/1.4769974, 2012.

[436] M. A. Henesian, M. D. Duncan, R. L. Byer and A. D. May, 'Absolute Raman frequency measurement of the $Q(2)$ line in D_2 using cw CARS', *Optics Letters*, **1**, 149–151, doi:10.1364/OL.1.000149, 1977.

[437] A. Hutchinson, *Diode Laser Studies of Trace Species and their Reactions*, D.Phil thesis, University of Oxford, 2006.

[438] P. Groner, S. Albert, E. Herbst, F. C. de Lucia, F. J. Lovas, B. J. Drouin and J. C. Pearson, 'Acetone: laboratory assignments and predictions through 620 GHz for the vibrational-torsional ground state', *The Astrophysical Journal Supplement Series*, **142**, 145–151, doi:10.1086/341221, 2002.

[439] M. Gianella and M. W. Sigrist, 'Infrared spectroscopy on smoke produced by cauterization of animal tissue', *Sensors*, **10**, 2694–2708, doi:10.3390/s100402694, 2010.

[440] F. di Francesco, R. Fuoco, M. Trivella and A. Ceccarini, 'Breath analysis: trends in techniques and clinical applications', *Microchemical Journal*, **79**, 405–410, doi:10.1016/j.microc.2004.10.008, 2005.

[441] S. Chen, L. Zieve and V. Mahadeva, 'Mercaptans and dimethyl sulfide in breath of patients with cirrhosis of liver - effect of feeding methionine', *Journal of Laboratory and Clinical Medicine*, **75**, 628–635, 1970.

[442] C. J. McClain, L. Zieve, W. M. Doizaki, S. Gilberstadt and G. R. Onstad, 'Blood methanethiol in alcoholic liver disease with and without hepatic encephalopathy', *Gut*, **21**, 318–323, doi:10.1136/gut.21.4.318, 1980.

[443] H. J. Blom, P. Ferenci, G. Grimm, S. H. Yap and A. Tangerman, 'The role of methanethiol in the pathogenesis of hepatic encephalopathy', *Hepatology*, **13**, 445–454, doi:10.1016/0270-9139(91)90297-9, 1991.

[444] K. Yaegaki, 'Oral malodorous compounds are periodontally pathogenic and carcinogenic', *Japanese Dental Science Review*, **44**, 100–108, doi:10.1016/j.jdsr.2008.06.003, 2008.

[445] S. S. Sehnert, L. Jiang, J. F. Burdick and T. H. Risby, 'Breath biomarkers for detection of human liver diseases: preliminary study', *Biomarkers*, **7**, 174–187, doi:10.1080/135475001101, 2002.

[446] F. J. Zieve, L. Zieve, W. M. Doizaki and R. B. Gilsdorf, 'Synergism between ammonia and fatty acids in the production of coma: implications for hepatic coma', *The Journal of Pharmacology and Experimental Therapeutics*, **191**, 10–16, 1974.

[447] I. A. May and E. L. Pace, 'The vibrational spectra of methanethiol', *Spectrochimica Acta Part A: Molecular Spectroscopy*, **24**, 1605–1615, doi:10.1016/0584-8539(68)80209-0, 1968.

[448] F. L. Bettens, K. V. L. N. Sastry, E. Herbst, S. Albert, L. C. Oesterling and F. C. de Lucia, 'The millimeter- and submillimeter- wave spectrum of methyl mercaptan (CH_3SH)', *The Astrophysical Journal*, **510**, 789–794, doi:10.1086/306633, 1999.

[449] F. Adler, P. Masowski, A. Foltynowicz, K. C. Cossel, T. C. Briles, I. Hartl and J. Ye, 'Mid-infrared Fourier transform spectroscopy with a broadband frequency comb', *Optics Express*, **18**, 21861–21872, doi:10.1364/OE.18.021861, 2010.

[450] V. L. Kasyutich and P. A. Martin, 'On quantitative measurements in phase-shift off-axis cavity-enhanced absorption spectroscopy', *Chemical Physics Letters*, **446**, 206–211, doi:10.1016/j.cplett.2007.08.032, 2007.

[451] S. G. Baran, *Gas-Phase Detection Methods Using Diode Lasers*, D.Phil thesis, University of Oxford, 2009.

[452] K. A. Kvenvolden and B. W. Rogers, 'Gaia's breath - global methane exhalations', *Marine and Petroleum Geology*, **22**, 579–590, doi:10.1016/j.marpetgeo.2004.08.004, 2005.

[453] Nuphoton Technologies, 'Nuphoton', URL `http://nuphoton.com/`.

[454] CRD Optics Inc., 'CRD Optics', URL `http://www.crd-optics.com/index.html`.

[455] P. Mochalski, B. Wzorek, I. Sliwka and A. Amann, 'Improved pre-concentration and detection methods for volatile sulphur breath constituents', *Journal of Chromatography B: Analytical Technologies in the Biomedical and Life Sciences*, **877**, 1856–1866, doi:10.1016/j.jchromb.2009.05.010, 2009.

[456] A. Tangerman, M. T. Meuwese-Arends and J. H. M. van Tongeren, 'A new sensitive assay for measuring volatile sulphur compounds in human breath by Tenax trapping and gas chromatography and its application in liver cirrhosis', *Clinica Chimica Acta*, **130**, 103–110, doi:10.1016/0009-8981(83)90263-2, 1983.

[457] N. Ochiai, M. Takino, S. Daishima and D. B. Cardin, 'Analysis of volatile sulphur compounds in breath by gas chromatography-mass spectrometry using a three-stage cryogenic trapping preconcentration system', *Journal of Chromatography B: Analytical Technologies in the Biomedical and Life Sciences*, **762**, 67–75, doi:10.1016/S0378-4347(01)00343-7, 2001.

[458] P. A. Bélanger, 'Beam propagation and the ABCD ray matrices', *Optics Letters*, **16**, 196–198, doi:10.1364/OL.16.000196, 1991.

[459] W. S. C. Chang, *Principles of Lasers and Optics*, Cambridge University Press, Cambridge, UK, ISBN 0521642299, 2005.

[460] M. Polyanskiy, 'Refractive Index Database', URL `http://refractiveindex.info/`.